

# The Fabrication and Functionalisation of Schottky Barriers on Stainless Steel

Submitted in accordance with the requirements for degree of Doctor of  
Philosophy

University of Leeds, School of Electronic and Electrical Engineering and  
School of Chemical and Process Engineering

Niamh Ellen Ryall

December 2017

# Declaration

The candidate confirms that the work submitted is his/her own, except where work which has formed part of jointly authored publications has been included. The contribution of the candidate and the other authors to this work has been explicitly indicated below. The candidate confirms that appropriate credit has been given within the thesis where reference has been made to the work of others.

**Chapters 3, 4 and 5** includes the following work:

Ryall, N. E., Crook, R. & Weinstein, J. A. A dye-sensitised Schottky junction device fabricated from nanomaterials on a stainless steel substrate. *Mater. Res. Innov.* 1–6 (2017).

The work in detailed within this paper was all the candidate's own with guidance from all the authors.

This copy has been supplied on the understanding that it is copyright material and no quotation from the thesis may be published without proper acknowledgement.

© 2017 The University of Leeds and Niamh Ellen Ryall

The right of Niamh Ellen Ryall to be identified as Author of this work has been asserted by her in accordance with the Copyright, Designs and Patents Act 1988.

# Acknowledgements

I would like to express my gratitude to my supervisors, Dr Rolf Crook and Professor Julia Weinstein, for their support and advice.

I would also like to thank the directors of my Centre for Doctoral Training in Molecular-Scale Engineering and my funders, the EPSRC and the hosts of my laboratory placements. I would like to thank my fellow students from the CDT who have been such fantastic company.

Thank you to the occupants of the Energy and Resources Building at the University of Leeds for the endless cups of coffee and great conversation. Also to the assorted chemists and physicists of the University of Sheffield who have brightened my day over the years in particular Nicola, Andy, Dan, Will and Liam.

A special thanks to my friends, especially Tom, George, Steven, Michael, Aidan and Ed and also to Martin and John for supporting me through this work. A special thanks to John and Ness for their company walking and cycling.

I am grateful to my mother, Mary, who was endlessly patient of my unusual interests and my frequently making a mess. I am also indebted to my sister, Aishling, for all she has taught me.

# Abstract

Schottky barriers are a rectifying contact that can form between a semiconductor and a metal. The rectification is due to the formation of a depletion region in the semiconductor. This has been shown to be useful in the formation of a simple photovoltaic device on a stainless steel substrate, using silver nanowires to form the Schottky barrier.

In this work, knowledge from crystal growth and rheology studies were used to inform a method of solvothermal synthesis of  $\text{TiO}_2$  in water and deposition on steel, avoiding the use of organic additives. TiN coated steel was used as a substrate, resulting in highly rectifying contacts.

Although it was possible to model the current-voltage characteristics accurately, fits to thermionic emission theory were usually poor due to the impact of the changing surface at the range of temperatures used, the scan speed and environment. From the few accurate fits, estimates of dopant density and thus depletion region could be made and photocurrent efficiency in these regions estimated.

As would be expected, the devices have a photocurrent in the UV region, where  $\text{TiO}_2$  absorbs light. However, the photocurrents observed on sol based devices are measured in both directions, the "reverse" direction is consistent with band gap excitation and the "forward" current is in the opposite direction. The other strongly absorbing species other than the  $\text{TiO}_2$  is the silver nanowires. The presence of the sol has a large impact on the UV-vis absorption profiles of silver nanowires and shows a peak at the same energy as the "forward" photocurrent. This is also present in the visible region in the presence of some dyes. This may suggest a plasmonic photocatalytic mechanism can be dominant under some conditions and this reaction may be sensitized by dyes such as  $\text{Ru}(\text{dcbpy})_2(\text{NCS})_2$  or alizarin red.

# Contents

1. Chapter One: Context, Introduction and Aims	
1.1. Context .....	1
1.1.1. The current state of energy production.....	1
1.1.2. Climate Change.....	2
1.2. Aim and Thesis outline.....	3
1.3. Introduction .....	6
1.3.1. Current solar technologies .....	6
1.3.2. Cost .....	6
1.3.3. Photovoltaic devices .....	7
1.3.4. Semiconductors .....	9
1.3.5. Band theory .....	9
1.3.6. TiO <sub>2</sub> as a compound semiconductor .....	12
1.3.6.1. Band structure .....	12
1.3.6.2. Doping.....	13
1.3.6.3. Oxygen vacancies .....	13
1.3.6.4. Phase.....	14
1.3.7. Conductivity of Mesoporous films.....	14
1.3.8. Fields in particle films.....	16
1.3.9. Memristive switching .....	17
1.3.10. Electron-hole separation.....	17
1.3.11. Schottky barriers .....	17
1.3.11.1. Electrochemical analogy .....	18
1.3.11.2. The Schottky-Mott rule.....	20
1.3.11.3. Breakdown of the Schottky-Mott rule .....	22

1.3.12. Band bending.....	24
1.3.13. Diode Characteristics .....	26
1.3.14. Photoelectric measurements.....	26
1.4. Conclusion .....	27
2. Chapter Two: Literature Review	
2.1. Overview .....	28
2.2. Introduction to Schottky barrier photovoltaics .....	28
2.2. Direct excitation in the visible region.....	29
2.3. Direct excitation in the UV region.....	31
2.3.1. Constant response above the band gap .....	31
2.3.2. Peaks in response above the band gap .....	32
2.3.3. Summary of visible and UV sensitive Schottky barrier devices .....	33
2.4. Large area nanoparticulate Schottky barriers using sensitized films .....	35
2.5. Current collection at Schottky barriers by catalysed chemical reaction ..	38
2.6. The use of Schottky barriers to improve current collection in DSSCs .....	39
2.7. Conclusion.....	41
3. Chapter Three: Device fabrication	
3.1. Overview .....	41
3.2. Methods and Analysis .....	42
3.2.1. SEM .....	42
3.2.2. XRD .....	42
3.2.3. Electrochemical measurements .....	43
3.2.4. UV-vis spectroscopy .....	43
3.2.5. Photocurrent measurements .....	43
3.2.6 Arc Lamp Calibration .....	43
3.2.7. Solvothermal synthesis and dip coating.....	44
3.2.8 Silver nanowire deposition.....	45
3.2.9. Capacitance measurements.....	46

3.2.10. Dyes.....	47
3.2.11. Quantum dots.....	47
3.2.12. TaON.....	48
3.2.13. Spin coating dense TiO <sub>2</sub> layers .....	48
3.2.14. Steel preparation.....	48
3.3. Introduction.....	48
3.3.1. Fabrication of Schottky barriers.....	49
3.3.2. Stainless steel at high temperatures .....	51
3.3.2.1. Oxide scale.....	51
3.3.2.2. Impact of temperature.....	51
3.3.2.3. Impact of salts.....	52
3.3.3. Substrates and the impact of metal diffusion .....	52
3.3.4. Formation of crystalline titania films .....	54
3.3.5. Phase.....	55
3.3.6. The amorphous to anatase transition.....	55
3.3.7. Solvothermal synthesis .....	57
3.3.7.1. The effect of pH .....	58
3.3.7.2. Aging and solvothermal synthesis .....	58
3.3.7.3. Partial crystallinity of annealed TiO <sub>2</sub> films.....	59
3.3.7.4. DSC studies of crystallisation.....	59
3.3.8. Film formation .....	61
3.3.8.1. Electrostatic characteristics .....	61
3.3.8.2. Literature on film formation .....	61
3.3.8.3. Metal-TiO <sub>2</sub> interactions .....	65
3.3.9. TiO <sub>2</sub> films on sheet materials .....	65
3.4. Results .....	66
3.4.1. Overview of fabrication work .....	66
3.4.2. Fabrication of Schottky barrier devices on stainless steel.....	66
3.4.2.1. Optimisation of sols .....	66

3.4.2.2. Diffusion barrers .....	70
3.4.2.3. Temperature and time of sintering.....	73
3.4.2.4. Steel grade and impact of temperature .....	74
3.4.3. Diffusion from other metal substrates and its impact .....	77
3.4.4. Film thickness.....	77
3.4.5. Continuity of TiO <sub>2</sub> films .....	77
3.4.6. Crystallinity.....	78
3.4.7. TiN coated steel as a potential substrate .....	83
3.4.8. TiN devices .....	84
3.5. Conclusion.....	86
4. Chapter Four: Electrical characterisation	
4.1. Overview .....	87
4.2. Introduction.....	87
4.2.1. Electrical characteristics and models .....	88
4.2.2. Schottky barrier height.....	89
4.2.2.1. The hole barrier .....	91
4.2.3. Depletion regions and capacitance .....	91
4.2.4. Capacitance and applied bias .....	94
4.2.5. The Ideal Diode Equation .....	98
4.2.6. Impact of applied potential to barrier height.....	98
4.2.7. Methods for measuring barrier height .....	99
4.2.7.1. Current-voltage measurements of Schottky barrier diodes.....	99
4.2.7.2. Thermionic emission theory.....	99
4.2.8. Electrical characteristics and models .....	100
4.2.9. Changing IV characteristics of Schottky barriers with UV light.....	100
4.3. Results and Analysis.....	102
4.3.1. The measurement of devices by current-voltage measurements.....	102
4.3.2. Silver nanowire corrosion .....	103

4.3.3. Fitting IV curves with built-in MATLAB functions .....	104
4.3.3.1. Improvements to fitting to model exponential function .....	106
4.3.3.2. Pre-exponential factor variation.....	107
4.3.4. Other electrical transport fits .....	108
4.3.5. Speed studies.....	109
4.3.6. Changes in electrical characteristics with water .....	110
4.3.6.1. Water and light .....	112
4.3.7. Geometry arguments for limits of geometry .....	113
4.3.8. Fits to thermionic emission theory .....	115
4.3.8.1. Temperature dependency of reverse saturation currents .....	116
4.3.8.2. Example relatively successful thermionic emission studies .....	117
4.3.8.3. Thermionic emission fits at high speed.....	119
4.3.9. Attempts to improve area of the devices .....	119
4.3.10. Frequency domain analysis.....	120
4.3.11. Sol based derived device capacitance .....	121
4.3.11.1. Frequency .....	121
4.3.11.2. Phase .....	122
4.3.11.3. Absolute values of capacitance .....	122
4.3.11.4. The impact of water on capacitance.....	124
4.3.12. Summary of sol results .....	127
4.3.13. Comparison to TiN derived devices .....	127
4.4. Conclusions and future work.....	129
5. Chapter Five: Photocurrent from band gap excitation in Schottky barrier devices	
5.1. Overview .....	131
5.2. Introduction.....	132
5.2.1. The limitation to efficiency of $V_{OC}$ to Schottky barrier devices.....	132
5.2.2. Contributions to photocurrents in $TiO_2$ Schottky barrier devices....	133
5.2.3. Quantum dots.....	133

5.2. Results.....	134
5.2.1. Visible light photocurrents from semiconductors.....	134
5.2.1.1. TaON.....	134
5.2.1.2. CdSe, CdS and CdTe.....	135
5.2.2. UV photocurrents.....	136
5.2.2.1. Increasing crystallinity in devices.....	136
5.2.2.2. Deposition of TiO <sub>2</sub> on silver nanowires.....	138
5.2.3. Improving UV efficiencies by layered structures.....	140
5.2.4. Impact of silver structures.....	142
5.2.5. Impact of sintering time.....	145
5.2.6. TiN/Steel samples for higher efficiency devices.....	145
5.2.7. Reduction of series resistance with spun coat dense layers.....	147
5.2.8. Area estimates to calculate efficiency.....	147
5.2.9. Efficiency estimates from area measurements.....	149
5.2.10. Photocurrent under nitrogen.....	150
5.3. Conclusion.....	151
6. Chapter Six: Competing photocurrent processes in the UV region	
6.1. Overview.....	152
6.2. Introduction.....	153
6.2.1. Predictable photo-action spectra for Schottky barrier devices.....	155
6.2.2. Metal-Semiconductor interaction mechanisms.....	155
6.2.3. Introduction to plasmonics.....	156
6.2.3.1. Frequency dependence.....	157
6.2.3.2. Drude and Lorentz models.....	157
6.2.3.3. Models to describe plasmonic excitation.....	158
6.2.3.4. Quantized energy levels.....	159
6.2.3.5. Localised surface plasmons.....	159
6.2.3.6. Modelling the production of hot carriers.....	160

6.2.4. Silver nanowire plasmonics .....	161
6.2.5. Plasmonic Photocatalysis .....	162
6.2.5.1. Examples of plasmonic photocatalysis .....	163
6.2.6. Field enhancements by particle geometry .....	164
6.2.7. Light absorption .....	164
6.2.8. Energy transfer .....	165
6.2.9. Plasmonic solar cells .....	165
6.2.10. Polarisation sensitivity to direct excitation .....	168
6.2.11. Criticism of charge transfer mechanisms .....	168
6.2.12. Photocatalytic plasmonic reductions .....	168
6.2.13. Photocatalysis of TiO <sub>2</sub> .....	169
6.2.13.1. Surface states .....	169
6.3. Results .....	170
6.3.1. Competing photocurrent processes in the UV region .....	170
6.3.2. Possible mechanisms .....	171
6.3.2.1. Controlling for silver nanowire absorption .....	173
6.3.2.2. Setting a convention .....	174
6.3.3. The simplest case: P25 on an early device .....	174
6.3.4. Chromia layers .....	175
6.3.5. Current direction .....	177
6.3.6. Directionality and energy of peaks in increasing crystallinity of sols .....	182
6.3.7. Temperature and time of annealing .....	185
6.3.8. UV-vis studies .....	187
6.3.8.1. UV/vis absorption studies .....	187
6.3.8.2. Concentration studies .....	187
6.3.8.3. Impact of solvent .....	190
6.3.9. Temperature studies .....	190
6.4. Conclusions .....	192

7. Chapter 7: Competing photocurrent processes in the visible region	
7.1. Overview .....	195
7.2. Introduction .....	196
7.2.1. Dye functionalisation of Schottky barriers .....	196
7.2.2. Dye degradation .....	197
7.2.3. Material considerations in dye degradation .....	198
7.2.4. Mechanisms for dye photocatalysis .....	199
7.2.4.1. Increased light harvesting .....	199
7.2.4.2. Amplification of absorption by dyes .....	200
7.2.4.3. Sensitization mechanism .....	200
7.2.4.4. Interaction of the LUMO and the conduction band .....	201
7.2.4.5. Direct excitation over the band gap of a material .....	202
7.2.5. Impact of surface states on dye degradation .....	203
7.2.6. Metal nanoparticles as electron sinks .....	204
7.2.7. Reduction of oxygen .....	204
7.2.8. Prevention of electron transfer .....	205
7.2.9. Summary of literature results .....	206
7.3. Results .....	209
7.3.1. Optimisation .....	210
7.3.1.1. Amorphous devices and quantum dots .....	210
7.3.1.2. Partially crystalline devices .....	210
7.3.2. The use of dyes .....	213
7.3.3. Ru(dcbpy) <sub>2</sub> (NCS) <sub>2</sub> dye on amorphous devices .....	214
7.3.4. TiN devices .....	214
7.3.5. Area estimates .....	216
7.3.6. Organic dyes .....	217
7.3.7. Dyes on sol substrates .....	219
7.3.7.1. Partially crystalline sol .....	219

7.3.7.2. Single wavelength radiation.....	222
7.3.8. UV-vis studies silver nanowires.....	227
7.3.8.1. Comparing photocurrents and Ru(dcbpy) <sub>2</sub> (NCS) <sub>2</sub> .....	228
7.3.8.2. Impact of dye choice.....	230
7.3.8.3. Impact of solvent.....	230
7.4. Discussion of mechanism .....	231
7.5. Conclusion.....	236
8.1. Conclusion.....	237
8.2. Future Work .....	241
8.2.1. Chapter 3.....	241
8.2.2. Chapter 4.....	241
8.2.3. Chapter 5.....	242
8.2.4. Chapter 6.....	243
8.2.5. Chapter 7.....	243
Appendix 1: Thermionic emission fits for sol devices .....	244
Appendix 2: UV-vis photocurrent and Tauc fits for increasing solvothermal reflux times.....	247
Appendix 3: Dielectric constants, pKa and the impact of solvent on the difference gradient for increasing silver nanowire concentration .....	250

# Abbreviations

A: Amp

AC: Alternating current

AFM: Atomic Force Microscopy

AgNW: Silver nanowires

AM 1.5: Reference Solar Spectral Irradiance at 37 ° degree tilt

ASTMG173-03: Reference Solar Spectral Irradiance at 37 ° degree tilt

DC: Direct current

DFT: Density Functional Theory

DSC: Differential Scanning Calorimetry

DSSC: Dye Sensitized Solar Cell

EDX: Energy-dispersive X-ray spectroscopy

$E_F$ : Fermi energy

EQE: External Quantum Efficiency

FTO: Fluorine doped Tin Oxide

FWHM: Full Width Half Maximum

HOMO: Highest Occupied Molecular Orbital

IR: Infra-red

I: Current

$I_0$ : Reverse saturation current

IPA: Isopropyl alcohol

ITO: Indium Tin Oxide

IV curve: Current-voltage curve

FTO: Fluorine Doped Tin Oxide

FWHM: Full Width Half Maximum

LSPRs: Localised surface plasmon resonances

LUMO: Lowest Unoccupied Molecular Orbitals

MB: Methylene blue

MBE: Molecular Beam Epitaxy

NHE: Normal Hydrogen Electrode

P3MT: Poly(3-methylthiophene)

PEDOT:PSS : Poly(3,4-ethylenedioxythiophene) polystyrene sulfonate

QD: Quantum Dot

RCP: Representative Concentration Pathways

$\text{Ru}(\text{dcbpy})_2(\text{NCS})_2$  : *cis*-Bis(isothiocyanato)bis(2,2'-bipyridyl-4,4'-dicarboxylato)ruthenium(II)

SEM: Scanning Electron Microscopy

SHE: Standard (or Normal) Hydrogen Electrode

TiN: Titanium nitride

UV: Ultraviolet

V: Voltage

$V_{\text{RMS}}$ : Root mean squared voltage

XRD: X-Ray Diffraction

# List of Figures

## Chapter 1

Figure 1.1: Blue line: AM 1.5 from ASTM G173-03 is the spectral intensity as averaged at  $37^\circ$  tilt for the latitude of mainland US over 1 year, shown in blue.<sup>1</sup> Some common semiconductor band gaps are shown as orange lines and are, in increasing wavelength, diamond, GaN, SiC, ZnSe, AlP, ZnTe, GaP, AlAs, AlSb, GaAs, InP, Si, Ge, InAs.<sup>2</sup> Semiconductors made from abundant materials have band gaps shown as grey lines and in increasing wavelength are  $\text{TiO}_2$ ,  $\text{C}_3\text{N}_4$ ,  $\text{WO}_3$ ,  $\text{Fe}_2\text{O}_3$ ,  $\text{Cu}_2\text{O}$  and Si.<sup>2</sup>

Figure 1.2: Illustration of how bands form from a number of orbitals, illustrating how bonding and antibonding orbitals become bands.

Figure 1.3.: Illustration of band theory from the linear combination of orbitals. On the right, the overlap of bands is illustrated to explain how some materials such as divalent metals can show high conductivity.

Figure 1.4: Demonstrating absorption for a range of  $\text{TiO}_2$  sols used in this work and inset showing Tauc plots for the same sols.

Figure 1.5: Electrode in contact with ion containing solution.

Figure 1.6: Illustration of the formation of a Schottky barrier.

Figure 1.7: Illustration of the lining up of vacuum levels to derive the Schottky-Mott rule.

Figure 1.8.: Illustration of non-continuity in vacuum level. Left; simple measurement of metal Fermi level,  $E_F$ . Centre; demonstrating periodicity in metal  $E_F$ , right; demonstrating this in terms of an unequal vacuum level if the  $E_F$  is assumed to be constant.

Figure 1.9: Modelling Poisson's equations to relate carrier density to electric field and energy. At 0 on the x-coordinate is the contact between the metal (negative direction) and the semiconductor (positive direction).

## Chapter 2

Figure 2.1: Architectures for Schottky barrier devices, showing excitation across the band gap in the depletion width. The barrier can be sensitized or a metal contact can catalyse a reaction at this interface.

Figure 2.2: Illustration of direct excitation of a PbSe nanocrystal film with electrical characteristics. <sup>3</sup>

Figure 2.3: Device operating by internal photoemission, merbromin (left) was used to functionalise a gold film. Following excitation, electrons can travel through a gold film and the current it collected at the Schottky barrier (centre) resulting in electrical characteristics (right).

Figure 2.4: Diagram showing a method by which a Au nanoparticle film contact can be formed on TiO<sub>2</sub> by bifunctionalised ligands. This device can be functionalised with merbromin.

Figure 2.5: Schematic of mechanism of improvement to current collection when Schottky barriers are formed at interfaces in DSSCs, limiting the rate of recombination with redox mediator or dye due to the acceleration of electrons away from the interface.

## Chapter 3

Figure 3.1: Calibrated photon outputs from the power output plots from the commercial photodiodes. The number of photons per cm<sup>2</sup> is calculated from the responsivity plot from the manufacturers from the Series 7 EO Super UV Silicon Photodetector (blue line) and Centronic OSD5.8-7Q Full Spectrum Si diode (orange line).

Figure 3.2: Resistance between two points showing a reduction of resistance with time and temperature. The resistance drops to some tens of Ω's in a brief period of time then resistance remains approximately constant.

Figure 3.3: SEM images of silver nanowire films on early devices of thick titania films, demonstrating their ability to bridge gaps in TiO<sub>2</sub>.

Figure 3.4: Illustration of the technical challenge of forming a TiO<sub>2</sub> sol on a stainless-steel substrate.

Figure 3.5: Demonstrating a depletion region extending into an area around a silver nanowire.

Figure 3.6.: Time required to achieve 100% anatase phase in the solid state. <sup>4</sup>

Figure 3.7: SEM images of a range of films fabricated with a range of small molecule additives.

Figure 3.8: Oxidised 304 Stainless steel showing protective chromia layers. Top left shows an SEM image, the EDX maps are top left; Cr K $\alpha$ 1, bottom left; Fe K $\alpha$ 1 and bottom right; O K $\alpha$ 1.

Figure 3.9: Top left: 316 annealed steel showing chromia plates. Top right: thin TiO<sub>2</sub> coating on 304 type steel. Below: EDX images of top right section; (centre left) O K $\alpha$ 1, (centre right) Ti K $\alpha$ 1, (bottom left) Cr K $\alpha$ 1 and (bottom right) Fe K $\alpha$ 1.

Figure 3.10: SEM image (left) and EDX map (right) for Fe K $\alpha$ 1. This demonstrates the importance of film thickness and non-uniformity to the concentration of Fe at the interface.

Figure 3.11.: EDX maps of films with the two regions for quantitative analysis shown as two labelled white dots.

Figure 3.12: Schematic (left) and SEM image (right) of the Schottky barrier device showing a substrate, coated in a titania film, with deposited silver nanowires.

Figure 3.13: SEM images of protective scales formed on the surface of stainless steel heated to high temperature.

Figure 3.14: EDX (top) and SEM (bottom) image of protective scales showing a near uniform distribution of Cr and Fe but a lower concentration of O in areas corresponding to the edges of scale according to the SEM image.

Figure 3.15: Reverse saturation current values (left) for a range of devices treated with NaCl in IPA. The reverse saturation currents showed no trend (left) but series resistance was in general lower for treated devices (right).

Figure 3.16: 304 temperature and annealing times and their impact of the conditions on reverse saturation current.

Figure 3.19: Temperature profile is used for annealing for 1 minutes (left) and 5 minutes (right).

Figure 3.18: Photocurrents for films sintered for low times at a range of temperatures.

Figure 3.19: Lower photocurrents for higher temperature and longer annealing times.

Figure 3.20: Heated steel, left, and sol on steel, right.

Figure 3.21: Left showing 8 hour hydrolysed sol device showing some TiO<sub>2</sub> peaks and austenite peaks. Right shows P25 peaks for comparison.

Figure 3.22: Comparison of a wide range of photocurrents for devices for completely amorphous and partially crystalline sols.

Figure 3.23: FWHM of peaks (left) decreasing in width with time under reflux (left) and the estimated particle size from Scherrer equation for a sol with time of reflux (right).

Figure 3.24: Showing narrow peak widths for a sol refluxed for 32 hours, indicating a high degree of crystallinity.

Figure 3.25: Absorption onsets red shift to longer wavelengths following longer annealing times. Tauc plots of the form  $(Abs \cdot hv)^2$  fits for each absorption plots, showing a correlation between band gap estimates and reflux time.

Figure 3.26: Showing TiN devices images following annealing between 0 and 240 minutes at 500 °C.

Figure 3.27: Current-voltage curves for an 8-hour annealed device demonstrating high rectification ratios (maximum forward current = 858 × maximum reverse current).

## **Chapter 4**

Figure 4.1: Schottky barrier, centre, and under reverse and forward bias, left and right respectively. Left shows the reverse bias case which causes the width of the depletion region to increase. Right shows the forward bias case where the width of the depletion region decreases. In all three cases, the Schottky barrier height is the same.

Figure 4.2: Basic equivalent circuit diagram showing diode equivalents, the shunt resistance and the series resistance.

Figure 4.3: Prediction of the formation of the Schottky barrier from two materials demonstrating the relationships between measurable characteristics of the materials.

Figure 4.4:  $V_{\text{rms}}$  shows the applied alternating potential, the Capacitance line (green) indicates the measured current through an ideal capacitor and the Inductance line (grey) indicates the measured current through an ideal inductor.

Figure 4.5: Illustrating the value of the dielectric constant. Left shows a charged parallel plate with no dielectric material, having a  $\epsilon = 1$ . Right shows a material with  $\epsilon = 3$ , able to sustain 3 times as high a density of electric field.

Figure 4.6: Out of phase current ( $90^\circ$  relative to applied  $V_{\text{rms}}$ ) at applied DC bias values, demonstrating a linearity in response for a commercial capacitor.

Figure 4.7: A uniformly doped semiconductor, demonstrating the factors impacting the ability of a material to change in response to an applied field

Figure 4.8:  $1/C^2$  against applied voltage for a ceramic capacitor.

Figure 4.9: Scanning an example device for 50 repeated scans, showing consistency in electrical characteristics over time.

Figure 4.10: SEM images of redeposited silver nanowires on top of corroded nanowires.

Figure 4.11: Current-Voltage curve for a device showing forward sweeps in potential between 0 and 1 V, demonstrating for one curve how the initial currents and potentials can be fit as an estimate of leakage current (aqua line) and fitting the last results can be used to fit an estimate of series resistance (red line).

Figure 4.12: Linear Schottky barrier height estimates for high quality fits to the diode equation. Most of these fits are between 0.5 and 1.0 V, with an average of 0.76 eV.

Figure 4.13: Demonstrates the different potential drops across the device.

Figure 4.14: Example fit (red) for experimental data (blue) showing a close fit for the improved model by adjusting the fit for the potential drop due to series resistance.

Figure 4.15: Different scan speeds for current-voltage curves for the same device. At the relatively slow scan speed of  $2 \text{ mV s}^{-1}$ , the accumulation of vacancies would appear to reduce the barrier height, as the current becomes limited by the series resistance at  $0.5 \text{ V}$ . This occurs at a much higher potential at  $5000 \text{ mV s}^{-1}$ .

Figure 4.16: Top left; representative IV curve for first 770 seconds, bottom left; showing maximum forward currents for this range of scans. Top centre; representative IV curve for 800-1750 seconds with, bottom centre; decreasing maximum forward currents for these devices. Top right; representative IV curve for 1830-4000 seconds, bottom right; maximum forward currents.

Figure 4.17: A partially crystalline sol device, as a control. Hysteresis is observed for the devices with the water. There is much lower resistance, as the current is much higher. Under illumination, the scans show similar hysteresis and appear to show a progressively higher turn-on voltage.

Figure 4.18: Example scan to higher potential for a device under light with water.

Figure 4.19: SEM image of silver nanowires on a titania sol. The silver nanowire mesh were shaded in order to analyse the area shadowed by the silver nanowires.

Figure 4.20: SEM image of a TiN derived  $\text{TiO}_2$  film, showing lighter areas, corresponding to regions of oxidation (A). B shows a number of options of “binning” the image by thresholding. At lower proportions 256 shades being included in light regions, details of the film between light areas are included. C shows the extrapolation of the 91 % binning to the whole SEM image.

Figure 4.21: Reverse saturation currents fits for a range of temperatures, showing an abrupt change in characteristics at  $394 \text{ K}$ .

Figure 4.22: Measured capacitance compared to applied bias, showing the expected decrease in capacitance, though this is non-linear. As expected, the current also increases with frequency.

Figure 4.23: Decrease in capacitance with higher frequency.

Figure 4.24: Capacitance against applied bias and the  $1/C^2$  plot for a device. The  $1/C^2$  plot is non-linear.

Figure 4.25: Average capacitance (markers) and range (bars) for a range of devices fabricated from sols refluxed for increasing lengths of time, showing increasing capacitance across the series. The orange markers show capacitance for devices in air, blue shows the devices soaked in water. Without averaging, the  $R^2$  values are 0.42 and 0.50 respectively.

Figure 4.26: Measured built-in potentials for devices fabricated with sols with increasing reflux, showing a smaller built-in potential for higher reflux times.

Figure 4.27: Demonstrating a model of apparent Schottky barrier height, whereby its height is hypothesised to be related to the Schottky-Mott estimate of height, minus the impact of a dipole at the interface.

Figure 4.28: Capacitance for applied potential for a TiN derived device.

Figure 4.29: Left; TiN derived device capacitance with applied bias, right; sol derived device at applied bias, showing decreasing capacitance, as expected, with applied potential.

## **Chapter 5**

Figure 5.1: TaON device photocurrent, demonstrating an onset at ~560 nm, showing this architecture is compatible with visible light absorbing semiconductors.

Figure 5.2: Photocurrent response of devices fabricated through spun coat films of CdS suspended in toluene. Following fabrication, the devices were passivated with tartaric acid.

Figure 5.3: A range of methods were used in the attempt to improve photocurrents for a range of devices, however, in general devices that had undergone an 8-hour reflux step showed higher photocurrents.

Figure 5.4: Maximum efficiency for a range of comparable devices fabricated from an IPA refluxed sol compared to a water refluxed sol showing higher photocurrents in general for devices fabricated from sols refluxed in water rather than IPA.

Figure 5.5: Photocurrent of devices of increasing crystallinity and defect density showing increasing photocurrent with duration of reflux time, error bars show the range of device photocurrents.

Figure 5.6: Demonstrating the typical depletion region shown around a silver nanowire contacted on a semiconductor.

Figure 5.7: Schematic of deposition of  $\text{TiO}_2$  sol on a device to show how  $\text{TiO}_2$  could be used to improve the active area of the device.

Figure 5.8: Peak UV efficiency for a range of the same devices, showing a generally higher efficiency following deposition of 5  $\mu\text{L}$  of sol.

Figure 5.9: TiN photocurrents for a range of devices. The deposition of 5  $\mu\text{L}$  of sol onto the same devices mainly resulted in higher efficiency devices.

Figure 5.10: Percentage improvement to the photocurrents for a range of  $\text{TiO}_2$  sol and TiN derived devices, showing that typically, photocurrent response increases more drastically for TiN devices.

Figure 5.11: Schematic of attempts at architecture allowing for transparent devices that could be stacked.

Figure 5.12: Schematic of attempts at using a stack of silver nanowire architectures.

Figure 5.13: Photocurrent measurements for a range of devices, average with bars to show the range of measurements for those devices. Left; photocurrents in air, right; following passivation with water.

Figure 5.14: Showing a small photovoltage response for a device treated with  $\text{AgNO}_3$ .

Figure 5.15: Diagram to demonstrate fabrication of devices for the attempt to grow silver structures laterally across the surface to avoid the problems of short circuiting.

Figure 5.16: Impact of  $\text{AgNO}_3$  deposition on a series of devices, showing generally the photocurrent efficiencies were improved for treated devices in the UV region (left) and visible region (right).

Figure 5.17: Maximum photocurrent efficiencies for increasing annealing times for a range of devices, demonstrating lower UV efficiencies for extended sintering times.

Figure 5.18: Photocurrent (left) and direct Tauc plot for photocurrent measurement (right).

Figure 5.19: Photocurrents for a range of devices with water showing high photocurrents and a predictable response above the band gap.

Figure 5.20: Showing the highest photocurrents achieved for a dense spun coat layer of  $\text{TiO}_2$  demonstrating a smaller photocurrent than those measured for TiN derived devices.

Figure 5.21: Illustrating the estimation of depletion areas from the width of silver nanowires and depletion region from capacitance measurements.

Figure 5.22: The magnitude of the photocurrent increases under nitrogen and illumination. On releasing the positive pressure of nitrogen, the photocurrent decreases in magnitude.

## **Chapter 6**

Figure 6.1: Diagrams of mechanisms by which electrons can travel into the semiconductors. Band gap excitation, excitation of surface states, plasmonic enhancement at surfaces and excitation within plasmonic nanostructures themselves followed by decay and electron injection are all consistent with excitation across the semiconductor band gap.

Figure 6.2: Diagrams of possible mechanisms for electron transfer into the silver nanowires. There are fewer reported mechanisms for electron accumulation in silver nanowires and many are untenable.

Figure 6.3: Mechanisms involved in the enhancement found for plasmonic excitations from nanoparticles on semiconductor.

Figure 6.4: Mechanisms in a plasmonic solar cell; i) Excitation ii) injection of electrons over a Schottky barrier iii) transport of electron through the film iv) harvesting of electrons at an ohmic contact.

Figure 6.5: Measured photocurrents demonstrating the opposing currents that were seen for a device fabricated from a commercial  $\text{TiO}_2$  (P25) sol. There are two peaks showing currents in opposite directions.

Figure 6.6:  $(EQE)^2$  plot, giving an intercept of 333 nm for a Tauc plot, indicating an indirect mechanism of the excitation in this device.

Figure 6.7: Normalised transmittance of silver nanowires (top left), the output from the lamp accounting for transmittance of the nanowires (top right), the impact of this on calculated efficiencies (bottom left) and Tauc plots (bottom right).

Figure 6.8: Photocurrent from a P25 based device (top left) showing opposing peaks. IV curve of this device (top right) showing rectifying behaviour of the junction.  $Abs^2$  (grey points) and  $Abs^{1/2}$  (blue points) and best fits from absorption for the "negative" peaks (bottom left).  $Abs^2$  fits from absorption spectrum (bottom right).

Figure 6.9: Selected band gaps of semiconductors. <sup>2</sup>

Figure 6.10: Photocurrents for two amorphous devices passivated with tartaric acid passivation showing two opposing current directions.

Figure 6.11: Picture of battery control, showing a battery as analogous to the cell. By keeping the configuration the same, the electrons travel through the negative contact (red) through the red contact to the amplifier, whereby they show a negative response, as is seen by the reading of -2.864 on the ammeter.

Figure 6.12: Diagram to show battery as analogous to the Schottky barrier device under light.

Figure 6.13: Polished titanium device fabricated by D. Jacques, showing a photocurrent in the "reverse" direction, consistent with band gap excitation.

Figure 6.14: Photocurrent (left) and Tauc plot demonstrating a current in the opposite direction to that expected for a "reverse" current (right).

Figure 6.15: Deposition of water and alcohols on the device shown in Figure 6.14 showing a reversal of the current direction.

Figure 6.16: Potential mechanism for a plasmonic redox reaction that leads to current observed in the opposite direction to that of direct excitation across the band gap.

Figure 6.17: Comparing the UV response of devices fabricated from sols having undergone 8 hour (left) and 32 hour (right) reflux times.

Figure 6.18: Average reverse photocurrent, error bars calculated from the range of devices at these reflux times.

Figure 6.19: Impact of sintering temperature and times on photocurrents.

Figure 6.20: effect of temperature and time of sintering for the high energy and low energy peaks.

Figure 6.21: Absorption of silver nanowires subtracting solvent background.

Figure 6.22: UV-vis difference spectra of TiO<sub>2</sub>/AgNW mixtures showing non-linearity in absorption. The legend values refers to the ratio of TiO<sub>2</sub> to AgNW (e.g. 10 uL of TiO<sub>2</sub> to 40 uL of AgNW = 0.25)

Figure 6.23: Absorption of increasing volumes of AgNW (left) and TiO<sub>2</sub> (right) showing an exponential fit to the former and linearity of the latter at 400 nm.

Figure 6.24: 26 to 48 uL of silver nanowires and a 10 uL TiO<sub>2</sub> sol (1/10<sup>th</sup> conc.) control (dashed line) (left) the same volumes of AgNW with 10 uL TiO<sub>2</sub> sol (1/10<sup>th</sup> conc.) (centre) and difference between the observed and estimated absorptions (right).

Figure 6.25: Gradient in absorption difference at 400 nm vs pKa of the solvent.

Figure 6.26: Photocurrents measured for a device at a range of temperatures for a device. Left shows photocurrents that increase in magnitude at higher temperatures for a device in air. Centre and right also show an increase in magnitude of the photocurrent with increasing temperature.

Figure 6.27: Photocurrent measurements for a range of temperatures for a device (right) and an Arrhenius plot of the results (right).

## **Chapter 7**

Figure 7.1: Diagrams showing possible mechanisms to produce reactive species through excitation of plasmonic modes, dyes and across semiconductor band gaps.

Figure 7.2: CdS drop cast on amorphous devices showing a small visible light photocurrent response.

Figure 7.3: The visible photocurrent response for a device functionalised with CdTe quantum dots.

Figure 7.4: The visible photocurrent response for a device functionalised with CdS quantum dots.

Figure 7.5: Photocurrent of a CdS functionalised device deposited with MPA in EtOH deposited device.

Figure 7.6: Ru(dcbpy)<sub>2</sub>(NCS)<sub>2</sub> functionalised amorphous devices photovoltages (left) and photocurrent (right).

Figure 7.7: Visible dye, Ru(dcbpy)<sub>2</sub>Cl<sub>2</sub>, treated with tartaric acid, showing a very small response in the visible region.

Figure 7.8: Ru(dcbpy)(NCS)<sub>2</sub> functionalised TiN derived device.

Figure 7.9: The photocurrent measurements for a Ru(dcbpy)<sub>2</sub>(NCS)<sub>2</sub> over 345 nm to 400 nm for 10 seconds at each wavelength, showing a mainly constant photocurrent for most wavelengths.

Figure 7.10: Photocurrent (3-9-21 800 nm dye water 3) showing the measured UV and visible response in photocurrent (left) and the external quantum efficiency (right).

Figure 7.11: The dyes used to investigate the sensitisation of the device.

Figure 7.12: Photocurrents for a range of organic dye functionalised devices demonstrating different absorption profiles in the visible region.

Figure 7.13: EQEs for a range of organic dye functionalised devices a peak in efficiency in different visible region.

Figure 7.14: 8-hour IPA refluxed sol, partially crystalline soaked in Ru(dcbpy)<sub>2</sub>(NCS)<sub>2</sub>, showing a UV/visible response, which varies in direction with wavelength.

Figure 7.15: Ru(dcbpy)<sub>2</sub>(NCS)<sub>2</sub> dye on range of devices fabricated from sols, demonstrating directions that oppose the UV response for water passivated devices.

Figure 7.16: Structure of aurintricarboxylic acid.

Figure 7.17: A range of dyes on highly crystalline sols, showing that the visible region response is opposing the UV region response for celestine blue but agrees in the cases of the other dyes for these devices.

Figure 7.18: Aurintricarboxylic acid functionalised partially crystalline devices following using aurintricarboxylic acid in water/EtOH solution.

Figure 7.19: Photocurrent under 400 nm LED demonstrating the reverse direction under illumination.

Figure 7.20: Photocurrents for a device in water demonstrating a large reverse response but a compensation for this when the light it turned off.

Figure 7.21: Photocurrents for a device in the presence of alizarin red showing a large forward response, in the opposite direction to that observed in the presence of water.

Figure 7.22: Methylene blue photoresponse under UV light.

Figure 7.23: Plot of maximum photocurrents of 19 consecutive illuminations of a methylene blue functionalised device shows convergence around approximately 41 nA.

Figure 7.24: Decrease in photocurrent over 20 minutes for a MB functionalised device under UV light showing a “positive” forward current that decreases over time.

Figure 7.25: Ru(dcbpy)<sub>2</sub>(NCS)<sub>2</sub> dye (left) and Ru(dcbpy)<sub>2</sub>(NCS)<sub>2</sub> dye amplified by silver nanowires of increasing concentration in IPA.

Figure 7.26: Left increasing concentration in silver nanowires, Centre shows the raw absorption of dye and silver nanowires. The dashed line is against the secondary axis, showing the much weaker absorption of dye. Right shows the difference between the two spectra showing the difference in caused by nanowires.

Figure 7.27: Photocurrents (dotted black lines) for TiN derived devices (dotted) and TiO<sub>2</sub> sol derived devices (dashed) and absorption difference (solid lines) for a range of concentrations of silver nanowires and TiO<sub>2</sub>.

Figure 7.28: Absorption difference for a range of silver nanowires and TiO<sub>2</sub> sol demonstrating a strong absorption at ~300 nm above the sum of both components at this wavelength.

Figure 7.29: The impact of pKa of the solvent used on the change in absorption of increasing concentrations of silver nanowires and sols.

Figure 7.30: Mechanisms of plasmonic mechanisms on metal/semiconductor systems.

# List of Tables

## **Chapter 2**

Table 2.1: Summary of visible and UV sensitive Schottky barrier devices.

## **Chapter 3**

Table 3.1: Results of anatase crystallinity extent from literature.

Table 3.2: Some typical literature methods and observations for a range of methods of producing TiO<sub>2</sub> films on a range of substrates.

Table 3.3: Number of diodic devices out of total synthesised.

Table 3.4: Pre-treated steel temperature dependency to form a rectifying device.

Table 3.5: Photocurrents for devices fabricated from a TiN substrate following the annealing of the substrate for 1-8 hours.

## **Chapter 4**

Table 4.1: Reported voltage dependencies for current through interface limited current conduction.

Table 4.2: Representative parameters and details of curve fitting in Matlab.

Table 4.3: In a number of these cases, the model requires the field, not the applied voltage, however, assuming the distance over which the field is applied is constant, so applied voltage is used instead.

Table 4.4: Thermionic emission studies fits for a range of devices across 4 batches showing a wide range of estimated areas and Schottky barrier heights.

Table 4.5: Thermionic emission studies for a batch of TiN derived devices showing a more consistent range of areas.

Table 4.6. Estimates for built-in potential, defect density estimate and depletion width for Batch 4 samples from Table X, using thermionic emission fit estimates for area.

## **Chapter 5**

Table 5.1: Photocurrents, peak position and Tauc plot intercept for three TaON devices.

Table 5.2: Photocurrents for devices fabricated from a TiN substrate following the annealing of the substrate for 1-8 hours.

Table 5.3: Efficiency at 330 nm and estimated efficiency from thermionic emission fit

## **Chapter 6**

Table 6.1: Tauc plot intercepts for low and high energy peaks with their direction, in air.

Table 6.2: Tauc plot intercepts for low and high energy peaks with their direction, in water.

## **Chapter 7**

Table 7.1: Selected papers on dye degradation detailing the study and the conclusion the authors draw from their results.

Table 7.2.: Quantum efficiencies of visible response for quantum dot functionalised devices.

Table 7.3: Quantum efficiencies of visible response for quantum dot functionalised devices treated with organic additives.

Table 7.3: Quantum efficiencies of visible response.

Table 7.4: Quantum efficiencies of visible response.



# 1. Chapter One: Context, Aims and Introduction

This chapter will detail the Context, introducing climate change and the need for renewable energy. The Aims will be followed by the Introduction, describing the technologies currently in use. Chapter 2 describes literature examples of the Schottky barriers described in the literature.

## 1.1. Context

### 1.1.1. The current state of energy production

With over 82% of global primary energy use being provided by fossil fuels and facing a changing environment due to the impact of CO<sub>2</sub> and other pollutants on the climate, it is clear new solutions are needed to meet the increasing energy demand. Though the Paris Agreement sets a goal of holding the global average increase in temperature to below 2 °C above pre-industrial levels, only the most optimistic of the Intergovernmental Panel on Climate Change emission scenarios give a multi-model best estimate of less than 2 °C.<sup>5</sup> The Representative Concentration Pathways 2.6 scenario estimates an end of century average global warming increase of 1.6 °C (likely range: 1.0-2.2 °C) compared to the 1850-1900 average temperature, which assumes peak CO<sub>2</sub> emissions by 2020, negative CO<sub>2</sub> emissions from 2070 onwards and a peak in radiative forcing in the middle of the century.<sup>5</sup> Radiative forcing, the difference between the incoming and outgoing radiation of the earth, also includes the impact of methane, halocarbons, NO<sub>x</sub> compounds, water vapour, ozone and aerosols. CO<sub>2</sub> is an effective greenhouse gas as it absorbs strongly in regions where water vapour does not absorb.

The UK government has legislated to reduce CO<sub>2</sub> emissions by 80% by 2050 compared to 1990 values.<sup>6,7</sup> Further, the cost of not taking action on climate

change will be more costly than investing now to prevent the worst impacts of climate change. <sup>8</sup>

### 1.1.2. Climate Change

The surface of the planet (land and ocean surface temperature) has already warmed 0.85 °C between 1880 and 2012. There is a loss of ~half a million square kilometres of winter sea ice extent in the Arctic and ~215 gigatonnes of water lost from the Greenland ice sheet each year. It is likely that this temperature increase has caused more heat waves and heavy precipitation events as well as tropical cyclones and high sea levels. 90% of the energy accumulated on the surface of the Earth has been stored in the oceans, as well as 1/3<sup>rd</sup> of anthropogenic CO<sub>2</sub> emissions.<sup>9</sup> Anthropogenic CO<sub>2</sub> emissions are not simply from fossil fuel emission, but also deforestation and poor soil management. <sup>10,11</sup>

One of the difficulties in predicting the impacts of climate change is in positive feedbacks mechanisms. Some substantial feedbacks include the impact of increased temperature on vegetation, the carbon cycle and atmospheric chemistry. These include the impact of water vapour and clouds, albedo effects of snow and ice and the loss of methane hydrates from permafrost, loss of vegetation through loss of soil carbon or Amazon forest die-back. <sup>5</sup>

There are many countries that will see much of the negative results of climate change but without having been responsible for the emissions. There are estimated 1.4 billion people globally without access to electricity, the majority in rural areas, whilst the use of traditional biomass in cooking is estimated at 2.6 billion people.<sup>12</sup> This results in an estimated 1.45 million premature deaths a year from household air pollution, expected to increase by 2030 to cause more premature death than malaria or tuberculosis at that time.<sup>12</sup> Biomass harvesting, disproportionately affects women and children who are most exposed to household emissions.<sup>12</sup> Solar energy can provide clean and abundant energy without the need for energy infrastructure. <sup>13</sup>

## 1.2. Aims and Thesis outline

### 1.2.1. Aims

The aims of the work are to develop potential architectures and methods for the production of a third-generation photovoltaic cell based on a Schottky barrier formed with silver nanowires. A Schottky barrier is a rectifying junction that can form between a metal and a semiconductor. Similar to the pn junction used in silicon photovoltaics, the internal field acts to separate charges at the interface. The mechanism of action of a Schottky barrier solar device is the separation of charge at the internal field formed between a metal and a semiconductor. The stainless steel will provide a substrate for the materials, forming an ohmic contact with the  $\text{TiO}_2$  and allowing current collection. Stainless steel is ubiquitous and resistant to a variety of chemical conditions and temperature.

The novelty of this device will be its production compatible with lower cost, abundant sheet materials, such as stainless steel.

The aims will be achieved through:

- Fabrication of a rectifying device on stainless steel and its electrical characterisation
- Optimisation of the device to produce a UV photocurrent
- Activating the visible region through the use of dyes
- Analysis to understand how these devices can be further improved.

The following section (Section 1.3) describes the background necessary for the work. A range of reported Schottky barrier devices are described in Chapter 2, in particular those formed of a nano-crystalline film of quantum dots followed by the evaporation of a metal. Sensitized films, using the knowledge gained from Dye Sensitised Solar Cells (DSSCs) coupled with the simple formation of a junction has also been demonstrated and is one of the inspirations for work that is reported here.

Chapters 3 to 7 describe the experimental work;

Chapter 3 describes the methods used, fabrication work and some analysis. The fabrication method needs to be sensitive to the materials used. In DSSCs high temperatures can be used to sinter films but is impossible here due to diffusion from the substrate. This results in the need to create a sol and

method compatible with the materials used, resulting in the development of a solvothermal method to result in a highly crystallinity sol.

Chapter 4 describes electrical analysis, followed by Matlab analysis. This allows the linking of methods used in the formation of the devices to the electrical characteristics. The persistent failures of modelling with thermionic emission theory result in difficulty quantifying the active areas these devices.

Chapter 5 is an extension of the early fabrication work. It shows the improvement in UV results and that optimisation of geometry can result in higher UV efficiencies.

Chapter 6 is an analysis of the bi-directionality of the photocurrent response, the photocurrent in the UV was unexpectedly complex and showed photocurrents in two directions.

Chapter 7 describes how this opposing mechanism is also present in the visible region. However, relatively high efficiency sensitized visible responses were also possible.

Chapter 8 concludes this work and describes possibilities for future work.

### 1.1.2. Thesis outline

In this work, a range of methods were used to fabricate Schottky barriers between  $\text{TiO}_2$  and silver nanowires. Previously, similar devices were made through the electropolishing of a titanium substrate and its oxidation at high temperature, followed by deposition of silver nanowires. In this work, a solvothermal method was used to synthesise  $\text{TiO}_2$  sols followed by improvements to this methodology and that of the deposition and sintering of the  $\text{TiO}_2$  film. An extended reflux step was used to increase crystallinity but likely at the cost of increasing strain. Low temperatures or short times of sintering were required due to metal diffusion from the stainless steel substrates. TiN coated steel was oxidised in air at high temperatures and resulted in devices with high photocurrents and high degrees of rectification.

Fitting of the current-voltage curves was performed by fitting to an exponential function. This resulted in close fits in most cases. However, there were few good fits of the reverse saturation current to temperature according to thermionic emission theory. This resulted in few estimates of area despite

the large number of devices tested. This was attributed to the impact of water desorption on defect states and the impact of this on transport through the Schottky barrier. Capacitance studies were therefore limited in their usefulness in terms of estimating depletion regions. Further, the capacitance did not vary with applied potential as expected, possibly due to the impact of the “dopant” profile and a significantly different geometry to that of the “parallel plate” equations. It is therefore difficult to estimate the efficiency of the active areas, however it would appear that they are likely to be high even from the upper range of active areas and assumptions of the widest possible depletion regions.

Photocurrent measurements showed the sensitivity of the UV photocurrent to the fabrication method. The high efficiencies of the “active” areas suggested by photocurrent, areas from thermionic emission and capacitance studies, led to work to improve the geometry by deposition of sol and wires, with some success. The low active areas and lack of optimisation would suggest much greater improvements are possible.

Further investigations showed that rather than a single photocurrent response in the direction of direct excitation of the semiconductor above the band gap, two directions were seen and the dominant, high energy peak was in the opposite direction. That could have been attributed to high energy processes such as the reduction of oxygen by silver, but it was also present in the visible response of devices functionalised with dyes. The presence of the Schottky barrier should accelerate electrons in the opposite direction, this photocurrent direction can be of greater magnitude than that of excitation of the semiconductor.

With no clear mechanism available for current to travel through this device despite the Schottky barrier, the mechanisms of plasmonically enhanced reactions in the literature are examined. It would appear likely that there are a number of redox processes occurring, particularly in dyes that have several redox active groups available.

## 1.3. Introduction

### 1.3.1. Current solar technologies

The sun supplies more energy in an hour than is consumed in the world in a year, providing the impetus for capturing solar energy cheaply and reliably. The future energy mix is likely to be made up of solar, biomass, wind, hydroelectricity, geothermal, nuclear and tidal power. Though some stored energy such as hydroelectric plants can fill gaps in supply and demand, there is also ongoing research on the catalytic production of "solar fuels" such as hydrogen or carbon-based fuels from the reduction in CO<sub>2</sub>.

Covering just 0.1% of the Earth's surface with 10% efficient solar panels would provide enough energy for current usage.<sup>13</sup> This equates to an area of 510,072 km<sup>2</sup> of solar panels, or twice the area of the United Kingdom. Safe, available and cheap materials and processing could also drive global access to cheap and reliable electricity locally without the need for an electricity grid.

The photoelectric effect provided the first academic studies of materials that can convert light into electricity and early photography provided the first studies of sensitized semiconductors. However, this brief review will focus on photovoltaics in common use, starting with first generation technologies as they provide examples for the use of the Shockley-Queisser limit.

### 1.3.2. Cost

The cost of solar energy has been falling; the cost of the module can be as low as 23% of the total cost and the decrease in module cost has accounted for approximately half of the decrease in cost of a complete panel between 2009 and 2016.<sup>14</sup> This has occurred alongside with increases in average module efficiency (13.3% to 16.6%) for 2010-2015, which also reduces repayment time.<sup>14</sup>

Repayment time impact deployment as it makes the investment in solar energy dependent on interest rates and risk. Tariffs for the production of renewable energy can accelerate deployment, which was exponential in the UK for many years, though much of the recent growth is in large scale solar farms.<sup>15</sup> Energy production has a macroeconomic impact, with 34,000 jobs in the UK in 2013 dependent on solar energy.<sup>16</sup>

Si is the dominant deployed solar technology. New technologies may have different soft costs than the old ones and offer other advantages. The production of some thin film materials are by-products of battery manufacture and DSSCs can be manufactured to be transparent and used as power generating windows as well as an architectural feature. In 2010, buildings accounted for 19% of energy related greenhouse gas emissions, which could double or triple by 2050 under “business-as-usual” scenarios due to increased demand for housing and electricity from billions of people.<sup>16)</sup>

### 1.3.3. Photovoltaic devices

There are many architectures for solar devices, the objective is to generate an electron and hole from light and to separate these charges from one another. Therefore, the characteristic in common between all architectures is asymmetry. Recent research on an organic-inorganic ZnO-poly(3-hexylthiophene) device took this to a remarkable conclusion that playing pop music to their devices improved the efficiency by the acoustic vibration being at the resonant frequency of the nanotubes, inducing an electric field resulting in an efficiency under light and pop music that was greater than the sum of the piezoelectric and visible responses.<sup>17</sup>

Solar architectures are generally categorised as crystalline (1<sup>st</sup> generation), thin film (2<sup>nd</sup> generation) and compound (third generation) photovoltaics. 1<sup>st</sup> generation use crystalline silicon with high purity grown as wafers which demonstrate high efficiency. 2<sup>nd</sup> generation use thin films of highly absorbing materials such as CdTe, with another layer to form a junction, providing a lower cost starting material. 3<sup>rd</sup> generation include a diverse range of architectures but the functions of absorption and charge separation may rely on separate device constituents such as in DSSCs.<sup>18</sup>

The vast majority of installed solar capacity is silicon solar cells (1<sup>st</sup> generation). According to a detailed balance limit, a thermodynamic analysis described by Shockley and Quieser, a single junction cell of crystalline silicon, has a limit in efficiency of 30%, usually referred to as the Shockley-Quieser limit.<sup>19</sup> DSSCs and similar third generation devices often aim to produce large area devices from cheaper and non-toxic materials, potentially sacrificing efficiency, relying on lower costs, ease of manufacture and the potential for new architectures. It may be possible to use a range of materials

to match the solar spectrum rather than a single junction might allow for efficiencies above the single junction.

For semiconductors, light absorbed is proportional to the band gap. The photons below this band gap are not absorbed, and those above it create an electron-hole pair, which can potentially be separated. However, for energy above band gaps, electrons will thermalize to the top of a conduction band, heating devices which tends to increase resistance and lower their performance. Further, the voltage of the device will depend on the band gap of the material but the current generated is dependent on the number of photons absorbed, creating a trade-off between current and voltage. Figure 1.1 shows the absorption bands of several common semiconductors compared to spectral irradiance through 1.5 equivalents of atmosphere compared to the solar zenith, AM1.5, demonstrating the challenge of matching semiconductor absorption to the solar spectrum and the trade-offs that must be made when selecting a semiconductor for photovoltaic device manufacture. Assuming irradiation with black body radiation, the optimum band gap is 1.1 eV, which can give a maximum efficiency of 44%.<sup>19</sup> This corresponds to a wavelength of 1.13  $\mu\text{m}$ .

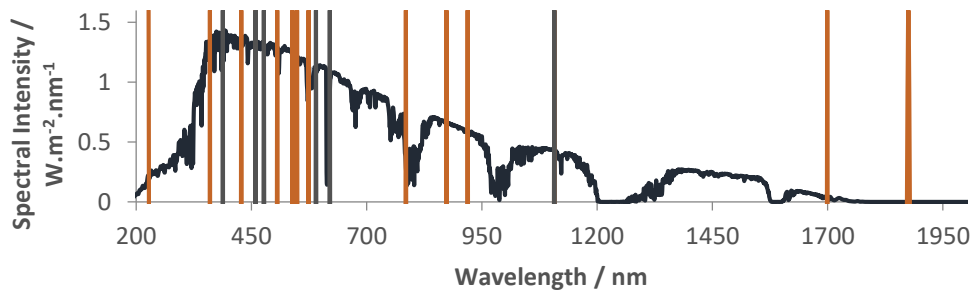


Figure 1.1: Blue line: AM 1.5 from ASTM G173-03 is the spectral intensity as averaged at 37° tilt for the latitude of mainland US over 1 year, shown in blue.<sup>1</sup> Some common semiconductor band gaps are shown as orange lines and are, in increasing wavelength, diamond, GaN, SiC, ZnSe, AlP, ZnTe, GaP, AlAs, AlSb, GaAs, InP, Si, Ge, InAs.<sup>2</sup> Semiconductors made from abundant materials have band gaps shown as grey lines and in increasing wavelength are TiO<sub>2</sub>, C<sub>3</sub>N<sub>4</sub>, WO<sub>3</sub>, Fe<sub>2</sub>O<sub>3</sub>, Cu<sub>2</sub>O and Si.<sup>2</sup>

#### 1.3.4. Semiconductors

Semiconductors are materials with conduction properties somewhere between those of conductors and those of insulators. Conductivity in common materials varies over 30 orders of magnitude such as that between copper and Teflon, 7 orders of magnitude greater than the difference between the size of an atom and the solar system.

#### 1.3.5. Band theory

In a single crystal of a few grams of material, there is on the order of  $10^{22}$  atoms. The free electron model assumes the valence electrons can move through the material experiencing a uniform potential, interacting neither with themselves nor the nuclei.

This model is sufficient for explaining some phenomena, such as the temperature dependence of conduction. It fails to explain why some materials, such as some bivalent materials are semiconductors. The band theory of solids considers atoms as possessing discrete energy levels, as described with atomic structure. When these are brought into close proximity, the wavefunction that describes their isolated state no longer holds due to the Pauli Exclusion Principle. In molecular orbital theory, molecular orbitals are calculated by combination of atomic orbitals, such as by linear combination of atomic orbital (LCAO) methods.

Considering two s-orbitals combining, the molecular orbitals formed are the bonding (constructive interference of the wavefunctions) giving rise to a sigma orbital and antibonding (destructive interference of the wavefunctions) giving rise to sigma\* orbitals. When there are  $10^{23}$  orbitals, a continuum of energy levels exist can form, as shown in Figure 1.2.

As in molecules, the electrons fill the lower orbitals, by the Aufbau principle. So in the case of  $n$  electrons, where  $n$  is large, typically the lower band is filled and the upper band is empty. In insulators, the gap is large compared to thermal energy, so electrons cannot be excited across the energy band and no electrons or holes can be used to conduct electricity. In semiconductors, if the temperature is high relative to the band gap,  $E_g$ , some electrons can move into the conduction band and provide free carriers for the conduction of charge.

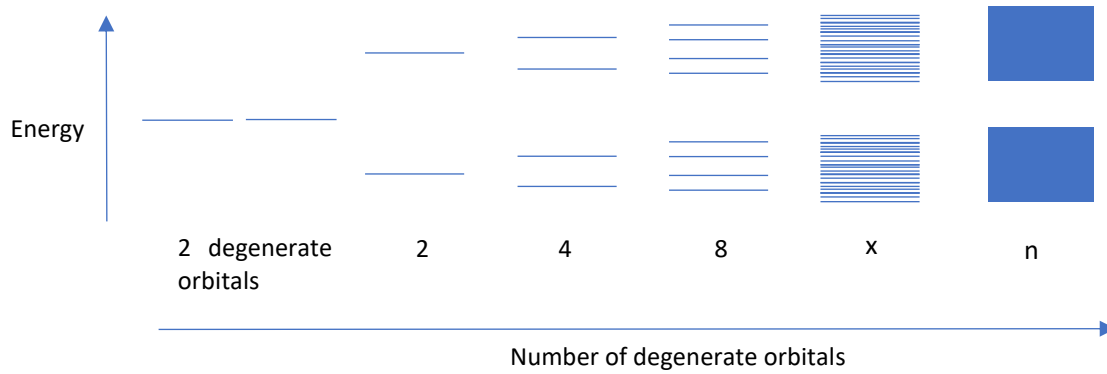


Figure 1.2: Illustration of how bands form from many orbitals, illustrating how bonding and antibonding orbitals become bands.

This explains what the free-electron model could not, that the conductivity increased with temperature for semiconductors. In conductors, the bands overlap or a band is only partially filled, therefore only small amounts of energy are required to move electrons into free orbitals.

Considering an alkali earth metal forming a bond, a filled low energy state and an unoccupied higher energy state would be predicted and as such, the alkali metals would be expected to be insulators from this band theory. However, if the discrete orbitals are close enough in energy to overlap or where there is hybridisation of orbitals, the bands can have characteristics of all the constituent orbitals. In this case, filling the lowest energy levels results in vacant states in both bands and high conductivity, Figure 1.3.

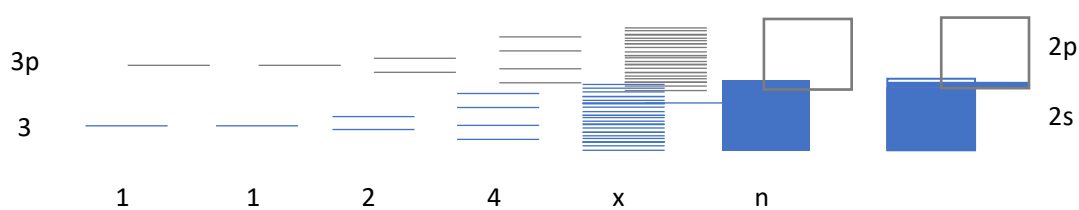


Figure 1.3.: Illustration of band theory from the linear combination of orbitals. On the right, the overlap of bands is illustrated to explain how some materials such as divalent metals can show high conductivity.

The Fermi level is defined as the energy level at which a state has a 50% probability of being occupied. This means that the Fermi level does not have to correspond to a “real” energy level, it can occur in the band gap. For instance, at absolute zero for an intrinsic semiconductor, the Fermi level lies

in the middle of the highest occupied energy level and the lowest unoccupied energy level.<sup>20</sup>

Direct band gap excitation occurs from the valence band and the conduction band can occur with a single photon with conservation of momentum, this is direct band gap excitation. If not, there may be some interaction with the involvement of photons or phonons to bridge the energy gap, resulting in indirect absorption. A common method for analysing the optical band gap and thus absorption onset of a semiconductor is by use of a Tauc plot. This relates the onset of absorption to energy according to Equations 1.1 and 1.2 for direct and indirect fits respectively.<sup>21,22</sup> The onset of absorption and Tauc plots are illustrated in Figure 1.4.

Equation 1.1:  $E_{bg} = (\alpha h\nu)^{1/2}$

Equation 1.2:  $E_{bg} = (\alpha h\nu)^2$

$E_{bg}$ : Optical band gap energy / eV

$\alpha$ : Absorption coefficient

$h$ : Planck's constant / eV s

$\nu$ : frequency of light / s

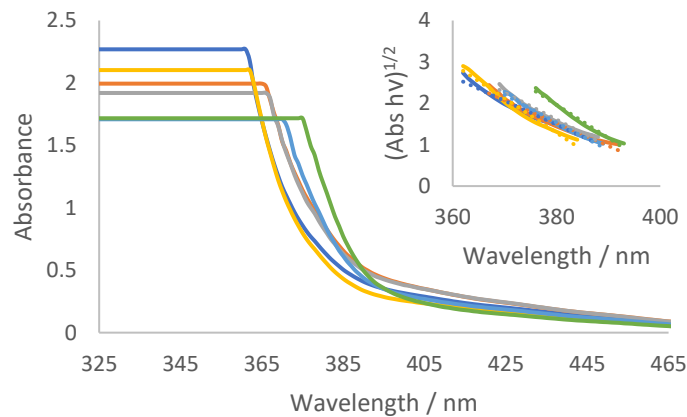


Figure 1.4: Demonstrating absorption for a range of TiO<sub>2</sub> sols used in this work and inset showing Tauc plots for the same sols.

The free energy of the exciton, however, is smaller – due to the coulombic force, which may be screened effectively in a high dielectric constant material such as TiO<sub>2</sub>, between the pair and the significant configurational entropy

arising from the large number of translational states accessible to the mobile carriers. Excitons rapidly decay by interaction with photons or phonons.

### 1.3.6. TiO<sub>2</sub> as a compound semiconductor

TiO<sub>2</sub> is an abundant and widely used compound semiconductor. It has many uses, with its use solely in pigments amounting to  $4 \times 10^6$  tonnes per year.

23

#### Band structure

The valence electron configuration of Ti is  $3d^24s^2$  and O is  $2s^22p^4$ . The orbitals involved in the formation of the valence and conduction band of TiO<sub>2</sub> would be expected to be the low energy O<sub>2p</sub> orbitals and the Ti<sub>3d</sub> orbitals respectively.

This is also the result derived from Density Functional Theory (DFT) and many-body perturbation theory studies of the three forms of TiO<sub>2</sub>. In this model, the d orbitals of Ti are split due to the distorted octahedron structure of anatase and rutile TiO<sub>2</sub>, analogous to the splitting of d orbitals into the doubly degenerate e<sub>g</sub> states and triply degenerate t<sub>2g</sub> states in an octahedral complex.<sup>23</sup> This splitting is extremely sensitive to the defects and vacancies, calculated with resonant photoemission.<sup>23</sup>

The rutile and brookite polymorphs have direct bandgaps and anatase has an indirect band gap but only 0.13 eV below the direct band gap.<sup>24</sup> The level of the conduction band limits the reducing capacity of a semiconductor and the top of the valence band limits the oxidising capacity. Similarly, in a DSSC, the open circuit potential is limited by the difference between the conduction band edge and the redox potential of the redox mediator. With a more positive conduction band, demonstrating a longer lifetime of photoexcited electrons, forming at a lower temperature and a higher surface area, anatase phase TiO<sub>2</sub> is usually favoured for DSSC production and photocatalysis.<sup>25</sup>

Models of TiO<sub>2</sub> of varying size and a range of stoichiometries show the average formal charge of Ti is +1.7 and oxygen of -0.85, showing a large degree of covalency.<sup>23</sup>

## Doping

Consideration of the bands as above provides the background to understand how doping such as by band gap narrowing, impurity levels and oxygen vacancies, impacts the structure of  $\text{TiO}_2$ . For instance, it is thought nitrogen doping of  $\text{TiO}_2$  provides more 2p states, which narrow the band gap.<sup>26</sup> Nitrogen doping could also introduce vacancies and block reoxidation.<sup>27</sup>

The energy of formation of a vacancy is on the order of 1 eV for oxide materials and they provide a path of relatively easy diffusion through a lattice.<sup>20</sup> Their quantity can be estimated from a Boltzmann distribution at a given temperature and energy of formation of the vacancy.<sup>20</sup>

## Oxygen vacancies

$\text{TiO}_2$  is rarely, in fact,  $\text{TiO}_2$ .  $\text{TiO}_2$  annealed in ultrahigh vacuum or in nitrogen produces reduced  $\text{TiO}_2$  due to the many stable phases and stoichiometries and have been observed to vary in stoichiometry due to Ti interstitials in stoichiometries  $\text{TiO}_{1.9996}$  to  $\text{TiO}_{1.9999}$ .<sup>23</sup>

Vacancies and interstitials result in a loss of net neutrality, changing the conductivity of the oxide. The conduction band is mainly Ti 3d in character, where the octahedral coordination splits the d-orbitals into two sub-bands. This makes the splitting extremely sensitive to the presence of vacancies due to the loss of octahedral coordination.<sup>23</sup>

In stoichiometric  $\text{TiO}_2$ , no surface states are observed. The reduced  $\text{TiO}_2$  surface (with  $\text{Ti}^{3+}$  defect states), there are effectively extra electrons, creating an accumulation layer in the near-surface region, causing a downward band bending.<sup>23</sup> There is an “unbending” of the conduction band following exposure to oxygen.

Molecular oxygen dissociates to fill the vacancies, quenching the defect state. From resonant photoemission, the state has Ti 3d character.<sup>23</sup>

Vacancies and defects are crucial to some reactions, such as the dissociation of water and has been modelled to be exothermic by DFT and Scanning Tunnelling Microscopy at vacancies.<sup>28</sup> The reversibility of water dissociation may also depend on whether it occurs with defect healing. The variability in these results may be due to the vastly different surfaces formed by different synthesis methods.

The vacancies in  $\text{TiO}_2$  are important as they diffuse and drift, impacting transport in dielectric films and transport at the Schottky barrier, influencing the field at the interface and conduction through the film itself (Section 1.3.7).

#### Phase

There are two phases of  $\text{TiO}_2$  typically encountered for uses in solar devices and photocatalysis; anatase and rutile. Anatase has higher electron mobility, low dielectric constant and lower density than rutile  $\text{TiO}_2$ . A DFT study into anatase and rutile phases found the increasing efficiency of photocatalysis of anatase phase corresponded with the lifetime of the photo-generated electrons and holes in anatase phase, resulting in a more efficient migration to surfaces.<sup>25</sup> This is consistent with the indirect band gap of excitation resulting in a slower rate of recombination. Anatase phase  $\text{TiO}_2$  also has a slightly higher  $E_F$ , lower capacity to absorb  $\text{O}_2$  and higher degree of hydroxylation than rutile  $\text{TiO}_2$ . There is also thought to be more surface band bending in anatase  $\text{TiO}_2$  than rutile  $\text{TiO}_2$  so that surface hole trapping dominates.<sup>29</sup>

At high temperatures of annealing, some pores collapse in the transition from amorphous to anatase phase, resulting generally in reduced surface areas for more crystalline catalysts. The usual anatase to rutile transition occurs from 600 – 800 °C affected by preparation conditions, precursors, impurities, oxygen vacancies and primary particle size.<sup>29</sup>

High efficiency catalysts have been produced by heating  $\text{TiO}_2$  to the rutile transition temperature in order to create a mixed phase catalyst. There is a slight mismatch in the  $E_F$  levels of the conduction and valence bands, thought to result in the accumulation of electrons on the rutile phase and holes in the anatase phase.<sup>30</sup>

#### 1.3.7. Conductivity of Mesoporous films

One of the surprising successes in DSSCs was the ability to harvest electrons using a  $\text{TiO}_2$  film formed of many nanoparticles rather than a defect free, large single crystal as is typical in first generation devices. In highly crystalline, defects provide recombination sites and need to be avoided.

Electron mobility depends on the crystal phase and morphology of single crystal films. However, mesoporous films also show remarkable conductivity.

A pressed pellet of CdSe showed 70% of the current obtained from a single crystal.<sup>31</sup>

Conductivity in TiO<sub>2</sub> is due to oxygen vacancies, which are composed of Ti 3d states, resulting in a band slightly below the conduction band, giving TiO<sub>2</sub> the characteristics of an n-type semiconductor.<sup>20,23</sup>

The TiO<sub>2</sub> particles sintered into a mesoporous film may provide many sites for recombination. But, given the ability to achieve relatively high DSSC efficiency, the carrier diffusion lengths must be at least as long as the thickness of the mesoporous films.<sup>31</sup> The diffusion length is defined by the average distance the charge carrier travels and relies on a chemical potential gradient.

In DSSCs and perovskite devices, through the film is often on the order of tens of microns at least one charge carrier must have a diffusion length of at least this magnitude in mesoporous TiO<sub>2</sub> films.<sup>31</sup>

There is proposed to be little potential drop in a TiO<sub>2</sub> film contacted with a concentrated electrolyte, with a potential drop instead found at the FTO interface due to the accumulation of electrons.<sup>32</sup> For this reason, the majority of charge movement occurs under diffusion.

The diffusion coefficient and the equivalent term in the presence of a field is described by the Einstein-Smoluchowski relations, Equation 1.3 and 1.4. The mobility term relates the particles drift velocity to the applied force. This gives diffusion lengths and lifetime according to Equation 1.3 and 1.4.

Equation 1.3: 
$$D = \mu kT/q$$

Equation 1.4: 
$$L_d = (D\tau)^{1/2}$$

D: Diffusion coefficient / m<sup>2</sup> s<sup>-1</sup>

L<sub>d</sub>: Diffusion length / m

q: unit charge / C

kT: thermal energy / J

μ: mobility / m s<sup>-1</sup>

τ: charge lifetime / s

Where charge lifetime to refer to the minority lifetime until recombination or extraction.

The light is absorbed in a very thin layer at the interface of the semiconductor so the rest of the semiconductor film is considered to be "field-free" in a nanoparticulate film. The field at the interface, however, further enhances the above effect, as holes accumulate at the interface and electrons drift rather than diffuse for the distance of this light absorption. After this, the electrons diffuse for 10s of  $\mu\text{m}$ , these long diffusion lengths are maintained by continuing syphoning of charge at a conductive interface.<sup>31,33</sup> The impact of this in the UV region is discussed in DSSCs is discussed in Section 2.6.

#### 1.3.8. Fields in particle films

The diffusion lengths in nanoparticle films are reasonably long, but understanding the mechanism of carrier transport may further improve efficiencies. Generally, increasing the temperature of sintering of a film improves its conductivity as crystallinity increases and there are fewer grain boundaries. In a study of spun coat  $\text{TiO}_2$  films on FTO glass, conductivity increased with dwell time at 450 °C, until a limit was reached, thought to be due to the growth of the crystals into amorphous regions until no further improvement could be made.<sup>34</sup>

However, the lower conductivity of nanoparticle films of  $\text{TiO}_2$  compared to single crystals of other semiconductors cannot just be due to grain boundaries. In a terahertz time domain spectroscopy experiments, Hendry et al., found the mobility of electrons in sol films to be several orders of magnitude lower, than in single crystals.<sup>35</sup>

The authors propose a 2 order of magnitude loss due to the effect of shielding by induced dipoles in the  $\text{TiO}_2$  due to the high polarizability of the material. This is consistent with an effective medium approximation, where the dielectric constant of the material is represented by a space filling factor, the dielectric constants of air and  $\text{TiO}_2$ . The large difference in electron mobility is therefore been proposed due to local field effects.<sup>35</sup> The large dependence of the efficacy of DSSC current collection on the electrolyte concentration may result from the local electric fields being screened in order to aid current collection. <sup>35</sup>

### 1.3.9. Memristive switching

A memristor is a passive component that has a resistive state that depends on the potential that has been applied to it in the past, its “memory”. TiO<sub>2</sub> has high dielectric constant, resulting in renewed interest in TiO<sub>2</sub> as potential replacement for SiO<sub>2</sub>, for high speed electronics.<sup>23</sup> TiO<sub>2</sub> films often do not have a constant resistance making TiO<sub>2</sub> films between two metal contacts a potential candidate for memristors.

This is reported on in TiO<sub>2</sub> literature due to the observation of hysteresis in current-voltage curves in devices of metal-TiO<sub>2</sub>-metal architecture. This is usually attributed to the diffusion of oxygen vacancies and other defects towards high resistance interfaces. Some literature has described the usefulness of methods that rely on the changing conduction of a Schottky barrier, possibly by "shunting" it, as a potentially more reliable method for forming memristive switches compared to the formation of conductive filaments.<sup>36,37</sup> For instance, accumulation of vacancies at the terminals on single crystals has eliminated the Schottky barrier to achieve a programmable rectification between two platinum contacts.<sup>38</sup>

Though the formation of memristive components is tightly controlled by thickness of films and control of oxygen vacancies density, a similar hysteresis and shunting phenomena are observed in this work, so mechanisms underlying memristive switching are relevant.

### 1.3.10. Electron-hole separation

For optimal electron-hole separation, the potential drop across the space charge layer should be  $> 0.2$  eV.<sup>39</sup> The thickness of a space charged layer is related to the dopant level, high dopants should result in a narrower space charge region, but when the space charge layer is thin, penetration of light into TiO<sub>2</sub> greatly exceeds the width of the space charge layer, reducing the charge separation by the field induced by the light.<sup>39</sup>

### 1.3.11. Schottky barriers

When a metal forms a contact with a semiconductor, two types of contact can form; ohmic contacts or Schottky junctions, which is rectifying.

Early interest in Schottky barriers originated due to their ability to be used in radio receivers. Later, progress in the semiconductor industry led to

research in this field as any electronic component, such as a transistor will eventually need to be connected by a metal contact. This contact needs to be predictable, and usually, ohmic.

Schottky barriers have proved difficult to characterise, with unpredictable characteristics, unhelpful for the formation of electronic devices. Much of the early literature discusses the methods that can be used to prevent their formation and what impacts the height of the barrier formed.

However, they also provide a single junction capable of separating charge at an interface. Though they are hard to characterise and predict, the opportunity for much lower production cost and complexity for the formation of useful junctions for use in photovoltaics or photoelectrocatalysis has led to some research in this area.

Note: in the following discussions, only n-type semiconductors are considered. The arguments can be applied to p-type semiconductors in reverse.

#### Electrochemical analogy

Considering a metal electrode making contact with a solution of ions, for instance  $\text{Fe}^{2+}$  and  $\text{Fe}^{3+}$ , the ions have discrete states and the highest occupied energy level of  $\text{Fe}^{2+}$  is nearly the same level (though not exactly the same due to solvation) as the lowest unoccupied level of  $\text{Fe}^{3+}$ . The electrons will either transfer to or from the ions depending on whether they have energy above or below the Fermi level of the metal. It is easy to imagine that the potential between the surface and solution is dependent on the relative concentration of the ions, Figure 1.5.

The total chemical potential of the system depends on the amount of charge transferred. The reaction stops due to destroying the driving force, by removing the difference in potentials between the metal and the ions in solution. Under the condition on the left of Figure 1.5, the metal becomes more positively charged and the solution more negatively charged, this is the origin of the potential described by the Nernst equation. If an electron moves from a high level in the metal to a lower one on an ion, the Fermi level of the metal must decrease, as the average occupation of the electrons in the metal is lower. <sup>40</sup>

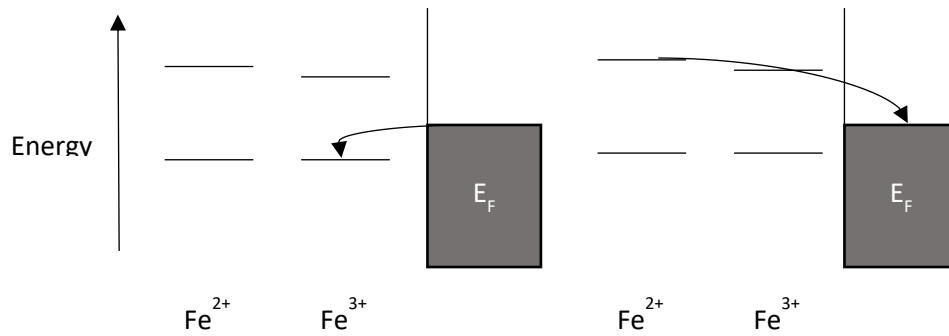


Figure 1.5: Electrode in contact with ion containing solution.

Similarly, on bringing a semiconductor into contact with an electrolyte, a flow of charge occurs and a built-in potential develops. In a semiconductor, however, this results in a greater change in  $E_F$  at the interface due to the much smaller density of states in a semiconductor compared to either the electrolyte or a metal. A semiconductor is capable of sustaining an electric field, resulting in a depletion region, extending, according to Poisson's equations, a width dependant on the doping concentration. This is a region with a steadily decreasing field away from the interface due to the changes in the number of ionised donors and is discussed in section 1.3.12.<sup>41</sup>

Analogously, on bringing a semiconductor, with discrete states, into contact with a metal, with continuous states, the Fermi level of the metal can fall between the valance band and the conduction band of the semiconductor (Figure 1.6, left). Yet again, electrons will move to the more energetically favourable position (Figure 1.6, centre). In this instance, as above, the actual number of electrons transferred is very small. Given the high density of carriers in a metal compared to a doped semiconductor, the increase in the metal Fermi level is negligible.

At the interface, the bands move upward as the electrons move and a potential builds up across the interface due to the charge transfer. Band bending is shown in the semiconductor, due to incomplete screening of charge, though not in the metal due to the inability for a long-range potential to build up in a metal, Figure 1.6.

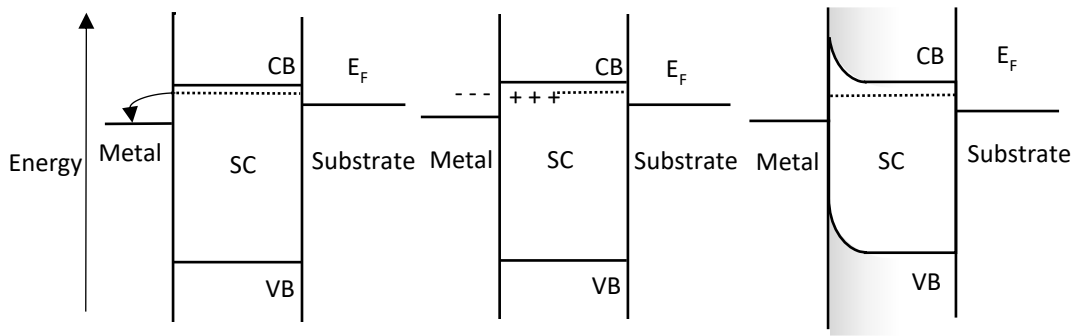


Figure 1.6: Illustration of the formation of a Schottky barrier.

The Schottky-Mott rule

From this description, it would be expected that the barrier would be proportional to the difference in the Fermi levels of the metal and the semiconductor, which can be calculated by lining up of vacuum levels outside the material.

This is described by the Schottky-Mott rule, Equation 1.5, and Figure 1.7.

Equation 1.5:

$$\Phi_b = \Phi_m - \chi_{SC}$$

$\Phi_b$ : Barrier height / eV

$\Phi_m$ : Metal workfunction / eV

$\chi_{SC}$ : Semiconductor electron affinity / eV

However, this is not what is observed. In fact, there is often no dependence on the metal work function, so that the barrier height has no dependence on the metal used to form the junction. This was an unexpected result and a vast amount of research was performed in order to relate some properties of the metal/semiconductor junction to the apparent barrier height. This phenomenon is referred to Fermi level pinning, where it is described in terms of the Fermi level of the semiconductor being “pinned” by states at the interface, so it does not move in the presence of different metal work functions.

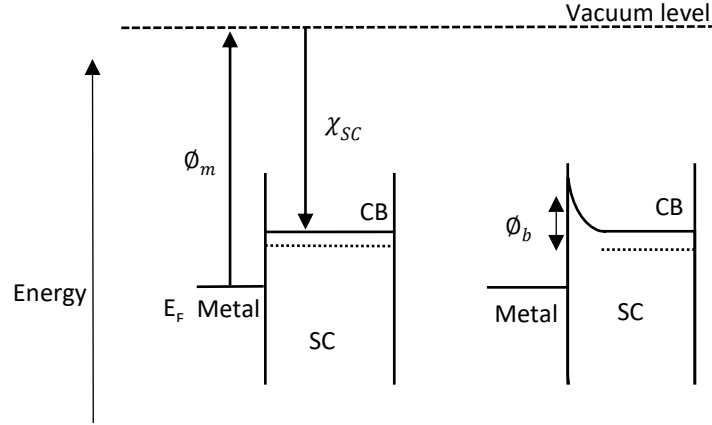


Figure 1.7: Illustration of the lining up of vacuum levels to derive the Schottky-Mott rule.  $\chi_{sc}$ ,  $E_F$ , SC, CB,  $\phi_m$ ,  $\phi_b$  are the semiconductor electron affinity, Fermi energy level, semiconductor, conduction band, metal workfunction barrier height respectively.

If there is an oxide or organic layer at the interface the change in barrier height could be accounted for by describing a dipole at the interface and can be described by Equation 1.6, though this still requires a linear response of metal work function to Schottky barrier height. Doping, metal deposition and organic molecule doping can impact this dipole.

Equation 1.6: 
$$\phi_b = \phi_m - \chi_{sc} - qD_{int}$$

$\phi_b$ : Barrier height / eV

$\phi_m$ : Metal workfunction / eV

$\chi_{sc}$ : semiconductor electron affinity / eV

q: unit charge / C

$D_{int}$ : dipole moment / C m

In the above model, there are many assumptions, one is in the measurements. The metal work functions and semiconductor electron affinities can be measured in a number of ways. Taking electron affinities as an example, typically electrons are removed with high energy lasers and the electron affinity is taken to be the difference between the energy used to bombard the surface and the energy measured after the electrons have been removed.

This is not the same as measuring the energy required to remove an electron, instantaneously, from a representative surface. The electron affinity of the material is also periodic, but is measured as an average, Figure 1.8. Given the periodicity is dependent on the crystal structure, it follows that the work function is also dependent on the crystal phase which changes the density of surface states, which is indeed observed.<sup>42</sup>

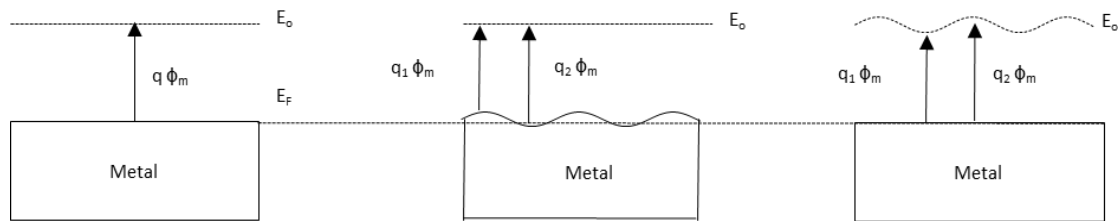


Figure 1.8: Illustration of non-continuity in vacuum level. Left; simple measurement of metal Fermi level,  $E_F$ . Centre; demonstrating periodicity in metal  $E_F$ , Right; demonstrating this in terms of an unequal vacuum level if the  $E_F$  is assumed to be constant.

Even accounting for the possibilities of dipoles at the interface, caused by formation of oxides and reactions between the metal and semiconductor surfaces, uncertainty in the measured electron affinity and work-functions due to the phase, periodicity and condition of the material, there are other failures in this model which account for the lack of a linear dependence of metal work-function.<sup>43</sup>

The height of the Schottky barrier often does not depend on the metal used but can be similar across a range of metals for the same anion, referred to as the common anion rule.<sup>44</sup>

#### Breakdown of the Schottky-Mott rule

The Schottky-Mott rule is expected to be reliable where the interface created is represented by the bulk values. This assumption is impossible as it would require the two bulk-like surfaces to come into contact whilst not disturbing the orbitals of either system, with no rearrangement of either surface occurring, whilst in close enough contact for charge to transfer. Just as an atomic orbital is not descriptive of a molecular orbital, there must be a formation of an interface, with the surface of both being effectively destroyed.

For a situation where the dangling bonds of a covalent semiconductor are exposed, with the condition of charge neutrality, such that the surface is uncharged, results in a half filled band of surface states. The occupation of surface states will depend on the crystal phase, orientation, stoichiometry and illuminatingly, the preparation method.

Cowley and Sze attempted to quantify some of these effects. In the Cowley and Sze model, the Schottky barrier relates the barrier height to the interfacial layer of a thickness, with a density of states depending on the potential of the gap states within the bandgap.<sup>45</sup> The charge of these states is determined by the position of this Fermi level of the states with respect to the barrier potential, Equation 1.7 and 1.8.

Equation 1.7. 
$$Q_{ss} = -qD_{it} [E_g - q(\phi_b - \phi_0)]$$

$Q_{ss}$ : Charge of surface states / C

$D_{it}$ : Density of interface states /  $m^{-3}$

$E_g$ : Band gap / eV

$\phi_b$ : Barrier height / eV

$\phi_0$ : Difference between the top of the valence band and the surface states / eV

$Q_m$ : metal charge density /  $m^{-3}$

Equation 1.8 
$$\Delta = \frac{Q_m \delta}{\epsilon \epsilon_0}$$

$Q_m$ : Metal charge density / C

$\delta$ : Width of the interfacial layer / m

Given the complexity of these systems, simple general rules have not been very successful, but detailed models of specific surfaces allow explanations of observed barrier heights.

Given the analysis of vast amounts of empirical data on crystalline semiconductor, the Schottky barrier can be expressed in Equation 1.9. The  $S^*$  factors are widely reported for semiconductors which relates the material to how much it obeys the Schottky-Mott rule. This  $S^*$  factor depends on the metal electronegativity.<sup>43</sup>

Equation 1.9. 
$$\phi_b = S^* X_m + \phi_o$$

$\phi_b$ : Observed barrier height / eV

$S^*$ : S factor

$X_m$ : Electronegativity / eV

$\phi_o$ : Calculated barrier height / eV

Given the deviation of materials from the Schottky-Mott rule, there are four types of deviation from the expected theory:

- Non-metal/insulator and physisorbed metal (ideal situation)
- Highly polarisable semiconductor and metal (weak bonding)
- Highly polarisable semiconductor reacting with the metal and forms compounds
- Thin metal passivating oxides form at barrier. <sup>43</sup>

To demonstrate the importance of the third mechanism, some authors relate the heat of the formation of a metal and a surface with silicide to the barrier height and found they relate linearly.

The flat band potential is modified when there is a charge present in the interfacial oxide layer. When the interface charge is positive, the Schottky barrier height is lower. When the states are negative, the barrier appears higher. <sup>43,46,47</sup>

### 1.3.12. Band bending

Following formation of a Schottky barrier, a depletion region exists in the semiconductor interface. This depletion width depends on the charge density ( $\rho$ ) and permittivity of the semiconductor ( $\epsilon$ ) relative to vacuum permittivity ( $\epsilon_o$ ), as described by Poisson's equations, as given in Equation 1.10 and integrating to Equation 1.11. <sup>20</sup>

Equation 1.10.: 
$$\frac{d^2V}{dx^2} = \frac{-\rho}{\epsilon\epsilon_o}$$

V: voltage / V

x: distance / m

$\rho$ : charge density / m<sup>-3</sup>

$\epsilon$ : semiconductor permittivity

$\epsilon_o$ : vacuum permittivity / F m<sup>-1</sup>

Equation 1.11.

$$\frac{dV}{dx} \epsilon \epsilon_0 = -\rho x + constant$$

which gives the potential with regard to the charge density at a distance,  $x$ . At the edge of the depletion layer, the electric field will be zero, so the constant must be  $\rho_d$ . Using the Poisson's equations, the decreased carrier density in the semiconductor formed at the interface can be related to a field, which can be related to the energy experienced for a charge carrier at the interface (Figure 1.9).

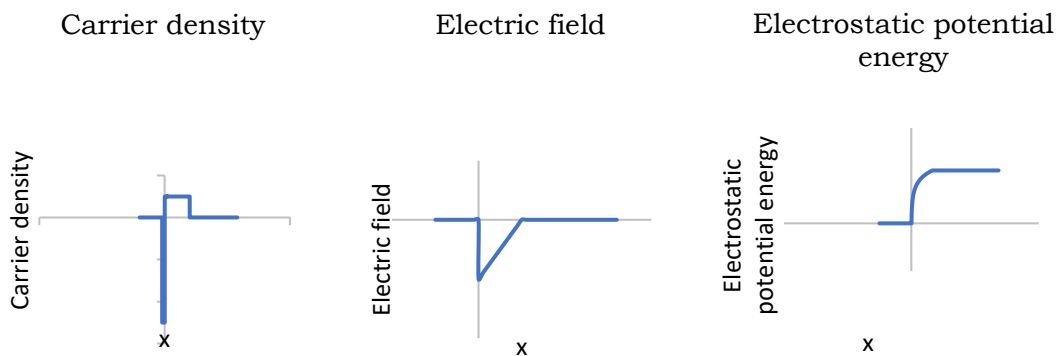


Figure 1.9: Modelling Poisson's equations to relate carrier density to electric field and energy. At 0 on the x-coordinate is the contact between the metal (negative direction) and the semiconductor (positive direction).

Modelling the interface in this way assumes negligible minority carrier concentration and that the doping level is constant outside the depletion region. The metal side is assumed to be a perfect conductor, resulting in a sheet of charge at an abrupt boundary, this is discussed further in Chapter 4.

For the formation of a Schottky barrier, the barrier height is dependent on the charge of the dopants, the density of dopants, the area and the distance of the depletion region. <sup>35,43</sup>

The depletion region can be visualised by use of Atomic Force Microscopy (AFM), due to the change in current flow in these regions. In the study of Cu clusters on rutile  $\text{TiO}_2$ , an area around the clusters demonstrated an apparent height change. This can be countered by the application of a potential to the AFM tip. <sup>48</sup>

### 1.3.13. Diode Characteristics

If diffusion is dominant in current transport, for an ideal diode, Equation 1.12 describes current through the device. <sup>43</sup>

Equation 1.12: 
$$I = I_0 \exp^{-E_a/kT}$$

I : Current / A

$I_0$  : Reverse saturation current / A

$E_a$ : Activation energy / J

kT: Thermal energy / J

Schottky barriers are modelled by analogy to the transport of high energy electrons over a barrier, analogous to thermal electrons being emitted from a hot wire in a vacuum. Therefore, there would be an expected temperature effect on the saturation current of the device with temperature. This is described by thermionic emission theory and is discussed in Chapter 4.

Low or no temperature dependence suggests that interface defects are responsible for the pinning of the Fermi level because their ionization entropy is only weakly dependent on the T. When the Fermi level is pinned, the T dependence of the barrier height is governed by the temperature dependence of the band gap. If governed by interface defects, their ionisation entropy would control the T dependence of the barrier height.

### 1.3.14. Photoelectric measurements

When a monochromatic light is incident on a metal, when the photon energy is higher than the barrier height, the photon will excite some electrons over the barrier. For photon energy above the barrier height, the photocurrent is given by Fowler theory, Equation 1.13. <sup>43</sup>

Equation 1.13: 
$$E_{hv} = B(h\nu - \phi_B)^2$$

$E_{hv}$ : Photon energy / eV

B: Constant

h: Planck's constant / eV s

$\nu$ : frequency / s<sup>-1</sup>

$\phi_B$ : Barrier height / eV

## 1.4. Conclusion

There is a need for a shift away from fossil fuel energy production to mitigate climate change and to bring electricity to those who still do not have access to it. Solar energy is the largest available resource and its deployment does not necessarily need large scale infrastructure. However, widely deployed Si first generation devices are limited in efficiency by thermodynamic limits as described by Shockley-Queisser limits.

Semiconductors are the backbone of all photovoltaic devices and a number of their important properties are described.  $\text{TiO}_2$  is a compound semiconductor which is often defective. Many of its important photocatalytic properties depend on defects such as oxygen vacancies. It is also typically present in amorphous, anatase and rutile phases for photocatalytic processes.

Schottky barriers provide a simple single junction device but they often deviate from their expected responses due to the non-ideality of the materials. Surface states and assumptions about bulk properties often result in a lack of predictability for Schottky barriers. Understanding their characteristics may result in improvements for Schottky barrier solar cells.

# 2. Chapter Two: Literature Review

## 2.1. Overview

Silver nanowires are being used in this work as a semi-transparent conductive layer that forms a Schottky barrier with  $\text{TiO}_2$ , but there exists a range of research on deployment alongside other existing technologies. For instance, the replacement of bus bars in traditional first generation solar cells, or as an alternative to Indium Tin Oxide or Fluorine doped Tin Oxide (ITO and FTO respectively) for conductive substrates for third generation devices.<sup>49,50, 51</sup> They can also be used as low resistance contacts for electrodes of III-IV LEDs.<sup>52</sup>

$\text{TiO}_2$  is a wide band gap semiconductor, but many n and p-type semiconductors that form a Schottky barrier with noble metals are considered here. There are many papers reporting on the formation of high quality, defect free Schottky barriers by atomic deposition techniques for use in low noise sensors and at extremely low temperature to study material properties. They are not reviewed here as the methods are incompatible with large area deployment and operation at room temperature. The scope of this literature review is therefore confined to Schottky barrier devices used as current generating devices, mainly by excitation across the band gap or by sensitized semiconductors.

## 2.2. Introduction to Schottky barrier photovoltaics

Figure 2.1, shows some of the possibilities for architectures of Schottky barrier current generating devices. Semiconductor films can be formed from a UV absorbing semiconductor, for use in UV sensors, the advantage of Schottky barriers in sensors include lacking an external power source or bias, high sensitivity and fast response due to the response being driven by majority carriers. Quantum dot films can extend the sensitivity of the film to the visible or infra-red region. These both rely on band gap excitation of the

semiconductor for both the absorption of light and the same semiconductor for the formation of the depletion region.

A sensitized Schottky barrier can be made by the use of dyes, quantum dots and even through plasmonic excitation. Plasmonic excitation is described further in Chapters 6 and 7. For detecting chemical reactions and the improvements in DSSCs, the Schottky barrier can be used to harvest the electrons at an interface where a redox reaction is taking place.

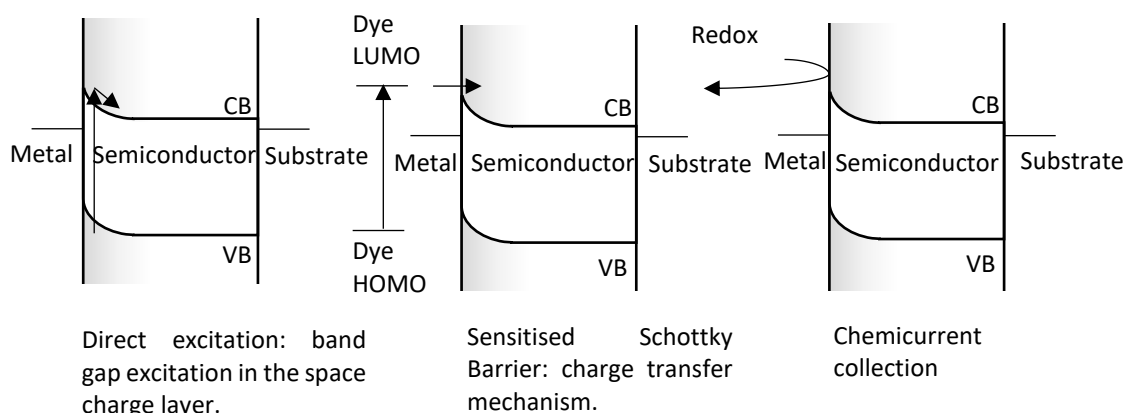


Figure 2.1: Architectures for Schottky barrier devices, showing excitation across the band gap in the depletion width. The barrier can be sensitized or a metal contact can catalyse a reaction at this interface.

## 2.2. Direct excitation in the visible region

One of the advantages of quantum dot based Schottky barrier is that it is possible to use IR sensitive quantum dots. This region makes up most solar radiation and quantum dots can be produced on flexible films. Further, ligands for solution processing can also contain functional groups for the passivation of surfaces, require no lattice matching and can be deposited by large-area coating methods. The quantum dots are also tuneable, offering the possibility of matching the absorption to the solar output.<sup>53</sup>

Luther et al., report on a p-type quantum dot (QD) device, with insulating ligands replaced with passivating thiol ligands, showing a 2.1% efficiency under AM1.5. Diode current-voltage (IV) curves and studies of work-function and open circuit voltage resulted in the hypothesis of the structure shown in Figure 2.2.

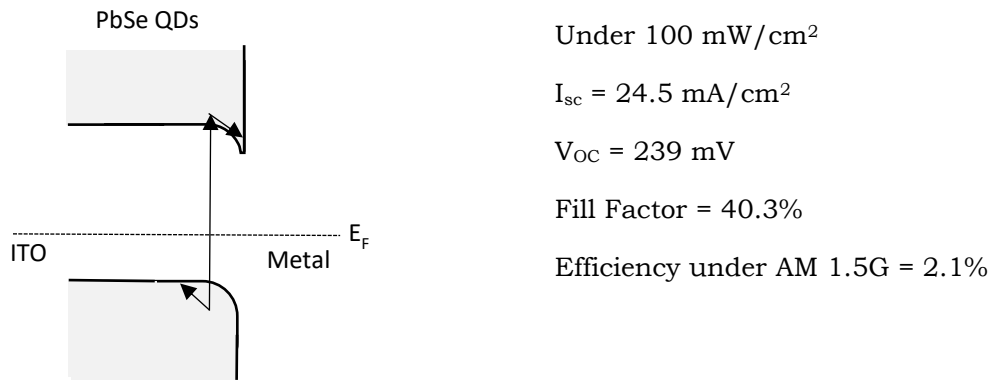


Figure 2.2: Illustration of direct excitation of a PbSe nanocrystal film with electrical characteristics. <sup>3</sup>  $I_{sc}$  and  $V_{OC}$  are the short circuit current and the open circuit voltage respectively. This band model was deduced from the IV curve and workfunctions measurements.

The confinement effect results in higher energy conduction bands and lower energy valence bands for smaller quantum dots. This allowed the authors to change the position of the conduction band and influence the open circuit voltage ( $V_{OC}$ ) predictably, without changing other properties at the interface. By changing the metal, an approximate correlation with the work function is observed, though the difference seen is smaller than would be expected and confirms the presence of the Schottky barrier, rather than a metal-insulator-metal structure. Similarly, thicker films result in poorer efficiency as charge separation at the “back” interface with the metal was less efficient.<sup>3</sup>

In this cell, the back Schottky contact prevents the absorption of enough light to allow high efficiency absorption of light. They are also unstable in air becoming ohmic after several minutes.<sup>3</sup>

A similar system is reported with an overall 3.6% power conversion efficiency in the IR region (70% EQE), using PbSe quantum dots with a magnesium layer and conductive bifunctional ligands. Changing the top contact from Mg to Al and Ag changed the efficiency and demonstrated the importance of the front contact in forming the charge separating Schottky barrier. <sup>54</sup>

Using capacitance methods to estimate depletion region thickness (65 nm) and the absorption density of the material, to estimate how far light penetrates the material (145 nm), the authors could make an estimation of the width of the region the charge carriers are generated in. This allows the

authors to determine that most of the light absorption is in fact happening in the quasi neutral region, with the majority of the transport therefore described by diffusion.<sup>54</sup>

These studies both emphasise the importance of formation of films and use a ligand exchange method to form a more conductive film. A PbS on ITO device with a LiF/Al metal contact to form a p-type Schottky barrier device was made and ligand replacement methods were monitored by IR. This systematic improvement resulted in a 5.2 % efficiency under AM 1.5, with a peak absorption of the PbS of 1100 nm. This shows how much the films could be improved by optimising solvents and cleaning.<sup>55</sup>

A polymer can also be used instead of a semiconductor, a Al/porphyrin-sensitized regioregular polythiophene Schottky barrier could be made on Au. The packing of the polythiophene impacts the currents observed, similar to the quantum dot films, where higher currents are observed where there is shorter distances between planes of the porphyrins. The illumination was performed through an evaporated Al layer, with the action spectra matching the absorption spectra of the polythiophene. By measuring the capacitance and dopant concentration for this system, an electric field at the interface of  $10^5 \text{ V cm}^{-1}$ , with a width of depletion layer of  $7 \pm 1 \text{ nm}$  was measured. This results in a 0.48 % efficiency under  $20 \mu\text{W cm}^{-2}$  radiation.<sup>56</sup>

## 2.3. Direct excitation in the UV region

### 2.3.1. Constant response above the band gap

Many devices described for UV detection are fabricated on p-type semiconductors such as GaN due to the low series resistance of these devices. High barrier heights are sought for highly sensitive UV detectors.

A high efficiency device can be formed with GaN as a low reverse saturation current resulting in a 65% efficiency, from a 70% transparent Pd contact.<sup>57</sup> In a similar device, the photo-responsivity of the device increases exponentially at the band gap of the semiconductor and plateaus above it. This is as expected for a Schottky barrier absorbing light at the semiconductor band gap.<sup>57</sup> Han et al., pushed the limits of efficiency further by growing a Au/Ga metal nanoparticle on a GaAs nanowire, resulting in an extremely abrupt junction, with a correspondingly large barrier height.<sup>58</sup>

Large barrier heights which can be an advantage in sensing applications can limit the efficiency of a photovoltaic device, as for an n-type ZnSTe on GaP grown by Molecular Beam Epitaxy (MBE) with an evaporated gold layer, which showed a high sensitivity which plateaus above the band gap, with a built in potential of 1.7 eV.<sup>59</sup>

### 2.3.2. Peaks in response above the band gap

Heavily doped diamond can provide excellent electrodes due to their chemical stabilities. Deep UV detector from tungsten carbide on boron doped diamond Schottky barrier. Responsivity varies linearly with UV light intensity. The Schottky barrier height was measured as 0.8 eV with a depletion region of 220 nm. There was a dramatic temperature dependence which differed with different metal contacts, attributed to a changing depletion regions, leading to the hypothesis of increased recombination of the carriers.<sup>60</sup>

In a UV photodetector fabricated from an evaporated Pt/Au layer on n-type GaN, a sub-band gap peak is seen in the photo-response. The integrals of electrons over the areas representing the widths of regions of absorption coefficients are measurable as well as width from the capacitance studies to give a quantity of electron-holes in these regions. This model explains the absorption above the band gap. Below the band gap, the current is proposed to be due to internal photoemission. The quantum efficiency is predicted by Fowler theory, where quantum efficiency depends on energy supplied, Equation 2.1. (51)

Equation 2.1: 
$$\text{Quantum efficiency} = x (E - \phi_{SB})^2$$

Which is indeed observed and gives a barrier height that agrees with the current-voltage-temperature measurements. Assuming a 10-nm ballistic transport in Pt films and suggests that the current measured may represent a roughly half efficiency for collection of the electrons, from their absorption and the distance which ballistic transport can take place. (51)

Photocurrent due to excitation from trap states is also seen in these devices and in fact, leads to photoconduction behaviour. The authors propose that when the effects of traps on the electrical field is greater than the photocurrent, the device acts as a photoconductor, this is significant for these devices as  $I_0$  is 0.8 mA/cm<sup>2</sup> at -1.0 V.<sup>61</sup>

### 2.3.3. Summary of visible and UV sensitive Schottky barrier devices

Table 2.1 shows a review of literature on some reported direct excitation Schottky barrier devices in the visible and UV region, with emphasis on the manufacture and key findings.

Experiment	Findings	Ref
<b>Direct excitation from quantum dot films</b>		
Layer-by-layer coating of PbSe quantum dots with oleate ligands were deposited, followed by washing in 1,2 ethanediol to form a film of 60-300 nm. Thiols were chosen to passivate surface states. Metal was evaporated onto the nanocrystal film.	Increasing band gaps by reducing particle size resulting in a higher open circuit voltage. Metal choice results in an approximate correlation with the Schottky-Mott rule.	3
PbSe with magnesium contact, replacing ligands in solution to form good quality films. A range of metals changed the IV characteristics and ability to generate a photocurrent.	3.6% power conversion efficiency in the IR region. Diffusion limits the efficiency. Carrier diffusion length = $\sqrt{(\mu\tau V_{bi})}/W$ where $\mu$ , $\tau$ , $V_{bi}$ , $W$ are the mobility, carrier lifetime, built-in voltage and width of the depletion region respectively.	54
5.2% efficient PbS device on ITO with LiF/Al following solvent and cleaning steps.	Solvents and cleaning is important to efficiency.	55
Infra-red sensitive PbS quantum dot devices fabricated between Al and ITO, with infra-red power conversion efficiency of 4.2%, with 37% quantum efficiency.	The estimated depletion region of 150 nm accounts for the majority of the ~230 nm thick film. Carrier recombination becomes dominant above 300 nm thickness, efficiency begins to decrease.	62
<b>UV sensitive direct excitation devices</b>		
Au/Ga alloy tips on GaAs nanowires, forming an atomically abrupt junction. The current scales with nanowire diameter with the same open circuit voltage, resulting in higher efficiency (2.8% at AM 1.5, $V_{OC}$ of 0.6 V, $J_{sc}$ of 11 mA/cm <sup>2</sup> for 70 nm diameter wires). Fill factor also increased due to the volume relative to surface effects.	Nanoparticles forming the tips on a nanowire are proposed to form an atomically abrupt junction.	58
Schottky barriers with an evaporated Pd contact with 70% transparency were formed on n-doped GaN on sapphire. The aim of the device was to use it as a UV sensor, requiring low series resistance. The photo-response of the device was over 65% efficient (0.18 A/W over 365 nm) with a fast response and high efficiency due to the low reverse	Predictable photo-responses were observed above the band gap of the semiconductor.	57

saturation current density of $6.3 \times 10^{-12}$ A/cm <sup>2</sup> .		
An evaporated Ti/Au contact on GaN on sapphire, p-doped to $7 \times 10^{17}$ with a residual n-doping of $1 \times 10^{17}$ with an activation energy of 1.5 eV. The responsivity of this device was 0.13 A/W for 1 nm <sup>2</sup>	Response of the device increases logarithmically at the band gap and plateaus above it.	63
An n-type ZnSTe layer was grown on GaP by molecular beam epitaxy with an evaporated Au layer to yield 0.13 A/W for a 3 mm square device (150 W xenon arc lamp) with a response time of 1.2 ns. The molecularly smooth layer could then be evaporated Au layer. This results in a built in potential of 1.7 eV.	The high barrier results in sensitive UV responsivity but limits the efficiency.	59
A range of porphyrins were used, an enhanced photocurrent can be obtained when the valence band (p-type) is more negative than the HOMO level of the porphyrin. Ortho substituted meso-porphyrin photocurrents gave lower photocurrents than meso-porphyrin, attributed to a larger distance between the planes of the porphyrin and the polythiophene with an Al contact.	The efficiency of the magnesium porphyrin was largest, attributed to the most facile oxidation of the magnesium, resulting in a self-doping.	56
Tungsten carbide on B-doped diamond with a quantum efficiency of 14% at 220 nm, with a depletion region of 275 nm. There is a decrease in photocurrent with temperature increase, as expected, attributed to a narrowing depletion region. This does not account for all the change. Changed metal contacts results in a different temperature dependence.	The proposed loss of photocurrent at high temperature is due to recombination, similar to Binet, below.	60
Ti/Al evaporated ohmic contact surrounding Pt/Au Schottky contacts (100 μm squares) on GaN on sapphire. Illumination from the sapphire side. Absorption and loss mechanisms (reflection and surface recombination) can both be described by integral equations to model the response, using absorption coefficients. Capacitance studies give depletion region measurements; 0.1 μm from the best fit.	There is a peak above band gap, rather than plateau. This is thought to be due to the absorption of light outside of the space charge region, increasing the amount of recombination. Absorption below the band gap is proposed to be due to internal photoemission.	61
<b>Visible light band gap Schottky barriers</b>		

<p>An n-GaAs oxide layer was removed with piranha solution and contacts formed with Au on an indium back contact. The barrier height and ideality factor were 0.86 eV and 1.95. The interface density drops 7-fold when a 0.5 V was applied. The deviation from ideality is due to series resistance. The <math>N_d</math> concentration is high at <math>4.3 \times 10^{17} \text{ cm}^{-3}</math>.</p>	<p>The <math>V_{oc}</math> and <math>J_{sc}</math> were 362 mV and <math>28.3 \mu\text{A} / \text{cm}^2</math> under AM 1. The relatively high ideality factor is attributed to oxide layers and interface states. Modelled according to the ideal diode equation and thermionic emission equation.</p>	<p>64</p>
<p>An 8.1% efficient p-type Schottky barrier was formed on p-Si using a Cr contact and Cu overlayer. A</p>	<p>Modelled with the ideal diode equation and thermionic emission theory. The overlayer of copper decrease the resistance by 2 orders of magnitude, the high efficiency is attributed to the low series resistance.</p>	<p>65</p>

Table 2.1: Summary of some visible and UV sensitive Schottky barrier devices reported in the literature.

## 2.4. Large area nanoparticulate Schottky barriers using sensitized films

One of the advantages of organic and quantum dots is the absorption of light is high absorption coefficients, resulting in thin photoactive layer. In Si photovoltaics, the long scale diffusion is an order or magnitude larger than that of the absorption of light. Both are considerably shorter in quantum dot and organic cells. Though the depletion widths in Schottky barriers is on the order of 100 nm typically, there is still a requirement for the most efficient absorption in  $\text{TiO}_2$ . There is a need to make the absorption as efficient as possible, providing an incentive for using dyes and quantum dots.<sup>53</sup> The following devices are those most similar to those presented in this work. The presence of an internal field at the interface can accelerate excited electrons into the  $\text{TiO}_2$  film, resulting in reduced recombination with redox mediators, described in Section 2.6.

MacFarland and Tang presented a novel “internal electron emission” device by using the high ballistic transport distance (20-150 nm in Au) to allow the sensitization of a metal film with merbromin, a commercially available mercury containing dye ( $8 \times 10^{14}$  molecules/cm<sup>2</sup>, the loading expected for a monolayer of dye on a gold film).<sup>66</sup> The metal Au film (10-50 nm) was electrodeposited on a  $\text{TiO}_2$  film formed at 500 °C film on Ti and following

work by Tang describes improvements to electrodeposited films to form large metal/semiconductor junctions. <sup>67</sup>

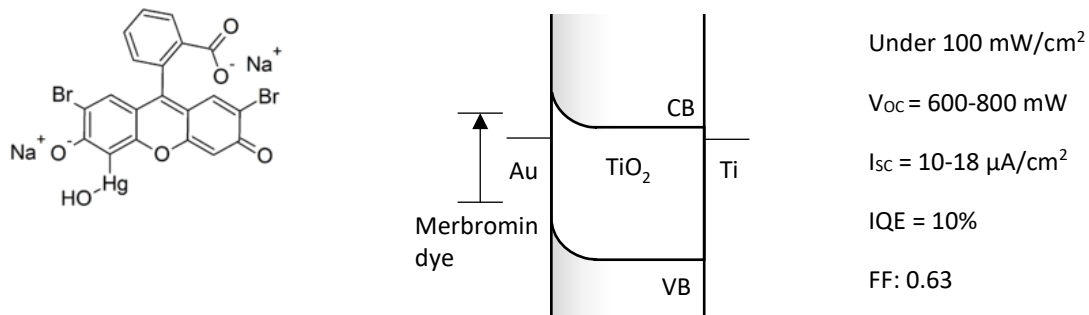


Figure 2.3: Device operating by internal photoemission, merbromin (left) was used to functionalise a gold film. Following excitation, electrons can travel through a gold film and the current it collected at the Schottky barrier (centre) resulting in electrical characteristics (right). CB and VB are valence band and conduction band respectively, IQE is the internal quantum efficiency,  $V_{oc}$ ,  $I_{sc}$  and FF are open circuit voltage, short circuit current and fill factor respectively.

The reduction of the dye occurs by electron transfer from near the Fermi level of the Au metal. The injection of energy into the gold sheet depends on either the electron transfer into the metal or the coupling of non-radiative excitation of the dye with metal conduction electrons. These must be greater than radiative emission and non-radiative de-excitation. De-excitation can occur through coupling to metal conduction band electrons. Though the authors believe electron transfer to be the dominant pathway, they concede they cannot rule out other mechanisms. <sup>66</sup>

The maximum photovoltage derived from this structure dependant on the difference under illumination of the Fermi level of the semiconductor and that of the metal contact. The electrons injected are under the forward bias,  $V_{oc}$ , so there is no net build-up of current. <sup>66</sup>

Equation 2.2 
$$V_{oc} = \left(\frac{nkT}{q}\right) \left[\ln\left(\frac{j}{T^2 A^{**}}\right) + q\phi_B/kT\right]$$

$V_{oc}$ : Open circuit voltage / V

n: diode ideality factor

J: photon absorption

k: Planck's constant / eV s

q: electron charge / C

T: temperature / K

$\phi_B$ : Schottky barrier height / eV

The efficient electron injection is supposed to depend on physical and electronic coupling of the chromophore to the metal conduction levels, the evidence provided is that of a blue shifted absorption peak of the merbromin on a gold film, though a similar shift is seen on glass.<sup>66</sup>

The method as described above required pure material and high vacuum. Su et al. used commercial TiO<sub>2</sub>, spin coated on ITO coated glass and annealed, followed by the formation of a device by a method shown in Figure 2.4.

It is proposed that dye molecules are absorbed on the gold nanoparticles. These cells are up to 0.95% at 0.1 Sun.<sup>68</sup>

A TiO<sub>2</sub> film was fabricated on an FTO substrate and Ru(dcbpy)<sub>2</sub>(NCS)<sub>2</sub> was used to interface between the semiconductor and a thin Au film, to observe a visible photocurrent from the gold plasmonic absorption and the dye, as well as the TiO<sub>2</sub>. This improved the rectification ratio of the device by two orders of magnitude and lowered the reverse saturation current. This was supposed to be due to changes in the fields caused by oxygen vacancies. Resistance of the device increases in oxygen atmosphere, as there are fewer vacancies and the activation energy for overcoming the barrier as the barrier height increases or the loss of trap-assisted tunnelling mechanisms. The density of states at compact TiO<sub>2</sub> interfaces is very high, reported to be on the order of 10<sup>20</sup> cm<sup>-3</sup>, resulting in inhomogeneity on the Schottky barrier height formed and tunnelling becomes important in the transport.<sup>69</sup> mechanisms, which is sensitive to temperature due to the occupation of surface states. Similarly, a device formed of p-type Si, methyl red as an electron rich interlayer and an evaporated Al layer showed electrical properties limited by the Si substrate.<sup>70</sup>

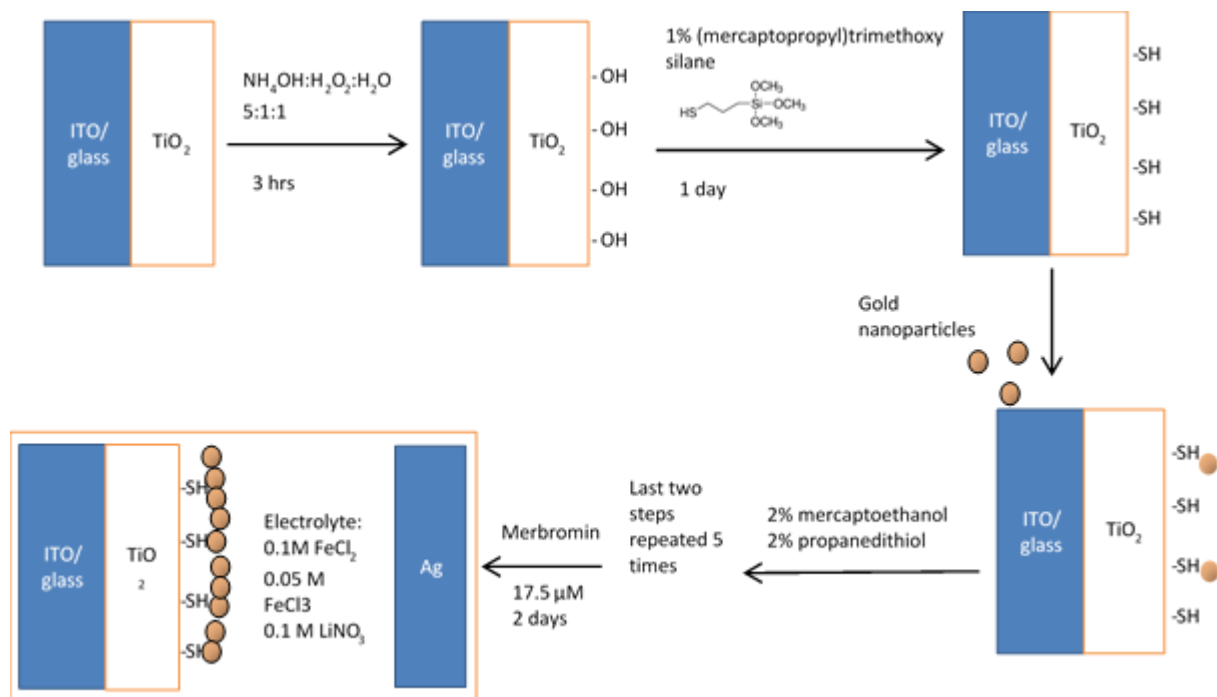


Figure 2.4: Diagram showing a method by which a Au nanoparticle film contact can be formed on TiO<sub>2</sub> by bifunctionalised ligands. This device can be functionalised with merbromin.

Another anodised TiO<sub>2</sub> film (rutile, 50-60 nm) on Ti with a Au thin layer was sensitized with merbromin and hydrophobic CdSe quantum dots. Similar to above, water and oxygen were essential for rectifications and high photocurrents, with a fall to 8% of the open vessel photovoltage for the closed vessel, alongside a decrease in rectification, which is recoverable in the presence of both air and water. The band-gap states are proposed to be 0.5 to 0.8 eV below the conduction level. Under UV light, more defect states are formed, with adsorbed water reversing this process.

Therefore, a protective layer for absorption, an “antenna” layer, maintaining the chemistry at the Schottky barrier interface should provide an efficient architecture.<sup>71</sup>

## 2.5. Current collection at Schottky barriers by catalysed chemical reaction

A set of studies have looked at how by catalysing reactions at metal nanoparticles on a semiconductor interface, a current can be collected through oxidation of a substance at a surface. This has been performed for

the oxidation of CO to CO<sub>2</sub> with 0.5 eq. O<sub>2</sub> with the production of 2 e<sup>-</sup> on a 5 nm Pt/TiO<sub>2</sub> Schottky diode.<sup>72</sup>

These "chemicurrents" are collected as part of a non-adiabatic process where energy is gained or lost by the system. For this reason, it is hypothesised that there is a spread of energies around the potential at which the CO oxidation took place, resulting in some electrons above the Fermi level of the metal, collected through the 5 nm film due to the higher ballistic transport of electrons in Pt, followed by injection over the 0.5 eV barrier.<sup>72</sup>

A later work was reported for a similar system, where CO was oxidised on Au nanoparticles on TiO<sub>2</sub> diodes. Although Au nanoparticles are not catalytically active, they show chemicurrents. The reaction was also dictated by the capping agent used on the nanoparticles.<sup>73</sup>

With a focus on possible use in photocatalysis RuO<sub>2</sub> was used as the metallic contact on a CdS semiconductor to form a Schottky barrier which showed an expected IV response under light and dark conditions typical of a low efficiency Schottky device, with a linear Mott-Schottky plot for 1/C<sup>2</sup> against applied voltage. Though the device was not optimised for optical absorption, or a grid for conductivity, there was a stress on the low overpotential of RuO<sub>2</sub> for oxygen evolution, suggesting this device could drive chemical reactions. This device was produced from fusing metallic indium and sputtering of RuO<sub>2</sub>.<sup>74</sup>

Though not strictly a chemicurrent, a dissociated molecule can also change the characteristics of the Schottky barrier, allowing gas sensing. The electrical field enhancement of Pt/nanostructured ZnO nanostructured Schottky diodes were fabricated and used in reverse bias as hydrogen sensors as the hydrogen dissociates and changes the Zn-O dipole by associating with the oxygen, weakening the dipole.<sup>75</sup>

## 2.6. The use of Schottky barriers to improve current collection in DSSCs

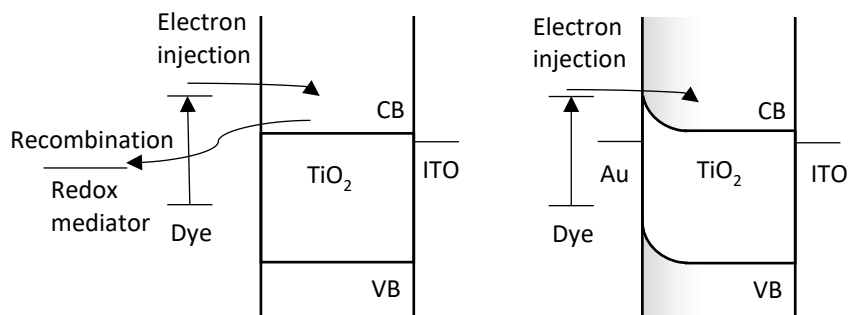


Figure 2.5: Schematic of mechanism of improvement to current collection when Schottky barriers are formed at interfaces in DSSCs, limiting the rate of recombination with redox mediator or dye due to the acceleration of electrons away from the interface.

Schottky barriers have been used in the improvement of efficiencies of DSSCs. As shown above, Au nanoparticles were deposited on ZnO to form Schottky barriers. The dynamics of electron injection from the dyes is the same, but a slower decay was attributed to a lack of recombination, resulting in an improvement of 130% efficiency improvement for the unfunctionalised device.<sup>76</sup> A similar TiO<sub>2</sub> on silver nanowires improved the efficiency by 1.5 to 2.0 times due to the increased electron harvesting by improving the transport of electrons. The Schottky barrier is proposed to hinder some of the competing processes to electron harvesting. The processes proposed to be hindered by the presence of the Schottky barrier are non-radiative de-excitation by coupling to conduction band electrons.<sup>77</sup>

Similarly, a Schottky barrier on the back contact of DSSCs are used to explain the so-called “UV-effect” of DSSCs. In this effect, under white light, the currents generated in the cell are higher than under monochromatic light in the region that the dye absorbs in. An increase in photocurrent is expected due to the movement of the conduction band to more negative potentials under UV light, leading to more efficient injection of electrons from dyes, however IV curves under illumination have an “S-shape” suggesting the presence of a barrier. It is known that TiO<sub>2</sub> forms surface states under UV light, utilised in photocatalysis, and it is these surface states that are proposed to “pin” the Fermi level of the semi-conductor, resulting in a low barrier of injection from the semi-conductor into the ITO. (29)

Snaith et al. investigated this by deposited a high-density layer with many oxygen vacancies by spray pyrolysis to form a Schottky barrier to FTO. An analogous version with an ohmic contact had a higher current density. <sup>33</sup>

## 2.7. Conclusion

In conclusion, Schottky barriers have been used both directly by excitation across the band gap of a semiconductor in the UV and visible region, including by the formation of visible or even IR absorbing quantum dot films. The Schottky barrier can also be sensitized with dyes and quantum dots, though this tends to be on evaporated films. The internal photoemission is comparable to the chemicurrents produced via oxidations taking place on a metal surface and they can show remarkable catalysis. In a similar fashion, the Schottky barrier can be utilised to reduce recombination on DSSCs.

# 3: Chapter Three: Device fabrication

## 3.1. Overview

Stainless steel is a low-cost and widespread building material and was chosen as the substrate for this work as the aim was to produce a scalable,

low cost Schottky barrier device compatible with formation of large area photovoltaics. However, stainless steel is also a complex material which self-protects due to the formation of corrosion resistant layers.

Early investigations show two problems would dominate the fabrication of these devices, diffusion and crystallinity. This was initially a roadblock for developing working cells as these problems led to small and unpredictable photocurrents. A solvothermal method was used to improve sol crystallinity.

The first part of this chapter describes the methods used in the formation of devices used in this work. The second part of this chapter examines the literature on  $\text{TiO}_2$  sols and their deposition on substrates and what impact diffusion has. This leads to experiments in forming and sintering  $\text{TiO}_2$  films were used to reliably form devices in a way compatible with forming high quality films on stainless steel.

## 3.2. Methods and Analysis

### 3.2.1. SEM

Samples are prepared by carbon sputtering and ozone cleaning. The SEM imaging was performed on a Hitachi SU8230. An Oxford Instruments Aztec Energy EDX (Energy-dispersive X-ray spectroscopy) system was used for simultaneous EDX measurements.

Typically, a working distance of 8 mm was used with a 2000 V accelerating voltage. A problem encountered frequently on these devices was astigmatism, whereby the focus of the SEM images is compromised. This can occur due to charging of the sample, which causes the circular beam being distorted into an ellipse. Electromagnetic coils can be used to compensate for this, but this method requires practice. EDX measures the X-rays produced by the atoms excited through bombardment by high energy electrons. The X-rays measured are characteristic of atomic transitions.

### 3.2.2. XRD

A Bruker V3 XRD was used for diffraction measurement, usually between 20 and 80°. A corundum sample with large crystal size, to quantify machine broadening. The Scherrer Equation was used to analyse particle size, described in Section 3.7.4.

### 3.2.3. Electrochemical measurements

A Gamry Potentiostat was used to run cycling voltammetry studies on a device. This was typically run between -1 V and +1 V with a 100  $\Omega$  resistor used in series with the device in order to limit the current through the silver nanowires.

### 3.2.4. UV-vis spectroscopy

A Multiscan GO UV-vis spectrometer was used with polystyrene well plates. Samples were prepared using micropipettes. The well plates absorbed strongly below 300 nm.

### 3.2.5. Photocurrent measurements

Photocurrent measurements were performed by sweeping from high to low wavelength with a Bentham arc lamp monochromator, controlled by a program written in C in-house by R Crook. In later experiments, higher powered LEDs with 400 and 425 nm output with a width of +/- 5 nm.

To measure a photocurrent, an amplifier was used. The transconductance amplifier was built in-house by R. Crook. This was connected to the device in such a way as to be consistent between devices. The amplifier was connected to voltmeter, such as the UT60A using the associated software to take a reading every second.

### 3.2.6 Arc Lamp Calibration

To calibrate the output of the Bentham Arc Lamp (Bentham SSM150Xe), two commercial Si photodiodes were used. The spectral response of a Series 7 EO Super UV Silicon Photodetector to give a responsivity in A/W between 800 and 400 nm using sensitivity documentation from the supplier. A Centronic OSD5.8-7Q Full Spectrum Si Photodiode was used to responsivity between 400 and 260 nm. Using the power output and the energy per photon for each wavelength, the photons per  $\text{cm}^{-2}$  can be calculated. The UV photodetector calibration is of interest due to the non-linear transmittance of the optical fibre and output at these wavelengths. Neither linear extrapolation from high wavelengths nor estimation of black body irradiation was sufficient to accurately predict the output at these wavelengths.

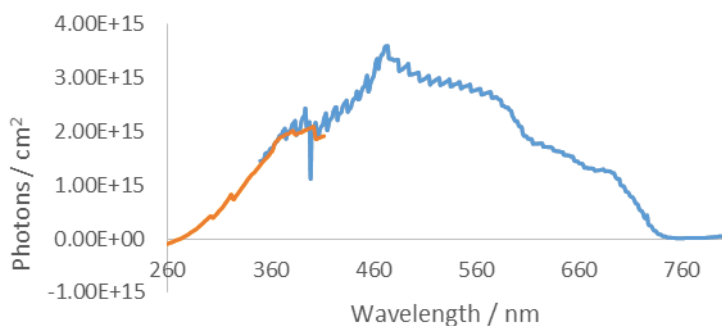


Figure 3.1: Calibrated photon outputs from the power output plots from the commercial photodiodes. The number of photons per  $\text{cm}^2$  is calculated from the responsivity plot from the manufacturers from the Series 7 EO Super UV Silicon Photodetector (blue line) and Centronic OSD5.8-7Q Full Spectrum Si diode (orange line).

### 3.2.7. Solvothermal synthesis and dip coating

In a typical sol synthesis, 1 ml of titanium isopropoxide,  $\text{Ti}(\text{iOPr})_4$  (97% Sigma-Aldrich) was added to a solution containing 1 ml concentrated nitric acid (68% Fischer) with 78 ml deionized water or isopropanol (IPA) dropwise. As the precursor was hydrolysed into  $\text{TiO}_2$  particles, a cloudy flocculate forms.

The suspension was stirred and resulted in a transparent solution as the particles were peptized. The suspension was stirred vigorously for 30 minutes. Peptization, the splitting of large agglomerates into small particles, is due to the presence of nitric acid, resulting in the formation of surface charges resulting from an electrical double layer.

Following this, the sol was refluxed, for 8 hours to 32 by increases in 4-hour intervals, with the solution being allowed to cool so sampling can take place. Following cooling, the sol was neutralised with 3.5% ammonia solution. The water based sol tended to bead off the surface of the steel and the sol was too concentrated. To counter both, an equal volume of solution was added to IPA.

To dip coat a substrate, a substrate was washed in IPA and water. A substrate was submerged in the suspension and withdrawn slowly by hand in several seconds. The substrate was then blotted onto absorbent blue roll paper to remove excess by capillary action. This film was dried at room

temperature and the process was repeated as necessary for the device, typically 4 coats were used.

To sinter the films, they were placed in a Nabertherm furnace (Nabertherm GmbH SN317975) and heated in air to the required temperature. When pre-treated steel samples were required, they were heated in air to high temperatures and allowed to cool before this process.

### 3.2.8 Silver nanowire deposition

Commercial silver nanowire suspensions were used throughout this work. Previous work in has resulted in uniform and consistent films with high transparency through use of a commercial paint sprayer. However, this was used for much larger areas than used in these devices and the spraying can result in a short circuit with the substrate. Drop casting was chosen for speed and reliability in forming the devices in this work.

A 0.5% wt/v suspension of 60 nm × 10 μm AgNW in IPA (Sigma-Aldrich) was diluted by half in IPA. This solution was drop cast using a micropipette in small volumes, typically 5 μL. Between coats, this solution dried at room temperature. In a typical device, 10 μL were used, which was found to be optimum for these devices.

To form the device, the silver nanowires were annealed to reduce the resistance of the nanomesh. A series of nanomeshes on glass were made, with two silver contacts. Although detailed work on the resistances of silver nanomeshes has been made, the resistance of the film falls at all temperatures between 180-280 °C, particularly in the first 5 minutes, Figure 3.2. Increased time continues to reduce resistance. The silver nanowires are typically stabilised with a polymer such as PVP to prevent agglomeration. Heating may melt the polymer or cause loss of the polymer and loss of solvent to bring the nanowires into contact. Further, the junction of the nanowires can be improved further by the increase in the junction area by heating. This results in a very highly conductive network due to the high conductivity of silver.

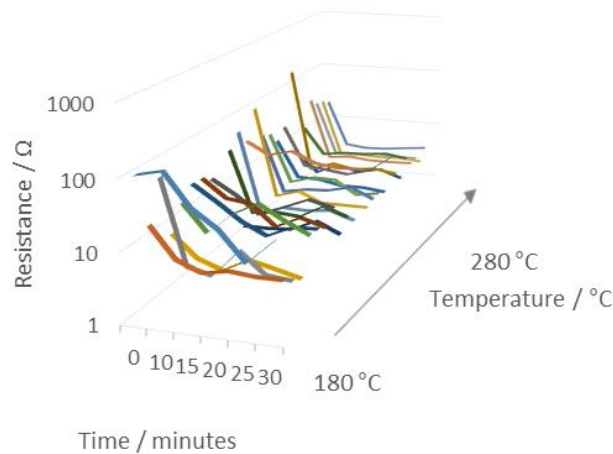


Figure 3.2: Resistance between two points showing a reduction of resistance with time and temperature. The resistance drops to some tens of ohms in a brief period of time then resistance remains approximately constant.

An intermediate temperature and time of 235 °C and 20 minutes was used to anneal the films unless otherwise stated.

Silver nanowires can span gaps in titania films, providing another advantage to the formation of conductive silver nanomeshes, Figure 3.3.

### 3.2.9. Capacitance measurements

To measure capacitance, a lock-in amplifier (Stanford Research Systems SR530 Lock-In Amplifier) and mechanical signal generator (Stanford Research Systems Model DS345) was used. The lock-in amplifier, by synchronizing with the AC supplied by the signal generator, can measure a phase sensitive signal, allowing for the detection of a signal, even in the presence of substantial noise. A lock-in amplifier takes an input signal and multiplies it by the reference signal and integrates over a specific time. All reported voltages in this work were root mean squared voltage and the waveform was sinusoidal.

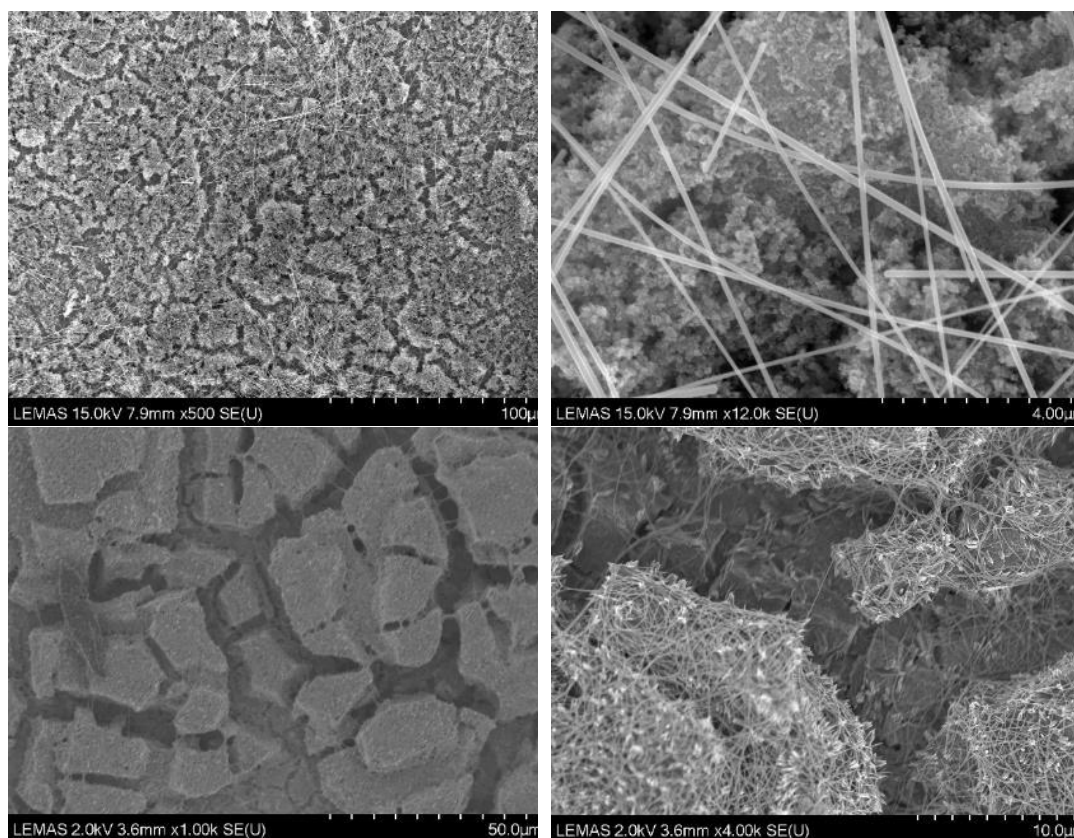


Figure 3.3: SEM images showing an incomplete TiO<sub>2</sub> film (top left and bottom left) showing plateaus of particles, dispersed with nanowires as bright wires. Silver nanowire films (bright lines) on early devices of thick titania films, demonstrating their ability to bridge gaps in TiO<sub>2</sub> (top right and bottom right).

The top contact was made to the silver nanowires through use of silver paint.

### 3.2.10. Dyes

*cis*-Bis(isothiocyanato)bis(2,2'-bipyridyl-4,4'-dicarboxylato)ruthenium(II) (Ru(dcbpy)<sub>2</sub>(NCS)<sub>2</sub>) (Sigma Aldrich - 95%) was dissolved in IPA. Organic dyes, celestine blue (Arcos Organics), alizarin red (Bio Basic Canada Inc.), alizarin yellow GC (Bio Basic Canada Inc.) were dissolved in diionised water. Methylene blue (AppliChem) was dissolved in ethanol and diluted with diionised water. Aurintricarboxylic acid (Alfa Aesar) was sparingly soluble in diionised water.

### 3.2.11. Quantum dots

Quantum dot films were typically formed by spin coating a total of 0.15 ml of 5 mg/ml CdS (Sigma Aldrich – size , peak absorption: 400 nm), CdSe (Sigma Aldrich – size, peak absorption: 560 nm) and CdTe (Sigma Aldrich –

size, peak absorption: 510 nm), with 5  $\mu\text{L}$  per deposition, with drying coats at 200  $^{\circ}\text{C}$  for 30 minutes to remove the ligands.

#### 3.2.12. TaON

Heavy doping of  $\text{Ta}_2\text{O}_5$  with nitrogen by ammonia at high temperature results in a transition to TaON, resulting in a red-orange powder.<sup>78</sup> A sample was kindly provided by R. Douthwaite, University of York.

To create a film of TaON on steel, 0.011g of TaON powder was suspended in 0.166 ml 1M acetic acid. 5  $\mu\text{L}$  of this sol was deposited with 5  $\mu\text{L}$  of IPA.

#### 3.2.13. Spin coating dense $\text{TiO}_2$ layers

Dense  $\text{TiO}_2$  films are produced using a method by spin coating three 2.4  $\mu\text{L}$  of  $\text{Ti}(\text{iOPr})_4$  (2.9  $\mu\text{L}$ ) solution in IPA (20 ml) layers, similar to a literature method.<sup>79</sup> The spin coating was performed on a (Spin Coater Prototyper) at 2000 rpm.

#### 3.2.14. Steel preparation

304 stainless steel contains 18-20% Cr, 8-10.5% Ni, <2% Mn, <1% Si, the remainder is Fe. 316 stainless steel also contains 16-18.5% Cr, 10-14% Ni, <2% Mn, <1% Si and 2-3% Mo, the remainder is Fe.

304 stainless steel and 316 stainless steel were procured from RS components and Alfa Aesar. TiN coated steel (2-3  $\mu\text{m}$  TiN coating on 316 steel – Goodfellow) and steel samples were chopped into  $\sim 1\text{ cm}^2$  samples by hand. Each sample was cleaned in IPA several times before use and dried on clean room cloths.

In some cases and for all devices fabricated on TiN coated steel, the substrate was heated in air in a Nabertherm furnace.

### 3.3. Introduction

Dye sensitized solar cells (DSSCs) and photocatalytic systems were the inspiration for the use of sol gel for the formation of a  $\text{TiO}_2$  film on a steel

substrate. Although some DSSC devices have been fabricated on steel, the use of corrosive electrolytes such as the iodide electrolytes usually used in DSSCs, which can corrode the substrate. There is a plethora of literature on forming reliable films on substrates.

The hydrolysis of precursor results in small primary particles stabilised in solvent and deposited on a substrate such as by doctor blading or spin coating. Usually an organic binder such as a cellulosic or a polymer can be used to prevent the cracking of a film at high temperatures of sintering.

High temperatures are used for sintering  $\text{TiO}_2$  films to crystallise the particles, form a continuous film through “necking” of the particles and adhering the film to the substrate. However, the high temperatures used in these methods results in the diffusion of ions from the substrate.

For DSSCs, the diffusion, typically of Sn or In from a transparent conducting oxide has been reported in literature and can be beneficial for the efficiency of DSSCs (Section 3.6) It has even been shown that for some photocatalytic devices of  $\text{TiO}_2$  on substrate can even be beneficial, with the ions aiding catalysis.<sup>80</sup>

### 3.3.1. Fabrication of Schottky barriers

The devices described in the Literature Review generally use an evaporated, pure metal layer. Large area devices use methods such as electrodeposition or chemical binding to form metal contacts. The aim in this work is to produce a device using a silver nanowire mesh, avoiding the use of toxic ligands or high vacuum methods that are incompatible with low cost large scale or roll-to-roll manufacture.

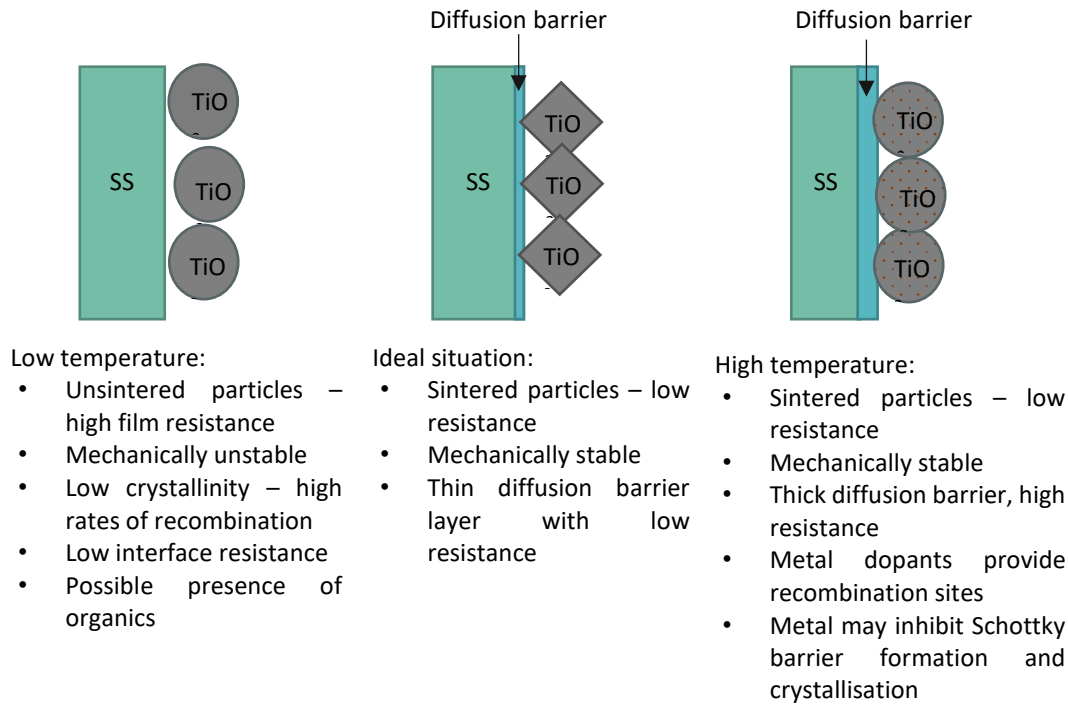


Figure 3.4: Illustration of the technical challenge of forming a  $\text{TiO}_2$  sol on a stainless-steel substrate.

There are several important advantages to the use of silver nanowires:

- 1) Research is ongoing into their production, purification, processing into large area films and passivation to result in stable conductive films without the use of rarer elements such as indium. This is emerging technology and improvements will continue to be made in this area.
- 2) Nanowires allow the formation of the conductive substrate and the Schottky barrier with the same material. This allows the use of new architectures. Further, if the depletion region extends in three dimensions around the nanowires as charge is transferred from the semiconductor to the silver nanowires, Figure 3.5, there is an area around the nanowires that can be functionalised, without the need for ballistic transport through a metal layer.

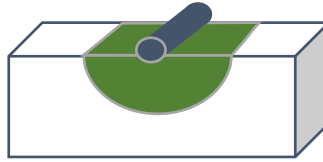


Figure 3.5: Demonstrating a depletion region extending into an area around a silver nanowire. The depletion region forms due to the transfer of small amounts of charge from the semiconductor to the silver nanowire.

### 3.3.2. Stainless steel at high temperatures

There is a global production of over 1,600 million tonnes of steel per year (2016)<sup>81</sup> with a plethora of grades of steel, using various alloying elements as well as carbon such as transition metal elements such as manganese, chromium, nickel, tungsten and molybdenum and non-metals such as phosphorous, sulfur and boron. The ability of stainless steel to resist oxidation, even at high temperatures or in contact with acids is one of its most useful properties. Stainless steels form a layer of an oxide which prevents the diffusion of oxygen to the internal structure.

#### 3.3.2.1. Oxide scale

The identity of the oxide scale formed on stainless steel has been studied broadly because of its importance in corrosion of steel at high temperatures. 304 and 316 stainless steels studies by XRD and infra-red spectroscopy showed the presence of  $\alpha$ - $\text{Fe}_2\text{O}_3$ ,  $\text{Cr}_2\text{O}_3$  and spinels of manganese chromium and oxygen, similar in both metals. On 304 stainless steel oxidised at 900 °C, the oxides identified by infra-red were  $\text{Cr}_2\text{O}_3$ ,  $\text{MnCr}_2\text{O}_4$ ,  $\text{NiO}$  and  $\text{SiO}_2$ . At higher temperatures, the  $\text{NiO}$  disappears and nickel ferrichromate can be seen.  $\text{Fe}_2\text{O}_3$  can be observed when the substrate is heated to or above 1000 °C, or when the surface has been treated with  $\text{HCl}/\text{HNO}_3$ .<sup>82</sup> The protective Cr-Fe spinel formed in an oxygen free environment, has different relative mobilities for ions through the scale, the order of the rate of diffusion was  $\text{Mn}^{2+} > \text{Fe}^{2+} > \text{Co}^{2+} > \text{Ni}^{2+} > \text{Cr}^{3+}$ .<sup>83</sup> As the scale relies on the formation of chromia layer, smaller grain sizes in the steel result in a larger flux of chromia into the protective but at the cost of less in the remaining material.<sup>84</sup>

#### 3.3.2.2. Impact of temperature

304 and 316 stainless steel differs in the protective oxide formed. Stress accumulates in 304 steel at higher temperatures, resulting in creep or

cracking of the scale. This takes 40 times longer on 316 stainless steel than 304 stainless steel.<sup>85</sup> Also,  $\text{Cl}^-$  seems not to be incorporated into the passive protective chromia layer for 316 steel.<sup>86</sup>

A study of Cr diffusion through  $\text{Cr}_2\text{O}_3$  on amorphous silicon showed that up to 500 °C, only a small fraction of the Cr will diffuse through the  $\text{Cr}_2\text{O}_3$ . Above 540 °C, the transport of metallic chromium is much faster.<sup>87</sup> This fast diffusion of Cr at high temperature may explain the chromium rich outer layer of steel oxides at high temperatures, above 700 °C compared to the iron rich oxide at 600 °C.<sup>88</sup>

The study of steel oxidation is complex due to the complexity of the oxide scales that are formed, which depend on the grade of steel, the temperature and the environment. 316 stainless steel produces a chromia rich layer more resistant to acid and high temperature oxidation.

#### 3.3.2.3. Impact of salts

The self-protective layer on stainless steel can be disrupted. The corrosion of steel is accelerated in salt water and where biomass or hydrocarbon combustion where there is a combination of salt and high temperature. Although the exact mechanism of this is under debate, particularly due to the complexity of steel given its large variation in crystallinity and composition around the eutectic compositions. However, it is thought alkali chlorides can react with a chromium layer to form a stable  $\text{A}_2\text{CrO}_4$ , where A is from the alkali chloride.<sup>89</sup> In the case of 304 steel with KCl at 600 °C, the growing scale consisted of hematite with  $\text{K}_2\text{CrO}_4$  particles embedded, with an inner layer of spinel oxide.<sup>90</sup> The same has been seen with NaCl, and even following the breakdown of the alkali chromates,  $\text{Cr}_2\text{O}_3$  nodules formed are not protective against a fast growing  $\text{Fe}_2\text{O}_3$  layer at 600 °C.<sup>91</sup> Given the protection of stainless steel is due to the inhibition of Fe diffusion to the surface, this represents failure of the corrosion protection.

#### 3.3.3. Substrates and the impact of metal diffusion

The importance of diffusion through a  $\text{TiO}_2$  layer is rarely mentioned in the literature on  $\text{TiO}_2$  sols on transparent substrates. The diffusion of metals into  $\text{TiO}_2$  in DSSCs is non-trivial, so the comparable lack of material on it, relative to, for instance the use of polymers to form consistent  $\text{TiO}_2$  films, may be due to the improvement in some DSSC characteristics following Sn diffusion

from a substrate. Indeed, in some papers, it is added to the sol intentionally to improve efficiency.<sup>92</sup>

One study of Sn diffusion by Energy-dispersive X-ray spectroscopy (EDX) from the substrate was performed by Kabre and LeSuer, by studying the diffusion of Sn through a typical doctor bladed and sintered layer of TiO<sub>2</sub> on SnO<sub>2</sub>:F coated soda lime glass was studied by EDX.<sup>93</sup>

Using Fick's second law of diffusion, the EDX spectrums were analysed and the SnO<sub>2</sub>:F is modelled as a depleting source of tin. At the interface, the change in concentration with distance is zero and the TiO<sub>2</sub> and glass is assumed to be infinite and that no Sn is present outside the film at the beginning, providing three boundary conditions for the fitting of the concentrations to Fick's second law in 1 dimension, Equation 3.1.<sup>93</sup>

Equation 3.1: 
$$\frac{\partial C_i}{\partial t} = D_i \frac{\partial^2 C_i}{\partial x^2}$$

C<sub>i</sub>: Concentration / mol m<sup>-3</sup>

D<sub>i</sub>: Diffusion coefficient / m<sup>2</sup> s

t: time / s

x: distance /m

Where C<sub>i</sub> is the concentration and D<sub>i</sub> is the diffusion coefficient. A model of Sn as a function of time and distance is described by Equation 3.2.

Equation 3.2: 
$$C_i = \frac{C_0}{(\pi D_i t)^{1/2}} \exp\left(-\frac{x^2}{4D_i t}\right)$$

C<sub>0</sub>: Initial concentration / mol m<sup>-3</sup>

At t=0, C<sub>i</sub> = 0

At t=0, C<sub>0</sub> = concentration of Sn in SnO<sub>2</sub>:F film

As EDX quantification of concentration is difficult, the EDX measurements were made by normalising the concentration in the SnO<sub>2</sub>:F film, determining relative changes in concentration.

Diffusion coefficients for Sn in this mesoporous P25 TiO<sub>2</sub> film at 3.2 × 10<sup>-5</sup> μm<sup>2</sup> s<sup>-1</sup> at 450 °C to 22 × 10<sup>-5</sup> μm<sup>2</sup> s<sup>-1</sup> at 500 °C and 59 × 10<sup>-5</sup> μm<sup>2</sup> s<sup>-1</sup> at 600

°C. These are much faster than typical diffusion constants through a crystal, which can occur interstitially or through cation vacancies. Grain boundaries provide other, faster, mechanisms of transport.<sup>93</sup> Andrei and Zerulla visualise the impact of Sn in TiO<sub>2</sub> films and its relation to efficiency of DSSCs with the EDX mapping of Sn through a TiO<sub>2</sub> film, the higher efficiency devices were sintered at 500 °C. The efficiency increase was due to the increasing open circuit voltage, due to the movement of the conduction band to more negative potentials.<sup>94</sup>

Another reason for the increased concentration of metals at surfaces following diffusion, is their oxidation, resulting in their accumulation. For instance, the extrusion of Al from a growing TiO<sub>2</sub> crystal during annealing has been used in the study of electron transport.<sup>95</sup>

From Zhu et al., the percentage of iron at the surface of a 90 nm sol-gel film was 7.1% after an hour sintering at 400 °C.<sup>96</sup> From a starting percentage of Fe in the steel of 71% and solving the equations used by Kabre and LeSeur, a diffusion constant from equation gave a value of  $9.9 \times 10^{-8} \mu\text{m}^2 \text{s}^{-1}$ .<sup>93</sup> This is much smaller value for  $D_i$  than that observed for the Sn through mesoporous TiO<sub>2</sub>,  $3.2 \times 10^{-5} \mu\text{m}^2 \text{s}^{-1}$  at 450 °C. This may be due to the difference in the production of the film. On steel, a sol-gel method was used to form the film. It may be that the individual P25 particles provide a much greater surface area or screw dislocation density due to the 3 detectable phases in the small ~25 nm particles.<sup>97</sup>

In a study of TiO<sub>2</sub> on nickel foam by dip coating in sol, followed by spinning at high speeds, a pre-calcined substrate resulted in a layer of NiO, resulting in less Ni<sup>2+</sup> in the TiO<sub>2</sub> film. This may have reduced the activity, as Ni<sup>2+</sup> increases the wavelength absorption edge, resulting in more absorption.<sup>80</sup>

#### 3.3.4. Formation of crystalline titania films

Thin films of nano-particulate TiO<sub>2</sub> can form nearly transparent coatings at visible wavelengths and porosity may influence the available area for photocatalysis or sensitization. Doping may be intentional or a result of diffusion from substrates and may influence absorption or crystallinity and the temperature of annealing reduces film thickness and changes crystal phase but may have to be chosen carefully to avoid damage, for instance to ITO coated polymers.

### 3.3.5. Phase

Density Functional Theory (DFT) studies on amorphous TiO<sub>2</sub> has shown the energy for formation of the oxygen vacancy in amorphous TiO<sub>2</sub> is much lower than in crystalline forms, resulting in relatively good hole transport and that the trapping of holes occurs more easily.<sup>98</sup> However, this will result in a TiO<sub>2</sub> film that has many defects, able to act as recombination centres. In a photocatalytic study amorphous particles of TiO<sub>2</sub>, negligible activity was found for the amorphous particles attributed to recombination and activity increased with fraction of anatase phase, measured by Differential Scanning Calorimetry (DSC), for three oxidation reactions.<sup>99</sup>

TiO<sub>2</sub> has 3 stable crystalline polymorphs, but given one of them, brookite is formed at high pressures, it is not discussed here. Anatase phase tends to be the phase used for catalysis and TiO<sub>2</sub> films used in DSSCs due to its high band gap and that it's lower temperature of formation as well as its high conduction band edge and long carrier lifetime. The indirect band gaps result in lifetimes that are high, which correlates with the increase in activity between anatase and rutile.<sup>25</sup> There is a large amount of literature about the anatase-rutile transition as rutile phase is used in a range of catalytic and optical applications but it is not discussed here.

Anatase is thought to be the better catalyst due to its higher and indirect band gap. The higher band gap results in more energetic carriers, at the cost of less solar output being able to excite across the band gap.

### 3.3.6. The amorphous to anatase transition

The driving force for crystallisation arises from formation of distorted octahedral complexes to form anatase crystals.<sup>39</sup> Stabilisation/phase transformation pathways are influenced by the pH and ion facilitating the orientation of octahedral species, resulting in the crystalline phase.<sup>100</sup> Rutile becomes the more stable polymorph at sizes over 14 nm. Once the rutile phase has formed, it grows quickly.<sup>100</sup>

In the formation of a crystalline material, there are three stages; supersaturation, nucleation and growth of the crystals. Following suspension of an amorphous TiO<sub>2</sub> hydroxylated titania species, such as Ti(OH)<sub>4</sub> formed by hydrolysis of a precursor, there is a nucleation of primary seed or embryos of the crystals, or some seed crystals can be added. The

driving force for the formation of the particles then is the reduced volume energy, by formation of the crystal, eliminating water. The surface energy relative to the bulk energy will be high at this stage and these seed crystals will be in dynamic equilibrium with the precursors, but at a point, reported to be 4-5 nm for  $\text{TiO}_2$ ,<sup>4</sup> the increasing volume energy dwarfs the surface energy for particles and growth is energetically favourable.<sup>101</sup> Small amorphous  $\text{TiO}_2$  particles on the scale 2.5 to 3.5 nm may be more thermodynamically stable.<sup>4</sup>

The next stage, that of crystal growth, can be evaluated according to a range of theories and kinetic models have also be used to model growth of  $\text{TiO}_2$  crystals. The limitations on growth may be energetic in which case, growth will occur simply where it has the lowest energy to lead to a lower overall energy due to reducing bulk energy. It may be kinetic, where diffusion or migration limits the process especially in cases where certain sites such as dislocations are more favourable for crystallisation. Generally, the consensus from a range of precipitation from titanium precursors studies seems to be that the nucleation rate is slow but the growth rate is relatively fast.<sup>102</sup>

The formation of anatase from amorphous phases in solution is described by the elimination of water from bordering octahedra. The first detectable anatase phase particles are typically 4-5 nm. One of the models for the formation of these particles is from the merging of two particles. In support of this is the observation that in anatase to rutile transitions occurring from 600 °C, the rate is proportional to the square of the number of particles.<sup>4</sup> A Raman study of amorphous octahedral units shared 2 units, as rutile does whilst anatase forms with 4 shared edges.<sup>103</sup> Also, to crystallise bulk  $\text{TiO}_2$ , temperatures beginning at 300 °C, but for a single nanocrystal, crystallisation begins above 550 °C.<sup>104</sup>

Figure 3.6 shows the temperature dependency of crystallisation between 300 and 400 °C, showing an exponential decrease in the reported values.<sup>4</sup>

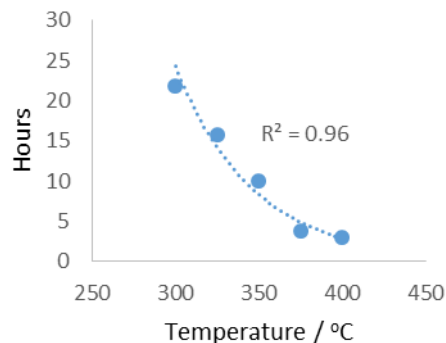
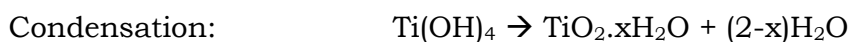


Figure 3.6: Time required to achieve 100% anatase phase in the solid state<sup>4</sup>

### 3.3.7. Solvothermal synthesis

As the reactions to produce crystalline TiO<sub>2</sub> occurs are: <sup>105</sup>



Water is often used as a solvent during production of titania sols. The treatment under hydrothermal conditions allows the transformation to anatase at a much lower temperature than would be expected from sintering studies in air.<sup>103</sup>

Sols were treated either in air or in the presence of water vapour, it was found that the crystallisation to anatase would occur at 30 °C at 75% humidity for 150 days, but not in vacuum. <sup>103</sup> Heating without water resulted in a lack of crystallinity at 430 °C. <sup>103</sup> Similarly, in the presence of water, anatase phase was detected at 300 °C but transition to anatase and rutile phases began at 650 °C and 1100 °C. This could be a demonstration of the strength of orientation in crystallisation and this is compared to the same transformation in water which occurred at 250 °C, with complete crystallisation occurring 750 °C lower than in air. The results for alcohols were similar, but higher in temperature. <sup>106</sup>

Due to the need for the orientation of crystals, water acts as a catalyst for crystallisation, orientating crystals to facilitate crystal growth. <sup>103</sup> Water molecules may act as a bridge between surface hydroxyls of different octahedra.<sup>100</sup>

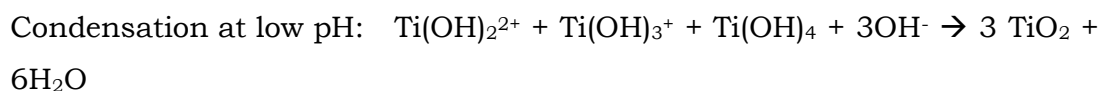
### The effect of pH

The effect of acid and base on this transition to anatase phase can be understood by the formation of triangular face with HO<sup>-</sup>, and subsequent elimination of water resulting in joined octahedrons. In a weakly acidic environment, the anatase phase is also promoted by OH groups in neighbouring octahedral sharing a partially protonated edge. Mineralisers can be used in the formation of crystal phases and anions can replace OH or OH<sub>2</sub><sup>+</sup> species. Acid may also favour growth, by stabilising the surface.<sup>100,107</sup>

The particles will have a surface charge, giving them a potential relative to their solution, a zeta potential. This will dictate agglomeration behaviour and be pH dependent. The surface charge will also give the surface an affinity for protons and hydroxyl ions.

By aging a Ti(iOPr)<sub>4</sub> suspension at 30 °C for up to 48 hours, it was possible to identify distorted TiO<sub>2</sub> crystals by XRD in nitric acid solution. This is much faster than in non-acidic environments.<sup>108</sup>

However, induction time studies of nucleation show supersaturation is achieved in acidic conditions but not at the lowest pH values, consistent with the following mechanism:<sup>109</sup>



This crystallisation could also occur under basic conditions. Boiling Ti(OH)<sub>4</sub> in NaOH results in an anatase and Na<sub>2</sub>TiO<sub>3</sub> phases. To eliminate Na<sub>2</sub>TiO<sub>3</sub>, the sols could be treated in a HCl solution for extended periods. The anatase peaks thus created were broad and mostly the powder was amorphous. However, heating at only 300 °C, results in a crystalline film. Increasing the temperature of the NaOH treatment of the sol resulted in a mixed phase sol, containing some rutile phase.<sup>110</sup>

### Aging and solvothermal synthesis

Many reports on hydrothermal synthesis, or reports that involve an “aging” step suggest the formation of crystals is possible at much lower temperatures than those observed for the formation of crystalline films, usually used in the formation of films for photocatalysis or DSSCs.

Precipitates of washed, neutral sols were annealed, becoming anatase phase at 400 °C and compared to those aged in boiling water for 24 hours or HCl at 60 °C at various molarities, where the sols were also reported to have good crystallinity. Further, anatase or rutile crystals could be formed through choice of molarity.<sup>111</sup>

The aging process can be performed at a range of temperatures. A sol of TiCl<sub>4</sub> in a solution of pH 9.5 in boiling 10% NH<sub>4</sub>OH, for between 0 and 48 hours followed by the calcination of the gel at 600 °C. The conclusion of this study was that crystallinity increased with aging time of the film.<sup>112</sup>

In a study of particle growth by Direct Light Scattering, growth under hydrothermal conditions was considerably faster above 80 °C.<sup>109</sup>

#### Partial crystallinity of annealed TiO<sub>2</sub> films

Although anatase films are referred to in the literature when a sol is annealed, the extent of crystallisation is rarely reported on. In a study of an amorphous film annealed at 450 °C for 30 mins, the extent of crystallinity can be inadvertently studied. An amorphous sol containing 5 % P25 (80% anatase and 20% rutile phases), should show a 1% rutile proportion (12% is seen). The proportion of anatase seen from the P25 should account for ~48% of the peaks. This suggests only 5.4 % of the total sol synthesised is anatase phase, or 5.7 % of the sol.<sup>113</sup> This is an unremarkable method and this may be a very common problem in the formation of TiO<sub>2</sub> films.

Given the extremely broad peaks seen in much of the literature on the formation of films, the existing crystal phase at these low temperatures could be due to a very small region of crystallinity within a larger amorphous particle.<sup>108</sup> It was found by Zhu et al., that the sintering of a 90 nm TiO<sub>2</sub> film on stainless steel even at temperatures up to 550 °C did not show the anatase phase by XRD, thought to be due to the hindrance to crystallisation due to the diffusion of Fe through the TiO<sub>2</sub>.<sup>96</sup>

A review of some the experimental methods where extend of crystallinity is described is given in Table 3.1.

#### DSC studies of crystallisation

By study of an amorphous sol by DSC, an endothermic peak is seen at 280 °C and is ascribed to the liberation or decomposition of bound water or

organic residue. Crystallization is measured to be at 436 °C, with a larger exothermic at a lower temperature of the peak seen when the TiO<sub>2</sub> is packed closely together, supporting the idea of interface nucleation.<sup>114</sup>

Seeded samples result in a DSC with two peaks, one at lower and one at higher temperature. The former is proposed to be due to growth on the seeded crystal. With an increased weight fraction of anatase crystals, the fraction of amorphous particles undergoing crystallisation increases, as would be expected. The limits of this is that the nucleation occurs in contact with an amorphous particle, and there is a larger amount that are capable of interface or surface nucleation.<sup>114</sup>

Conditions	% anatase phase	Conclusion	Ref
FTO glass, 1.0 – 2.0 g in 20 g ethanol, titanium ethoxide and 0.3 ml HCl were mixed. Dip coating and drying were performed to form a gel, which was ground and doctor bladed, then annealed between 350 – 550 °C for 30 minutes in air.	5.75 % anatase, after 450 °C for 30 minutes in air.	This is a typical synthesis of a TiO <sub>2</sub> film and showed a low concentration of anatase crystals.	113
5 ml TTIP and 15 ml IPA. 250 ml distilled water with HNO <sub>3</sub> or NH <sub>4</sub> OH was used to control pH. Heated 60-70 °C for 18-20 hours. The resultant suspension was white-blue and opaque. Precipitates were washed with EtOH and dried for at 100 °C for several hours, then annealed for 200 to 800 °C.	When pH level is above 2, a white suspension of rough precipitates is formed.  All samples are reported to be crystalline. Rutile is seen in 600 °C samples. Anatase still exists at 800 °C.	Crystallite sizes for anatase phase particles are: 7.6 nm (dried gel) 8.9nm (200 °C), 14.2 nm (300 °C), 28.4 nm (400 °C), 38.7 nm (600 °C). Rutile particle sizes are 47.5 nm (600 °C) and 53.4 nm (800°C).	105
Single nanoparticles were studied by synchrotron radiation, all anatase phase reported occurred very quickly.	The extent of crystallinity following 5 minutes at the following temperatures were: 500 °C: ~2%, 525 °C: ~5%, 550 °C: ~8 %, 600 °C: ~13%, 650 °C: ~17%, 700 °C : ~20%, 800 °C: ~21%, 900 °C: ~22%	Higher temperatures than are typically used in the formation of photocatalytic surfaces are required for very small crystals due to the impact of surface energy.	104
Kinetic model of TiO <sub>2</sub> crystallisation by coagulation model; orientated attachments.	100% anatase at: 300 °C: 21.9 hrs 325 °C: 15.8 hrs 350 °C: 10.0 hrs 375 °C: 3.8 hrs 400 °C: 3.1 hrs	Shows exponential decrease in time for achieving high crystallinity.	4

<p>Amorphous titania was prepared by addition of <math>\text{NH}_4\text{OH}</math> to <math>\text{Ti}(\text{OPr})_4</math>, the dense ppt was washed and dried thoroughly. Ammonia is likely to be released from the amorphous material following synthesis. Hydrothermal experiments were performed at 1 kbar pressure in cold seal hydrothermal bombs. 1: 10-12 solid to solution was used.</p>	<p>Above 0.1 M HCl and above 1.5 hours, the rutile phase dominates. Below this, anatase is forming.</p> <p>0.01M HCl at times between 168 and 235 hours, between 404 and 505 °C gave the anatase phase. At 597 °C for 264 hours gives 25% rutile phase.</p> <p>In water, around 300 °C, a time above 295 hours was required for forming the anatase phase. 304 hours was sufficient.</p>	<p>Extended times were required to achieve crystallinity at low temperatures.</p>	<p>115</p>
---	--	---	------------

Table 3.1: Results of anatase crystallinity extent from literature.

### 3.3.8. Film formation

Many of the models describing the behaviour of a  $\text{TiO}_2$  sol fail for small  $\text{TiO}_2$  particle sols. As sols are often used for doctor blading, spin coating or dip coating, their rheology will impact the films formed.

#### Electrostatic characteristics

Double layer theories used in the traditional semiconductor approach are based on the Gouy-Chapman model, involving a double layer surrounding a surface. Particles less than 10 nm are hard to model due to the assumption of a planar wall, assumptions significantly violated due to curvature of the double layer for small particles. Also, consideration of cations as point charges results in unrealistic charge densities, although  $\text{TiO}_2$  can acquire high charge densities relative to other semiconductor particles.

The surface charge of  $\text{TiO}_2$  can be influenced by a number of factors such as pH, ions and temperature.<sup>116</sup> At a particular pH, the surface charges can be neutralised, resulting in a neutral particle. Using concentrated electrolytes or strong acids and bases can change the electrical double layer. This has been used to fill pin holes in crystalline films of DSSCs by use of a solution of 3 nm particles.<sup>117</sup>

#### Literature on film formation

Due to the interest in  $\text{TiO}_2$  based DSSCs, there have been many reported methods for the formation of reliable films and their improvements. Some literature methods and findings are summarised in Table 3.2 and were used to inform methods used in this work. They also show how challenging it was

to use a method compatible with the corrodible nature of steel as low temperatures would be needed to be used for the production of the films.

Method	Finding	Ref
Ti(OPr) <sub>4</sub> was mixed with isopropanol, and added to a solution of HNO <sub>3</sub> or NH <sub>3</sub> as catalyst in water. Heated to 60-70 °C for 18-20 hours. Resultant suspension was opaque and white/blue. Prepared precipitates were washed in ethanol.	The peptidisation of the suspension at 60-70 °C for 18-20 hours reduces the volume by half, and the anatase phase can be seen from 100 °C during heating. Particle diameter is roughly 28 nm.	105
Ti(OBu) <sub>4</sub> was added dropwise to 15 ml EtOH + three drops of (HNO <sub>3</sub> : EtOH, 1:10). Ultrasonicated for 15 mins, gelatized for 5 days, spin coated (w/ or w/o poly(ethylene glycol)).	After 1hr annealing at 400 °C of a 90 nm film leads to 7% FeO <sub>3</sub> in the interlayer. Cr or Ni cannot be detected until the interlayer is reached, it exists as Cr and Ni metal in the film. At the interface, Ti exists as TiO <sub>2</sub> in the film and at the interface suggesting Fe and TiO <sub>2</sub> have not reacted.  These TiO <sub>2</sub> films on steel heated to 550 °C still do not show evidence of anatase films, possibly due to the diffusion of Fe into the TiO <sub>2</sub> film.	96
Between 1.0 and 2.0g Pluoronic P123 in 20 g of EtOH, 3.4g of titanium ethoxide and 0.3 ml of concentrated HCl were mixed. Dip coating, based on the solvent evaporation method, was used to prepare films. The synthesised gels were dried at room temperature, ground into a fine paste using DI water, 5% Degussa P25 was added as a binder and the paste was doctor bladed on to FTO glass. Sintered between 350 – 500 °C.	P25 acts as a binder during sintering to form crack free films. P123 has hydrophilicity drives the formation of micelles.  Films calcined at 350 °C show well ordered pores but is amorphous. With increasing temperature, crystallinity improves but mesoporous structure deteriorates. P25 show bigger pore diameter and high diffuse reflectance.	113
Gas phase pyrolysis from TiCl <sub>4</sub> from suppliers (30-150 nm) with a large 250 nm layer for enhancing the optical absorption of the visible light scattering effect. A suspension of the TiO <sub>2</sub> with different anatase proportions were used in a sol with titanium oxide, which acted as an inter-particle connecting agent.  The films were coated onto substrates by doctor blading or screen printing. The films were heated to 110-125 °C.	TiCl <sub>4</sub> was not used due to the deterioration of ITO substrates under acidic precursors. The paste needed to be viscous without the use of polymers, which prevent conduction, high adhesion to the surface and any liquid component must evaporate at low temperatures.  Dehydration is assumed to lead to interparticle connectivity. It is also assumed that the hydrogen bonding connection of main particles is enhanced by the use of the nonaggregated TiO <sub>2</sub> particles which have large amount of hydroxyl groups to react with the surface of main particles.	118
Ti(OPr) <sub>4</sub> and EtOH was added to water. 2 ml HNO <sub>3</sub> added, maintained at 20 °C. Sol was refluxed at 80 °C for 8 hours under vigorous stirring.  Catalysis measured by photooxidation of ethanol.  Heated at 115 °C for 15 mins.	The authors comment that highly catalytic films are incompatible with high sintering temperatures on glass due to the diffusion of sodium ions. Hydrolysis is rapid when [H <sub>2</sub> O]/[Ti] >2.  Water and acid promote hydrolysis by providing good leaving groups. But prevent polycondensation due to peptidisation.	119

<p>6.25 × 10<sup>-3</sup> mol of Ti(OPr)<sub>4</sub> was added to 25 ml aqueous solution of HClO<sub>4</sub> or NaOH with vol adjustments to give 0.1 mol dm<sup>-3</sup>.</p>	<p>Inert electrolytes have an effect on the formation of particles, there is an acceleration in the formation of haematite particles with NaCl, NaNO<sub>3</sub>, NaClO<sub>4</sub>. NaClO<sub>4</sub> retards rate of anatase formation.</p> <p>pH drops on heating of the sol at 100 °C seems to be due to the promotion of adsorption of HO<sup>-</sup> at the elevated temperature. Subsequent rise could be due to the liberation of the -OH adsorbed to the Ti(OH)<sub>4</sub> during its transformation to anatase phase.</p> <p>Adsorption of -OH was promoted by elevation in temperature. The formation of anatase TiO<sub>2</sub> from Ti(OH)<sub>4</sub> is inhibited for high pH and with electrolytes in high pH due to the impact of -OH.</p>	107
<p>Hydrolysis of Ti-triethanolamine complex by aging Ti(OH)<sub>4</sub> gel at 140 °C for 72 hours.</p>	<p>Yield of anatase TiO<sub>2</sub> was 100% below pH 9.6, dropping to 9% at pH 12.2. Explained by the reduction of the precursor complex Ti(OH)<sub>3</sub><sup>+</sup> and adsorption of the hydroxide ion. Triethanolamine appeared to lead to good size control.</p> <p>From review of other literature, the maximum transformation rate was at pH ~2 for anatase particles whilst very low pH could yield anatase and rutile particles even at room temperature.</p>	120
<p>Use of ammonia to produce viscous sols. Ti(OPr)<sub>4</sub> was mixed with glacial acetic acid in a glove box. This solution was added via dropping funnel to H<sub>2</sub>O under stirring, before addition of HNO<sub>3</sub>. Mixture was heated at 80 °C for 8 hours. TiO<sub>2</sub> sol converted to crystalline TiO<sub>2</sub> by autoclaving. 10 M NH<sub>3</sub> was added to 5g of this TiO<sub>2</sub> and concentrated to 12.5% wt of TiO<sub>2</sub>. Doctor bladed on ITO glass or glass, then heated at 150 °C for ¼ to 24 hours.</p>	<p>Surface-mediated couples CH<sub>3</sub>COO<sup>-</sup>NH<sub>4</sub><sup>+</sup> causes a reduction of the double layer repulsion between the particles, causing TiO<sub>2</sub> flocculate sufficiently to allow an increase in viscosity. (Note, Park improved similar films by using TiCl<sub>4</sub>).</p> <p>Studies in rheology found the change was due to particle flocculation. Presence of organics was confirmed after 24 hours at 150 °C.</p>	121
<p>H<sub>2</sub>Ti<sub>2</sub>O<sub>5</sub>.H<sub>2</sub>O precursor was used with a hydrothermal route in ammonia solution to produce N-doped TiO<sub>2</sub>.</p>	<p>Catalyst showed higher activities for the degradation of methylene blue and p-chlorophenol than P25 under visible light.</p> <p>Thought to be due to the formation of single-electron trapped O vacancies and inhibition of recombination of photogenerated electron-hole pairs by doped nitrogen.</p>	122
<p>Ti(OBu)<sub>4</sub> (20.42 ml) and diethanolamine (5.76 ml) were dissolved in anhydrous ethanol (70.74 ml), stirred for 1 hour at RT. A mixture of water: EtOH (1.08 ml : 2.0 ml) was added dropwise, then stirred at RT for 2 hours, then sealed and stored in the dark for 24 hours, resulting in a uniform, stable and transparent sol. Ni foam was cleaned with EtOH and water, then calcined 400-700 °C for 10 mins in air. Foam was dipped</p>	<p>Ni<sup>2+</sup> doping into TiO<sub>2</sub> films resulted in some extension of the absorption into the visible region. Enhanced activity was achieved by repeatedly coating and calcining the TiO<sub>2</sub> layers.</p> <p>The degradation of gaseous acetaldehyde is increased following calcining of the substrate above 550 °C, thought to be due to the formation</p>	80

<p>in sol, then rotated to form a film, dried for 12 hours, then calcined at 550 °C for 45 min in air.</p>	<p>of NiO, because Ni reacts with photogenerated electrons.</p>	
<p>1:8:32 Ti(<i>i</i>OPr)<sub>4</sub> : citric acid: ethylene glycol (molar ratio) were mixed. Ethylene glycol was heated to 60 °C, stirred, Ti(<i>i</i>OPr)<sub>4</sub>, citric acid added and heated to 90 °C. Stirred until clear. x:1 P25: Ti(<i>i</i>OPr)<sub>4</sub> by molar ratio is 7 to 18:1 paste was made and ball milled. Optimum proportion of P25 to sol was 10:1 .</p> <p>Screen printing was used, dry at 150 °C for 10 mins, followed by screen printed scattering layer, another drying at 150 °C for 10 mins, followed by annealing at 500 °C for 60 mins. Electroluminescence was used to measure homogeneity of the layer.</p>	<p>2 fold increase in efficiency for these films in favour of this sol gel method over sol gels containing terpineol.</p> <p>High surface area films with good electrical conductivity can be formed from sol gel methods to produce well connected grains and are sometimes treated with TiCl<sub>4</sub> treatment.</p>	123
<p>Pluoronic polymer (EO<sub>20</sub>PO<sub>70</sub>EO<sub>20</sub>, Mw=5800) was dissolved in DI water at 40 °C. H<sub>2</sub>SO<sub>4</sub> was added to the mixture. Ti(<i>i</i>OPr)<sub>4</sub> was chelated with 2,4 pentadione was slowly added to the surfactant, stirring. Kept at 50 °C until hydrothermal treatment at 90 °C for 12 hours.</p>	<p>Reported transparent TiO<sub>2</sub> films.</p>	122
<p>P25 was dispersed using a paint shaker, PEG (Mw: 20,000 g mol<sup>-1</sup>) or ethyl cellulose (Mw: 60,000 g mol<sup>-1</sup>). 21 g of P25, 3 g dispersant, 46 g terpineol. Ethyl cellulose was used at 1.8, 6.4 and 9.0 % of sample. Solvents used were terpineol, water, diethylene glycol.</p>	<p>Combinations of PEG/water, polyvinyl butyral/terpineol, ethyl cellulose/terpineol give crack proof films.</p> <p>Organic solvents are found to allow the formation of more uniform thin films in comparison with water based dispersions.</p>	124
<p>(Ti(<i>i</i>OPr)<sub>4</sub> was dissolved in ethanol and added dropwise to diionised water (4 °C) adjusted to pH 1.5 nitric acid.</p>	<p>Formed transparent sol (1.34 g/L). To isolate the effect of nitrate can result in the formation of hydroxyl radicals following photolysis. Perchloric acid instead of nitric acid showed the same results suggesting there was no difference in photocatalysis.</p>	125
<p>Ti(<i>i</i>OPr)<sub>4</sub> is added dropwise at RT to 0.1 M nitric acid under vigorous stirring. White precipitate forms instantly. Immediately after hydrolysis, slurry is heated to 80 °C and stirred vigorously for 8 hours to achieve peptidisation. Water added to adjust to 5% weight solids.</p>	<p>The microstructure is controlled by controlling different processing steps during the synthesis of the nanoparticles, such as the temperature and pH during the hydrothermal step.</p> <p>The average pore size is dependent on the size of the aggregates that are formed during the peptidization. TiCl<sub>4</sub> results in interparticle neck growth and facilitates the electron percolation through the TiO<sub>2</sub>.</p>	126
<p>Electrodeposited films were made by using a clean and dry ITO substrate at 1V against a Pt counter electrode with a silver reference electrode. 10 ml of sol (20 ml of 0.5 and 0.1 M HNO<sub>3</sub> + 1 ml Ti(<i>i</i>OPr)<sub>4</sub>, stirred at 70 °C for 3 hrs) was used with a pH 1 acetate buffer.</p> <p>Higher concentration of acid resulted in a higher crystallinity. Electrodeposition was performed on ITO glass at 1 V vs Ag/AgCl counter electrode vs a Pt electrode with 10</p>	<p>Broad peaks seen from in the XRD from RT to 400 °C (2 hr annealing). Narrow peak only seen at 400 °C. Higher concentration of acid improved crystallinity.</p> <p>The annealed film band gap is 1.8 eV is proposed to be due to the hydroxyl groups.</p>	127

ml and 1 ml acetate buffer at pH 1. Broad peaks from RT to 400 °C, then sharp peaks.	Photoluminescence shows a similar 2.14 eV is also well below band gap is also attributed to oxygen vacancies. Even photoluminescence attributed to the band gaps are at low energy for anatase films; 3.02 eV and 2.85 eV for the RT film, perhaps because of the amorphous bulk of the material.	
This method of hydrothermally treated TiO <sub>2</sub> sol (post 95°C reflux for 24 hours under reflux using TALH and urea as precursor and peptidizer, followed by hydrothermal treatment at 200 °C for 24 hours)	Titanium salt precursor collapses the electrical double layer, allowing formation of small particles of 3 nm. The small particles allow filling of pin holes with TiO <sub>2</sub> particles.	117

Table 3.2: Some typical literature methods and observations for a range of methods of producing TiO<sub>2</sub> films on a range of substrates.

#### Metal-TiO<sub>2</sub> interactions

To form a high-quality film on a substrate, the bonding between metals grown on TiO<sub>2</sub> can be studied. For instance, depositing TiO<sub>2</sub> on aluminium can result in the oxidation of Al, resulting in a high resistance Al<sub>2</sub>O<sub>3</sub> layer and the subsequent reduction of TiO<sub>2</sub>, potentially resulting in Ti<sup>3+</sup> defect states.<sup>23</sup> Further, the reduction of oxides by deposited metals is an important consideration for the formation of Schottky barriers.

Binding of metals to oxidised and reduced TiO<sub>2</sub> surfaces can be correlated with the electronegativities of the metals as the reduced surface is electron rich. The metal binding strength to TiO<sub>2</sub> correlates well with metal-oxygen bond strength (Co>Pt>Ni>Au) and metal diffusion was faster for reduced TiO<sub>2</sub>.<sup>128</sup>

#### 3.3.9. TiO<sub>2</sub> films on sheet materials

With the aim of corrosion protection TiO<sub>2</sub> was coated onto steel and copper sheets by dip coating from a sol and sintered between 200 and 800 °C. Above ~ 400 °C, the efficiency of the excitation of the TiO<sub>2</sub> is drastically improved, attributed to improved crystallisation and report the formation of Cu<sub>x</sub>O. The transition of electrons to TiO<sub>2</sub> despite the expected Schottky barrier formed is attributed to the Schottky barrier collapse due to defect states. An eventual collapse of the protective photocurrent at 800 °C is due to diffusion of Cu.<sup>129</sup>

Electrodeposition from titania precursors has also been demonstrated on steel, nickel and ITO coated glass, followed by sintering at 450 °C for 1 hour. The low efficiencies for DSSCs formed on these films is attributed to low surface areas of the films.<sup>130</sup>

Inverted architecture DSSCs have used titanium substrates, whereby titanium is polished and coated in TiO<sub>2</sub> paste to result in a low resistance contact with a high surface area. Two reports include an oxidation step in H<sub>2</sub>O<sub>2</sub> to oxidise the titanium before sol deposition. This gives the advantage of a flexible film with a 3D TiO<sub>2</sub> network forming a spongy interlayer.<sup>131,132</sup>

## 3.4. Results

### 3.4.1. Overview of fabrication work

Previous work in the group has focussed on the synthesis of Schottky barriers on oxidised titanium substrates. It was possible to show that a photocurrent generated in the visible region when they were functionalised with quantum dots. However, these devices have low efficiency, poor rectification ratios and electropolished titanium is not suitable for large area devices.<sup>133</sup>

To achieve the fabrication of Schottky barriers on a range of substrates, the use of a sol to form a TiO<sub>2</sub> film was used instead of oxidised titania. Commercial Ag nanowires could be drop cast from solution as has been done in previous work.<sup>49</sup>

However, the choice of substrate led to several technical challenges. The high temperatures used in the formation of anatase films in DSSCs are used to remove organic binders and solvents used in the deposition of uniform films and to crystallise the TiO<sub>2</sub> into the anatase phase. Whilst the diffusion of metal through TiO<sub>2</sub> films can lead to better devices in DSSCs (Section 3.4), the Schottky barrier can be effectively short circuited and the current will simply follow the easiest path, in this case, an ohmic response.

For these reasons, two technical issues are addressed:

- The formation of Schottky devices on stainless steel
- The manufacture of sols to improve crystallinity of the devices

### 3.4.2. Fabrication of Schottky barrier devices on stainless steel

Optimisation of sols

Some of the problems of fabricating the devices in this way can be illustrated by SEM images. TiO<sub>2</sub> film formation has been extensively studied for DSSCs, as many requirements must be met such as the continuity of the film, and the ability to remove organic contaminants without pores collapsing. Organic

binders such as ethyl cellulose and polymers must be removed at high temperatures, which were not possible on stainless steel substrates due to metal diffusion. Small organic binders were used here, Figure 3.7 to study whether it was possible to use small molecule binders to form uniform films.

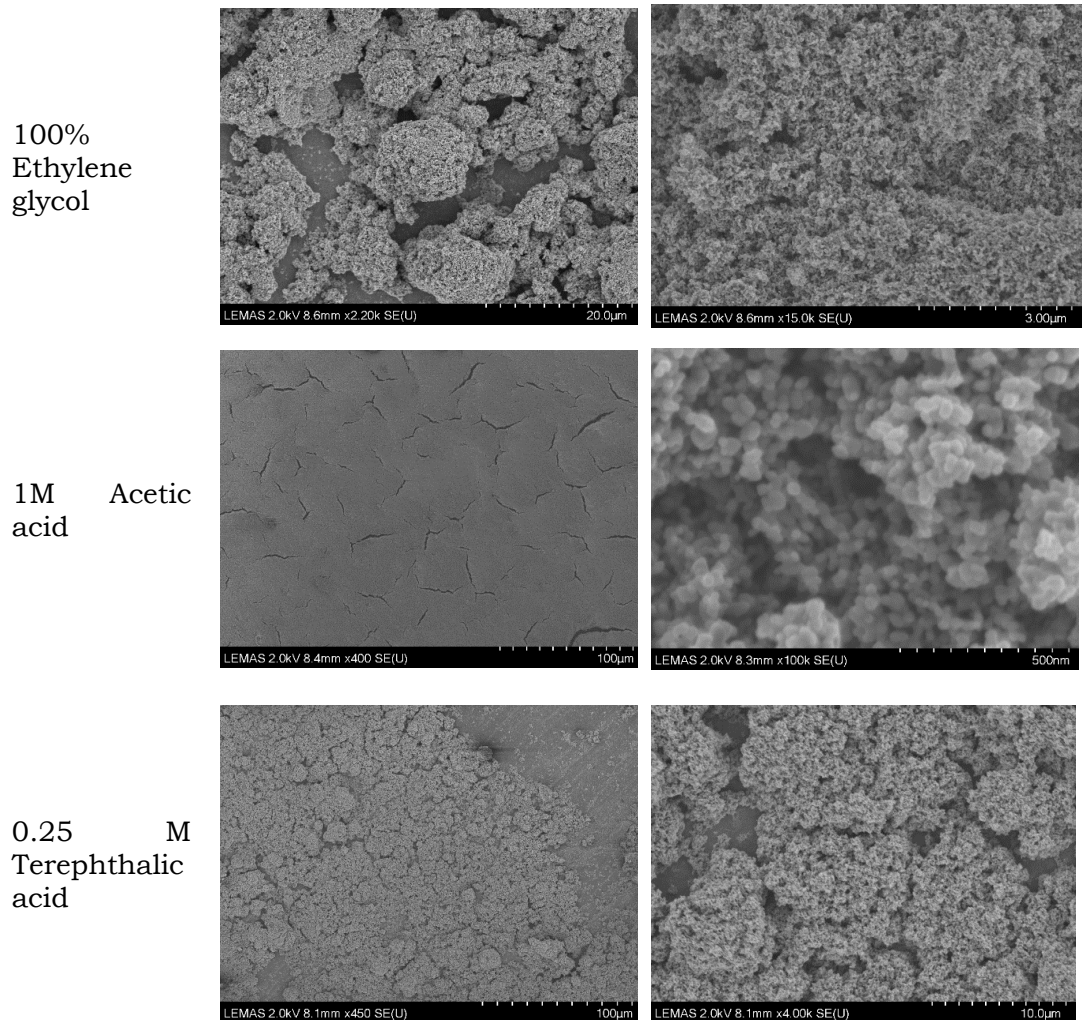


Figure 3.7: SEM images of a range of films fabricated with a range of small molecule additives.

Even small organic molecules could not be effectively removed from the  $\text{TiO}_2$  at the low temperatures required to prevent metal diffusion from the substrate, resulting in low conductivity through the films.

Chromia protective layers on steel

The chromia plates observed on stainless steel are protective, as discussed in Section 3.5. From the EDX image, though chromia, manganese and nickel are relatively uniform across the surface, there is areas low in oxygen and somewhat iron, Figure 3.8.

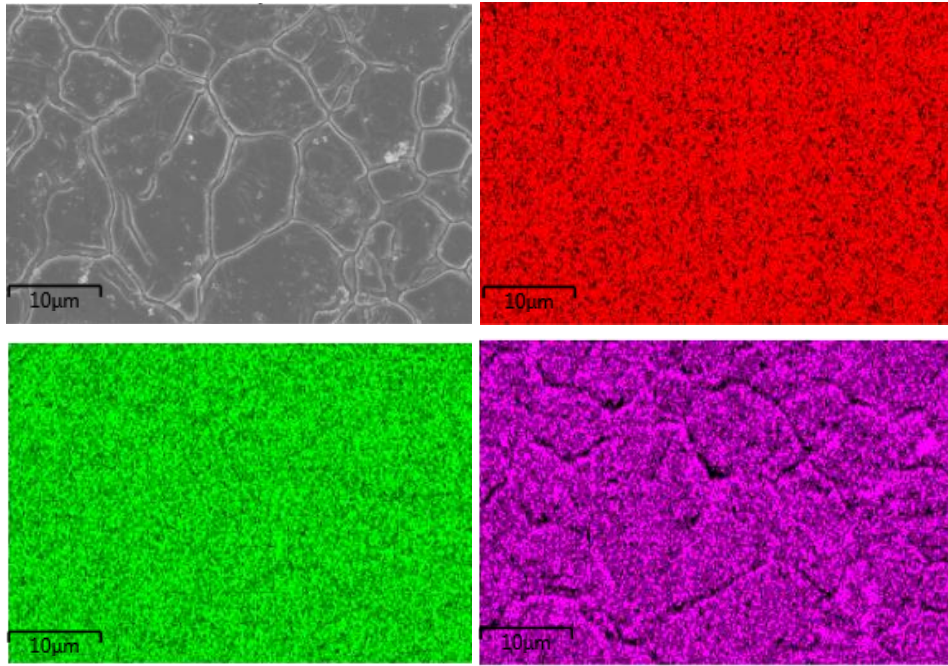
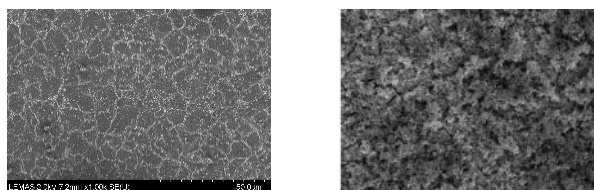


Figure 3.8: Oxidised 304 Stainless steel showing protective chromia layers. Top left shows an SEM image, the EDX maps are top left; Cr K $\alpha$ 1, bottom left; Fe K $\alpha$ 1 and bottom right; O K $\alpha$ 1.

The relatively low abundance of oxygen in the areas around the plates suggests there is a lack of protective oxides in these regions.

It was possible to observe how the position of the metal ions depends on the position of the chromia plates (top left). The TiO<sub>2</sub> layer shows high proportions as would be expected for Ti and O. However, in thin layers of the film it is also possible to see the high proportions of Cr and Fe in the gaps in the film. The initial excitation of the primary electron beam is expected to be several microns depth, and therefore the x-rays are characteristic of this depth too. As the films are thicker than this, the Cr and Fe is also present in the areas between the gaps. The proportion of Fe and Cr in these areas compared to the gaps is not as high as the difference between the Ti and O and the lack of these in the gaps. Incomplete films were chosen to have areas of substrate and TiO<sub>2</sub> film to compare EDX maps, Figure 3.9.



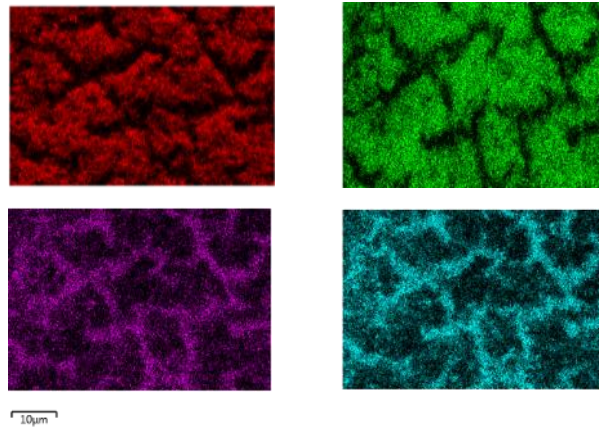


Figure 3.9: Top left:316 annealed steel showing chromia plates. Top right: thin  $\text{TiO}_2$  coating on 304 type steel. Below: EDX images of top right section; (centre left) O Ka1, (centre right) Ti Ka1, (bottom left) Cr Ka1 and (bottom right) Fe Ka1.

Due to the variance in the films, the proportions of metals in the sol decrease where the film is thicker. In the top left of the SEM image (left) of Figure 3.10, where the film is thicker there is little Fe in the EDX map.

As the films vary in thickness, quantifying the Fe in the EDX map is not possible, however, using an incomplete film, two areas can be compared. As expected, Figure 3.11 (right), shows the region for analysis of the sample shows a high proportion of Fe and Ti. Though lighter elements are detected and smaller quantities of trace elements, at these accelerating voltages, Fe and Ti dominate the spectra. The proportion of each relative to each other is as expected, with the substrate showing much more Fe, though some Ti, possible due to small  $\text{TiO}_2$  particles, possibly due to the wide sampling areas of the EDX excitation.

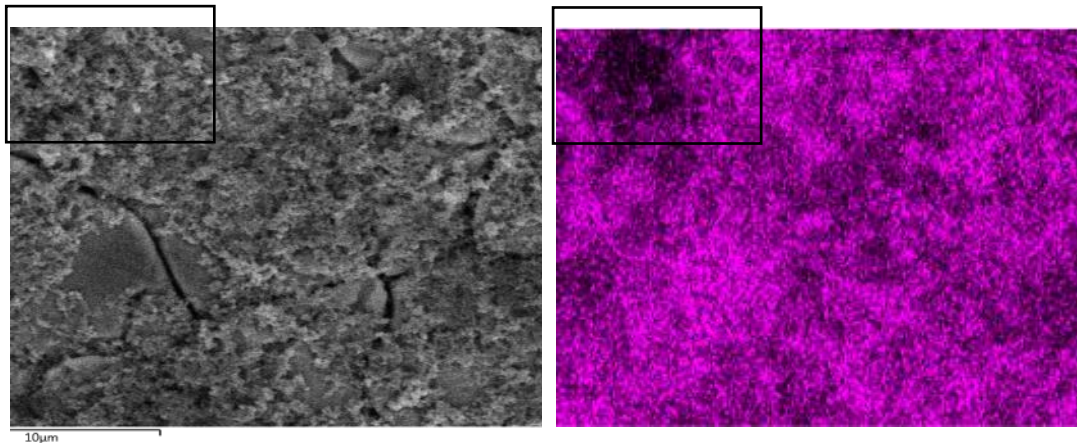
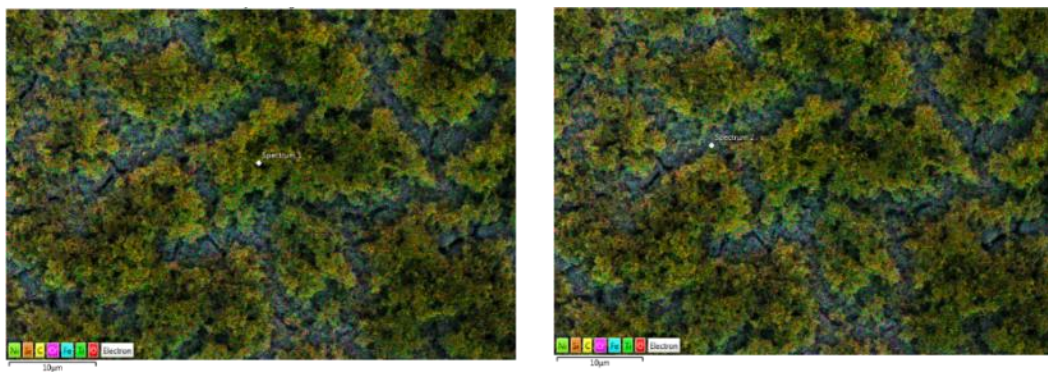


Figure 3.10: SEM image (left) and EDX map (right) for Fe K $\alpha$ 1. This demonstrates the importance of film thickness and non-uniformity to the concentration of Fe at the interface.



90% Ti  
10% Fe

79 % Fe  
21 % Ti

Figure 3.11.: EDX maps of films with the two regions for quantitative analysis shown as two labelled white dots.

#### Diffusion barrers

Sols were manufactured and deposited on stainless steel by dip coating. AgNWs were deposited from solution by drop casting from solution to give a randomly orientated mesh. The geometry of the device is shown in Figure 3.12.

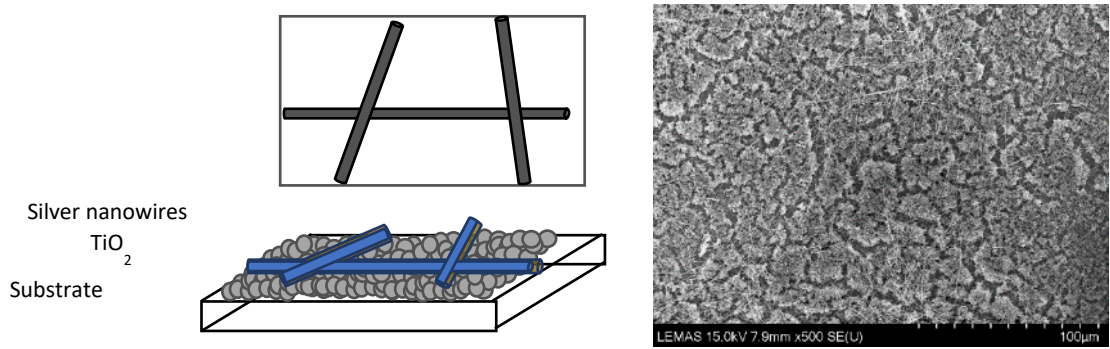


Figure 3.12: Schematic (left) and SEM image (right) of the Schottky barrier device showing a substrate, coated in a titania film, with deposited silver nanowires.

Chromia layers provide a diffusion barrier for steel substrates, preventing the diffusion of Fe ions to the surface and their subsequent oxidation at high temperatures. The chromia plates formed on the 304 samples are shown in Figure 3.13.

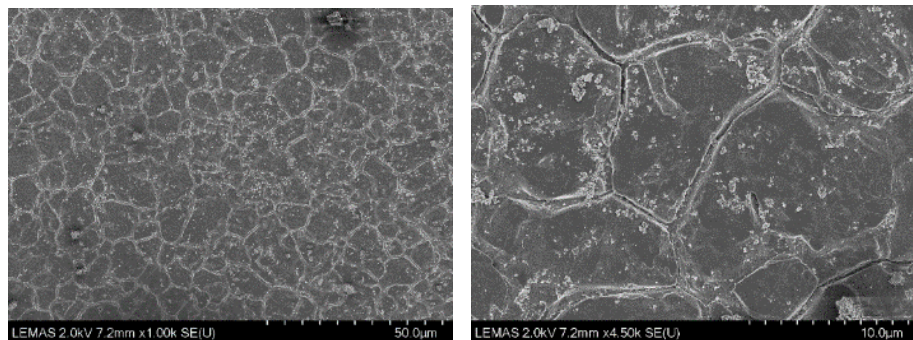


Figure 3.13: SEM images of protective scales formed on the surface of stainless steel heated to high temperature.

From the EDX map, the most abundant elements are Cr, followed by Fe and O. As can be seen, the O concentration is lower at the edges of the plates, in support of the hypothesis of plates of a chromia protective scale, Figure 3.14.

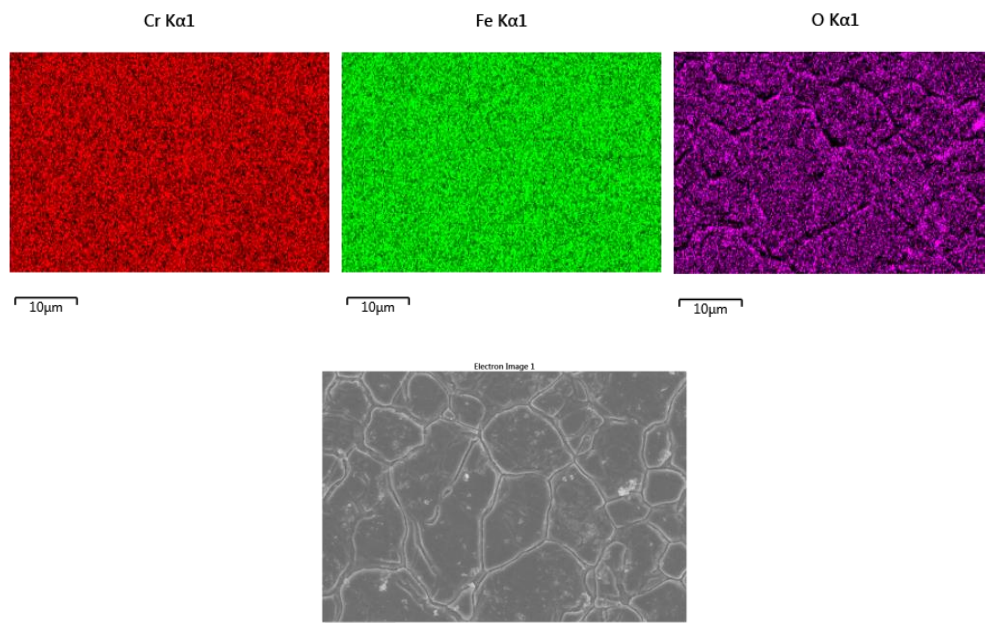


Figure 3.14: EDX (top) and SEM (bottom) image of protective scales showing a near uniform distribution of Cr and Fe but a lower concentration of O in areas corresponding to the edges of scale according to the SEM image.

To demonstrate the importance of this chromia film, heat treated steel was mechanically polished and compared to an intact surface. The devices with the chromia layer removed failed whilst most of the intact annealed devices were diodic. Similarly, the presence of salt causes faster corrosion and incomplete oxide scales forming, as discussed in Section 3.5.3.

Though the chromia layer provides protection from the diffusion of ions from the substrate, it is also a p-type oxide and could contribute substantially to the series resistance of the device. To test this, a saturated solution of NaCl in IPA was drop cast onto a stainless-steel substrate. Current-voltage measurements were analysed as described in Chapter 4. Figure 3.15 shows the reverse saturation current for the best fits to the model, showing no trend for reverse saturation current, nor estimates of Schottky barrier heights, but potentially an overall decrease in R series for the salt treated devices compared to the others. The increase from 10 to 40 uL may relate to the growth of the hematite layer.

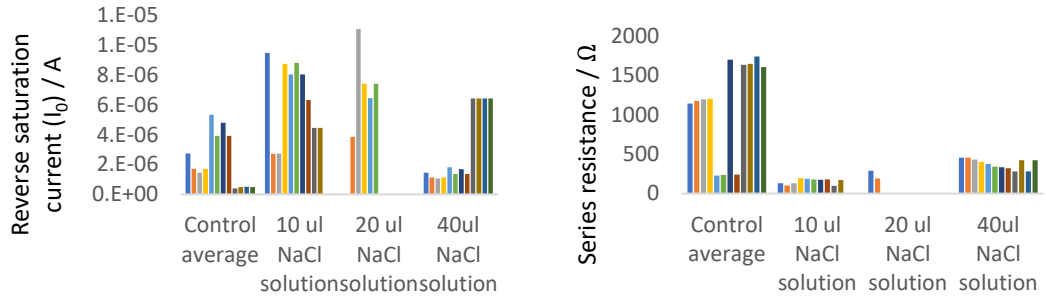


Figure 3.15.: Reverse saturation current values (left) for a range of devices treated with NaCl in IPA. The reverse saturation currents showed no trend (left) but series resistance was in general lower for treated devices (right).

Therefore, other than reducing series resistance is an advantage in the electrical characteristics of the devices, the photocurrent seems to decrease when NaCl was used. The lower series resistance would be predictive of a higher photocurrent, though the opposite is observed. This could be due to the impact of metal diffusion, as the breakdown of the  $\text{Cr}_2\text{O}_3$  layer results in more metal diffusion. However, the  $\text{Cr}_2\text{O}_3$  layer is p-type and thus its presence may contribute to the resistance at the back contact.

In an ideal case, the resistance of an effective diffusion barrier would be zero, resulting in no drop of potential across the diffusion barrier. In this case, a diffusion barrier in the form of a chromia layer results in smaller amounts of substrate metals in the  $\text{TiO}_2$  form, however, increasing the series resistance.

#### Temperature and time of sintering

The successful formation of the devices depended on the temperature at which the devices were sintered and the grade of steel used.

Through studying the reverse saturation current, more fully discussed in Chapter 3, as well as the reliability of photocurrent led to the optimisation of the conditions at low temperature on 304 stainless steel, Figure 3.16.

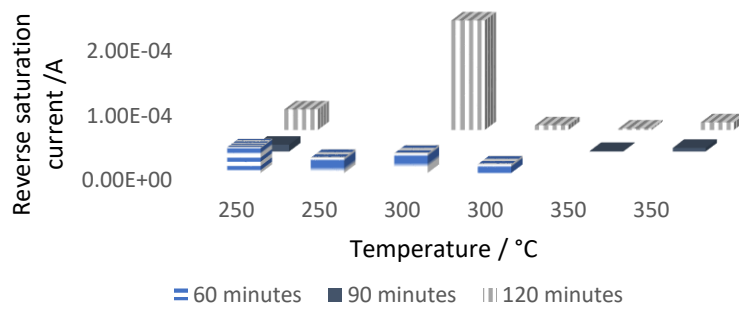


Figure 3.16: 304 temperature and annealing times and their impact of the conditions on reverse saturation current.

The most successful of these devices in terms of reliability and low reverse saturation currents were made on stainless steel at 350 °C for 90 minutes. The increased time required to anneal would be expected to increase the crystallinity or crystal size, necking of particles and elimination of carbon contaminants, all of which would be expected to improve the photocurrent observed, as an increase in crystallinity and crystal size would lead to better electron transport through the film, so an increased measured photocurrent.

Noteworthy is how these devices fail. The IV curves of these devices tend to be ohmic when times and temperatures are increased. This suggests that connectivity of the TiO<sub>2</sub> films is not limiting even for the low temperature sintering. Further, when the devices fail at high temperatures or increased times of annealing result in ohmic devices, as defects shunt Schottky barriers.

#### Steel grade and impact of temperature

Extending the studied range of temperatures shows the temperature dependence is not independent of steel grade (Table 3.3), again suggesting the protective scales is playing a role in the formation of reliable devices.

Some limited results on 316 type stainless steel show that the same temperatures with the same sols do not yield diodic devices. Higher temperatures may result in working devices on 316 stainless steel that did not on 304 stainless steel.

Steel Grade	Temperature / °C								
	300	350	400	450	500	550	600	700	800
304	1/4	4/4	2/15	0/5	0/5	0/3	0/3	0/3	0/3
316	0/2	0/2	0/2				2/2		

Table 3.3: Number of diodic devices out of total synthesised.

To demonstrate the importance of the protective layer that forms on oxidised steel, the steel was heated to a range of temperatures before deposition of the sol. As shown in Table 3.4, the proportion of working devices was low for 304 steel at high temperatures, but higher for 316 steel at high temperatures.

Steel Grade	Temperature / °C					
	400	450	500	600	700	800
304	2/2	0/2	0/2	0/2	1/2	0/2
316	1/3	1	1			1/2

Table 3.4: Pre-treated steel temperature dependency to form a rectifying device.

Many devices were synthesised with the above methodologies, whereby a low temperature is used in combination with 304 grade stainless steel to prevent the diffusion of metal ions through the substrate.

However, it is possible to form a device at higher temperatures by pre-treating the steel to form a diffusion barrier oxide scale. Given this allows annealing to take place at a higher temperature, which even at low times of sintering can facilitate the transition to a crystalline structure. For this reason, an attempt was made to anneal TiO<sub>2</sub> for fast enough times to prevent diffusion but at a high enough temperature to encourage the sintering and crystallisation of TiO<sub>2</sub> particles. Whilst annealing for 1 or 5 minutes exactly is impossible due to the different temperature coefficients of the TiO<sub>2</sub> film compared to the steel, leading to cracked films if they are cooled too quickly. Typically, the films were cooled slowly until 300 °C followed by faster cooling and typical temperature profiles are shown in Figure 3.17.

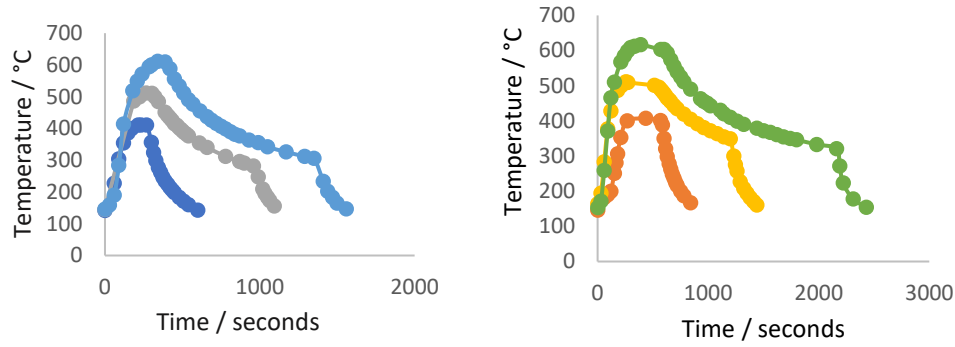


Figure 3.17: Temperature profile is used for annealing for 1 minutes (left) and 5 minutes (right).

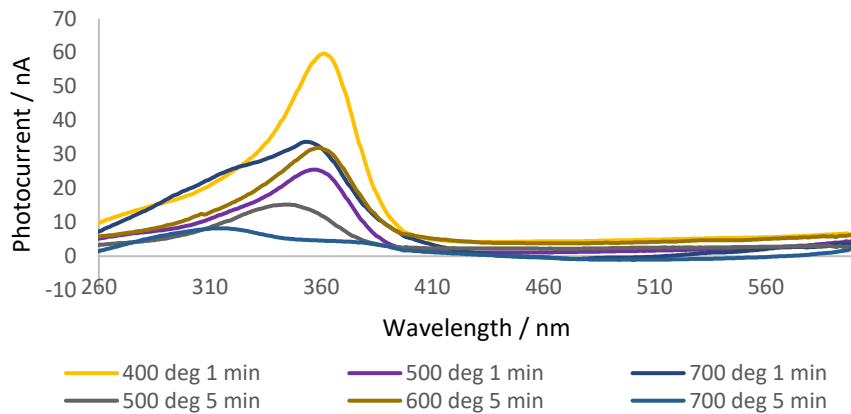


Figure 3.18: Photocurrents for films sintered for low times at a range of temperatures.

What is particularly interesting is that there are two peaks, an absorption that rises rapidly after about 390 nm, where the peak would be expected for a 3.2 eV excitation of a  $\text{TiO}_2$  sol, the Tauc plot has an intercept of 386 nm, and a high energy shoulder, Figure 3.18. This was unusual in the devices as is discussed in detail in Chapter 4.

The photocurrents are lower in both higher temperature and higher time results in lower photocurrent, Figure 3.19, this is potentially due to an increase in diffusion or increasing series resistance.

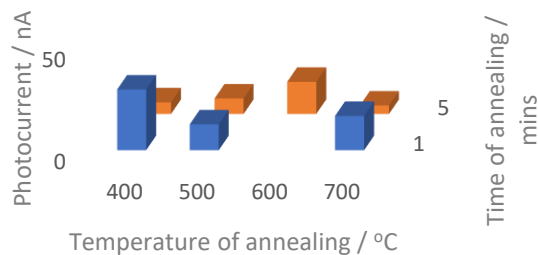


Figure 3.19: Lower photocurrents for higher temperature and longer annealing times.

### 3.4.3. Diffusion from other metal substrates and its impact

The oxidation of metals after diffusion through the substrate may also be important.  $\text{TiO}_2$  deposited on carbon or aluminium were failed or ohmic devices. Cu and Sn doped films at low temperatures formed poor diodes. Nickel devices were ohmic at low temperatures and diodic above 500 °C. This may be due to the failure to form NiO below these temperatures at the surface, whilst Cu and Sn may show the reverse trend, with failure once the oxidation temperature is reached. Further, it proved difficult to fabricate a diodic device on a transparent conductive oxide, potentially due to the diffusion or Sn as described above.

### 3.4.4. Film thickness

Unsurprisingly, there is an optimum thickness for the reliable fabrication of these devices. The details of the sol are in the following section (Section 3.8) but for the dip coating method, there is an advantage of to many dips of a thin film in order to form a continuous layer, to fill gaps but preventing the formation of very thick parts of the film which may flake off during annealing. The optimum concentration and number of dips were used in the case of each sol.

### 3.4.5. Continuity of $\text{TiO}_2$ films

The need to form continuous films has led to the use of polymeric materials in typical  $\text{TiO}_2$  films. The use of organic solvents and a range of additives can be used and can be seen by SEM to result in vastly different morphology of films.

Poor coverage of the surface can easily lead to short circuit of the device by the silver nanowires. Further, it is also clear from SEM that small cracks in

the film, which may lead to increased recombination in DSSCs and increased corrosion of the substrate, are likely to have less effect in these devices as the wires can bridge small gaps, as shown in section 3.1.7.

The need to use low temperatures to avoid diffusion from steel is discussed in Section 3.6 and thus only small molecule solvent and additives could be considered to reliably remove them at such low temperatures.

Yune et al. report on the effect of ammonia on  $\text{TiO}_2$  sols produced by a hydrothermal process.<sup>121</sup> They hypothesise that surface couples of the acetic acids they used as peptidisation, in the form of  $\text{CH}_3\text{COO}^-$  agent with  $\text{NH}_4^+$  reduces the double layer repulsion between the particles, causing  $\text{TiO}_2$  to flocculate and the sol to increase in viscosity. However, these organics remained following annealing of these films for 24 hours at 150 °C.

Nitric acid was used extensively as a peptidisation agent in the literature and was used in experiments here to produce continuous films. To avoid damage to the substrate, the nitric acid in the sol was neutralised prior to deposition and the strategy of using ammonia was chosen to improve the viscosity of the device, whilst avoiding the use of organics. Further, the neutralised salt, present in small quantities in the sol, decomposes at relatively low temperature and will not leave organic residues.

#### 3.4.6. Crystallinity

For many of the initial devices, a sol was simply made by the hydrolysis of a titanium precursor in water followed by its annealing at 350 °C on steel.

The anatase transformation solution has been reported at relatively low temperatures but generally, this temperature is insufficient for filming crystalline films on a substrate. The difficulty with the formation of the devices at 350 °C is that the sintering of a  $\text{TiO}_2$  film has three main objectives:

- The formation of a low resistance films through the "necking" of particles. This can, and has, been reported to occur through the elimination of  $\text{H}_2\text{O}$  at temperatures over 100 °C.
- The removal of organic contaminants
- Crystallising the particles.

It can be seen from XRD studies that the film shows no crystallinity where  $\text{TiO}_2$  peaks would be expected. The peaks that are present are attributable to austenite iron oxides or silver nanowires, Figure 3.20.

It was found by Zhu et al., that the sintering of a 90 nm  $\text{TiO}_2$  film on stainless steel even at temperatures up to 550 °C did not show the anatase phase, thought to be due to the hindrance to crystallisation due to the diffusion of Fe through the  $\text{TiO}_2$ .<sup>96</sup>

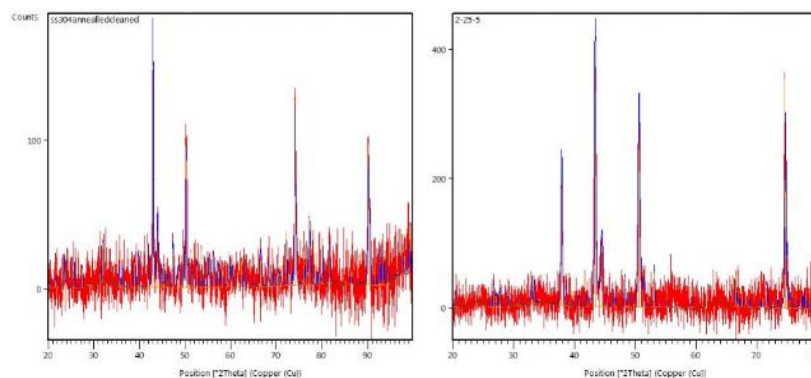


Figure 3.20: Heated steel, left, and sol on steel, right.

There have been many studies of low temperature synthesis of  $\text{TiO}_2$ . Although many papers such as those in Table 3.2, show that there is some evidence of anatase phase at low temperatures. A common methodology for producing crystalline films in DSSCs is the hydrolysis of sol, followed by a reflux step then annealing at high temperature. A sol was made more crystalline by incorporating an 8 hour reflux step in isopropanol. The effect of this can be seen for a device too, as in Figure 3.21 as a very broad peak centred at 25°, which can be compared to commercial P25  $\text{TiO}_2$ .

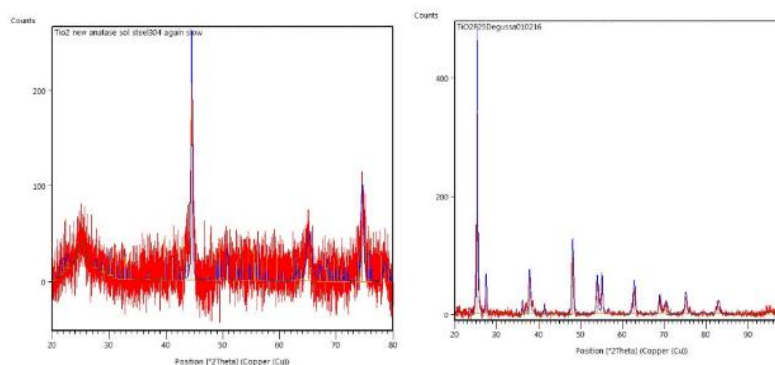


Figure 3.21: Left showing 8 hour hydrolysed sol device showing some  $\text{TiO}_2$  peaks and austenite peaks. Right shows P25 peaks for comparison.

This improvement in sol results in an increase in photocurrent generally. Although many methods have been used for the improvement of devices including passivation and a range of fabrication methods, the photocurrents for the more crystalline devices were higher than the less crystalline devices in general, as show in Figure 3.22.

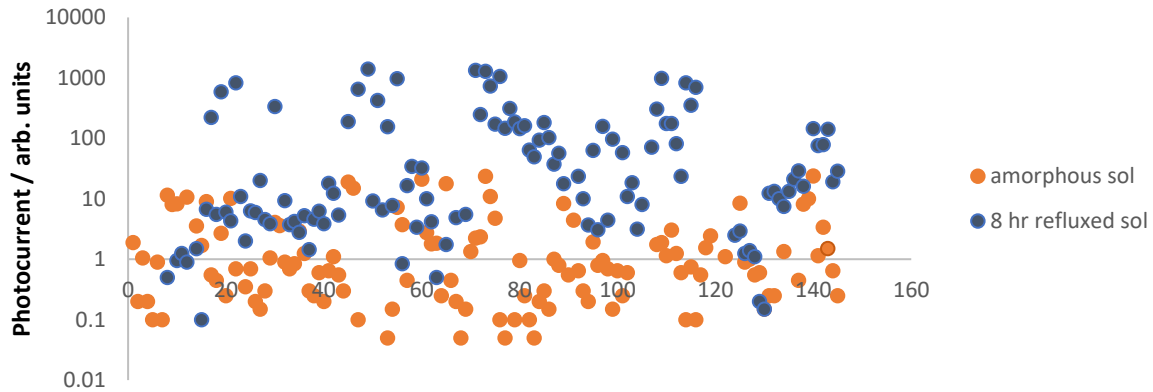


Figure 3.22: Comparison of a wide range of photocurrents for devices for completely amorphous and partially crystalline sols.

Although the photocurrent improves, from the width of the XRD peaks, the crystallite size can be assumed to be very small and the counts are lower than the P25 comparison, suggesting the extent of crystallinity is low. The aqueous refluxed sol showed an order of magnitude increase in photocurrents. This could be due to the increased crystallinity, leading to better charge separation.

From the literature discussed, the low temperature crystallisation of anatase phase  $\text{TiO}_2$ , the time required needed to achieve full crystallinity became exponentially lower with temperature. This figure would suggest that at  $350^\circ\text{C}$ , a time of  $\sim 9.5$  hours would be necessary to crystallise the film, during which time, there would be a large amount of diffusion from the substrate.

The phase transformation occurs differently in liquid phase and a large amount of research has been done on the hydrothermal synthesis of  $\text{TiO}_2$  in water at supercritical temperatures and pressures. Solvothermal methods, where small crystallites form during reflux stages, suggest that crystallites do form at low temperatures.

The solvothermal method was taken further, reflux was continued over extended periods. Using the Scherrer equation, Equation 3.3, which relates peak broadening in XRD to the size of crystalline grains.

Equation 3.3: 
$$\tau = \frac{K \lambda}{\beta \cos \theta}$$

$\tau$ : Peak width / °

K: Shape factor

$\lambda$ : X-ray wavelength / m

$\theta$ : Bragg angle / °

$\beta$ : Crystallite size / m

This analysis requires the use of large single crystals to quantify machine broadening, performed here with a corundum control sample. Further, there are several factors causing broadening, such as defects in the lattice. A Reitveld refinement would be necessary for deconvolution of the peaks into the broadening due to defects and those due to small crystallite size. There will be many defects in the crystals following solvothermal synthesis as relaxation of strain at high temperature will not occur. Much of the crystal growth will occur by the twinning of particles. Therefore, the estimate crystallite size of 31.5 nm includes broadening from defects and therefore may be an underestimate.

However, it can be seen that the FWHM of the peaks decreases linearly with reflux time, Figure 3.23 (left) and that the estimated size for the 32-hour refluxed sol shows a crystallite size larger than that of P25, which is 31.5 nm from this analysis, Figure 3.23 (right). The crystallite size in P25 crystals is reported to be approximately 20 nm.<sup>134</sup>

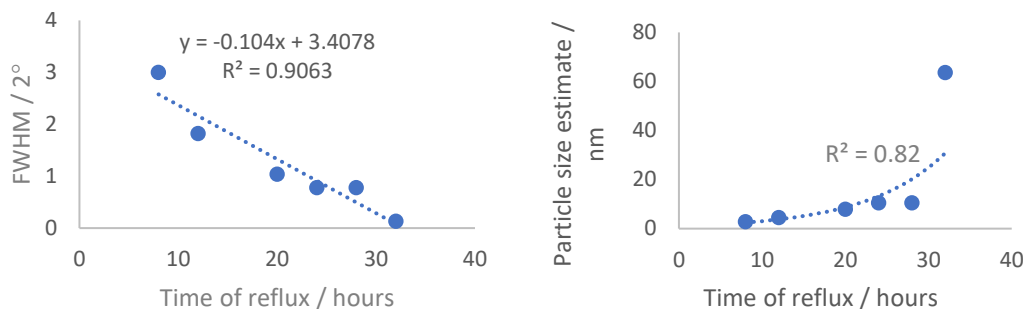


Figure 3.23: FWHM of peaks (left) decreasing in width with time under reflux (left) and the estimated particle size from Scherrer equation for a sol with time of reflux (right).

The XRD shows a clear anatase (110) peak at just over 25°, Figure 3.24. Some small peaks can be seen, though with lower intensity. This could be due to a preferential orientation on the substrate. There is also a shift of the peak wavelength, towards higher values, likely due to strain. The diffraction angle depends on the unit cell of the crystal, so strain can result in a shift in peaks.

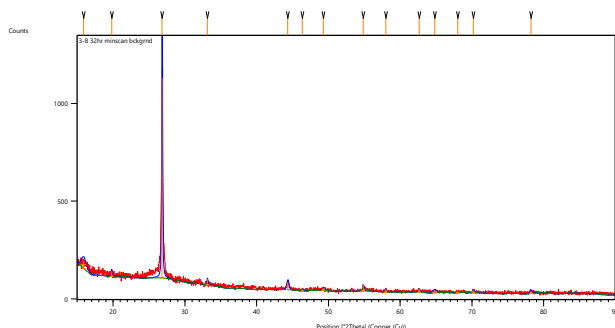


Figure 3.24: Showing narrow peak widths for a sol refluxed for 32 hours, indicating a high degree of crystallinity.

There is a complicated relationship around photocurrent for many of these devices and it is discussed more fully in Chapter 6. However, the expected improvement in photocurrent is observed with increasing crystallinity.

The absorption onset of the sols red shift over this growth time too, suggesting the smaller particles may have been subject to confinement effects, Figure 3.25.

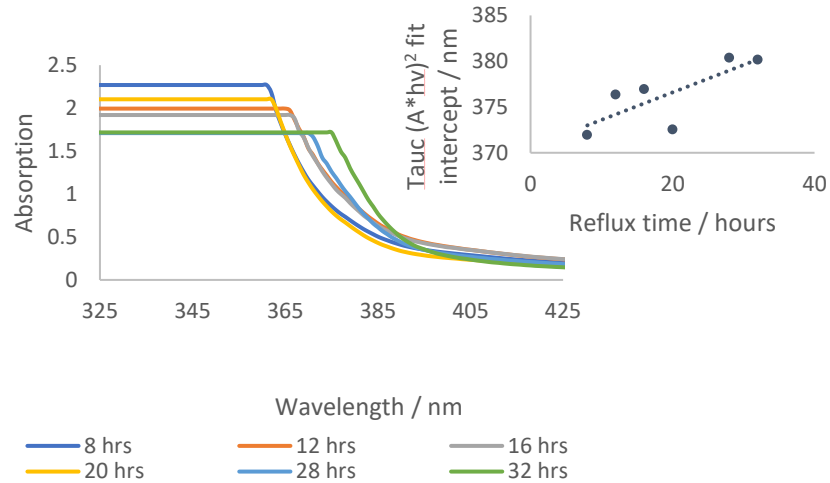


Figure 3.25: Absorption onsets red shift to longer wavelengths following longer annealing times. Tauc plots of the form  $(Abs \cdot hv)^2$  fits for each absorption plots, showing a correlation between band gap estimates and reflux time.

Shifts in absorption were observed for particles less than 12 nm.<sup>135</sup> From the XRD fit, sols above 24 hours would be expected to show a lack of confinement. The intercepts of the 28 and 32 hour sols were nearly the same. The confinement is relatively small for these sols. A sol produced through hydrolysis of the sol in tartaric acid, the intercept from the sols show a much higher energy absorption, and consistent from the transparent, well dispersed sol produced. This suggests tartaric acid can inhibit the growth of a crystal.

#### 3.4.7. TiN coated steel as a potential substrate

TiN coatings of steel are commercially available and TiN provides a protective coating for steel which protects the steel and forms a diffusion barrier. There are reports of oxidised TiN photocatalysts and therefore TiN coated steel may provide a substrate for the formation of TiO<sub>2</sub> layers on steel.

In a paper by Li et al. the authors propose a TiN/TiO<sub>2</sub> composite photo anode for use in DSSCs. TiN powder films were annealed for 0.5 to 4 hours at 500 °C with 1-hour devices showing the highest efficiencies.<sup>136</sup> Using these powders, films were made and photographs of the films show the lowest annealing time gives a strong absorbance across the visible spectra, making the film appear dark blue. This suggests narrowing, or mid-gap states. The

TiN device shows both anatase and rutile phases by XRD. Higher quantities of TiN resulted in better water electrolysis.<sup>136</sup>

The authors report the movement of the conduction and valence band as well as the flat band potential of the material. This changing flat band potential, provides a larger driving force triggers the water oxidation. The 4 hour sample have a reported valence band more than 1 eV lower than the 0.5 hour sample. <sup>136</sup>

The movement of the flat band potential, if the authors are correct, is dramatic and provides opportunity for tunable characteristics for Schottky barriers used in this work. The potential of the semiconductor above the metal drives the transfer of electrons into the metal, resulting in a Schottky barrier. Therefore, the barrier formed could be altered dramatically by such a change in the effective conduction band. However, this seems unlikely to be uniform over a film and may be an average value. Further, the same surface states may result in the same barrier height. This changing flat band potential however, would still provide a study to change the depletion regions.

#### 3.4.8. TiN devices

In a paper by Li et al. the authors propose a TiN/TiO<sub>2</sub> composite photo anode for use in DSSCs. TiN powder films were annealed for 0.5 to 4 hours at 500 °C with 1-hour devices showing the highest efficiencies. <sup>136</sup>

This method was used here to create TiO<sub>2</sub> film on a substrate. Figure 3.26 shows images of a range of films shown for 5 times of annealing and the current-voltage curves for a range of these devices. The leakage current decreases exponentially with annealing time. The series resistance increases linearly over this time.

Following heating at high temperatures for extended periods of times, a birefringent layer can be seen. This varies across the surface of the sample. The TiN layer is 2-3 micron thickness on the steel but the birefringence suggests an oxide layer of some hundreds of nanometres.

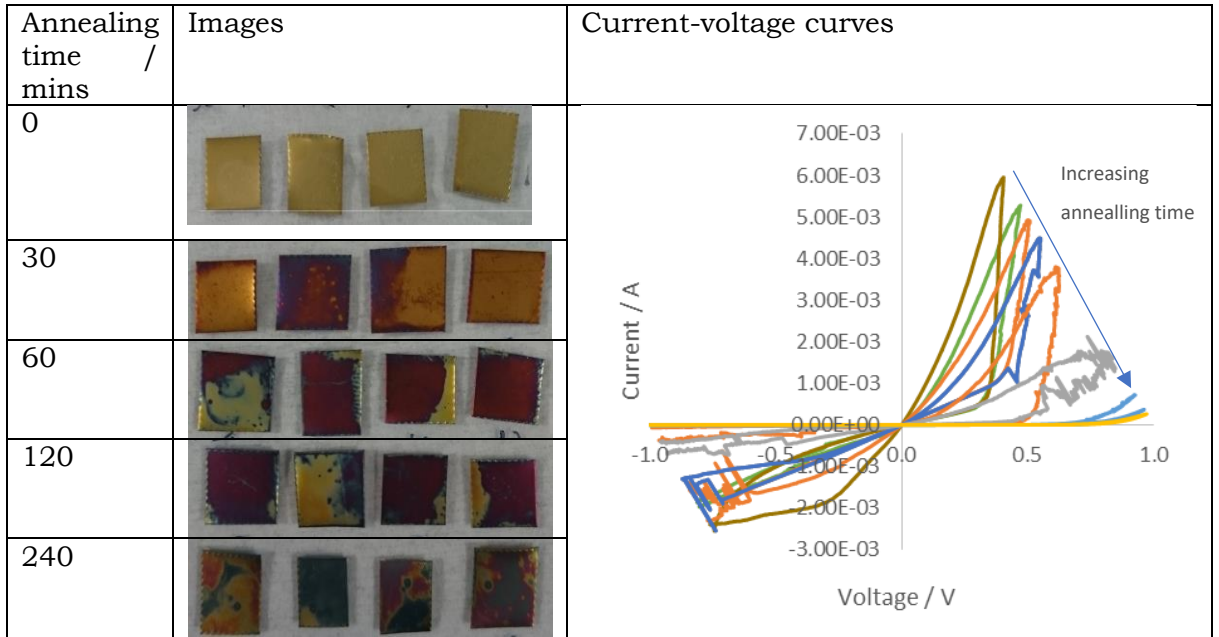


Figure 3.26: Showing TiN devices images following annealing between 0 and 240 minutes at 500 °C.

Though the current falls for the devices across the series, the rectification ratio improves, resulting in IV curves indicative of ideal diodes, Figure 3.27.

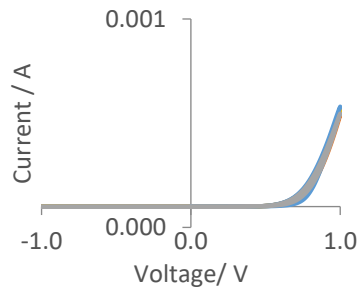


Figure 3.27: Current-voltage curves for an 8-hour annealed device demonstrating high rectification ratios (maximum forward current = 858 times higher than the maximum reverse current).

Sample photocurrent / nA	Annealing time / hours					
	1	2	3	4	6	8
1	14.8	4.2	24.1	16.5	7.0	18.2
2	19.8	27.0	10.6	8.4	10.0	6
3	47.1	-	7.7	-	13.4	7.4

Table 3.5: Photocurrents for devices fabricated from a TiN substrate following the annealing of the substrate for 1-8 hours.

This would appear to suggest that a shorter annealing time results in a higher photocurrent. However, the devices annealed at higher temperature results in more ideal diodes, with high rectification values.

These devices show improvement in electrical characteristics and photocurrent. The dependence of the photocurrents on these methods are discussed in Chapter 5.

### 3.5. Conclusion

In conclusion, many devices were fabricated in order to achieve the aim of diodic devices with an observable photocurrent. Generally, low temperatures and short annealing times seem necessary to result in devices that are diodic and with increased photocurrent. Formation of diffusion barriers can impact the photocurrent and diodic properties. The crystallinity of the sols improved with extended solvothermal synthesis at 100 °C. This leads to highly crystalline sols, though perhaps increasing in strain or defects. This led to higher photocurrents.

# 4. Chapter Four: Electrical Characterisation

## 4.1. Overview

In contrast with earlier work, the current-voltage (IV) characteristics more similar to ideal diodes and this allowed the modelling of the devices to the ideal diode equation using built-in curve fitting functions in MATLAB. However, fits to thermionic emission theory equations were generally unsuccessful.

Voltage dependency of current does not fit with reported models for direct or Fowler-Nordheim tunnelling. For sol derived devices, the presence of water and its desorption at higher temperatures changed the IV characteristics and therefore the changes in reverse saturation current with temperature can be lost amongst the changing surface characteristics. However, TiN which has less defects, also shows little temperature dependence, which may be due to pinning at the interface.

The importance of vacancies in TiO<sub>2</sub> and the impact of water has been widely discussed and clearly has an impact on the devices made here. Typically, on measuring devices in water, the resistance drops substantially and leakage currents increase. The marked deviation in IV behaviour resulted in the diode equation not being sufficient to describe the characteristics of these devices.

## 4.2. Introduction

The Introduction (Chapter One) and the Literature review (Chapter Two) detail the formation of Schottky barriers and their use as photoelectrochemical and photovoltaic devices. Schottky barriers are

rectifying contacts; current can travel in one direction but not in the other, Figure 4.1.

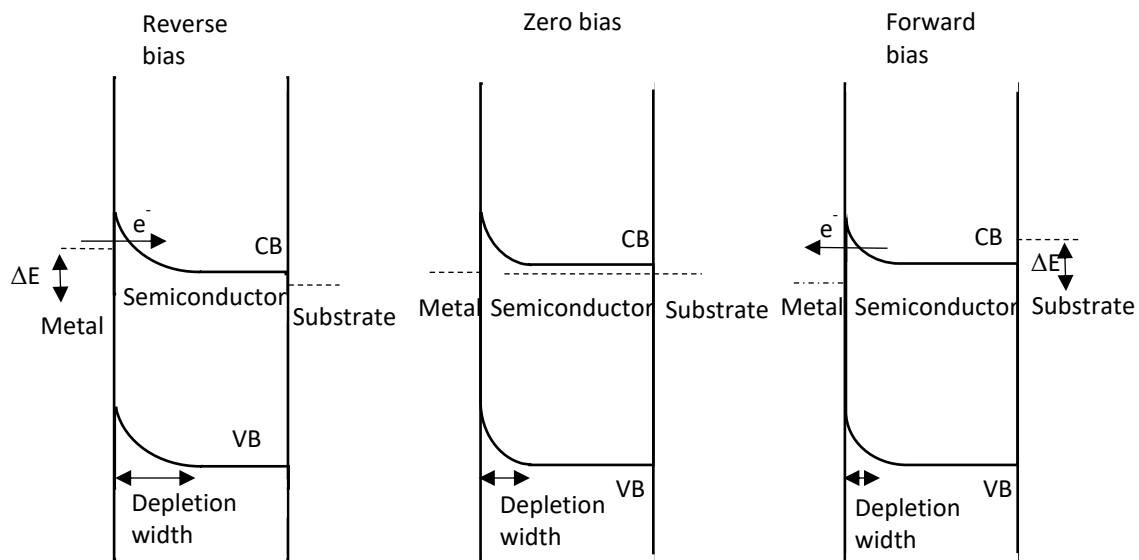


Figure 4.1: Schottky barrier, centre, and under reverse and forward bias, left and right respectively. Left shows the reverse bias case which causes the width of the depletion region to increase. Right shows the forward bias case where the width of the depletion region decreases. In all three cases, the Schottky barrier height is the same.

In all cases, the Schottky barrier height is constant, but in the forward bias case, the amount of charge that must be compensated for increases. This results in a wider depletion region and a larger potential drop across this region. The current that flows is very small due to the unlikelihood of tunnelling such large distances. However, when the applied potential reaches the avalanche potential, the materials become ionised, causing the rapid ionisation of more material and a rapid increase in conduction. In the opposite, forward bias case, the depletion region decreases in width and tunnelling this small distance can occur efficiently.

#### 4.2.1. Electrical characteristics and models

Solar devices, including photoelectrochemical cells, have been modelled with reference to an equivalent circuit. For instance, the conduction in  $\text{TiO}_2$  films and their contacting electrolyte have been mathematically modelled, along with using electrochemical impedance spectroscopy (EIS) in order to model the interfacial capacitance at both electrodes, electron migration through the  $\text{TiO}_2$  film and resistance of electrolyte solutions. <sup>137,138</sup> In an optimum device,

the materials absorb as much light as possible and sustain high internal electric fields to maximise high minority carrier lifetime and mobility.

Figure 4.2 shows the simplest solar cell equivalent circuit. In this case, in a device with low series resistance,  $R_s$  and high shunt resistance,  $R_{SH}$ , the efficiency of current collection will be high. Further, the reverse saturation current of the device should also be low. In an ideal p-n junction, an electron is excited from occupied states in a p-type material across the depletion region to the n-type material, where it is collected. If that diode was operated under forward bias, the electrons would flow from n to p type, depending on the magnitude of the reverse saturation current,  $I_0$ .

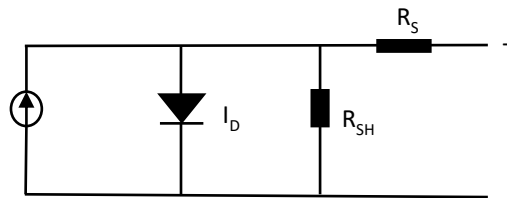


Figure 4.2: Basic equivalent circuit diagram showing diode equivalents, the shunt resistance and the series resistance.

There are many components in this circuit that drop potential, including the non-linear diode. The open circuit voltage ( $V_{oc}$ ) is used to describe the maximum voltage a device can generate. In a typical experiment, an illuminated device is swept to increasing potential until current no longer flows. This gives the short circuit current ( $I_{sc}$ ) at minimum bias and the open circuit voltage at minimum current density. The power is a product of the current and voltage. As losses will cause a deviation from the maximum power possible, the measured integral of the IV curve relative to this maximum power point gives the fill factor.<sup>126</sup> These definitions allow the comparison of devices between experiments and between research groups.

#### 4.2.2. Schottky barrier height

The Schottky barrier arises through the separation of charges, which also results in a high resistance region forming at the interface. The charges on the metal side form a thin sheet of negative charge within the metal screening distance, typically 0.05 nm. This is analogous to a thin Helmholtz layer in high molarity solutions of electrolytes which is usually between 0.3-1 nm.

The advantages of Schottky barriers are the simplicity of production as there is only one depletion region and one doping type. In theory, this offers simpler and potentially lower cost and temperature manufacturing methods as there is no need to dope or implant ions to achieve two oppositely doped regions as in p-n junctions. There is also the possibility of utilising long wavelength light, for instance in IR solar cells.

The Schottky barrier forms between a metal and a semiconductor. As discussed in Chapter 1, predicting the Schottky barrier formation is achieved by applying the superposition principle, “lining up” of the vacuum levels outside the two materials, Figure 4.3.

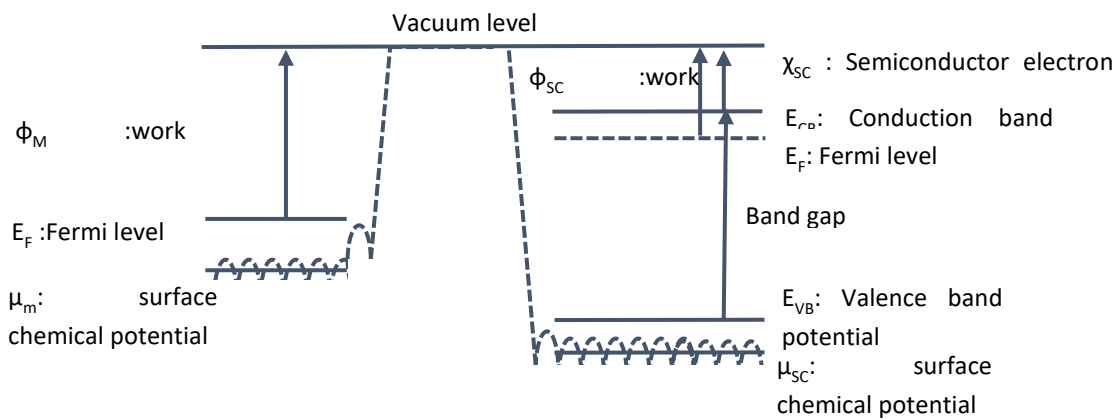


Figure 4.3: Prediction of the formation of the Schottky barrier from two materials demonstrating the relationships between measurable characteristics of the materials.

The Schottky barrier is predicted to be dependent on the difference between the metal work function and the semiconductor electron affinity, however there are many flaws with this model. The interior of each crystal has a periodic potential and surfaces tend to rearrange to minimise the potential energy which also depends on the specific orientation, the atomic structure and electronic structures of the semiconductors and the metal. The drop in potential energy at a surface can be described by a surface dipole contribution. Similarly; molecules and oxides at interfaces may form and their contribution can be described by a dipole. States related to the surfaces cannot exist when the interface is formed, they are both destroyed and there may be a net charge at the surface.<sup>43,139</sup>

The shape of the potential barrier can be calculated from the charge distribution of donors in the depletion region. Assuming the charge density is uniform in this region, the electric field strength rises linearly, forming a parabolic energy profile. <sup>139</sup>

#### 4.2.2.1. The hole barrier

The amount of band bending is predicted by Poisson's equation (Section 4.2.5) which states the divergence of an electric field equals the charge density divided by the dielectric constant. As the band gap is constant, the hole barrier is assumed to be the same and have the same profile as the electron barrier.

#### 4.2.3. Depletion regions and capacitance

Capacitance a measure of a devices ability to store charge. One of the simplest capacitors is two metal plates with a dielectric material between them. The amount of charge that can be stored is proportional to the area,  $A$ , and the dielectric constant of the material,  $\epsilon_m$ , and inversely related to distance,  $d$ , resulting in Equation 4.1 for an ideal parallel plate capacitor.

Equation 4.1. 
$$C = \epsilon_m \epsilon_o \frac{A}{d}$$

$\epsilon_o$ : vacuum permittivity

$\epsilon_m$ : relative permittivity

$A$ : area

$d$ : distance

The Schottky barrier also forms a depletion region between two relatively conductive materials. Studying the capacitance of Schottky barriers under applied potential allows the measurement of a range of characteristics. Impedance, the total opposition to the flow of current, can be studied by use of simultaneous alternating and direct current.

In a conductor, the passage of current can induce current in other conductors. This induction of current is particularly important in coils, and as expected, the more coils in an area, the greater the area enclosed by a coil and the lower the relative permittivity of the material, the greater the induction.

The other contribution to the current under AC bias depends on the capacitance of a device. On application of a bias to parallel plates of a capacitor, charges will accumulate until the voltage across the capacitor matches the bias applied. For a perfect capacitor, if the bias was removed, the charges would remain. Connecting this charged capacitor to an external circuit, current would flow through the external circuit, recombining, and discharging exponentially over time. Therefore, both induction and capacitance demonstrate a time dependency.

Applying an AC bias to an ideal resistive circuit results in a current that is in phase with the applied potential. However, an ideal capacitor and inductor have positive and negative phase shifts by  $90^\circ$  respectively.

Starting from an uncharged capacitor with no potential applied, as it increases to its maximum, the current through any ideal resistors would be expected to increase in phase. When the potential has reached its maximum and starts to decline, the capacitor has some charge. The capacitors contribution to the current in the circuit increases. When the potential is increasing in the negative direction, this will have the effect of reducing the potential across the capacitor, to zero, when the maximum negative voltage is reached. For this reason, current through an ideal capacitor lags the applied potential from a power supply by  $90^\circ$ , Figure 4.4.

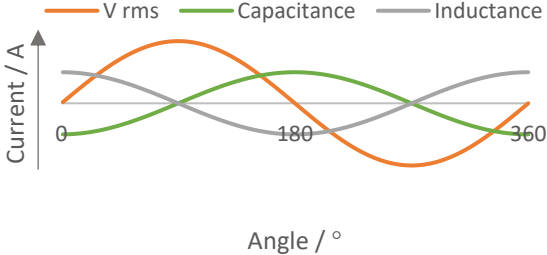


Figure 4.4:  $V_{rms}$  shows the applied alternating potential, the Capacitance line (green) indicates the measured current through an ideal capacitor and the Inductance line (grey) indicates the measured current through an ideal inductor.

The complex ratio of the voltage to the current through an AC circuit, then, is made up of the real part, the resistance, and the phase sensitive, imaginary parts, capacitance and inductance, which together are the

reactance of the circuit. Therefore, the current through a resistive and capacitive circuit can be written in complex form, Equation 4.2, where the angular term is simply  $2\pi \times$  frequency, Equation 4.3.

Equation 4.2: 
$$V = Z I$$

V: Voltage

I: Current

Z: reactance

Equation 4.3: 
$$I = V j\omega C$$

$j\omega$ : complex term

C: Capacitance

J is used instead of i as denotation for the imaginary component to avoid confusion with current. For a 100 pF capacitor, the expected current at  $90^\circ$  due to capacitance is given in Equation 4.3, and its value is given in Equation 4.4.

$$I = 20 \text{ mV} \times 2\pi \times 1337 \text{ Hz} \times 100 \text{ pF}$$

Equation 4.4: 
$$I = 16.8 \text{ nA}$$

Current measured at  $90^\circ$  was 12.3 nA for a  $V_{\text{rms}}$  value of 20 mV and frequency of 1000 Hz, allowing calculation of capacitance as given in Equation 4.5 which is similar and within the tolerance value of its advertised capacitance.

Equation 4.5: 
$$C = \frac{12.3 \times 10^{-9} \text{ A}}{20 \times 10^{-3} \text{ V} \times 2\pi \times 1000 \text{ Hz}} = 97.9 \text{ pF}$$

Capacitance depends on the dielectric constant of the material used, however, dielectric constants are not constant with frequency, resulting in the range of plasmonic effects discussed in Chapters 6 and 7. The dielectric constant is a measure of the ability of a substance to maintain the density of an electric field generated by a free electric charge relative to a vacuum, Figure 4.5. Therefore, an ideal dielectric can support varying charge with little dissipation of energy. Above  $\sim 10^{15}$  Hz, there are no modes of polarisation available to dielectrics, resulting in a permittivity dropping to zero.

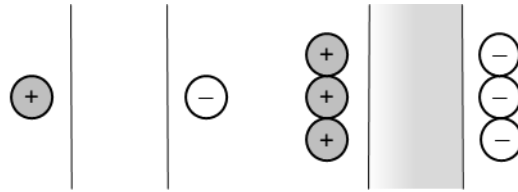


Figure 4.5: Illustrating the value of the dielectric constant. Left shows a charged parallel plate with no dielectric material, having a  $\epsilon = 1$ . Right shows a material with  $\epsilon = 3$ , able to sustain 3 times as high a density of electric field.

The ability of a substance to polarise in response to an applied field can help in the maintenance of relatively large charge, for instance, in the study of super-capacitor materials, the use of a highly porous material may reduce the capacitance as the dielectric constant of air is only slightly higher than a vacuum,  $\epsilon \sim 1$ . However, by using strong acids, the charged species can migrate to create dipoles equal in size to the applied field, allowing a larger potential to be sustained. <sup>140</sup>

If the frequencies are high enough the material may be unable to respond. This can lead to abrupt changes in the dielectric properties of a medium at frequencies at which, for instance, rotational modes cannot respond quickly enough, though these are much higher than those used here for capacitance measurements.

#### 4.2.4. Capacitance and applied bias

Applying a reverse bias to a Schottky barrier changes the amount of charge that must be compensated for in the space charge region, as discussed in Section 4.2 and Figure 4.1. The following discussion is based on a range of sources. <sup>43,141-143</sup>

Under applied bias, the depletion width increases, analogous to an increase in length between charged parallel plates, leading to a decrease in capacitance and as such the current measured out of phase, Figure 4.6.

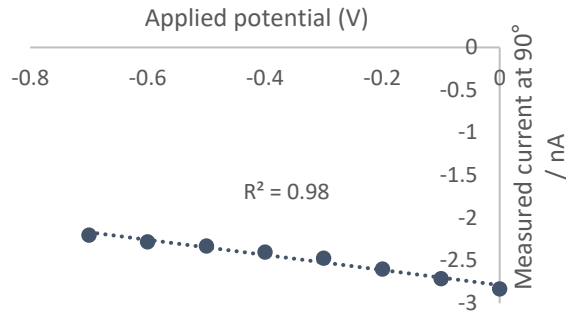


Figure 4.6: Out of phase current (90° relative to applied  $V_{rms}$ ) at applied DC bias values, demonstrating a linearity in response for a commercial capacitor.

Assuming the semiconductor is non-degenerate and uniformly doped, when a potential is applied, a volume of ionised donors, given by Equation 4.6 and illustrated in Figure 4.7 are required to compensate for an amount of charge.

Equation 4.6: 
$$Q = qA\rho_0x_d$$

Q: charge

q: charge on each donor

$\rho_0$ : dopant density

$x_d$ : distance

A: Area

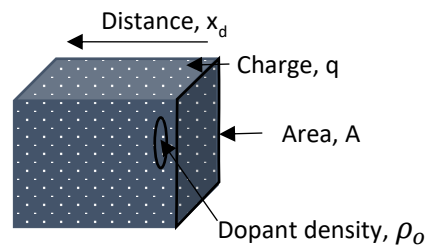


Figure 4.7: A uniformly doped semiconductor, demonstrating the factors impacting the ability of a material to change in response to an applied field

Poisson's equation is used to relate the charge density to change in electrical potential, Equation 4.7. This assumes completely ionised, uniformly distributed dopants of charge  $q$ , with density  $\rho_0$ .

Equation 4.7: 
$$\frac{d\phi}{dx} = \frac{q}{\epsilon} \rho_0$$

$\varphi$ : electric field

$q$ : charge

$\rho_o$ : dopant density

$\varepsilon$ : dielectric constant

Integrating this yields Equation 4.8.

Equation 4.8: 
$$\int \frac{d\varphi}{dx} dx = \varphi = \frac{q}{\varepsilon} \rho_o x + c$$

$x$ : distance

$c$ : constant

The voltage, or potential difference, is the change in electrical potential between two points. This can also be calculated by integrating the electric field. To solve Equation 4.8, for a Schottky barrier, two boundary conditions must be used to find numerical solutions. Here, the potentials at the boundary with the perfect ohmic back contact is set arbitrarily to zero,  $V = 0$ , the potential at the metal contact is equal to the applied bias ( $V_R$ ) and the built-in voltage ( $V_{bi}$ ). The built-in potential in a Schottky barrier can be understood as the energy expended to bring a charge to a position, in this case the movement of charge from the semiconductor to the metal. Integrating Equation 4.9 between  $x$ , the interface with the metal contact and  $x_d$ , the width the depletion region gives Equation 4.10.

Equation 4.9: 
$$V(x) = \int \frac{q\rho_o}{\varepsilon} (x + x_d) dx$$

Equation 4.10: 
$$V(x) = \frac{q\rho_o}{\varepsilon} \left( \frac{x}{2} + x_d \right) x + constant$$

However, we are interested in the potential difference across the junction, so can set one side of the junction to zero, whereby the distance, is equal  $x$  to  $x_d$  and solving for the constant gives Equation 4.11:

Equation 4.11: 
$$\frac{q\rho_o}{\varepsilon} (x_d^2) = constant$$

Which can be substituted back in to the above equation to give:

Equation 4.12: 
$$V(x) = \frac{q\rho_o}{\varepsilon} \left( \frac{x}{2} + x_d \right) x + \frac{q\rho_o}{\varepsilon} (x_d^2)$$

This is the voltage at any point between  $x$  and  $x_d$ . The difference in potential across the region is independent of the constant. From this, the applied voltage can be related to the dopants in density, Equation 4.13.

$$\text{Equation 4.13:} \quad V_R + V_{bi} = \frac{qp_0}{2\epsilon\epsilon_0} w^2$$

$V_R$ : Applied bias

$V_{bi}$ : Built in bias

$w$ : width

Differentiating with respect for width for the  $V_R$ .

$$\text{Equation 4.14:} \quad dV_R = 2 \left( \frac{qp_0}{\epsilon\epsilon_0} \right) w dw$$

From Equation 4.6, for a distance  $x_d$ , into a uniformly doped semiconductor,  $p_0$  over an area  $A$  with a dopant charge,  $q$ . Over the width,  $w$ , the change in charge,  $dQ$ , over this width,  $dw$ , is  $qAp_0 dw$ .

As the definition of capacitance is the change in charge with respect to applied voltage.

$$\text{Equation 4.15:} \quad C = \frac{\delta Q}{\delta V_R} = \frac{q\rho_0 A dw}{(q\rho_0/\epsilon\epsilon_0)w dw} = \frac{A \epsilon\epsilon_0}{w}$$

For capacitance across this width, using Equation 4.14, so  $dw = w$ ,

$$\text{Equation 4.16:} \quad C = A \sqrt{\frac{q\epsilon\epsilon_0\rho_0}{2(V_R + V_{bi})}}$$

Or;

$$\text{Equation 4.17:} \quad \frac{1}{C^2} = \frac{2}{A^2 q \epsilon \epsilon_0 \rho_0} (V_R + V_{bi})$$

Therefore, for a uniformly doped semiconductor, a plot of  $1/C^2$  against applied bias will yield a straight line with gradient,  $m$ , Equation 4.18 and intercept,  $c$ , Equation 4.19.

$$\text{Equation 4.18:} \quad m = \left( \frac{2}{A^2 \epsilon \epsilon_0 q \rho_0} \right)$$

$$\text{Equation 4.19:} \quad c = \left( \frac{2}{A^2 \epsilon \epsilon_0 q \rho_0} \right)$$

The plot of  $1/C^2$  against voltage will be linear for a uniformly doped capacitor as shown in Figure 4.8 for a ceramic capacitor.

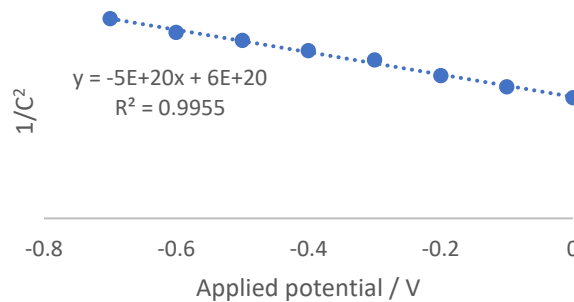


Figure 4.8:  $1/C^2$  against applied voltage for a ceramic capacitor.

#### 4.2.5. The Ideal Diode Equation

A diode can be described by the ideal diode equation, Equation 4.20. In this case, the leakage current depends on the applied potential and the shunt resistance, given by the final term in Equation 4.20.

Equation 4.20: 
$$I = I_0 \left( \exp \frac{qV}{nkT} - 1 \right) + \frac{V}{R_s}$$

$I$  = device current

$I_0$  = reverse saturation current

$q$  = elementary charge

$n$  = diode ideality factor

$V$  = device voltage

$R_s$  = shunt resistance

$k$  = Boltzmann constant

$T$  = absolute temperature

#### 4.2.6. Impact of applied potential to barrier height

Although an ideal Schottky barrier height is independent of potential, it is sensitive to the voltage across the depletion region. Since there is a field in the semiconductor, the zero-bias barrier height is different from the flat band barrier height. This is particularly the case where there is an interfacial region which is strongly impacted by applied bias, such as in the filling of surface states. It can also change under illumination.

Further, there is also an impact of image-force barrier lowering. When an electron is at a distance  $x$ , from the metal, in the semiconductor (in the conduction band), there exists an electric field perpendicular from the metal surface. The effect of this field on the barrier can be calculated by solving for an "image force" exactly opposite on the metal side.

Solving Coulombs laws to account for the attraction between an electron in the conduction band and the "image force" on the other side ( $F = -q^2 / 16\pi\epsilon_0 x^2$ ), a distance sensitive energy potential as well as the Schottky barrier results in a resultant barrier that is lower and has a slightly different profile to the original barrier.

#### 4.2.7. Methods for measuring barrier height

There are many methods for measuring the height of the Schottky barrier. Thermionic emission theory can provide barrier height by measuring the current voltage characteristics at a range of temperatures, as discussed in the following section. If the area is known, measuring capacitance under reverse potential can also yield a barrier height. Also, photoelectric measurements can yield the barrier height in a similar way to metal photoelectric effect measurements. (Sharma)

##### Current-voltage measurements of Schottky barrier diodes

The rectifying properties of Schottky barriers lead to their characterisation by measuring current at applied biases. An ideal diode has a very low leakage current, negligible series resistance and a small shunt resistance. As such, the current rises exponentially with forward voltage. With reverse bias, the current remains at the reverse saturation current at all applied biases.

##### Thermionic emission theory

Thermionic emission theory treats electrons as travelling away from a very hot surface into a vacuum. It is a good fit for many diodes operated under forward bias as the energy the electrons have is great enough to travel over the barrier and it is used extensively in the literature on Schottky barriers to measure properties such as barrier height. It is given in Equation 4.21.

Equation 4.21: 
$$I_0 = SA^*T^2 \left( \exp \frac{-\phi_s}{kT} \right)$$

S = junction area

$A^*$  = modified Richardson constant

$\Phi_s$  = Schottky barrier height

The modified Richardson constant accounts for the deviation of an electron from its vacuum values of charge and mass to those in the material.

#### 4.2.8. Electrical characteristics and models

The conduction mechanisms through the barriers are often not as simple as thermionic emission theory and many mathematical models have been applied to account for a range of phenomena that impact electron transport through dielectric materials, which are beyond the scope of this work, though some common reported mechanisms are included in Table 4.1.

Fowler-Nordheim tunnelling describes a very high field situation, whereby the field is large enough that the electrons can tunnel through the potential barrier into the conduction band. Similar to direct tunnelling mechanisms, there is no temperature dependence for this process, as it does not rely on thermally activated carriers.<sup>144</sup>

#### 4.2.9. Changing IV characteristics of Schottky barriers with UV light

A ZnO nanorod Schottky device showed a high sensitivity to UV showed a 9186% increase in current. The barrier heights of the device decreased with increasing power intensities. For comparison, a Ga/Pt alloy ohmic contact was also made demonstrated a response of 38% increase in current under UV light compared to no light.<sup>145</sup>

Despite the production of two Au contacts on ZnO on the nanorod devices, the authors find an antisymmetric IV curve, suggesting disparate characteristics for each end of the device and barrier heights of 0.68 and 0.75 eV for each end is reported. The Schottky barrier heights lower under UV irradiation, decreasing rectification, attributed to the dissociation of O<sub>2</sub>-adsorbed ions by UV generated holes.<sup>145</sup>

Thermionic emission theory	$I = SA^*T^2 \left( \exp \frac{-\Phi_s}{kT} \right) \left( \left( \exp \frac{qV}{nkT} \right) - 1 \right) + \frac{V}{R_s}$ <p>I: Current  S: Area  A*: Richardson constant  T: Temperature  Φ<sub>s</sub>: Barrier height  k: Planck's constant  q: charge  V: Applied voltage  n: diode ideality factor  R<sub>s</sub>: Series resistance</p>
Trap-limited transportation	$I = \alpha T^{\frac{3}{2}} E \mu \frac{m^*}{m_0} \exp \left( \frac{-q(\phi - \sqrt{qE/4\pi\epsilon_r\epsilon_0})}{kT} \right)$ <p>Terms as defined above.  α: constant  E: electric field  μ: mobility  m*/m<sub>0</sub>: relative mass  ε<sub>m</sub>: permittivity  ε<sub>0</sub>:vacuum permittivity</p>
Fowler-Nordheim tunnelling	$I = \frac{q^3 E^2}{8\pi h q \phi_B} \exp \left( \frac{-8\pi \sqrt{2qm_T^*}}{kT} \phi_B^{3/2} \right)$ <p>Terms as defined above.</p>
Direct tunnelling	$I = \frac{q^3 E^2}{8\pi h \epsilon \phi_B} \exp \left\{ \left( \frac{-8\pi \sqrt{2m_T^*}}{3hq E} (q\phi_B)^{3/2} \right) \cdot \left( 1 - \left( 1 - \frac{V}{\phi_B} \right)^{3/2} \right) \right\}$ <p>Terms as defined above.</p>

Table 4.1: Reported voltage dependencies for current through interface limited current conduction.

These liberated electrons are also proposed to increase the carrier density of the nanowire, thus apparently reducing the depletion width, increasing the field in the region.<sup>145</sup> A Gaussian distribution of Schottky barrier heights is

described in similar studies to explain non-linearity in thermionic emission plots.<sup>146</sup>

In a study of Pt on TiO<sub>2</sub> films prepared from spun coat colloidal suspensions use a diffusion theory, Equation 4.21, to model the temperature dependence of barrier height due to the low carrier mobility in these films.<sup>147,148</sup>

The IV curves could be dramatically altered by the presence of water and oxygen, useful for potential applications in gas sensing. The authors report the data fitting to fit the ideal diode equation with  $n$  values of around 2.5 in air and report a barrier height at high temperature of 1.7 eV, while at low temperature, the Arrhenius plot approach values of 0.3 eV. This is attributed to the change of the  $E_F$  in the TiO<sub>2</sub> defects (on surface or bulk) or barrier lowering due to tunnelling lowering.<sup>148</sup>

This also explains the much weaker temperature dependence seen for devices at low temperature. However, in a dry N<sub>2</sub> environment, this effect is weaker, suggesting a lower defect density in the depletion region. The authors also report a difference in the photoconductance decay time between dry nitrogen and humid nitrogen, attributed to the change in electron drift mobility. From trap filling studies, in the nitrogen environment there is the lowest defect densities.<sup>148</sup>

In a study of TiO<sub>2</sub> films in aqueous, ethanolic and acetonitrile solvents, the frequency sensitivity of the capacitance suggests the capacitance originates from stored charges at the particle surface and that the latter two solvents had higher rates of surface trap filling than water, which showed a change in capacitance under UV illumination up to 100 Hz.<sup>149</sup>

## 4.3. Results and Analysis

The devices were manufactured as described in Chapter 3. The SEM images and EDX mapping show some of the problems in manufacturing these devices in terms of continuity of TiO<sub>2</sub> films and diffusion from the substrate.

### 4.3.1. The measurement of devices by current-voltage measurements

The devices varied in their properties depending on the conditions of production, but were more "ideal" than those produced previously in the group through the electro-polishing and oxidation of titanium metal.

The current-voltage characteristics tended to be reasonably constant over time, Figure 4.9. For 50 cycles, the forward cycles maximum current is 0.234 mA (range: 0.224 to 0.299 mA, standard deviation: 0.012 mA) and reverse minimum currents is -0.0179 mA (range: -0.010 to -0.025 mA, standard deviation: 0.0033 mA). Much of the variation is seen in a small decrease in the first few cycles. This could be due to charges such as oxidation at the metal/semiconductor interface. The variation between the measurements could be due to the diffusion of defects such as oxygen vacancies at the interface.

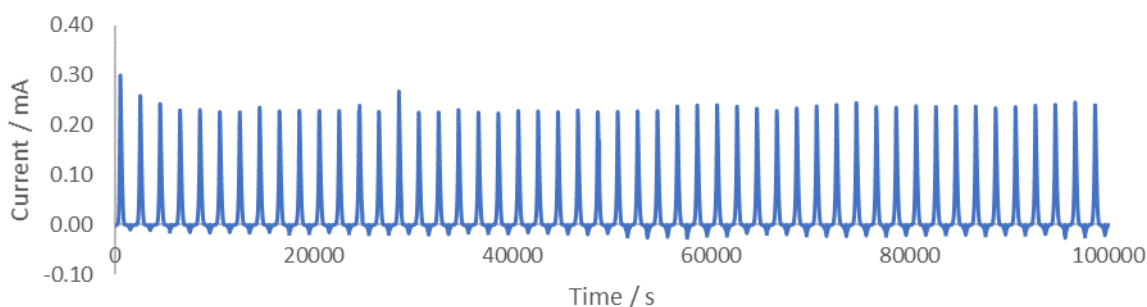


Figure 4.9: Scanning an example device for 50 repeated scans, showing consistency in electrical characteristics over time.

#### 4.3.2. Silver nanowire corrosion

Silver nanowires corrode over a period of weeks. This has been studied previously in similar experiments and can be seen for a TiN derived device in Figure 4.10, where the nanowires appear furred and bent.<sup>49</sup> In order to continue to study the same device over a long time period, occasionally it was necessary to re-deposit and anneal another set of silver nanowires over the first for some continuity between results.

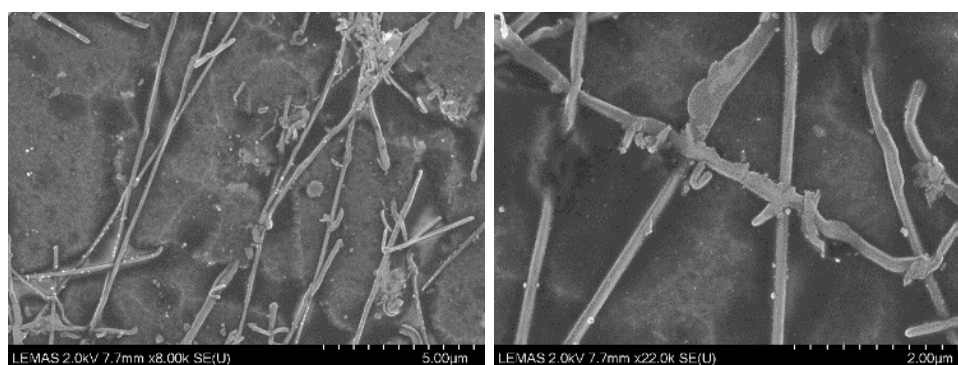


Figure 4.10: SEM images of redeposited silver nanowires on top of corroded nanowires.

### 4.3.3. Fitting IV curves with built-in MATLAB functions

Previous devices have often not been ideal enough to model directly with the diode equation. Previously, an iterative method was used in an attempt to model the devices.<sup>150</sup> However, this method often converged on local minima and took a large amount of computational power, with each curve fitting taking nearly one hour, therefore for one thermionic emission study, tens of hours of fitting was necessary, which often resulted in poor thermionic emission theory fits.

With the advent of more ideal diodes, it became possible to use built-in curve fitting algorithms to fit the IV curves to a model with much lower computational cost, with results printed within 7 seconds, and giving much more reliable results. Only forward sweeps were used to avoid the impact of hysteresis on the fits. Details of the curve fitting and some representative parameters are given in Table 4.2.

Program Version	Matlab – 2015a
Curve-fitting algorithm	Levenberg-Marquardt
Lower limits	-Infinity for all variables
Upper limits	Infinity for all variables
Starting points	a: 0.0357, b: 0.8491, c: 0.9340

Table 4.2: Representative parameters and details of curve fitting in Matlab.

The initial model used was the simplest and is expressed in Equation 4.22, after accounting for the current limiting resistor by Kirchhoff's laws.

Equation 4.22: 
$$I = a(\exp(bV)-1) + c$$

As the c term represents current travelling through the diode through other mechanisms, it was insufficient to describe it as a constant. A potential dependent term was included, Equation 4.23.

Equation 4.23: 
$$I = a(\exp(bV)-1) + cV$$

Figure 4.11, shows the method used to estimate series resistance. The voltage measurements were typically recorded to 1 V, so the last 0.1 V of readings, between 0.9 and 1 V were used to estimate series resistance, on

the assumption that at these potentials, electrons can overcome the barrier and so the resistance measured is that of the device. Conversely, current travelling at very low voltages (0 to 0.1 V) were used to estimate the leakage resistance, Figure 4.11.

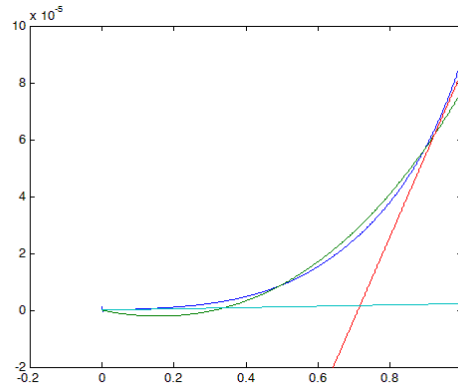


Figure 4.11: Current-Voltage curve for a device showing forward sweeps in potential between 0 and 1 V, demonstrating for one curve how the initial currents and potentials can be fit as an estimate of leakage current (aqua line) and fitting the last results can be used to fit an estimate of series resistance (red line).

For fits with an  $R^2$  value above 0.99 and with  $I_0$  fits above zero, Figure 4.12 shows the range of values for the linear Schottky barrier height measurements made on a range of devices (as demonstrated in Figure 4.11). Many are near zero as ohmic controls devices are often made incidentally in a series of devices. Many of these results converge between 0.5 eV and 1 eV. Of 4427 fits, 1885 have  $R^2 = 0.99$  and positive  $I_0$  values, 1521 have linear Schottky barrier heights above 0.5 and below 1.0 eV and the average of these values is 0.76 eV.

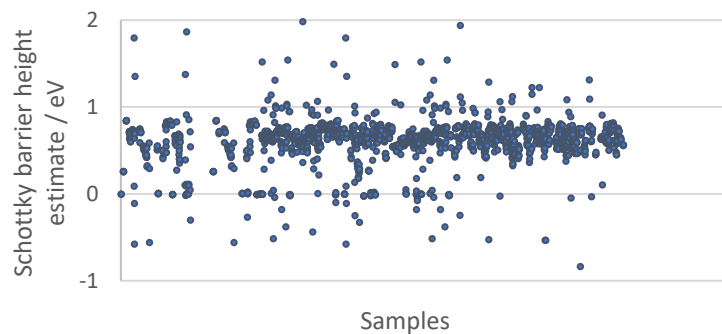


Figure 4.12: Linear Schottky barrier height estimates for high quality fits to the diode equation. Most of these fits are between 0.5 and 1.0 V, with an average of 0.76 eV.

Sometimes the fit to the ideal diode equation with result in an exponential term that gives a negative Schottky barrier height. As some of the IV curves measured were due to control devices in series of experiments, some of these fits were ohmic or showed little forward current.

Improvements to fitting to model exponential function

The limitation of Equation 4.23 is that the potential term  $V$  does not include the potential drop due to series resistance. A more complete fit is described by Figure 4.13 and Equation 4.24.

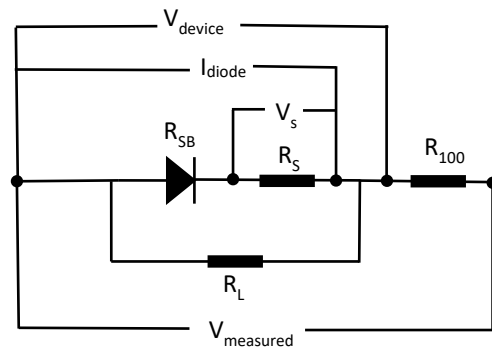


Figure 4.13: Demonstrates the different potential drops across the device.

Equation 4.24: 
$$I - I_{SH} = a(\exp(b(V_{device} - (I \times R_{series}))) + cV$$

In order to fit the results to a model such as this, the current through the Schottky barrier is assumed to be zero at low voltages used to measure the leakage resistances which are assumed to be ohmic. This leakage current is subtracted for each potential. The measurement of the resistance at high voltages allows estimation of series resistance. This, in turn allows the  $V_{diode}$  to be split into the additive components ( $V_{SB} + (I_{device} \times R_{series})$ ) to calculate the potential across the Schottky barrier, Figure 4.14.

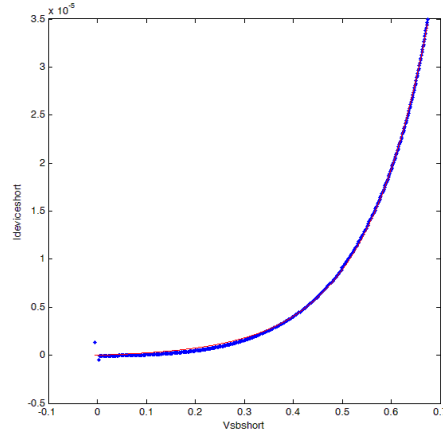


Figure 4.14: Example fit (red) for experimental data (blue) showing a close fit for the improved model by adjusting the fit for the potential drop due to series resistance.

For the above fit, there is a high  $R^2$  value of 0.9996, the reverse saturation constant is  $1.85 \times 10^{-7}$ , close to the previous fit of  $5.8 \times 10^{-7}$  A, from the simpler model, Equation 4.23. There was a calculation of an  $n$  value of 5 for this fit. Ideality factors for p-n junctions are related to the recombination in the depletion region. As these devices are formed of particle films and the electron migration through the device is expected to be due to diffusion rather than drift due to the large distances of the film thicknesses compared to the depletion region, a large diode ideality factor is expected and may not be a useful for characterising the device.

This fitting algorithm repeatedly finds local minima for an input of "b" so it was varied manually for the large deviations. The previous code required less computational power and did not rely on the estimates for  $R_{series}$  or  $R_{leakage}$ , so results of the previous model are used in the remainder of this discussion, at the expense of poorer fits to the ideality factor,  $b$ .

#### Pre-exponential factor variation

A much larger impact is from the pre-exponential value, 'a' in the above equations. To avoid the possibilities of local minima, particularly for devices derived from TiN, where  $I_0$  values can be very high, an iterative model is used to vary the "a" term initial value over 8 orders of magnitude. This was useful for TiN devices, which showed a large degree of change in reverse saturation current for variation across a series.

As the TiN derived devices were often very different in electrical characteristics from the sol derived devices, to improve thermionic emission studies, the two techniques were combined, varying the pre-exponential factor over 8 orders of magnitude and accounting for current travelling through leakage paths and the potential dropped over series resistance as shown in Equation 4.24. There were no improved fits for thermionic emission theory fits for these results.

#### 4.3.4. Other electrical transport fits

As discussed in the Introduction (Section 4.2), there are a number of electrical models that can be used to describe the current through the device. From the current-voltage fits, the external resistances dominate above the barrier height and failure mechanisms tend to be due to the device having ohmic IV curves. Therefore, bulk limited transport mechanisms are not expected to limit current. The devices are expected to be high in defects at the interfaces, perhaps allowing the dominance of defect assisted tunnelling through devices.

Attempts were made to fit experimental data to the range of models shown in Table 4.1 (Section 4.7), with each of the potential dependencies for a representative device, Table 4.2. Often the best fit has negative values for the coefficients. To improve fits, the coefficients were given minimum values of zero, as negative coefficients suggest there are mechanisms by which currents are flowing in the opposite direction to the applied bias. However, oxygen vacancies are modelled as cationic over a range of Fermi levels for surface and subsurface states, so could represent a mechanism for current transport in the opposite direction to the electrons.<sup>145</sup>

This suggests that thermionic emission theory may indeed be the best fit for the data, despite its limitations. A more complete model would need to account for the drift of oxygen vacancies in TiO<sub>2</sub> under potential and the impact the oxygen vacancies had, both on conducting charge and by defect assisted tunnelling, and the changing field and thus barrier height at the interface, similar to a number of examples given in the literature review. This term would depend on the amount of time that the potential had been applied. Also, the total current through the device would depend on the steel interface too, which given chromia is a p-type oxide, to form a small barrier

in the opposite direction to the silver/TiO<sub>2</sub> interface. From the low series resistance and high forward currents, the barrier height is much lower than the Schottky barrier.

Model	Potential dependency	Fits			
		a	b	c	R <sup>2</sup>
Thermionic emission	$aV(\exp(bV))+cV$	$1.2 \times 10^{-4}$	3.2	$-2.6 \times 10^{-4}$	0.995
Thermionic emission (all fits above 0)	$aV(\exp(bV))+cV$	$1.1 \times 10^{-6}$	9.6	$9.6 \times 10^{-6}$	0.889
Trap limited transportation	$aV(\exp(b-(c*V)^{1/2}))$	3.5	-11.2	-7.55	0.905
Fowler-Nordheim tunnelling	$aV^2(\exp(b/V))$	$6.0 \times 10^{-4}$	$1.0 \times 10^{-5}$	-	0.8216
Direct tunnelling	$aV(\exp(b-(cV^{3/2})))$	29.3	-12.5	-18.1	0.944
	$a(\exp(b(V^{3/2})))$	$2.5 \times 10^{-5}$	27.7	-	0.9153

Table 4.3: In a number of these cases, the model requires the field, not the applied voltage, however, assuming the distance over which the field is applied is constant, applied voltage is used instead.

#### 4.3.5. Speed studies

The speed of measurement had a large impact on the measured device characteristics. The phenomena of vacancy drifting has been discussed in the Introduction (1.3.9). The faster scans show a higher rectification ratio whilst slow scans are nearly ohmic. This could be due to the drift of oxygen vacancies through the TiO<sub>2</sub> film. The slow speed scan shows the series resistance becomes limiting at ~0.5 V, Figure 4.15 (right). The rapid increase in current expected from a diode is also at a higher voltage for the fast scan (Figure 4.15 (left)). At high speeds, the current is dominated by thermionic emission through the Schottky barrier. There is also an apparently high Schottky barrier, which is smaller in the low speed scans, likely to be due to the accumulation of oxygen vacancies at the interface.

5000 mV s<sup>-1</sup>

2 mV s<sup>-1</sup>

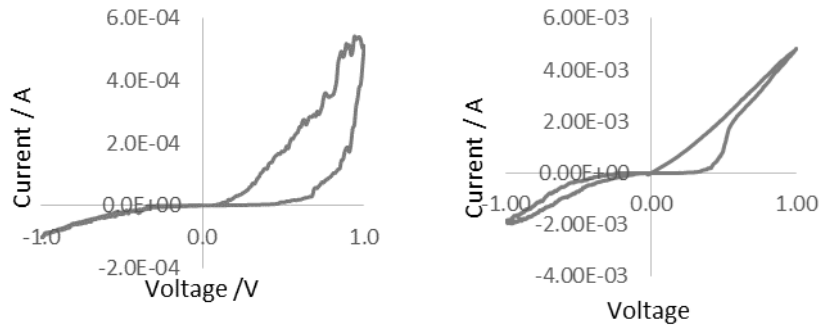


Figure 4.15: Different scan speeds for current-voltage curves for the same device. At the relatively slow scan speed of  $2 \text{ mV s}^{-1}$ , the accumulation of vacancies would appear to reduce the barrier height, as the current becomes limited by the series resistance at  $0.5 \text{ V}$ . This occurs at a much higher potential at  $5000 \text{ mV s}^{-1}$ .

#### 4.3.6. Changes in electrical characteristics with water

Whilst the scans are reasonably constant over extended periods of time in air, as shown in Figure 4.16, in nitrogen there was a large degree of change. The initial device shows a large degree of hysteresis and low reverse saturation current. The hysteresis is probably due to the migration of vacancies under applied potential, providing low resistance paths. However, prior to this, the maximum forward current and hysteresis increases with repeated scans. This suggests a build-up of low current paths at the interface. This would be consistent with water or oxygen desorption leaving unpassivated surface states. However, after more time, the device becomes rectifying again. This could be due a restructuring of the surface to minimise the high surface energy states.

The Schottky barrier re-establishes, but with much smaller forward currents. This may be the thermionic emission current, which is dwarfed previously by the defect assisted tunnelling or diffusion of defects. The maximum current after this secondary Schottky barrier formation is remarkably constant, with no variation with number of scans and may represent a way to achieve steady characteristics for these devices, and thus better thermionic emission fits. The thermionic emission fits can be used to fit for area by measuring reverse saturation currents for a device in nitrogen at a range of temperatures.

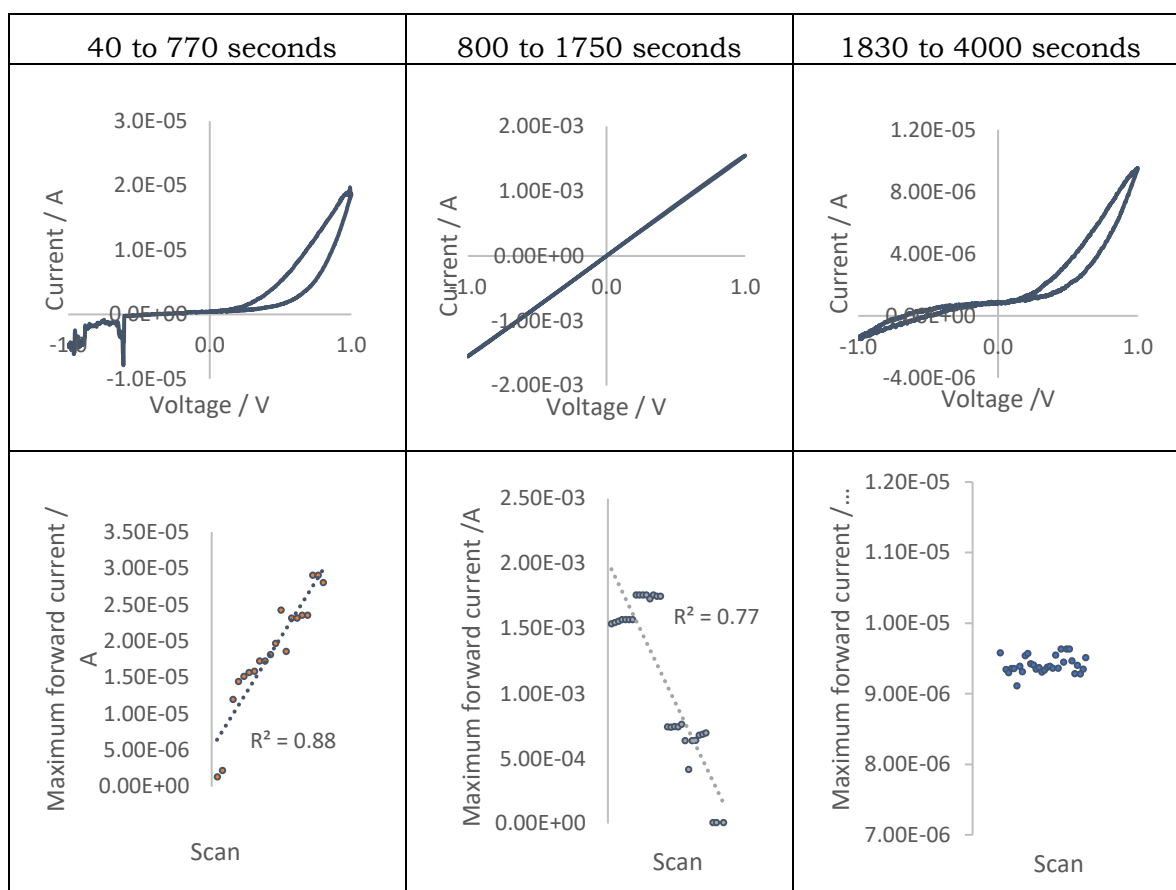


Figure 4.16: Top left; representative IV curve for first 770 seconds, bottom left; showing maximum forward currents for this range of scans. Top centre; representative IV curve for 800-1750 seconds with, bottom centre; decreasing maximum forward currents for these devices. Top right; representative IV curve for 1830-4000 seconds, bottom right; maximum forward currents.

When a beaker of water was included in the nitrogen environment, the switch to ohmic then rectifying properties took longer. With warm water, this transition was faster. Whilst water would be expected to cool as it vaporises under a flow of nitrogen, possibly reducing its concentration over time, if water was the only deciding impact, warm water would be expected to slow the transition to a defect heavy state. However, gases are less soluble in warm solvents, so there may be an impact from the dissolved oxygen in the solvent with the solvent providing a reservoir. The impact of dissolved oxygen cannot be easily distinguished by use of solvents in which oxygen doesn't dissolve as much oxygen as there will also be a change in how the solvent bonds with the  $\text{TiO}_2$  surface. Nitrogen could be saturated with water or oxygen in nitrogen to separate these effects.

## Water and light

Whilst the base device is rectifying, with water, the forward currents are considerably higher. From the shapes of the curves, the barrier height is similar. The water may provide a shield for charges moving within  $\text{TiO}_2$ , which has been suggested as a reason why DSSC electrolytes need to be extremely high in concentration in order to achieve a current.<sup>151</sup>

However, there would appear to be another mechanism at play given the difference between the light and dark response. Repeated scans under light showed decreasing current, but also, a seemingly increasing barrier height, Figure 4.17.

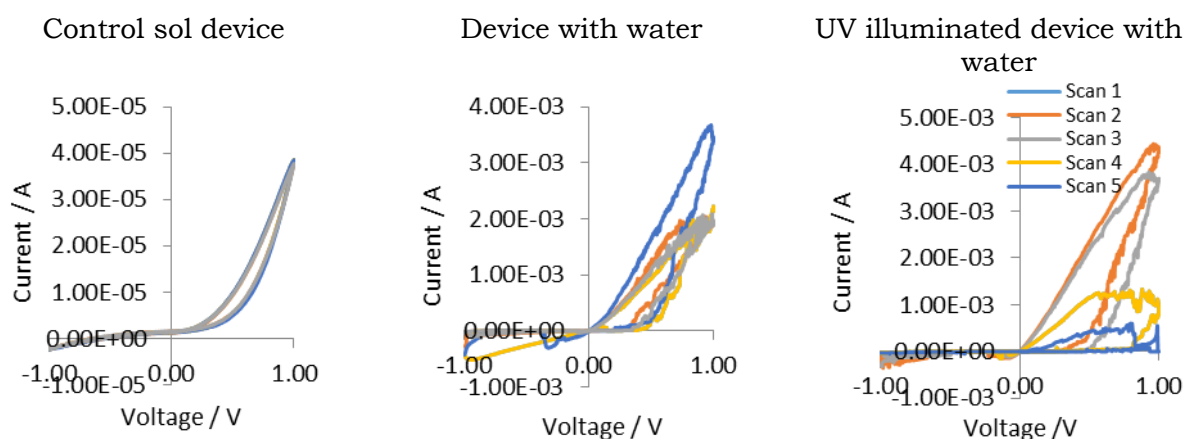


Figure 4.17: A partially crystalline sol device, as a control. Hysteresis is observed for the devices with the water. There is much lower resistance, as the current is much higher. Under illumination, the scans show similar hysteresis and appear to show a progressively higher turn-on voltage.

One explanation is that defects on  $\text{TiO}_2$  are not passivated by water until exposed to light. Mechanisms of water passivation tend to involve a dissociative mechanism, so one possibility is that under light, the water is not simply adsorbed, but becomes dissociated under light to form OH species capable of passivating oxygen vacancies on the surface. The reason for the appearance of the lower current could be due to an “unpinning” of the barrier previously caused by oxygen vacancies and defects, but this conversely means a higher Schottky barrier height and potentially higher efficiency for charge collection.

In literature reports of anatase TiO<sub>2</sub> Schottky barriers, the presence of oxygen is given as the reason for a high turn-on voltage in that case, as discussed in the Literature Review for some devices.<sup>152</sup>

As the potential is not high enough in Figure 4.17 to deduce whether there is simply a lower current due to a higher Schottky barrier or higher resistance, a scan was made to higher potentials. This results in a rapid increase in current, above ~1.1 V, which rapidly becomes dominated by external resistances, suggesting the low currents in Figure 4.17 are not due to increased resistance but a higher barrier height. However, this device also shows a large degree of hysteresis, Figure 4.18.

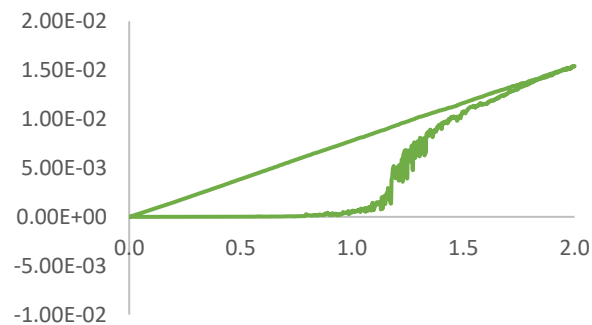


Figure 4.18: Example scan to higher potential for a device under light with water.

The hysteresis in this case could be due to formation of reactive species at these high potentials. Illuminatingly, the TiN derived devices do not show this propensity, showing similar IV curves in ambient conditions to those in water and with water under illumination. This could be due to a much lower defect density of TiN devices.

#### 4.3.7. Geometry arguments for limits of geometry

To deduce what are reasonable values for the area measurements by thermionic emission studies, some geometry arguments can be made in order to set an upper limit to the likely values and set values from thermionic emission in some broader context.

Simply, using bulk values for the density of silver and the geometries from the manufacturers allows calculation of areas from the amount of silver nanowires deposited. Using a maximum of ~59  $\mu\text{g}$  per cell (30  $\mu\text{L}$  of 0.25%

m/v AgNW in solvent with an average geometry of  $60 \times 10,000$  nm), gives a total of  $\sim 3 \times 10^9$  wires per cell. Similarly, using SEM to count wires in an area of  $6.25 \mu\text{m}^2$  gives a value of roughly 200 wires, corresponding to  $\sim 3.2 \times 10^9$  wires per cell of roughly  $1\text{cm}^2$ , in agreement with the value from the argument above. The silver nanowires give a surface area roughly 60 times the cells geometric size. Coverage is  $\sim 13.4\%$  in this case, Figure 4.19 and referred to as shadow area.

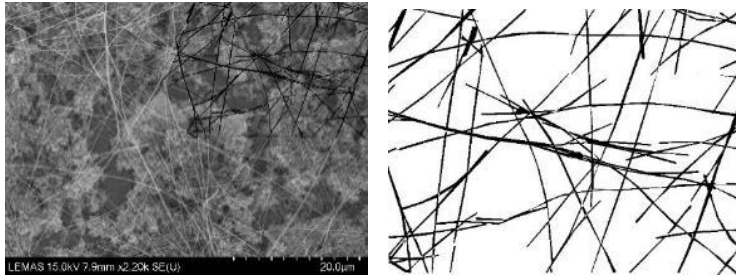


Figure 4.19: SEM image of silver nanowires on a titania sol. The silver nanowire mesh were shaded in order to analyse the area shadowed by the silver nanowires.

Large silver contacts were painted onto some test devices and showed smaller forward currents than the silver nanomesh, suggesting the silver paint top contact is not limiting current. Literature values for the upper limits of current density of Joule heating estimates for silver nanowires for higher current densities than seen in these devices.<sup>153</sup> For this reason, the silver nanowire mesh or its connection to the electrode, nor the semiconductor is expecting to be limiting the current through this device under bias.

From SEM imaging of TiN derived devices, the oxidised regions, formed around plates, are lighter. XRD showed no peaks attributable to  $\text{TiO}_2$ , but only those attributable to titanium nitrides, possibly due to the thin  $\text{TiO}_2$  film. From the SEM images,  $\text{TiO}_2$  appears it is forming mainly at the edge of plates (Figure 4.20 A). Assuming the  $\text{TiO}_2$  layer on the surface of these plates is thin and does not contribute much to active area of the device, the coverage of the  $\text{TiO}_2$  can be estimated by using a thresholding tool to bin the image (Figure 4.20, B) to highlight the brighter part of the images. For the image below, this was done manually, to remove the details of the film.

Applying this to an image (Figure 4.20, C) showed a coverage of approximately 11%.

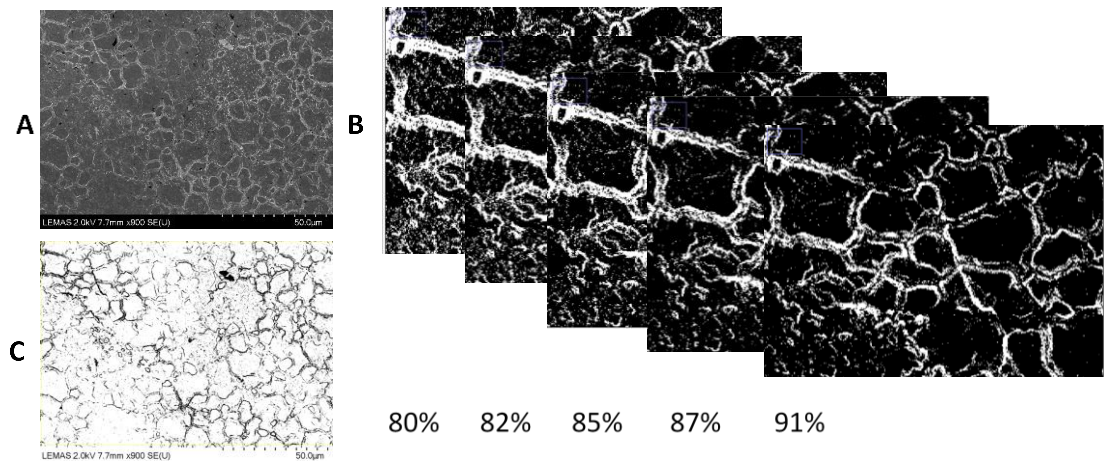


Figure 4.20: SEM image of a TiN derived  $\text{TiO}_2$  film, showing lighter areas, corresponding to regions of oxidation (A). B shows a number of options of “binning” the image by thresholding. At lower proportions 256 shades being included in light regions, details of the film between light areas are included. C shows the extrapolation of the 91 % binning to the whole SEM image.

A coverage of semiconductor of approximately 11%, multiplied by a roughly 13% silver nanowire coverage, results in an upper estimate of 0.0143% area.

This represents an upper estimate for the area of the Schottky barriers and as the SEM images show, there may poor contacting between the silver nanowires and the substrate, so only a fraction of those used are in contact with the substrate. Further, it suggests the TiN derived devices may show a large degree of improvement by the formation of thicker, more light absorbing,  $\text{TiO}_2$  layers.

#### 4.3.8. Fits to thermionic emission theory

Fits to thermionic emission theory were difficult due to three compounding factors:

- The variation between devices, including in electrical transport
- The change in water adsorption and its impact on the electrical properties
- The errors in fitting the data to the models.

Temperature dependency of reverse saturation currents

From thermionic emission theory, there would be expected to be a temperature dependence for the reverse saturation current, as discussed in the Introduction (Equation 4.25):

Equation 4.25: 
$$I_0 = SA^*T^2 \left( \exp \frac{-\Phi_S}{kT} \right)$$

$I_0$ : reverse saturation current / A

S: Richardson constant

$A^*$ : Area /  $m^2$

T: Temperature / K

$\Phi_S$ : Schottky barrier height / eV

k: Boltzmann constant

From the above equation, area is calculated from the intercept of the logarithmic plot, compounding the inaccuracy in the measurements. The unexpected results for reverse saturation fits around 100 °C is possibly due to desorption of water and are generally removed from fits. From the current-voltage curves and Arrhenius plots in Chapter 6, the barrier height is expected to be ~0.7 eV.

There is undoubtedly an impact on the electrical properties of the devices when water is deposited (Section 4.13.1). In the thermionic emission fits, this results in a rapid change in reverse saturation current above the boiling point of water, in this case at 394 K, Figure 4.21. The higher temperature was possibly due to the strength of adsorption of the water to the TiO<sub>2</sub> surface.

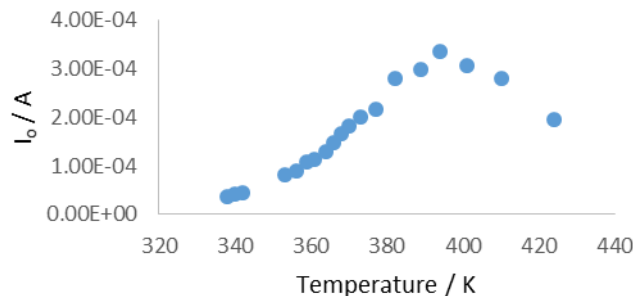


Figure 4.21: Reverse saturation currents fits for a range of temperatures, showing an abrupt change in characteristics at 394 K.

Example relatively successful thermionic emission studies

In the thermionic emission studies, typically a fit to the  $I_0$  values gave a good fit to either the Schottky barrier height or the area. Example fits are shown in Appendix 1 and summarised in Table 4.3 for a range of sol devices. Many of the thermionic fits and especially those that are from the same batch, Batch 4, show areas of between microns and hundreds of microns. Some part of this variance is due to variation in the devices and thus would be expected. Clearly only parts of the silver nanowires will be involved in the formation of devices, as can be seen from SEM images such as in Chapter 3.

Batch	SBH / eV	Area / microns <sup>2</sup>	R <sup>2</sup>
1	0.53	<b>7.1 × 10<sup>2</sup></b>	<b>0.88</b>
1	<b>0.91</b>	1.4 × 10 <sup>8</sup>	0.98
2	0.38	<b>8.1 × 10<sup>-1</sup></b>	<b>0.86</b>
2	<b>0.99</b>	4.3 × 10 <sup>10</sup>	0.90
2	0.19	<b>4.3 × 10<sup>4</sup></b>	<b>0.88</b>
3	0.43	<b>8.4 × 10<sup>1</sup></b>	<b>0.90</b>
4	0.13	<b>9.7</b>	<b>0.91</b>
4	0.11	<b>2.1</b>	<b>0.98</b>
4	0.005	<b>2.0 × 10<sup>-1</sup></b>	<b>0.96</b>
4	0.22	<b>8.2 × 10<sup>1</sup></b>	<b>0.60</b>
4	0.20	<b>1.03 × 10<sup>2</sup></b>	<b>0.99</b>
4	0.15	<b>1.24 × 10<sup>2</sup></b>	<b>0.97</b>

Table 4.4: Thermionic emission studies fits for a range of devices across 4 batches showing a wide range of estimated areas and Schottky barrier heights.

9 of 11 values are within a sensible set of values, with a maximum value of  $1 \times 10^4 \mu\text{m}^2$  of a maximum possible area of approximately  $1 \times 10^8 \mu\text{m}^2$ . The average value is  $124 \mu\text{m}^2$ . These are similar to estimates for the TiN areas, Table 4.4.

Batch	SBH / eV	Area microns <sup>2</sup> /	R <sup>2</sup>
5	-0.09	<b>1.01 × 10<sup>-2</sup></b>	0.16
5	0.005	<b>2.22 × 10<sup>-1</sup></b>	0.96
5	0.35	<b>1.60 × 10<sup>3</sup></b>	0.33
5	0.24	<b>1.33 × 10<sup>2</sup></b>	0.98
5	-0.011	<b>5.2 × 10<sup>-2</sup></b>	0.50
5	0.093	<b>2.93</b>	0.33

Table 4.5: Thermionic emission studies for a batch of TiN derived devices showing a more consistent range of areas.

From Equation 4.6.2, current depends on the area of the device, the barrier height, the reverse saturation current, the diode ideality factor and the temperature. It appears that better estimates of the pre-exponential factor may result in poorer fits to the exponential fits and vice versa. This results in expected fits to areas resulting in poorer fits to barrier height. As argued in Chapter 7, these device areas are consistent with visible responses in dye functionalised devices, whilst where the area estimates are poor, the Schottky barrier estimates are consistent with the IV curves (Figure 4.12) and estimates of barrier height with an Arrhenius study in Chapter 6.

This could be due to the expected change in diode characteristics with temperature and the sensitivity of each device to these. As well as the sensitivity of the diode to temperature, the population of surface states may impact pinning of the barrier as well as desorption of water resulting in changes in defect density, changing the conduction through the barrier. In literature on a p-type Si/Methyl red/Al Schottky barrier, an analysis involving plots of  $dV/d(\ln(I))$  vs  $I$  were also attempted to find fits for resistance and ideality factor.<sup>70</sup> The ideality factor relates to the interface state density and this is the reason given for the difficulty in modelling this junction, as well as series resistance and the voltage drop across the interfacial layer.

The same analysis was attempted on some representative experimental data and resulted in estimates of diode ideality factors around 10 for  $V > 3kT$ . The fits were of reasonable quality, failure to fit for  $n$  results from the poor fit of the model to the device.

Thermionic emission fits at high speed

As described in an above section, the speed at which the measurement is taken also has a striking impact on the current-voltage curves. At high speeds, the currents are lower and more unsymmetrical. In theory, with lower scan speeds, there can be more diffusion of vacancies and defects, resulting in defect assisted tunnelling and short circuiting of the Schottky barrier.

For this reason, in order to model the temperature with thermionic emission theory and minimise the impact of drift of vacancies, a series of IV curves were measured at a decreasing temperature measured with a thermocouple and high speed, 5000 mV s<sup>-1</sup>, scan speeds.

However, the thermionic emission plots tend to be poorer. The reverse saturation current seems to not show a temperature dependency in reverse saturation current. This could suggest the background current is also not described by thermionic emission. If high speed scans result in a lack of defect accumulation at the interface, there could feasibly be higher fields at the interface and transport might be better described by a different model in this instance.

#### 4.3.9. Attempts to improve area of the devices

The amount of the silver nanowires used should result in a functionalisable area of ~60 fold the geometrical area of ~1 cm<sup>-2</sup>. Also, the area of the Schottky barriers is considerably smaller than the available geometrical area. Chapter 4 shows better photocurrent responses for devices where TiO<sub>2</sub> sol was deposited over the nanowires.

In similar attempts, a range of methods were used in an attempt to grow more continuous films of silver onto TiO<sub>2</sub> layers. McFarland and Tang who reported the internal emission device of merbromin functionalised electrodeposited Au film on TiO<sub>2</sub> also worked on a pulsed electrodeposition in order to achieve large area device. The junctions they manufactured in this way showed higher barriers than those grown by electron beam evaporation with a nucleation and growth mechanism.<sup>67</sup> The problem as noted by the authors is that the film must grow uniformly but not thickly. Conditions were adjusted until the islands coalesce, though significant deviation from thermionic emission theory, the higher barriers could be due

to the chemical changes in the interface, where the O<sup>-</sup> group, increasing the interfacial dipole.<sup>66</sup>

To improve active areas of the devices used in this work, an attempt was made to electrically deposit silver nanoparticles onto completed Schottky barriers, similar to literature reports. Zhu et al. report on a method whereby Au nanoparticles were electrodeposited at 4.5 V for 1, 2 or 8 minutes.<sup>154</sup>

silver nanoparticles were synthesised by a “green chemistry” method, whereby silver nitrate was reduced with glucose and electrodeposited.<sup>155</sup> Similarly electrodeposition of silver from silver precursors was attempted. pH was adjusted to maximise interaction between silver and TiO<sub>2</sub> using NH<sub>3</sub> and NaOH.<sup>156</sup> Bifunctional chemical linkers, such as mercaptopropionic acid, were also used. As silver is known for growing dendrites from solid silver in electrical circuitry, the application of potential to the silver nanowires could also potentially grow dendrites. These methods were in general, unsuccessful. Very few showed any improved photocurrents and most short circuited. As the TiO<sub>2</sub> films are not complete, even uniform deposition would result in a short-circuited device.

#### 4.3.10. Frequency domain analysis

As described in Section 4.2.5, capacitance can be studied in devices using AC applied potentials and studying the phase dependence of the response. The capacitance of the device relates to the properties of the depletion region, and the width of the depletion region can be changed by the application of potential. By changing the width of the depletion region under a small change in potential, a density of compensating ionised donors can be calculated.

This methodology was used here, with typically small  $\sim 0.05 V_{\text{rms}}$  sinusoidal biases applied using a signal generator in phase with a lock-in amplifier whilst small DC biases were applied and the current was monitored in and out of phase. As the amplification is of both in-phase and out-of-phase currents, very small  $V_{\text{rms}}$  applied signals need to be used. If the leakage current or reverse saturation current is high, only a small amount of values can be measured.

As expected, the in-phase and out-of-phase current increases with higher  $V_{\text{rms}}$ , whilst out of phase decreases for applied DC bias, as capacitance

(inversely proportional to depletion region) decreases (Figure 4.22, left). This is however, non-linear. This is likely to be due to the non-uniform nature of the dopants throughout the film, its porous nature and the geometry which all deviate from the parallel plate derivation of the equations in Section 4.2.4. Further, the capacitance also decreases with higher frequencies, as expected, Figure 4.22, right).

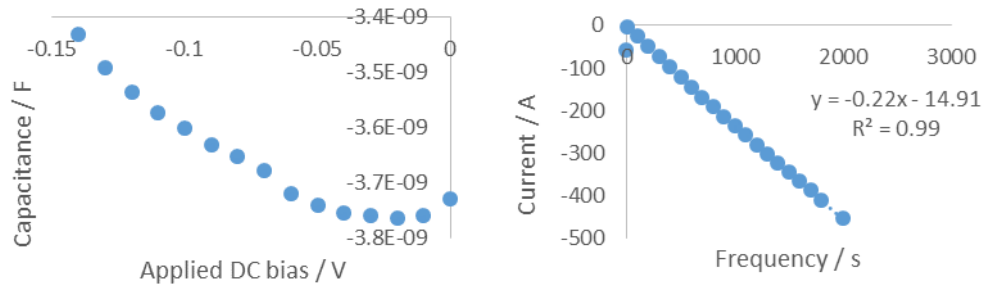


Figure 4.22: Measured capacitance compared to applied bias, showing the expected decrease in capacitance, though this is non-linear. As expected, the current also increases with frequency.

#### 4.3.11. Sol based derived device capacitance

Frequency

Capacitance decreases with frequency, this could be understood in terms of the lack of the build-up of charge on each plate. This is linear with  $1/C$  for frequency, as according to Equation 4.3. The capacitance becomes too small to measure. At 2 kHz, the current drops to near zero. A similar result is seen for 1.8 kHz for the TiN device, Figure 4.23.

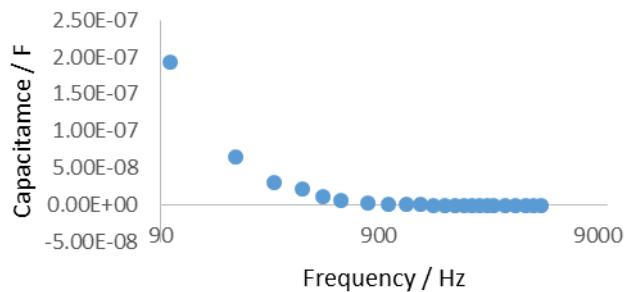


Figure 4.23: Decrease in capacitance with higher frequency.

## Phase

One of the most unusual responses observed in these devices is that the phase is not often in the direction expected. The angle measured is expected to be a sum of a resistor and capacitor in series. Therefore, the phasor angle would be expected to be negative, for any amount of resistance and capacitance. However, in these studies, the phasor is often positive. One reason for a positive phase response is induction. However, inductors are typically dense large coils which induce potential in nearby conductors. There are no components expected to act as an inductor in this way and as such, it is likely a better description of this system is the superposition of capacitive components, resulting in an unusual phase response as seen in other interconnected semiconductor particle grain boundaries.<sup>157</sup> A mesoporous film is better described by a range of capacitors in series and parallel, as the interface between each particle will have its own capacitance and this will distort the measured phase angle.

## Absolute values of capacitance

Some of thermionic emission fits gave areas, and the same devices were analysed for capacitance.

The profile of capacitance with reverse potential and the  $1/C^2$  against applied bias,  $V_R$  are shown in Figure 4.24, demonstrating the non-linearity of plots in these cases, for a device with an estimated area of  $2.1 \mu\text{m}^2$ .

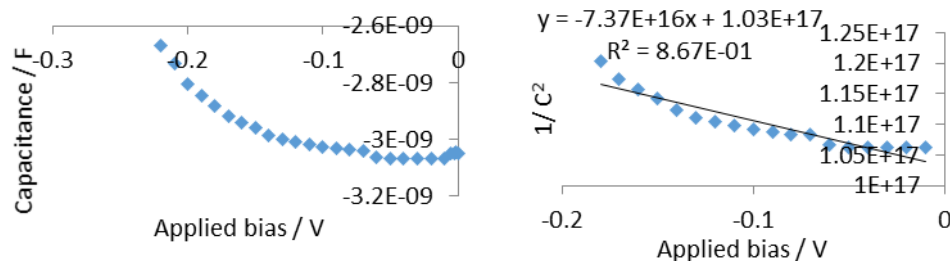


Figure 4.24: Capacitance against applied bias and the  $1/C^2$  plot for a device. The  $1/C^2$  plot is non-linear.

The non-biased capacitance,  $3.05 \times 10^{-9}$  F, when compared to the parallel plate capacitance equation,  $C = \epsilon\epsilon_0 A/L$ , and using a  $\epsilon_0$  value of  $8.85 \times 10^{-12}$  F/m. Assuming the dielectric constant is approximately 18, as for a mainly amorphous film which is the case for this particular device, this results in

the area/width = 19.15, resulting in a length of 110 nm from an area of 2.1  $\mu\text{m}^2$ .<sup>158-160</sup>

From the built-in potential of 1.4 V from the gradient and intercept and the width of 110 nm, from Equation 4.26, an estimate of defect density of  $2.3 \times 10^{23} \text{ m}^{-3}$  can be made.

Equation 4.26: 
$$V_R + V_{bi} = \frac{qp_0}{2\epsilon\epsilon_0} w^2$$

$V_R$ : Applied reverse potential / V

$V_{bi}$ : Built in potential / V

q: elementary charge / C

$p_0$ : dopant density /  $\text{m}^{-3}$

w: width / m

$\epsilon$ : relative permittivity

$\epsilon_0$ : vacuum permittivity /  $\text{F m}^{-1}$

Using the gradient and intercept of Equation 4.26 and 4.27 (derived as 4.13 and 4.19 in the introduction to this chapter), below, as described in the Introduction, the dopant density can be calculated from the built-in potential, using the area as calculated in by thermionic emission fits.

Equation 4.27: 
$$c = \left( \frac{2V_{bi}}{A^2 \epsilon \epsilon_0 q p_0} \right)$$

c: intercept

A: Area /  $\text{m}^2$

$p_0$  is equal to  $2.14 \times 10^{24} \text{ m}^{-3}$ , or  $2.14 \times 10^{18} \text{ cm}^{-3}$ , compared to  $3.2 \times 10^{22}$  for a  $\text{cm}^{-3}$  atoms in  $\text{TiO}_2$ , or 0.007%. As discussed in the introduction, the stoichiometry of  $\text{TiO}_2$  annealed in reducing environments has been reported as  $\text{TiO}_{1.9996}$  for bulk  $\text{TiO}_2$ , whilst this defect density is much higher, at  $\text{TiO}_{1.987}$ . This dopant density gives a depletion width estimate of 36 nm. This is the same order of magnitude as the estimate above.

The literature on depletion regions suggests this depletion region is reasonable. Widths are generally less than 1  $\mu\text{m}$  and a similar method for a PbS colloidal film forming a Schottky barrier with Al resulted in a depletion region between 90-150 nm.<sup>43,53,161</sup> The narrow depletion region in this case

may be due to higher levels of defects in this film. From the non-linearity of the capacitance fits, a better estimate may be made through the use of wire on plate capacitance models to account for the geometry.

#### The impact of water on capacitance

The capacitance of sol derived devices whereby the sols were refluxed for increasing periods, as described in Section 2 were studied in air and water. The series show an increase in capacitance, Figure 4.25.

The capacitance for the water covered devices are much lower than the same devices in air. This may reflect the passivation of defects by water. The intentional formation of defects in  $\text{MnO}_2$  films to increase capacitance whilst improving charge transfer resistance has been reported.<sup>162</sup> The presence of water passivating the defects may result in a smaller dipole and lower capacitance. The surface defects in these cases are acting as stores of charge at the interface.

Water filling  $\text{TiO}_2$  pores would be expected to displace air, with its relatively lower dielectric constant, and provide a higher average dielectric environment and higher capacitance. Further, the dipolar nature of water would expect to facilitate the formation of dipoles at the surfaces, enhancing capacitance. However, the opposite is observed, suggesting the water is in fact eliminating these states, reducing the capacitance. This is consistent with the Section 4.3.6, where IV curves appeared to have higher Schottky barrier heights following illumination in water, suggesting the removal of pinning at surface states.

The increase in crystallinity may also have an impact, with a deformed octahedral structure, crystalline  $\text{TiO}_2$  able to sustain a dipole and has a higher dielectric constant.<sup>159</sup> The increases in air and with water are approximately 3-fold and 4-fold for the 32-hour sol relative to the 8-hour sol. This could reflect the increases in crystallinity. It may also be that the increased strain in the crystals results in more defects which providing increasing capacitance. However, the water is in vast excess to the  $\text{TiO}_2$  so these states would be expected to either be unchanged or passivated and not vary substantially across the series. The change in the "in-water" increase in capacitance, then, could be due to the increase in crystallinity of the  $\text{TiO}_2$ ,

whilst the increase in the "in-air" capacitance could result from changes to the surface of the TiO<sub>2</sub>.

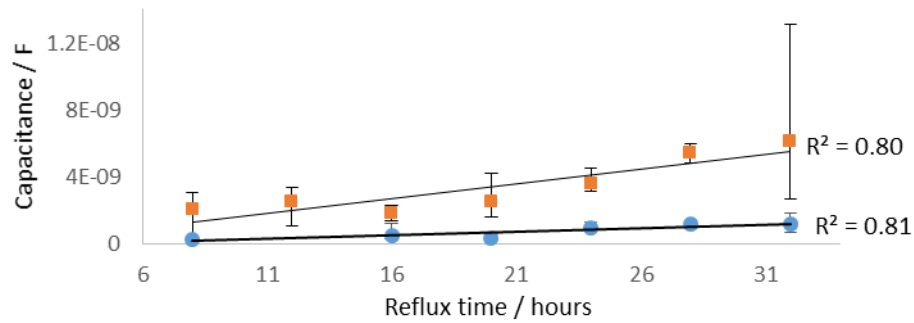


Figure 4.25: Average capacitance (markers) and range (bars) for a range of devices fabricated from sols refluxed for increasing lengths of time, showing increasing capacitance across the series. The square (orange) markers show capacitance for devices in air, circle (blue) shows the devices soaked in water. Without averaging, the  $R^2$  values are 0.42 and 0.50 respectively.

As area and width would not be expected to change with the reflux time of the sol, the increase in capacitance will relate to the increasing crystallinity and the increase in dopant concentration. If these two factors explain all of change in capacitance, the increase in crystallinity would account for ~24% of the increase, with the remainder being due to surface states.

Besides the first and last points, there is a good relation between the built-in potential and the hours of reflux of the sol, Figure 4.26. The built-in potential results from the transfer of electrons at the interface until no more transfer can take place. A reduced built-in potential is observed across the series. The movement of charge should be the approximately the same as the bulk properties in terms of relative energy levels are similar, so the same driving force for the formation of the depletion region would be expected. Without reliable estimates of area, the number of dopants cannot be estimated from this data alone, it would appear there is a large change in the surface dipole.

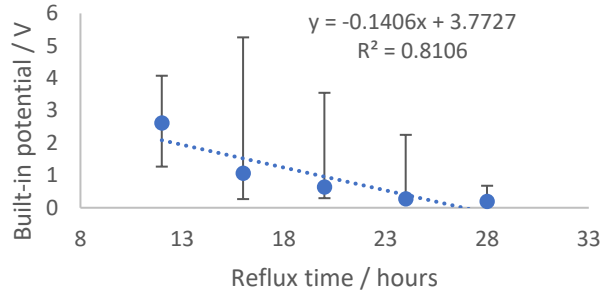


Figure 4.26: Measured built-in potentials for devices fabricated with sols with increasing reflux, showing a smaller built-in potential for higher reflux times.

Similar to the capacitance measurements, this may suggest there is a dipole forming at the interface and would suggest these states are negatively charged, to oppose the dipole formed from the separation of charge in the formation of the Schottky barrier. This could be coherent with the speed studies, whereby slower speeds result in more ohmic behaviour, as the defects that accumulate under forward potential at the Schottky barrier interface would be expected to be positive as the TiO<sub>2</sub> film is relatively negative under forward bias. Further, from the results above, there are more of these states following the extended reflux of the sol, illustrated in Figure 4.27.

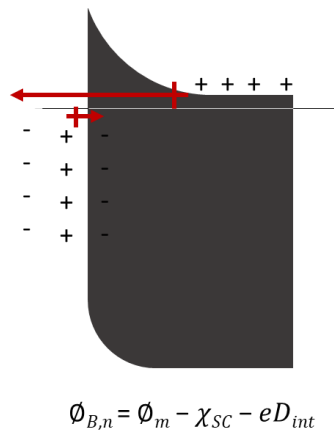


Figure 4.27: Demonstrating a model of apparent Schottky barrier height, whereby its height is hypothesised to be related to the Schottky-Mott estimate of height, minus the impact of a dipole at the interface.

#### 4.3.12. Summary of sol results

The more reliable estimations of area are shown in Table 4.5, from thermionic emission. The capacitance studies that have reliable areas from thermionic emission, results in higher estimates for the depletion regions than the above example. These are several microns in several cases, which is likely to be an overestimate.

Sample	Area / $\mu\text{m}^2$	Built-in potential	Defect density estimate / $\text{cm}^{-3}$	Depletion region width / nm
1	9.7	0.003	$6.3 \times 10^{12}$	1040
2	2.1	1.411	$2.1 \times 10^{18}$	36
3	0.2	1.347	$1.4 \times 10^{20}$	4
4	82	4.191	$5.8 \times 10^{14}$	3793
5	124	2.912	$4.0 \times 10^{14}$	3809

Table 4.6. Estimates for built-in potential, defect density estimate and depletion width for Batch 4 samples from Table 4.3, using thermionic emission fit estimates for area.

#### 4.3.13. Comparison to TiN derived devices

TiN derived devices show an unusual capacitance, with a very small capacitance measured near 0 V, but a linear capacitance measured on the application of a small bias. From Figure 4.28, the smallest value is approximately  $1.8 \times 10^{-10}$ , similar to 4 other devices at 0 bias.

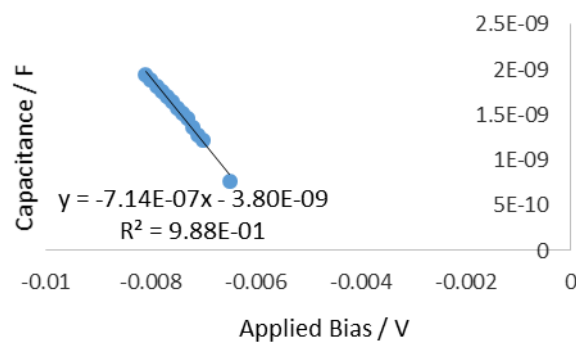


Figure 4.28: Capacitance for applied potential for a TiN derived device.

These are lower in capacitance than the  $2.1 \times 10^{-9}$  F for a sol based device. Given the high efficiency of TiN derived devices, this is an unexpected result. The  $\text{TiO}_2$  layer formed would be expected to have at least a similar dielectric constant to that of the sol devices, if not, higher due to the expected higher

crystallinity of the films formed on TiN due to the higher temperatures and times of preparation. The defect density is estimated to be lower from the capacitance studies, consistent with a higher photocurrent. The change in the capacitance over this applied potential is also much greater for the TiN device than the sol based device. However, for all the TiN devices, the measured built-in voltage is low.

The birefringence of the TiN surfaces and the lack of an observable  $\text{TiO}_2$  peak from XRD under the same conditions as the sol film suggest the  $\text{TiO}_2$  film is much thinner, on the order of hundreds of nanometres, which may explain the low capacitance. As discussed in the previous section, much of the capacitance for the sol derived devices is likely due to the defects, which are expected to be plentiful on the sol devices.

Estimating the depletion width using the parallel plate capacitor equation for a TiN based device from a small capacitance with the extremely small area estimates from thermionic emission theory, results in an unfeasibly large distance.

Only one sample can be used for both studies, with a small calculated area with a poor thermionic emission fit,  $0.0101 \mu\text{m}^2$ . With a capacitance measured of  $2.38 \times 10^{-11} \text{ F}$ , resulting in a width estimate of 68 nm. However, within an applied bias of a few millivolts, this falls to  $1.25 \times 10^{-9} \text{ F}$ , resulting in a width of 1.28 nm.

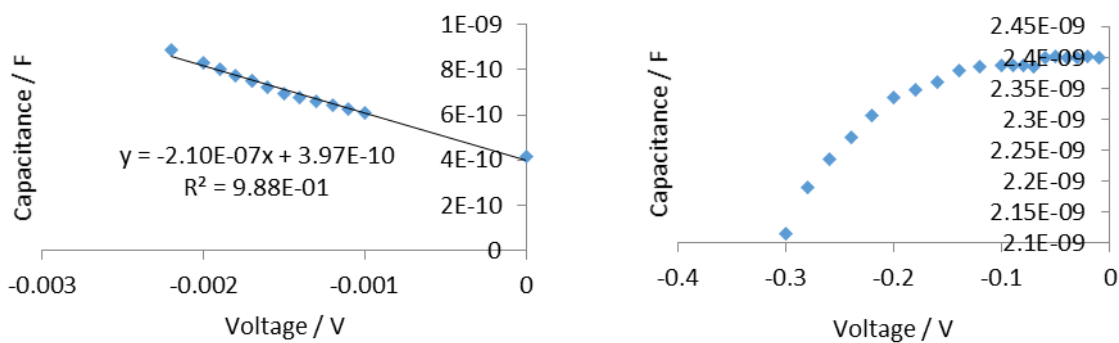


Figure 4.29: Left; TiN derived device capacitance with applied bias, right; sol derived device at applied bias, showing decreasing capacitance, as expected, with applied potential.

The capacitances increase rather than decrease with applied potential, Figure 4.29. The dramatic change in capacitance with applied bias is not

likely to be due to an increase in the width of the depletion region. The estimate of TiN from the  $(1/C^2)$  vs  $V_R$  devices would suggest a much lower concentration of defects than that for the sol device, consistent with the higher photo-efficiencies of these devices (Chapter 5 and 6), the birefringence and the IV curves. Further, the capacitance is *increasing* with applied potential. There would be expected to be involvement of other parts of the device in capacitance. Capacitance is equal to  $dQ/dV$ , so as an estimate, the change in capacitance from a device of  $2.1 \times 10^{-7}$  F/V is equal to the change in charge over the distance of 1.28 nm from the thermionic emission fits for area, and assuming a single charge on each dopant, this corresponds to a profile of  $2.05 \times 10^{18}$  m<sup>-1</sup>, or  $2.05 \times 10^{22}$  cm<sup>-3</sup>, equal to  $\sim 2/3$ rd the number of atoms. This is the number of charge carriers to compensate for the applied potential, to compensate for the potential, an unrealistic density of dopants.

The build-up of charge may result in this capacitance. The rapid change in capacitance could be due to the occupation of surface states, particularly the nitrogen doping states from the TiN proximate TiO<sub>2</sub> to the silver nanowires across from the low defect TiO<sub>2</sub> region. A change in surface states has been reported for a Al/methyl red/p-Si device for a 0.12 V change in potential results in a 30 fold increase in surface states. This is still much lower and is likely to be the occupation of surface states.<sup>163</sup> This is much larger than the above change in density. The device may be better described by metal-insulator-metal model.

Another difference in the capacitance in these devices is the lack of change with water. The capacitance is much lower than in the sol films, though following water deposition, there is very little change in the TiN devices. This is possibly due to a lower defect surface, therefore showing less passivation, whilst the water-passivated sol device shows a similar capacitance to the native TiN device.

#### 4.4. Conclusions and future work

The changing characteristics of the device in the presence of water, drastically reducing the series resistance. Further, the IV curves change with exposure to water and UV light, suggesting dissociation of water, leading to the passivation of surface states. This leads to the observation of higher Schottky barrier heights. That the current isn't being inhibited is evident

from measuring the device at higher potential, reverting to resistance dominated by series resistance by 1.2 V.

This change in electrical characteristics makes thermionic emission studies difficult. There are a small number of fits whereby good fits to the reverse saturation currents can be measured across a range of temperatures. Only some of these studies result in good fits to thermionic emission theory. Of these, the area estimates result to logarithmic fits, resulting in estimations of areas on the scale of square microns. For TiN devices, there many thermionic emission fits which also give similar estimates. This is below the estimations of the product of TiO<sub>2</sub> coverage and silver nanowire coverage for these devices. The low active areas of these devices are predictable from the low photocurrents.

The capacitances of the sol devices increase across the series. The capacitance of the sol devices with water deposited are similar to the lower defect TiN devices. This is concurrent with a decreasing built-in potential, possibly due to the defects forming a large dipole between the defects on the semiconductor and the metal contact.

Whilst exact figures have been difficult to obtain, those devices which demonstrate both a good fit to thermionic emission theory, by fitting to the ideal diode equation at a range of temperatures, followed by reasonable values of capacitance, results in estimates for dopant densities that are high relative to bulk crystalline TiO<sub>2</sub>, a not unexpected result. Further, these measurements have allowed for the estimation of depletion widths for several devices, allowing estimations of efficiency which were of use in Chapters 5-7.

One notable feature of the devices as they were cooled after annealing was that the films were yellowish before they cooled. Above temperatures at which water is desorbed, this could be due to the formation of vacancies at these higher temperatures and may provide a useful knowledge of the likely numbers of these defects at lower temperatures by use of a partition function and observation of these films at high temperature with UV-vis spectroscopy.

# 5. Chapter Five: Photocurrent from band gap excitation in Schottky barrier devices

## 5.1. Overview

A working Schottky barrier photovoltaic device on stainless steel can be made as detailed in Chapter 4. Devices that respond to visible light were also demonstrated using N-doped Ta<sub>2</sub>O<sub>5</sub>, TaON and quantum dot films. Higher efficiency devices were formed by sintering for shorter time periods, attributed to the lower concentration from metal dopants that diffuse from the substrate. Also, literature on TiN powders showed that oxidation at 500 °C for extended periods resulted in an efficient TiN/TiO<sub>2</sub> catalyst. This method was used to oxidise commercial TiN coated steel, demonstrating both high photocurrents and rectifying properties, showing a good fit to a direct excitation and a Tauc plot intercept of 3.26 eV, as expected for anatase TiO<sub>2</sub>.

From Chapter 4, the areas estimated from thermionic emission theory are often very small. The active area of the device can be improved through drop casting TiO<sub>2</sub> sol onto a completed device, increasing the amount of TiO<sub>2</sub> in contact with silver nanowires. However, further depositions can result in poorer results, potentially due to upper layers obstructing UV light reaching active parts of the device or due to damage to the silver nanowire mesh. Comparing areas to efficiency, the depletion regions would appear to be

efficient at separating charges. However, when water is used at the contacts, the efficiencies are no longer tenable, suggesting the area that is active in current production is much higher when water is present.

## 5.2. Introduction

The methods of manufacturing Schottky barriers are diverse offer opportunity for new architectures. However, the formation of defects is usually used to explain the low Schottky barrier heights, resulting in a much lower power output than would be expected.

Some high efficiency quantum dot devices have been described which absorb in the visible and IR range. This tends to show that treatment and sintering of the nanoparticles, for instance to remove insulating long chain ligands, is important for high efficiency. In the UV region, many of the high purity crystalline devices show high internal quantum efficiencies, suggesting that when photons are absorbed within the depletion region, separation is very efficient. Electrical characteristics of the devices made here show reverse saturation currents and predictable Schottky barriers. There is an impact of speed measurements on the current-voltage measurements show that the device tends to be more ideal at higher scan speeds. The area studies from thermionic emission suggest active areas for absorption is low. A TiN device showed a large depletion region due to lower defects, the low efficiencies here are likely to be due to the low active areas of such devices.

### 5.2.1. The limitation to efficiency of $V_{OC}$ to Schottky barrier devices

The low efficiencies of Schottky barrier devices are usually attributed to the low and unpredictable Schottky barrier heights, which limit the open circuit voltage of the device, for instance, regardless of the choice of metal Schottky barrier heights on  $Cu_2O$  were 0.7-0.9 eV, due to a large density of states at the interface.<sup>164</sup> This limits the efficiencies of the devices despite the relative ease of forming large single crystals and having a near optimum visible band gap. This results in relatively good efficiency  $Cu_2O$  Schottky barrier devices typically being reported with efficiencies lower than 1%. In an early analysis (1979), efficiencies could be increased to 1.5% with antireflection coating if high shunt resistances can be achieved.<sup>164</sup> However, substantive improvements in efficiencies of these devices still has not been achieved.

### 5.2.2. Contributions to photocurrents in TiO<sub>2</sub> Schottky barrier devices

Much of the work on Schottky barriers formed on semiconductors shows the predicted photocurrent response that rises at the band gap of the material and then plateaus. For an anatase TiO<sub>2</sub> nanowire array over a thin film rutile substrate over p-type Si, with Ag contacts, the photoluminescence is best described by 4 contributions to the photocurrent, one that peaks at 2.66 eV, thought to be due to the excitation of electrons from oxygen vacancies, one from the inter-band transition in the TiO<sub>2</sub>, due to e<sup>-</sup> h<sup>+</sup> recombination at oxygen vacancies, and contributions from the rutile (3.1 eV peak) and anatase (3.3 eV peak) transitions. A similar set of peaks are seen in the responsivity of the device. The slight blue shifting of the positions of the peaks relative to where they would be expected is proposed to be due to the confinement effect in these nanostructures.<sup>152</sup>

### 5.2.3. Quantum dots

Some of the first results presented here use solution processed quantum dots to absorb in the visible region. Quantum dots can have smaller band gaps than the bulk materials due to confinement effects. They are available in a range of architectures, shapes and sizes, changing their optical properties.

Due to their exceptional optical properties such as tuneable absorption and fluorescence, Cd based quantum dots are available in a range of architectures in a range of sizes and with a range of ligands and have been studied for solar cell applications. Literature reports suggest electron injection into TiO<sub>2</sub> occurs on the 1-100 ps timescale, depending on the offset of the quantum dot and the TiO<sub>2</sub> conduction bands.<sup>165</sup> However, as well as tuning the absorption onset with size and shape, the position of the bands can be tuned through choice of ligand.<sup>166,167</sup> One of the technical challenges in quantum dot solar devices is the use of electrolytes, whilst the polysulfide electrolytes used typically in these devices can passivate oxidative damage on sulphide or selenide based materials, this can be relatively slow, resulting in the accumulation of holes. Similarly, iodide electrolytes common in analogous dye devices result in rapid corrosion of the quantum dots.<sup>168</sup>

## 5.2. Results

### 5.2.1. Visible light photocurrents from semiconductors

It is possible to use a light absorbing semiconductor in place of the UV light absorbing  $\text{TiO}_2$  with the same silver nanowire Schottky barrier architecture. This section details how an experimental material made with TaON and visible light absorbing quantum dots, could be used to make a Schottky barrier photocurrent device.

#### 5.2.1.1. TaON

These devices were made by simply suspending the TaON material (see Chapter 3) in acetic acid followed by dip coating. Optimisation and repeats were not possible due to a lack of material, however, Table 5.1 and Figure 5.1 show the photocurrent responses.

Device	PI peak (nA)	Peak position (nm) (+/- 10 nm)	Intercept from Abs plot (nm)
1	1.65	390	502
2	6.7	380	508
3	9.6	400	476

Table 5.1: Photocurrents, peak position and Tauc plot intercept for three TaON devices.

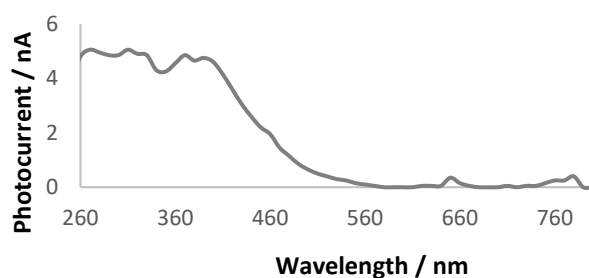


Figure 5.1: TaON device photocurrent, demonstrating an onset at  $\sim 560$  nm, showing this architecture is compatible with visible light absorbing semiconductors.

The small currents of these devices are expected given the lack of optimisation and what is likely to be due to a very thick film of TaON. Further, this is heavily nitrogen doped in order to absorb in the visible region, potentially increasing recombination. However, this being the case, it still demonstrates that a Schottky barrier device can function in the visible region

with use of visible light absorbing semiconductors, despite their heavy doping. The heavy doping could result in a narrow depletion region which might need a higher coverage of silver nanowires being required.

In the TaON device, the absorption above the band gap plateaus. There is a good agreement between the indirect Tauc plots from the UV-vis spectra of the material (intercept: 559 nm,  $R^2$ : 0.993) and the same plot for the photocurrent (intercept: 559 nm,  $R^2$ : 0.987). The indirect fits were a better fit than the direct fits of photocurrent and absorption.

#### 5.2.1.2. CdSe, CdS and CdTe

Quantum dots have been used previously on oxidised titanium Schottky barriers fabricated from silver nanowires, and show a visible response and a sensitivity to post-fabrication treatment.<sup>133</sup>

Here, they are used as the semiconductor in the Schottky barrier architecture with little success. The dots were spun coat into layers, then they had to be annealed to remove the organic (insulating) ligands. These tended to be long chain ligands used to solubilise the particles in an organic solvent and prevent agglomeration. The fabricated devices were passivated with tartaric acid, resulting in a measurable photocurrent in the visible region though dwarfed by the UV response, Figure 5.2. The contribution of the tartaric acid is due to the passivation of the surface, by bonding to  $Ti^{3+}$  surface states by the acid groups.

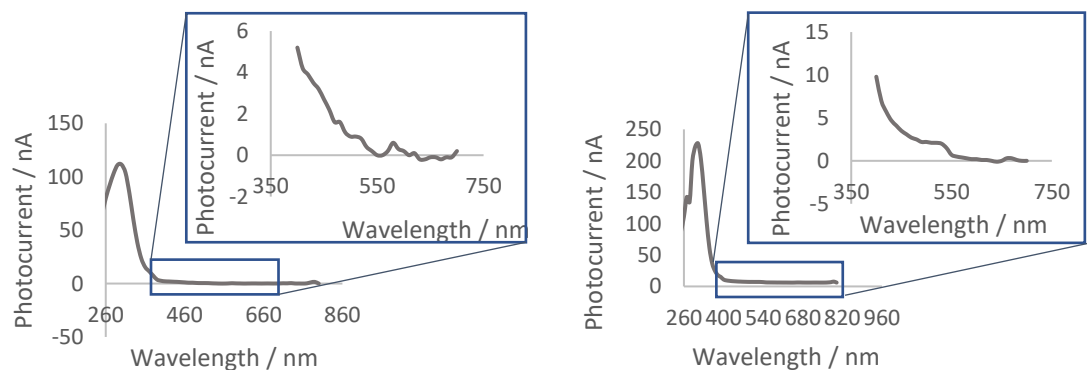


Figure 5.2: Photocurrent response of devices fabricated through spun coat films of CdS suspended in toluene. Following fabrication, the devices were passivated with tartaric acid.

This is not a feasible approach for the large scale production of devices but it does demonstrate a working architecture. Similar work has been described in quantum dot films as described in the literature review.

### 5.2.2. UV photocurrents

Increasing crystallinity in devices

As discussed in Chapter 3, one of the technical challenges in forming Schottky barriers on steel is that metal diffusion prevents the formation of the Schottky barrier. To combat the need to heat the sols for an extended period on the substrate, a solvothermal method was used to produce more crystalline sols.

Figure 5.3 shows that the photocurrent tends to be higher for sols which had undergone an 8 hr reflux step. From Chapter 3, it can be seen from the XRDs that the sol is far from highly crystalline and the size of the crystallites is likely to be small.

These sols result from a reflux of the sol for 8 hours in isopropanol. However, isopropanol refluxing temperature is 82.6 °C. As discussed in Chapter 3, crystallisation was found in the literature to increase drastically above 80 °C and water can catalyse the transition to anatase phase.<sup>169</sup> A simple expedient is to use a solvent with a higher boiling point solvent. Water was used and higher efficiencies were found for these devices, compared to controls refluxed in IPA, Figure 5.4.

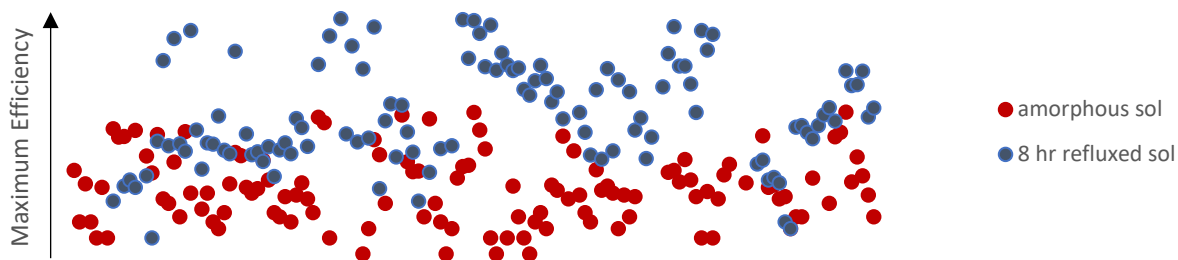


Figure 5.3: A range of methods were used in the attempt to improve photocurrents for a range of devices, however, in general devices that had undergone an 8 hour reflux step showed higher photocurrents.



Figure 5.4: Maximum efficiency for a range of comparable devices fabricated from an IPA refluxed sol compared to a water refluxed sol showing higher photocurrents in general for devices fabricated from sols refluxed in water rather than IPA.

To measure the impact of the time of reflux, a sol was refluxed for 8 hours to 32 hours with samples removed in 4-hour intervals. As discussed in Chapter 3 and 4, the crystallinity of the sol increased drastically, but as did a likely strain or number of defects. There were often two photocurrents in opposing directions as discussed in Chapter 6. The photocurrent in the direction of excitation across the band gap increases across the series, Figure 5.5.

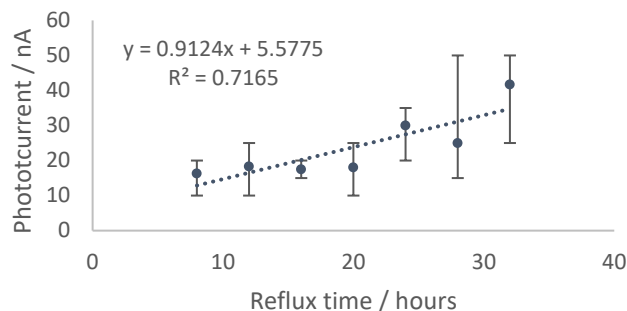


Figure 5.5: Photocurrent of devices of increasing crystallinity and defect density showing increasing photocurrent with duration of reflux time, error bars show the range of device photocurrents.

This is not a strong correlation given the increase in crystallinity and crystallite size in this series (Chapter 3, Figure 23). In an attempt to correlate dopant density with photocurrent, capacitance measurements were compared to the photocurrents for this series and showed no correlation, though this may be due to the different active areas of the devices.

#### Deposition of TiO<sub>2</sub> on silver nanowires

There is need to improve the geometry of the devices. Further, from capacitance studies, the depletion regions extend several hundred nanometres around the nanowires, providing an area of functionalisation, Figure 5.6.

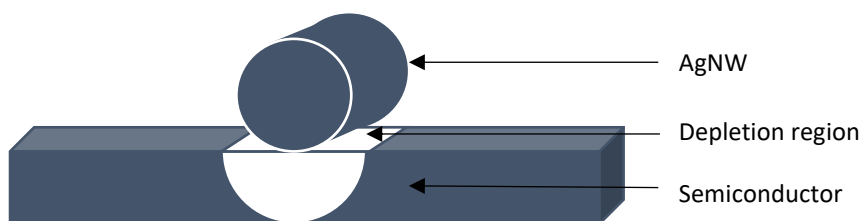


Figure 5.6: Demonstrating the typical depletion region shown around a silver nanowire (AgNW) contacted on a semiconductor.

Solvothermal methods are potentially compatible with the production of silver nanowires and a range of architectures and fabrication methods could be possible by fabricating complete silver nanowire films followed by the growth of TiO<sub>2</sub> films. As discussed in Chapter 4, there are approximately  $3 \times 10^9$  silver nanowires on each cm<sup>2</sup>, corresponding to a surface area roughly 60 times the geometric area of the device which could be functionalised. The semi-transparency of the device could mean a greater density of wires could

be supported or a series of layered devices could be produced on thin substrates.

Following deposition of sol over the silver nanowires, illustrated in Figure 5.7, there is also an improvement in the efficiency, Figure 5.8, though not as large as might be expected from the improvement to the geometry of the device.

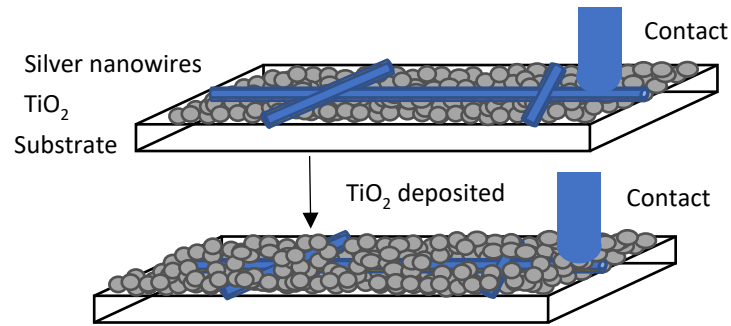


Figure 5.7: Schematic of deposition of  $\text{TiO}_2$  sol on a device to show how  $\text{TiO}_2$  could be used to improve the active area of the device.

The flaw in this method is the possibility of too much  $\text{TiO}_2$  being deposited, resulting in UV absorption outside of a depletion region, this was seen for two sol depositions, with  $10 \mu\text{L}$  of sol often showing poorer results than  $5 \mu\text{L}$ . There is another problem in this geometry, the sintering of the  $\text{TiO}_2$  particles must be performed in such a way that the silver nanowire mesh is maintained, therefore, it must occur at low temperature and involve a highly crystalline sol.



Figure 5.8: Peak UV efficiency for a range of the same devices, showing a generally higher efficiency following deposition of  $5 \mu\text{L}$  of sol.

This was also the case for the higher efficiency TiN devices, Figure 5.9.

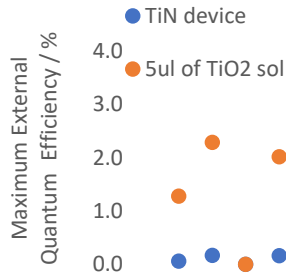


Figure 5.9: TiN photocurrents for a range of devices. The deposition of 5 μL of sol onto the same devices mainly resulted in higher efficiency devices.

The Figure 5.10 below shows the relative improvement in TiN and TiO<sub>2</sub> sol devices following the deposition of a sol. The TiN devices generally improve more but are similar to the TiO<sub>2</sub> devices. The improvements are much higher for the TiN devices than the sol based devices, Figure 5.10, the low series resistance and high Schottky barriers may result in the high efficiencies of the deposited sol.

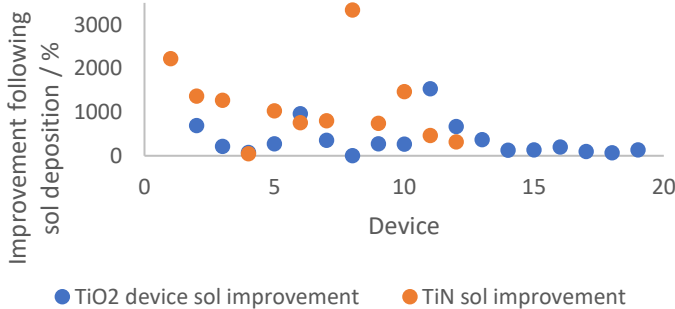


Figure 5.10: Percentage improvement to the photocurrents for a range of TiO<sub>2</sub> sol and TiN derived devices, showing that typically, photocurrent response increases more drastically for TiN devices.

### 5.2.3. Improving UV efficiencies by layered structures

There is a need to create functionalised silver nanowires with the minimum amount of crystalline TiO<sub>2</sub>. As there is a need to rapidly screen methods for their suitability, a change in architecture was attempted whereby the advantage of the semitransparency of the nanowires can be utilised by the stacking of numerous layers.

TiO<sub>2</sub> sols were used to contact the silver nanowires to the ITO substrate, to counter the lateral resistances through the TiO<sub>2</sub> film. The contacts were pressed together and dried at 100 °C for 30 minutes, in an architecture illustrated in Figure 5.11. Though some few of the devices showed some

rectification, photocurrents were always absent. This could be due the low of UV transparency of both sandwiching materials.

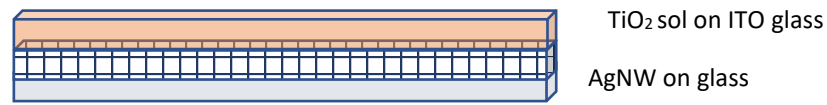


Figure 5.11: Schematic of attempts at architecture allowing for transparent devices that could be stacked.

This architecture makes short circuits possible between not fully covered silver nanowires and the ITO substrate, but can also lead to the opposite, with a lack of connectivity through the  $\text{TiO}_2$  sol and high series resistance.

To avoid the problem of reliably forming the ohmic contact with  $\text{TiO}_2$ , the base of a working device was chosen to improve upon. To do this, silver nanowire and  $\text{TiO}_2$  sol were alternatively deposited and annealed, Figure 5.12.

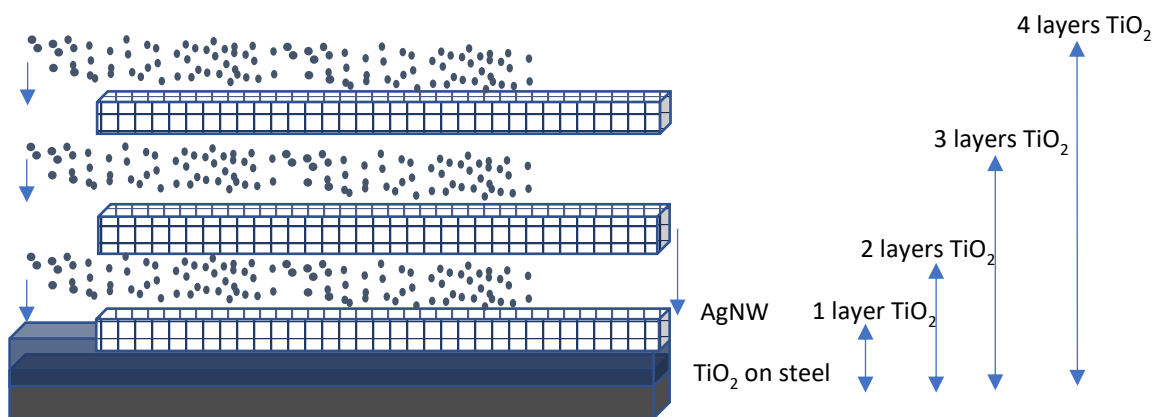


Figure 5.12: Schematic of attempts at using a stack of silver nanowire architectures.

From transparency studies performed, an approximately 70-80% transmittance for a low resistance film on glass in the visible region has been fabricated.<sup>49</sup> For this reason, the maximum amount of layers would not be expected to exceed 4 for a high efficiency device. A more dilute concentration of AgNW was used in order to reach the edges of the sample to ensure contact with the previous layer (right hand side of Figure 5.12)

Figure 5.13 shows average values and the range of results for devices fabricated in this way for the devices, left and the devices under water, right.

This shows there is a weak correlation between the number of layers and the photocurrent. This suggests that improving the active area of the device can be improved to some extent by depositing sol on silver nanowires.

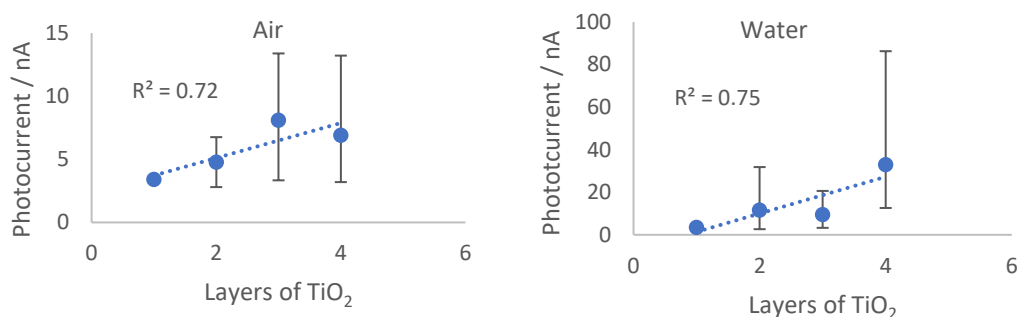


Figure 5.13: Photocurrent measurements for a range of devices, average with bars to show the range of measurements for those devices. Left; photocurrents in air, right; following passivation with water.

Though this methodology could be improved through optimisation of the density of the silver nanowire mesh and the TiO<sub>2</sub> sol, the temperatures used for sintering, the method of deposition and the nature of the sol used. At some point, when all the light has been absorbed, any extra layers will be redundant. Also, the eventual functionalisation with dye will have a different sensitivity to the number of layer, due to the impact of wavelength dependent scattering.

#### 5.2.4. Impact of silver structures

The estimations of areas are small and for this reason, many attempts were made to improve the active area in an attempt to improve efficiency. Literature on the fabrication of large area silver structures include methods such as the use of silver nanoparticle electrodeposition. Silver nano-trees have been grown from nanoparticles into the pores of a TiO<sub>2</sub> scaffold to demonstrate this approach.<sup>170</sup> Reduction of silver directly from precursors is also possible, it has also been demonstrated that sulfate ions can rapidly accelerate the growth of dendritic structures in precursor solutions on copper foil.<sup>171</sup>

However, electrodeposition often resulted in short-circuited devices despite a range of methods and precursors being used. To facilitate silver formation on the TiO<sub>2</sub> surface rather than short circuiting the device, attempts were also made at soaking films in AgNO<sub>3</sub> and reacting them with reductants such

as ascorbic acid, citric acid and  $\text{CuSO}_4$  and illumination with UV light. These methods were also unsuccessful. This could be due to the reduction of the  $\text{TiO}_2$  surface resulting in more defect states and lowering the Schottky barrier.

In support of this, one of the few successes came from results where the  $\text{TiO}_2$  had been treated with ammonia to yield a negatively charged hydroxylated surface, followed by the deposition of  $\text{AgNO}_3$ , whereby a photovoltage was measured and showed a peak in the visible region, Figure 5.14. This could also be the result of the formation of ammoniacal silver in the proximity of the  $\text{TiO}_2$  surface. As nanoparticles of silver can absorb light at a range of frequencies, this would be an added benefit to improving the efficiencies through the growth of silver nanostructures.

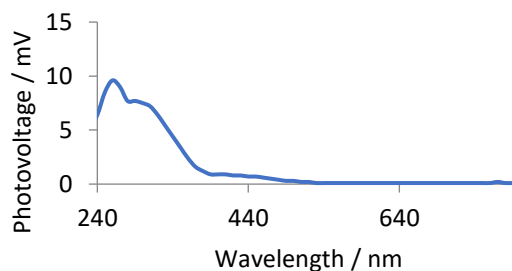


Figure 5.14: Showing a small photovoltage response for a device treated with  $\text{AgNO}_3$ .

Often the controls in the electrodeposition experiments outperformed the silver deposited devices. This was attributed to the change in surface conditions such as the oxidation of contaminants or surface states. It was found that applying 3.0 – 4.5 V with the  $\text{TiO}_2$  film as anode in water improved the photocurrent. This may be due to the oxidation of organic species at the interface or oxidation of  $\text{Ti}^{3+}$  defect states. Applying the opposite potential resulted in poorer results.

To prevent the short circuiting of the device and to improve surface area, an attempt was made to encourage growth of silver dendrites laterally along the device, a sacrificial copper contact was made to the  $\text{TiO}_2$  followed by the deposition of  $\text{AgSO}_4$ , Figure 5.15.

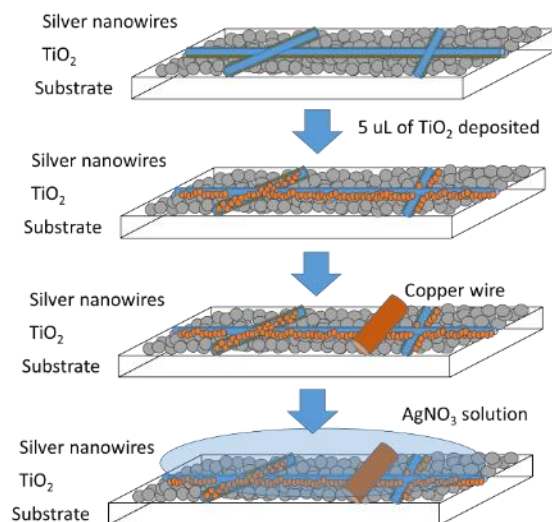


Figure 5.15: Diagram to demonstrate fabrication of devices for the attempt to grow silver structures laterally across the surface to avoid the problems of short circuiting.

Figure 5.16 shows this method results in a small amount of improvement to the devices. However, it has also been shown that reducing  $\text{AgNO}_3$  at the junctions of silver nanowires can reduce contact resistance in silver nanowire meshes,<sup>172</sup> as such, improvements from this method could result from silver sulfate reduction resulting in reduced series resistance or changes to the surface states such as passivation. An SEM study of the wires would need to be used to determine whether the silver nanowires can grow dendrites.

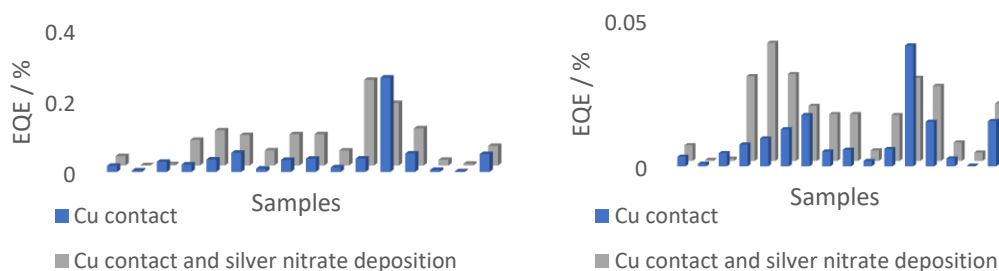


Figure 5.16: Impact of  $\text{AgNO}_3$  deposition on a series of devices, showing generally the photocurrent efficiencies were improved for treated devices in the UV region (left) and visible region (right).

### 5.2.5. Impact of sintering time

As discussed in Chapter 3, a range of temperatures and time has been reported for sintering nanoparticulate TiO<sub>2</sub> films, to achieve a low resistance and crystalline film.

However, there is also the impact of metal diffusion. For the increasing sol time, the 8 hr IPA refluxed sol was annealed at 350 °C for up to 4 hours. The maximum UV efficiency decreases with extended annealing times, Figure 5.17.

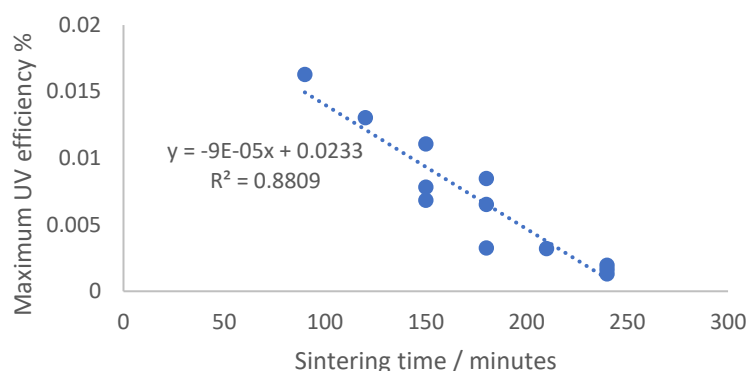


Figure 5.17: Maximum photocurrent efficiencies for increasing annealing times for a range of devices, demonstrating lower UV efficiencies for extended sintering times.

As the TiO<sub>2</sub> film would be expected to be becoming more continuous and more crystalline, this is attributed to metal diffusion. This is consistent with the challenge in forming rectifying rather than ohmic junctions.

### 5.2.6. TiN/Steel samples for higher efficiency devices

The 6-hour method was used for most TiN derived devices, as in the series of increasing annealing time, it resulted in the most diodic devices.

For devices manufactured on TiN the current tended to be predictably large and in the direction of excitation across the Schottky barrier (discussed in Chapter 6). Furthermore, direct Tauc plots show a good direct fits to a typical photocurrent response and a direct band gap intercept of 3.26 eV, close to the indirect band gap of anatase TiO<sub>2</sub>, 3.2 eV, demonstrated in Figure 5.18.

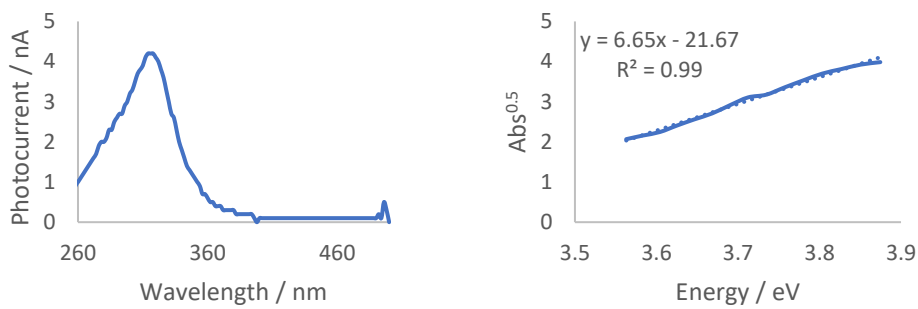


Figure 5.18: Photocurrent (left) and direct Tauc plot for photocurrent measurement (right).

Responses of a range of these devices photocurrents, following functionalisation with water are shown in Figure 5.16, demonstrating higher photocurrents.

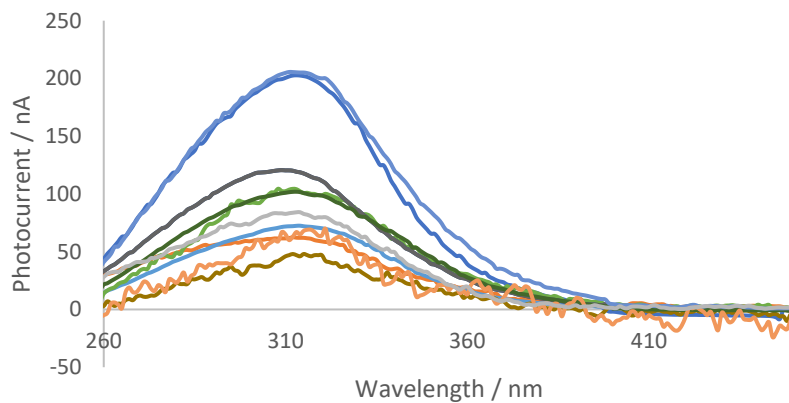


Figure 5.19: Photocurrents for a range of devices with water showing high photocurrents and a predictable response above the band gap.

The TiO<sub>2</sub> devices may contain many fewer defects at the interface due to the extended high temperature annealing used in their manufacture, as is estimated from capacitance measurements (Chapter 4). A slow cooling stage was found to be necessary for the formation of rectifying devices on TiN, which may also help with the formation of low defect states films and prevent cracking of the TiO<sub>2</sub> layer. However, there may still be oxygen vacancies having an impact on the surface, which are passivated by the presence of water or oxygen. Soaking the device in anatase sol gave current improved 16 to 67 times for three similar devices, the use of tartaric acid increased these

further, suggesting they are also sensitive to the improvement to geometry discussed in the previous section.

### 5.2.7. Reduction of series resistance with spun coat dense layers

One of the characteristics of the TiN derived devices is that the series resistance is very low. A spun-coat dense TiO<sub>2</sub> device was fabricated using a method similar to a literature method,<sup>79</sup> and the dense TiO<sub>2</sub> layer was sintered, to give a low resistance device. Many of the devices were ohmic. For the working devices, the series resistances were around 50 Ω, similar to the TiN based devices. This may be due to the contribution of the silver nanowires to the resistance. The photocurrents were similar to sol based devices and not on the same order of magnitude as TiN derived devices. Some typical photocurrent responses are shown in Figure 5.20.

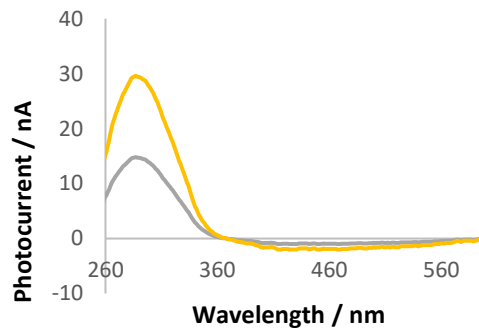


Figure 5.20: Showing the highest photocurrents achieved for a dense spun coat layer of TiO<sub>2</sub> demonstrating a smaller photocurrent than those measured for TiN derived devices.

The higher photo-efficiency of the TiN devices is not accounted for by their much lower series resistance. Similarly, for many hundreds of modelled devices and measured photocurrents, there was no correlation between the estimated series resistance and the photocurrents measured.

### 5.2.8. Area estimates to calculate efficiency

As discussed in Chapter 4, Section 4.15 it has been difficult to estimate a typical active area of such devices, and the most reasonable estimates correlate with a poor estimate for the barrier height.

However, from Table 4.3 and 4.4, the best estimate is that of tens of square microns. Using one of the best thermionic fits, with an area of 82 μm<sup>2</sup>, the

permittivity of the TiO<sub>2</sub> samples to be low at 19 as for a similar film and within the ranges reported for TiO<sub>2</sub> films, it is possible to estimate dopant density of  $5.8 \times 10^{14} \text{ cm}^{-3}$ , as discussed in Chapter 4.<sup>158,159,173</sup> This is comparable to literature values, for instance, in a DFT study, a typical O vacancy/OH defects were estimated at  $5 \times 10^{13} \text{ cm}^{-3}$ .<sup>174</sup> The higher value of defect density in the samples made here would be expected to be higher than a rutile crystal. Compared to literature, where these distances are reported to be less than 1  $\mu\text{m}$ ,<sup>43</sup> a film is made of colloidal PbS films on aluminium had a depletion region width of 90-150 nm.<sup>161</sup>

Simply considering these areas with regard to the photocurrents, taking a photocurrent for a device of  $4 \text{ nA cm}^{-2}$  and the area under discussion of  $82 \mu\text{m}^2$ , this results in an untenable current density of  $4.9 \text{ mA cm}^{-2}$ , considerably higher than a commercial Si photodiode of  $239 \mu\text{A / cm}^{-2}$ .

For the area calculation, the depletion region calculation was as described in Chapter 4 as 3793 nm for this device area, made of 60 nm wide silver nanowires with a pentagonal profile, this results in a contact area of 41.5 nm.<sup>49</sup> These calculations use the highest possible depletion region and estimating none of these areas overlap, this is in order to underestimate efficiency.

For a  $82 \mu\text{m}^2$  device, this results in an equivalent 50.6  $\mu\text{m}$  lengths of 41.5 nm wide silver nanowire contacts. Assuming each nanowire does not overlap and has a depletion region width of 3793 nm (Table 4.5) results in a total depletion area of  $2047 \mu\text{m}^2$  as well as the contact area of  $82 \mu\text{m}^2$ , this measurement is illustrated in Figure 5.21.

This gives a density of  $4 \times 10^{-9} \text{ A}$  in an area of  $2.1 \times 10^{-5} \text{ cm}^{-2}$ , or  $0.195 \text{ mA cm}^{-2}$ , or  $195 \mu\text{A / cm}^{-2}$ , slightly less than the Si photoanode. Adjusting the 0.00021 % EQE for photons hitting the device in the depletion region results in an 10.4 % efficiency. This is reasonable compared to similar Schottky barrier devices (Chapter 2) and demonstrates the importance of active area. It may be an underestimate as the silver nanowire depletion areas would be expected to overlap.

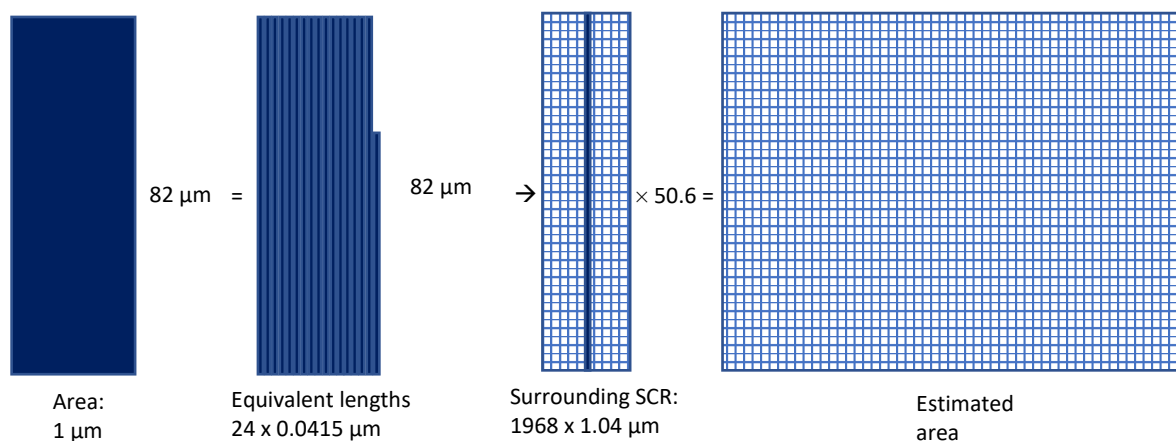


Figure 5.21: Illustrating the estimation of depletion areas from the width of silver nanowires and depletion region from capacitance measurements.

The results converging from thermionic emission, capacitance and photocurrents are in accord with literature and consistent with each other. Though the exact area proposed here is likely to be an underestimate, a value of several hundred square microns is a reasonable value. This suggests the efficiency is high in the depletion regions. This shows the vast potential for efficiency in the surface areas of these devices.<sup>161,174</sup>

### 5.2.9. Efficiency estimates from area measurements

For TiN devices, a range of EQE values could be calculated, Table 5.3.

Area / microns <sup>2</sup>	Photocurrent / nA	EQE 330 nm / %	Photocurrent / nA (w/ water)
1.01 x 10 <sup>-2</sup>	17.2	0.15	223.5
2.22 x 10 <sup>-1</sup>	12.1	0.50	755
3.28 x 10 <sup>3</sup>	41.1	0.46	697.2

Table 5.3: Efficiency at 330 nm and estimated efficiency from thermionic emission fit.

Using the areas from thermionic emission theory, the calculated internal quantum efficiencies for these devices prior to water deposition of some tens of percent and is similar to the maximum currents seen for dye-sensitization experiments discussed in Chapter 6. Following water deposition are 1459 x 10<sup>6</sup> %, 224 x 10<sup>6</sup> %, and 0.014 x 10<sup>6</sup> %, assuming a 500 nm depletion region.

However, from capacitance measurements following the application of a small bias to a TiN derived device results in a much lower defect density of

$7.2 \times 10^{11} \text{ cm}^{-3}$ , resulting an estimated depletion region width of  $43 \text{ }\mu\text{m}$ . This might help explain the dramatically higher photocurrents seen for devices such as these, as the effect of low defect density in these devices would be two fold, one that it prevents recombination and that the depletion region will extend further. However, from the improvements seen from sol deposition, the lower recombination outside of the depletion region and lower series resistance is also important.

Accounting for the depletion region does not fully account for the increase in photocurrent seen following water deposition. To account for an efficiency of 0.5% at 330 nm, or several percent for a titanium nitride device, suggests the depletion regions are not the only active regions for devices illuminated under water.

#### 5.2.10. Photocurrent under nitrogen

Although the use of passivating agents such as tartaric acid and water appear to increase the photocurrent, a study of photocurrent under nitrogen suggests that the absence of water also increases the photocurrent, Figure 5.22. The negative direction in Figure 5.22 corresponds to excitation across the band gap of the semiconductor and is discussed in Chapter 6.

However, the device is also under UV light. One possibility is that this is the same mechanism and the surface is being passivated by the “filling” of surface states by UV illumination. This light soaking mechanism has been used to explain why some photovoltaic devices increase in efficiency when exposed to light initially.

However, upon removal of the positive pressure of nitrogen, the photocurrent decreases again with zeroth order kinetics. It may be that even in these devices, the oxygen is being reduced some proportion of the electrons from the conduction band on excitation to form the  $\text{O}_2^-$  radical.

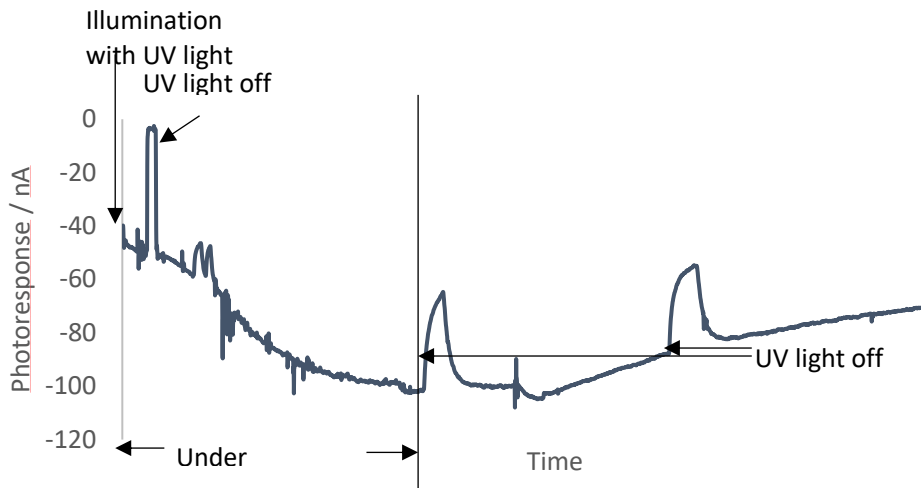


Figure 5.22: The magnitude of the photocurrent increases under nitrogen and illumination. On releasing the positive pressure of nitrogen, the photocurrent decreases in magnitude.

### 5.3. Conclusion

In conclusion, a visible photocurrent can be measured for a range of Schottky barrier devices fabricated from sols and by oxidising TiN films to TiO<sub>2</sub> resulting in a high photocurrent. Increasing sol refluxing time and crystallinity increases with annealing time as do photocurrents. Increasing annealing times generally results in lower photocurrents, attributed to metal diffusion.

Attempts to improve active areas were somewhat successful by the use of layers of AgNW and TiO<sub>2</sub> and depositing sols onto completed devices. This did result in some higher photocurrents. Attempts to grow more extensive silver structures were generally not successful though the high surfaces offered by dendritic structures and the increased visible absorption would make this a potentially useful line of inquiry. Some limited improvement was seen in attempts to grow silver structures laterally.

Thermionic emission studies suggest areas with the reasonable efficiencies for including the depletion region around the metal nanowires. However, following covering the device with water, the small areas calculated for these devices result in untenably high efficiencies, even assuming extensive depletion regions. This suggests there is another mechanism, such as photocatalysis.

# 6. Chapter Six: Competing photocurrent processes in the UV region

## 6.1. Overview

The previous chapter describes the improvements possible to the UV response of a Schottky barrier photovoltaic device. These methods outlined included improvements to the fabrication of the device such as repeated coatings of a relatively dilute sol and deposition of a sol over silver nanowires. The choice of temperature and substrate affects diffusion from the substrate and the crystallinity of the sol. As such, to ensure high crystallinity of the sol, a solvothermal method compatible with low temperature silver nanowire processing was developed.

Further, a method was developed of oxidising a commercial TiN coated steel in order to form a very thin TiO<sub>2</sub> layer, this resulted in a very efficient device. Most of these changes are predictable; higher crystallinity, lower diffusion and lower series resistance resulted in more efficient devices.

For many devices two photocurrents were observed in the UV region, in opposing directions. In this Chapter, the absolute directionality of the current was measured and some large currents in the opposite direction to that expected for direct excitation over the band gap were measured. This was often non-trivial, the current attributed to band-gap excitation was often

dwarfed by current in the opposite direction. This calls for a hypothesis that accounts for a direction opposite to that expected.

## 6.2. Introduction

The local potentials found at metal/semiconductor interfaces have been reported to be very high over small distances. Table 4.5 shows estimated built-in potentials at the Schottky barrier interface which on the order of several volts over what is undoubtedly a small area. This field accelerates electrons into the semiconductor in a Schottky barrier device. However, there is clearly a mechanism which drives electrons into the silver nanowires as evidenced by the direction of the photocurrent. The only other strongly absorbing species present is the silver nanowire mesh and whilst plasmon photocatalysis has been widely discussed in literature, in this case there seems to be an extremely strong dependence on how the device has been made and very little on the environment of the silver nanowires as studied by UV-vis (section 6.3.8).

This introduction concerns itself with the literature on plasmonic photocatalysis and photovoltaics. The results begin with assigning a convention for these results and a demonstration of opposing currents in the UV region, demonstrating how the absolute directionality of currents were arrived at, followed by Tauc plots that show absorption onsets for these processes for sols of increasing crystallinity. Many plasmonic systems studied are nanoparticles, these devices provides a system where direction can be measured, offering new insights.

Figure 6.1 shows the proposed mechanisms for the current direction by which electrons travel into the semiconductor. Figure 6.2 shows some hypothetical mechanisms for current resulting from electrons into silver nanowires.

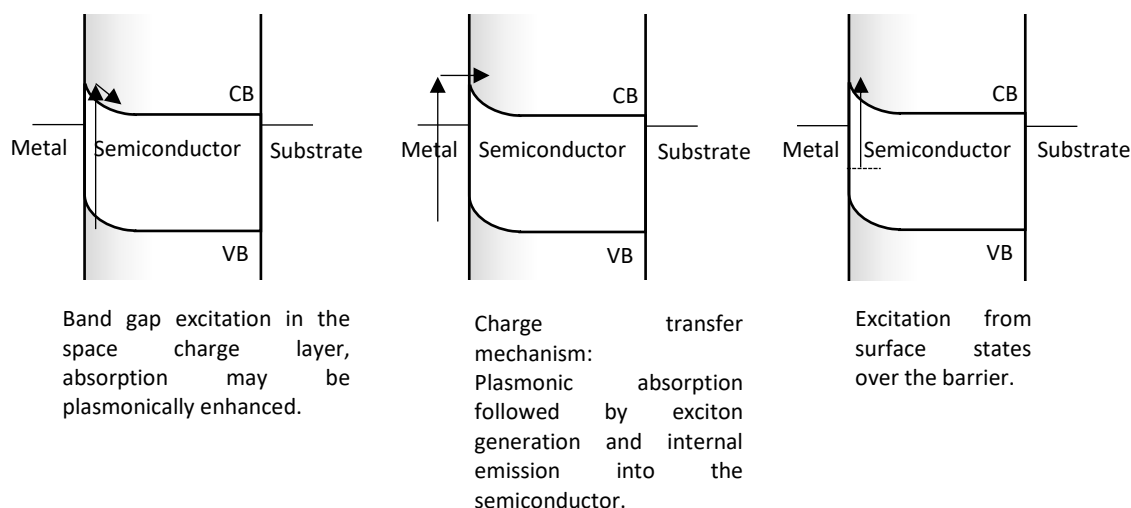


Figure 6.1: Diagrams of mechanisms by which electrons can travel into the semiconductors. Band gap excitation, excitation of surface states, plasmonic enhancement at surfaces and excitation within plasmonic nanostructures themselves followed by decay and electron injection are all consistent with excitation across the semiconductor band gap.

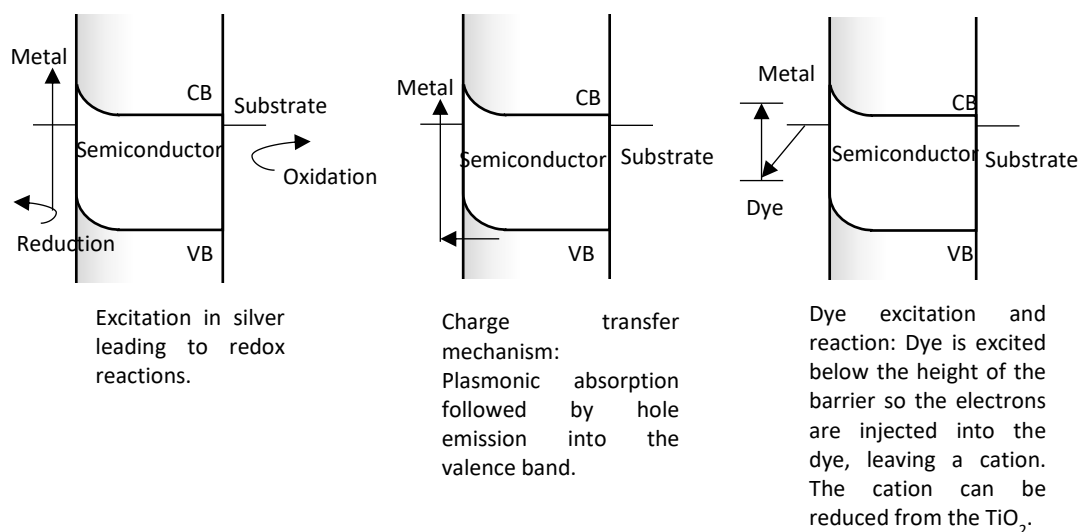


Figure 6.2: Diagrams of possible mechanisms for electron transfer into the silver nanowires. There are fewer reported mechanisms for electron accumulation in silver nanowires and many are untenable.

The mechanisms presented in Figure 6.2 are an attempt to describe any contribution to current in the opposite direction to band gap excitation. Excitation of surface states would rapidly be depleted as a mechanism for photocurrent generation. If a charge transfer mechanism was at play, resulting in an electron density below the barrier height, but a hole energy

high enough to inject over the barrier, this could lead to the observed current direction. However, the TiO<sub>2</sub> films used here were thick and the hole mobility in TiO<sub>2</sub> films would not be expected to be as high as the electron mobility, due to its n-type nature.

The current could result from a series of redox reactions at the silver nanowires resulting in the device operating as a photoelectric cell. Excitation of holes over the hole barrier is unlikely as this current would fall rapidly and holes would have a short lifetime, similarly for a hole based plasmonic excitation.

#### 6.2.1. Predictable photo-action spectra for Schottky barrier devices

The response of Schottky barriers to light is well documented as can be seen in the Literature Review (Chapter 2). This generally leads to predictable action spectra. For instance, for a TiO<sub>2</sub> nanowire array (anatase) over a thin film substrate (rutile) over p-type Si, with Ag contacts, the photoluminescence is best described by 4 contributions to the photoluminescence. These are contributions from the direct excitation of anatase and rutile, with a small confinement effect. Excitation of electrons from oxygen vacancies and another is from the inter-band transition in the TiO<sub>2</sub>, due to e<sup>-</sup> h<sup>+</sup> recombination at oxygen vacancies. A similar set of peaks are seen in the photoresponsivity of the device. The presence of oxygen is proposed to significantly increase the Schottky barrier height, accounting for the high turn-on voltage for these devices. <sup>152</sup>

However, in the devices discussed in the results section, there were two opposing current directions. As silver is the only other absorbing species and silver plasmonic absorptions are known to drive photocatalysis, the impact of plasmonic resonances on photovoltaic and photocatalytic systems will be discussed.

#### 6.2.2. Metal-Semiconductor interaction mechanisms

There are many studies of metal nanoparticle/semiconductor composites with greater light activity for photocatalysis. Three mechanisms are commonly used to explain the enhancement of plasmonics:

- The excitation of electrons over the Schottky barrier formed between the metal and the semiconductor, resulting in the metal acting as an electron sink resulting in a longer charge separated state
- The enhancement of absorption by coupling the plasmonic absorption with the incoming radiation, the absorption cross section can be many times larger than the geometry of the particles
- Excitation of plasmonic absorption in the metal nanoparticles can result in decay and electron injection by a charge transfer mechanism.<sup>175</sup>

This plasmonic excitation often results in absorption in the visible region and is tuneable by size and shape of the particle as well as its environs. In DSSCs, a one step “direct” excitation resulting in an extremely fast injection of electrons is possible for some dyes, due to the contribution of the semiconductor orbitals to the LUMO of the dye on a semiconductor. However, in plasmonic systems, there is no analogous LUMO or hybrid state. For this reason, the plasmonic absorptions of metals will now be examined to better understand the nature of the excitation.

### 6.2.3. Introduction to plasmonics

Plasmons are excitations due to the collective oscillation of charges. The following discussion is described by references <sup>20,176,177</sup>.

Electrons are influenced by the fluctuating electric and magnetic fields of incoming light radiation. An oscillating electric field can generate a perpendicular magnetic field and vice versa. The speed for which this becomes self-sustaining is the speed of electromagnetic radiation.

If an electric field is applied to a sphere of material, a field will develop inside the material and electrons will move to cancel the field, nuclei can be assumed to be stationary. If the electric field diminishes, the electrons will move back, repelled by each other, and continue to oscillate in this fashion until the energy is lost by dampening.

The interaction between the charges and the field results in a momentum of the plasmon being larger than a photon of the same frequency and this difference must be bridged. This can be achieved practically through prism coupling, a periodic pattern in the metal surface or scattering from surface defects such as a protrusion or hole.<sup>178</sup>

Plasmonic absorptions are often much more dramatic for nanoparticles. The advantage of plasmonic nanoparticles are that there is less visible light scattering than large particles, it is possible to tune the plasmonic modes by shape and size of the particle and the large surface area to volume ratio, so changes at an interface are amplified. This results in being able to shift absorption by changing the local environment of the nanoparticle. This is the basis of many sensor-type applications of plasmonic excitations.

Frequency dependence of the dielectric properties of a material to a field  
 The system responds to a changing field until it a frequency is reached where it is unable to, when that mode of polarisation is no longer available and “switches off”. This can be seen most easily in liquids where they can be frozen out by lowering the temperature.

The restoring forces of each of these (the attraction of the nucleus, repulsion of the electrons, the strength of the bonds, the ability of molecules to re-orientate) will depend on the strength of the field and the frequency of the changing field. This is also a way that energy is dissipated within the dielectric.

This results in a term by which the ability to sustain the electric field, the polarizability of the material, expressed as a multiple relative to that of a vacuum;  $\epsilon$ . There are three main polarisation mechanisms; 1) individual atom polarisation (or electronic or induced polarisation) where the electron cloud is polarised relative to the nucleus 2) molecule dipole orientation (orientational polarisation) and 3) stretching bonds (molecular or ionic polarisation).<sup>20</sup>

At high frequencies, the only polarisation mechanism which remains is the atomic polarisation. This usual resonance is  $10^{15}$ - $10^{16}$  Hz, so all materials the dielectric constant drops to a low value in the UV and there is a strong absorption.

#### Drude and Lorentz models

To model these systems considering the electrons as masses on springs, with a restoring force, the Lorentz model is used.

Equation 6.1. 
$$m_e \frac{d^2\mathbf{r}}{dt^2} + m_e\gamma \frac{d\mathbf{r}}{dt} + m_e \omega_0^2\mathbf{r} = -e\mathbf{E}$$

$r$ : relative separation

$m_e$ : mass, in this case of the electron

$\mathbf{E}$ : electric field

$e$ : electric charge

$\omega$ : frequency

$b$ : damping constant (which depends on rate of displacement)

However, given that the electrons are considered bound, this gives frequencies for the resonant peaks at extremely high frequencies with a background at other frequencies. Considering removing the restoring force yields the Drude free electron model, which assumes the electrons behave similarly to a perfect gas; Coulombic interactions between them are negligible, collisions are instantaneous and elastic and they do not interact with atoms. The Drude model fails to account for heat capacities, underestimating electron-electron interaction and predicting semiconducting behaviour, though can often predict the frequencies of oscillations in some materials.

#### 6.2.3.3. Models to describe plasmonic excitation

Plasmonic excitation can be modelled with a range of methods, briefly:

- Firstly, it is an oscillation as described above. Drude's model allows estimation of frequency from  $n$ , the charge carrier density, from conduction measurements. The oscillations of these charge carriers can be modelled to find the frequency of harmonic resonance.
- Secondly; it is the study of how a field changes in a particle. This suggests an electrodynamics approach. By modelling regions of arbitrary size, Maxwell's equations can be applied to the electrodynamics of the dipoles.<sup>176</sup>
- Thirdly, it's a quantum system, with energy levels and density of states functions. Given its limitations, the free electron model can be "quantised" by creating energy levels dictated by the size of the geometry, such as Equation 6.2. DFT can be used to calculate the occupation and energy of states involved and the coupling between them. It can easily be envisaged that the top two approaches would fail to predict what would happen at very small length scales,

especially the interactions between electrons. For large systems, this method untenable and it is necessary to model the large numbers of electrons in a plasmonic system. <sup>176</sup>

#### Quantized energy levels

By quantising the available energy states, incrementing  $n$  as dictated by the geometry of the particle under consideration (eg. a 3D box for Equation 6.2), the electrons can be modelled to have a density of states depending on the energy available. This results in a Boltzmann distribution of energies in quantised states, with occupation from the Aufbau principle.

Equation 6.2. 
$$E = \frac{h^2}{8 m_e L^2} (n_1^2 + n_2^2 + n_3^2)$$

$E$ : energy

$h$ : Planck's constant

$m_e$ : free electron mass

$L^2$ : length

$n_1, n_2, n_3$ : energy level

With a Boltzmann distribution of energies, Equation 6.3.

Equation 6.3. 
$$D_e(E) = \frac{4 \pi V (2 m_e)^{3/2}}{h^3} \sqrt{E}$$

$D_e$ : Density of states

$V$ : volume

From these models, it is possible to model plasmonic excitation in real systems with some limitations.

One particularly successful approach is the Mie theory used to predict scattering and absorption based on the Drude model. It has been used successfully to model silver nanowires.<sup>49</sup> Mie scattering is solved from a differential equation for a harmonic oscillator with driving force proportional to the electric field. The resonance condition is met when  $\epsilon_{particle} + 2\epsilon_{medium}$  is near zero.

#### Localised surface plasmons

The advantage of plasmonic particles can be the effect of far-field scattering, near field localised surface plasmons resonances (LSPRs) and surface

plasmon polaritons. The LSPRs provide strong electric fields, which can be used to increase absorption by dyes by interaction of the molecular dipole and the enhanced electric field. Coating metal nanoparticles with a thin layer of semiconductor can help with the absorption of dyes whilst preventing the metal particles becoming recombination sites and preventing the corrosion of the particles.<sup>179</sup>

LSPRs include dipole, quadrupole and higher order plasmon modes. The absorption cross section can be 10's of times larger than the physical size due to the large electric dipole, causing an intense electric field (10,000's times greater than that of the light), called the near-field enhancement, which decays quickly away from the nanoparticle.<sup>180</sup> This can make challenging catalysis possible.<sup>181</sup>

Illumination of particles with different shapes can result in changing plasmonic interactions depending on the direction of the light. Further, plasmons can couple with each other in order to turn these nanoscale "artificial atoms" (as nanoparticles can be called on account of their quantum confinement effects being analogous to atomic orbitals) to "artificial molecules" due to the formation of bonding and antibonding coupling of plasmons analogous to bonding and antibonding orbitals formed between molecules.<sup>182</sup>

#### Modelling the production of hot carriers

Manjavacas et al., used a free electron model in silver spheres with the number of electrons equal to the conduction electrons to solve the radial Schrödinger's equation where the "height" of the potential well is the work-function of silver, 4.5 eV. This could be used to fit experimental estimates of plasma frequency and dampening to the plasmon absorptions in the particle, leading to DFT models of the hot carriers and their energy distribution probabilities per unit time.<sup>181</sup>

Hot carriers thermalize through electron-electron, electron-phonon and electron-surface (or adsorbate) scattering and eventually cool by phonon scattering. If this is non-radiative the surface plasmons first decay into single electron excited state, this might be followed by photoemission if the electron energy exceeds the work function of the metal.<sup>180,183</sup> The power absorbed by the nanoparticle is controlled by the parameters of the Drude model and the

geometry of the nanoparticle.<sup>181</sup> These decay processes depend on the size, shape and carrier concentration of the nanostructures.<sup>183</sup> The LSPR can overlap with interband transition in Ag, optimum for creating high energy electrons.<sup>180</sup> Hot electrons may have energies around 1-4 eV, and those above the barrier may tunnel through a Schottky barrier.<sup>180</sup>

By investigating the coupling of excitations in the systems, the scattering mechanisms can be investigated. The first calculations were of the plasmon excitations around 3.65 eV for particles between 5 and 25 nm. Efficiency of carrier generation depends on the particle size and the carrier lifetime. Efficiency decreases with increasing diameter and increases with lifetime, as expected. Shorter carrier lifetimes results in more homogeneous spatial distributions due to the contribution of a range of states with small energies.

181

The plasmonic excitation frequency is influenced heavily by the environment, for instance by changing the surroundings of a gold nanoparticle from water to TiO<sub>2</sub>, or the degree to which a nanoparticle is embedded in a semiconductor, the LSPR can move from 294 nm to 600 nm.<sup>184</sup> Field enhancements can occur wherever there is a change of shape, for instance, as the corners of triangular shapes and the shape will influence how many resonances there are depending on the direction or in arrays.<sup>184</sup>

#### 6.2.4. Silver nanowire plasmonics

Propagation distances in silver have been reported to be 10-100  $\mu\text{m}$  due to low losses in the visible region. This is discussed for silver nanowires below.<sup>185</sup>

Compared with the transverse mode, the longitudinal plasmon mode of silver nanorods is more effective in extending LSPR absorption and increasing the intensity and distribution range of the near field. The enhancement of activity induced by the Au nanorod is larger than the transverse mode.<sup>180</sup>

Wei et al., describe a nanowire system coated with spun-coated quantum dots, which are excited by electric fields in the nanowires, allowing visualisation of the electric fields. Finite Element Modelling was used to calculate the lowest energy modes for plasmon modes in wires. Above the fundamental mode, the field intensity was distributed separately on the two sides. The higher plasmonic modes result in spatially separated fields that

can be chiral in nature. The peaks in intensity can be separated by several hundred nanometres.<sup>185</sup>

### 6.2.5. Plasmonic Photocatalysis

In a review by Zhang et al., the major processes in a plasmonic photocatalysis were described, Figure 6.3.<sup>184</sup>

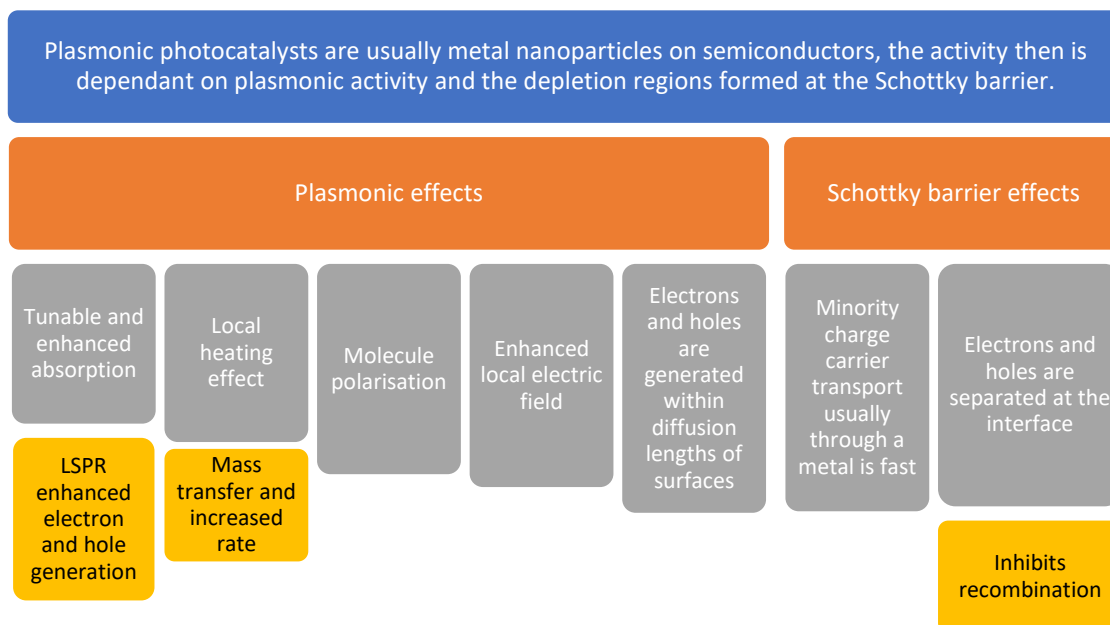


Figure 6.3: Mechanisms involved in the enhancement found for plasmonic excitations from nanoparticles on semiconductor.

Many of the plasmonic effects are also co-operative. For instance, the LSPR enhances the generation of electron hole pairs with a diffusion length of a surface, whereby they may be near the Schottky barrier formed at a surface and can therefore be accelerated in different directions.<sup>184</sup>

Plasmon driven reactions may be the excitation of plasmons followed by electron transfer (indirect) which may be resonant or take place via a relaxed state, or via direct interaction of plasmons with adsorbates.<sup>186</sup>

Energy transfer is accepted to be an important process in plasmonic photocatalysis and is a more important mechanism in small nanoparticles. Non-radiative mechanisms of plasmon relaxation such as electron-electron and electron-phonon relaxation are dominant for these particles, resulting in a Fermi-Dirac distribution of hot carriers. If electrons are above the energy of the barrier are injected into the semiconductor conduction band like the

DSSC mechanism, such that this is referred to as the "LSPR sensitization effect".<sup>184</sup>

There is also the excitation of electrons at the Fermi level of the metal over the barrier. The electrons therefore also flow into the semiconductor by this mechanism. Another mechanism is the generation of electrons and holes in the semiconductor, followed by electrons travelling through the semiconductor, and accelerated by the field, and the holes into the metal.<sup>184</sup>

Though there is agreement in the literature, the degradation of organic materials is enhanced by the local electric field and enhanced electron-hole generation, the mechanisms by which charge transfer is achieved is controversial. One route is the direct transfer of charge carriers, followed by charge transfer or a radiative photon transfer.<sup>184</sup>

To separate out these effects, the authors point out that any mechanism could be active under one condition (depending on whether photons capable of exciting plasmons or excitons or both are present and the contact between the three phases; nanoparticle, semiconductor and environment).<sup>184</sup>

#### Examples of plasmonic photocatalysis

The importance of plasmonic absorption to photocatalysis has been demonstrated using a Au/TiO<sub>2</sub> samples to oxidise 2-propanol to acetone, with a peak of  $\sim 3 \times 10^{-4}$  % quantum efficiency at  $\sim 550$  nm, coincident with the maximum plasmonic absorption.<sup>184</sup>

Simultaneously doped and deposited Ag was studied to capture photoinduced electrons and holes. Photoluminescence intensity decreases with more silver up to 5 %, suggesting some of the charge carriers are captured, reducing photoluminescence. Ag content also increases the ability to adsorb oxygen. Studying the materials by surface voltage spectroscopy showed transitions that are attributed to trap-to-band transitions from oxygen vacancies and hydroxyl groups.<sup>187</sup> The decrease in activity above 5 % is a result of more silver, there is less absorption and more agglomeration. The number of active sites for inhibiting recombination decreases with high doping.<sup>187</sup>

The oxidation of alcohols was attempted, using an electron donating redox mediator, using gold nanoparticles on TiO<sub>2</sub>. In both catalytic studies, the

absorption and action spectra matched between the internal quantum efficiency in the production of current matched the absorption spectrum of the gold nanoparticles on TiO<sub>2</sub>. To demonstrate the direction of current, the electrode becomes more negative in potential in a two electrode system with a Pt or Au counter electrode. The electrons in TiO<sub>2</sub> were observed in a band at 680 nm, similar to applying a negative potential, this absorption decreases when O<sub>2</sub> was bubbled through the solvent.<sup>188</sup>

Ethylene epoxidation on silver nanocubes on  $\alpha$ -Al<sub>2</sub>O<sub>3</sub> was studied. The rates for oxidation under light at 2-3 sun intensity was that of a catalyst 40 K higher in temperature. To demonstrate the dependence on plasmon density – the source intensity was multiplied by the extinction spectrum and integrating the product over the wavelengths was found to linearly relate to the photocatalytic rate.<sup>189</sup>

From kinetic isotope studies, the authors propose an electron assisted O<sub>2</sub> dissociation process, specifically through transfer of an energetic electron to the antibonding O-O 2 $\pi^*$  orbital, facilitating dissociation. This would appear to be backed up by a DFT study which shows the lack of occupation of the O-O 2 $\pi^*$  orbital and a difference between this orbital and the Fermi level of 2.4 eV. However, the authors point out that they cannot distinguish between excitation of energetic electrons and their transfer and a direct interaction between the silver plasmons and the adsorbates.<sup>189</sup>

#### 6.2.6. Field enhancements by particle geometry

Linic et al. report possible field enhancements around plasmonic structures 10<sup>-3</sup> at isolated particles and double that between almost touching particles.<sup>190</sup> If a direct energetic electron driven photocatalysis is occurring on a plasmonic nanostructure, there would be a linear dependence of rate on intensity, a larger kinetic isotope effect, different product selectivity compared to the same reaction by heating.<sup>190</sup> The plasmon driven process depends on the availability of low lying orbitals, the energy of neutral and charged adsorbates, the lifetime of the charged adsorbate state, intensity of the surface plasmon and the temperature of the system.<sup>190</sup>

#### 6.2.7. Light absorption

Hot carrier generation using metals is possible when there is a large density of electronic states, such as in silver and gold d bands. These can lead to the

efficient absorption of light by these structures, with absorption cross sections much larger than the size of the nanoparticles possible.<sup>191</sup> This is often used directly in plasmonic solar cells, where nanoparticles can be added to light sensitive layers in order to increase absorption in the layer and thus reduce the volume of absorption layer needed, such as in gold nanoparticles embedded in a conductive polymer, P3MT/PEDOT:PSS, architecture which also enables the potential to form photovoltaic devices on new substrates.<sup>176</sup>

#### 6.2.8. Energy transfer

Direct observation of electron injection into  $\text{TiO}_2$  by femtosecond IR studies of the conduction band of  $\text{TiO}_2$  and was observed within 240 femtoseconds.<sup>180</sup> This seems confirmed by the LSPR driven reduction of  $\text{AgNO}_3$  on  $\text{TiO}_2$  with sodium citrate as a hole scavenger when the wavelength matches the LSPR of gold nanoparticles on  $\text{TiO}_2$ .<sup>180</sup> Some electron transfer to semiconductors have not been observed despite the low height of some Schottky barriers, for instance on  $\text{Fe}_2\text{O}_3$ . A theoretical explanation of this would be the lack of effective hybridization of the unoccupied states in the metal and semiconductor.

A theoretical study of Au on metal-semiconductor interfaces suggest the surface plasmon polaritons (SPPs) would decay to form, preferentially, hot holes, potentially due to the lack of available inter-band transitions in Au. Holes, accumulating in the metal structure following plasmonic excitation, may cause an oxidation of the nanoparticles, destroying in turn, the LSPR. Therefore there needs to be an electron donor in contact with the nanoparticle.<sup>180</sup>

Energy transfer by dipole-dipole coupling, not just by electron transfer to a semiconductor, has been demonstrated by the insertion of an electron injection blocking layer between Ag and  $\text{Cu}_2\text{O}$ .<sup>180</sup>

#### 6.2.9. Plasmonic solar cells

There have been several reviews in this field recently, one of the most interesting is that which discusses the theoretical limits of this area of research, analogous to the Shockley-Queisser limit, for plasmonic devices that rely on internal photoemission to generate current. As it covers many

important points when considering the possibilities of plasmon induced photocatalysis or a plasmonic solar cell.

White and Catchpoles analysis is applied for an energetic electrons or holes extracted via internal photoemission across a Schottky junction. This is plasmon-enhanced internal photoemission as opposed to plasmonics being used to enhance scattering or trapping of light for use in a DSSC mechanism.

The mechanism for this device is i) Absorption of photons by the metal and generation of hot electrons, ii) transport of electrons through the metal to the interface, iii) emission of electrons across the junction and iv) collection of electrons at the ohmic contact, summarised in Figure 6.4.

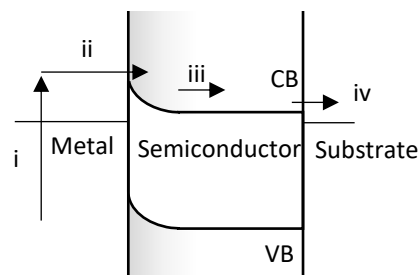


Figure 6.4: Mechanisms in a plasmonic solar cell; i) Excitation ii) injection of electrons over a Schottky barrier iii) transport of electron through the film iv) harvesting of electrons at an ohmic contact.

To give an estimate for an upper limit, the process of harvesting the electrons and ballistic transport is assumed to be perfect for a film less than 40-50 nm, the mean free path for electrons in Ag and Au.<sup>192</sup> It is also assumed all electrons reach the barrier before thermalisation and they have enough momentum in the direction of the barrier, this assumption is due to the likelihood of reflection a number of times at the interfaces.

Therefore, the limitations of this device mainly on the first process, the generation of hot electrons, though the absorber is assumed to absorb all of the solar spectrum. Once generated, the electrons lose energy through scattering or re-emission of light or by generation of electron-hole pairs.<sup>192</sup>

Then, the absorption depends on the initial and final density of states. In this study, a model of the hot electron energies was used, EDJDOS, which includes band structure and energy bands below the metal Fermi level. This

gives a DOS similar to the free electron gas model, where density is proportional to root of the energy of the state,  $E^{1/2}$ .

Assuming a lack of inter-band transitions and a barrier height of 1.2 eV and a density of states for the excited electrons which is seemingly reasonable, a photon energy twice that of the barrier gives an electron distribution of energies where only 54% have enough energy to overcome the barrier. <sup>192</sup>

The maximum current through the cell is assumed to be the short circuit photocurrent less the reverse saturation current of the Schottky barrier, Equation 6.5 (discussed in Chapter 4), resulting in the combining the diode equation with Thermionic emission theory. <sup>192</sup>

$$\text{Equation 6.5: } I = I_{sc} - SA^*T^2 \left( \exp \frac{-\Phi_s}{kT} \right) \left( \left( \exp \frac{qV}{nkT} \right) - 1 \right)$$

I: device current / A

$I_{sc}$ : short circuit current / A

$A^*$ : Area /  $m^2$

S: Richardson constant /  $A m^{-2} K^{-2}$

$\Phi_s$ : Barrier height / eV

q: elementary charge / C

n: diode ideality factor

V: device voltage / V

$R_s$ : shunt resistance /  $\Omega$

k: Boltzmann constant / eV  $K^{-1}$

T: temperature /K

The only material parameter in this is the Richardson constant, quoted as  $6.71 \times 10^6 \text{ Am}^{-2}\text{K}^{-2}$  for  $\text{TiO}_2$ . However, this has a very weak overall impact on efficiency. The maximum efficiency is calculated to be 7.2% for a barrier height of 1.2 eV. This is low despite the optimistic assumptions about the efficiency of each process. <sup>192</sup>

One assumption made is the decrease in the density of states (DOS) below the Fermi level in the metal structure, this may give an overly conservative estimate, as peaks in DOS may occur in noble metals a few tens of eV below the Fermi level, leading to a preferential excitation of higher energy electrons. This leads to more electrons having enough energy to overcome the barrier.

Assuming the effective conduction band edge is 0.15 eV below the  $E_F$ , (that there is a high DOS near the Fermi level), the maximum efficiency increases to 22.6% for a 1.4 eV barrier height.<sup>192</sup> This vast improvement points the way to higher plasmonic efficiencies as available DOS in the metal results in a vast change in efficiency.

#### 6.2.10. Polarisation sensitivity to direct excitation

Schottky barriers and ohmic devices can be compared to discuss plasmonic and band gap excitation effects. By using light below the band gap but above the height of the Schottky barrier, a photocurrent can be generated by excitation of plasmonic modes within a gold layer.<sup>191</sup> Further, this photo-excitation can be sensitive to the polarisation of the light in 2D metal nanostructures, for instance in metal nanowires on a semiconductor surface, imaged by raster scanning across the surface.<sup>191</sup>

#### 6.2.11. Criticism of charge transfer mechanisms

One of the criticisms of the charge transfer mechanism is that there is no analogous HOMO-LUMO for metal nanoparticles of the size for even nano-sized metal particles. Hou and Cronin assumed the charge carriers to be at the Fermi energy level of the metal, and thus there is no potential difference between the redox potential of the reactants and the Fermi energy level.<sup>175</sup>

The same authors previously reported the plasmonic enhancement of water splitting in 1 M KOH solution. This has also been seen by other authors for a AgNP functionalised film in 1.0 M NaOH under visible light.<sup>193</sup> These authors observe a 66 times improvement in the photocurrent measured at 633 nm (1.96 eV). In UV light, the opposite was true, with plasmonic nanoparticles hindering the catalysis, explained by a lack of light being able to penetrate the  $TiO_2$  and less contact with the solution. The authors report on a model of 1000-fold enhanced field between nearly touching Au islands, coupling light to the surface with a field up to 1000-fold the control material.<sup>193</sup> Plasmonic enhancement of catalysis at a surface by the enhancement of fields is also seemingly supported by its tolerance to defect density and its necessity for photocatalysis.<sup>175,193</sup>

#### 6.2.12. Photocatalytic plasmonic reductions

Plasmonic reductions have been suggested to study the light driven catalysis on silver which can be very selective. 4,4'-dinitroazobenzene and 4-nitro-4'-

aminoazobenzene can both be reduced to their amine form using a plasmon-driven catalytic reaction, but the oxidation of diaminoazobenzene could not be oxidised. This suggests the plasmon reductions are easier than oxidation in this case, in aqueous environments. One hypothesis is that electrons in the molecule can overcome the Schottky barrier, while the surface surface plasmon decayed holes cannot diffuse to the molecule.<sup>194</sup> The resonance of molecules overlapping with the surface plasmon resonance may increase the chance of a Förster energy transfer mechanism or the excited state may be easier to reduce. <sup>194</sup>

### 6.2.13. Photocatalysis of TiO<sub>2</sub>

TiO<sub>2</sub> is among only a few semiconductors that are stable, have a negative (vs NHE) in order to reduce protons to hydrogen and a band gap above the energy needed to meet the minimum energy requirement to split water. It has been found that powdered catalysts tend to be inefficient due to the reduction of oxygen with the produced hydrogen. <sup>29</sup>

#### Surface states

TiO<sub>2</sub> surface states have been well researched due to their importance for photocatalysis. In particular, one of the most researched is the oxygen vacancy, where an atom is missing from the lattice. The defect induced 3d states are usually observed by photoemission at 0.8 eV under the Fermi level. <sup>29</sup>

A review by Xiong et al. emphasises the difference between the Ti<sup>3+</sup> state and the oxygen vacancy. On formation of a reduced Ti<sup>3+</sup> state from the Ti<sup>4+</sup> state, to maintain electroneutrality in the lattice, an oxygen vacancy can form, however, they are separate defects. The Ti<sup>3+</sup> state is important for material properties of the surface including hydrophobicity and metal bonding. They can formed in myriad ways including by heating, vacuum, presence of reducing atmosphere, particle bombardment and by UV radiation and chemical reduction with, for example CO, H<sub>2</sub> or C. Under UV light the excited electrons can become trapped, reducing Ti<sup>4+</sup> states. Oxygen vacancies also cause lattice distortion as the Ti<sup>3+</sup> will move within the octahedron to the most stable position, resulting in a strongly polarised state.<sup>195</sup> A study using samples annealed in O<sub>2</sub> atmospheres lead to the modelling of the TiO<sub>2</sub> hydrophilicity is described by a long range attraction between TiO<sub>2</sub> and water mediated by the delocalised electrons in traps on the surface. <sup>29</sup>

The phenomena of reversible switchability of hydrophilic and hydrophobic states in TiO<sub>2</sub> can give an indication of the surface chemistry and its sensitivity to environment. The hypothesis proposed by the authors is a UV light triggered transition between Ti-O-Ti + H<sub>2</sub>O and 2 Ti-OH, given the obvious necessity of hydroxyl groups to surface wettability.<sup>196</sup> Using XPS studies of the surface of TiO<sub>2</sub> which shows two peaks for the O 1s peak, the higher energy of which corresponds to dissociatively adsorbed water. This peak decreases in size in the dark.<sup>197</sup>

Dissociative water coverage on defective TiO<sub>2</sub> surfaces was found to be less than one monolayer and independent of the density of oxygen vacancies. Surface defects have been reported to increase in some cases, suggesting bridging oxygen may react to produce two bound OH groups. However, oxygen does appear to bind at surface defects as a O<sub>2</sub><sup>-</sup> species, and is dissociated at high temperature.<sup>29</sup>

#### 6.2.12.3. Photoelectrochemistry of water splitting on TiO<sub>2</sub> surfaces

Fujishima and Honda discuss the oxidation of water on a TiO<sub>2</sub> electrode in 1972.<sup>198</sup> This sparked a large amount of interest in water splitting, as it solves problems of energy intermittency of solar energy. The semiconductors used to perform water oxidation must be stable enough for this reaction, have a large enough band gap and have conduction bands at a negative (vs NHE) to efficiently reduce protons and a positive enough valence band to oxidise water (1.23V).

Following excitation, an electron and hole are generated within 200 fs, whereby the hole reacts 2-3 times faster than the electron. The reactions to split water take microseconds or longer. DFT studies have suggested the overpotential required for water splitting is related to the O<sup>•</sup> binding energy, which is seen for a range of oxide catalysts in alkaline conditions.<sup>199</sup>

## 6.3. Results

### 6.3.1. Competing photocurrent processes in the UV region

Very early studies showed some intriguing results; the rise in photocurrent and the UV-vis absorption peaks of the silver nanowires and TiO<sub>2</sub> sol is not where they would be expected to be, rising above the band gap of the semiconductor followed by a plateau. This assumes that charge separation

occurs at the interface between the two materials, in the depletion region of the semiconductor.

This is the working principle behind this device and those detailed in the Literature Review. A functionalised device would also use this mechanism, using the interface to separate charge. However, initial photocurrents were very low, likely due to the low crystallinity of the devices, and high numbers of defects and therefore high levels of recombination. The crystalline regions in these early devices were very small and the quantum confinement effect was expected to shift the absorption energy to lower wavelengths.

However, as the sols were continually improved though extended crystallisation and eventually showing larger crystallite sizes than P25, the quantum confinement effect was not a satisfactory explanation for the continued photocurrent being at a higher energy than expected. Two opposing photocurrent directions were even seen for some very early devices made using P25 powder, Figure 6.5.

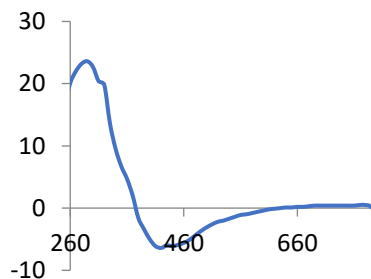


Figure 6.5: Measured photocurrents demonstrating the opposing currents that were seen for a device fabricated from a commercial  $\text{TiO}_2$  (P25) sol.

There are two peaks showing currents in opposite directions.

### 6.3.2. Possible mechanisms

As well as the observation of opposing currents, when directionality was studied, it was found there were large currents in the opposing direction to that of direct excitation over the band gap. Given the lack of absorption below the band gap in  $\text{TiO}_2$ , besides defect states, the absorption is likely due to silver nanowires or an interaction between the two. This impact of the

composite on the absorption is observed by UV-vis spectroscopy. That this is sensitive to the material is clear from the lack of these unexpected current directions on TiN, quantum dot or TaON derived devices. Further, there is no evidence that crystallinity of the sol impacts this unexpected current.

Some of the findings in sections below show the necessity of discussing the results in terms of a new, potentially plasmonic, photocatalytic mechanism. The outline of these arguments are:

- The photocurrent for the devices does not correlate with the band gap of the semiconductor. Amorphous 25 nm thick films of TiO<sub>2</sub> have a reported band gap of 3.35 eV, still lower than that seen in these results.<sup>200</sup> The dominant peak even in highly anatase samples with large crystallite size was around 333 nm, 3.72 eV from external quantum efficiency (EQE) from Tauc plots, Figure 6.6.

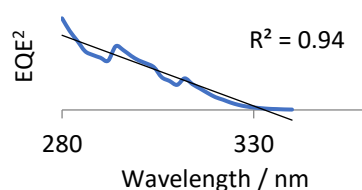


Figure 6.6: (EQE)<sup>2</sup> plot, giving an intercept of 333 nm for a Tauc plot, indicating an indirect mechanism of the excitation in this device.

- The same is true of the amorphous devices, suggesting these peaks are independent of phase.
- Previous work in the group also results in two adjacent peaks in the same direction from oxidised (rutile) also attributed to "plasmonic resonances", making one peak appear to be two, though in these devices, the currents are in the same direction.

However, current can be measured in both directions. If electrons were injected extremely quickly into the conduction band, as has been documented in DSSCs, they would be separated by the field in the semiconductor.

- Surface modification by water, organic acid or dyes can change the position, size and direction of the photocurrent.

### Controlling for silver nanowire absorption

UV-vis spectroscopy showed that absorption due to the combination of silver and TiO<sub>2</sub> was different to the sum of both parts. However, the silver nanowires transmittance is variable across the spectrum (Figure 6.7, top left) which may alter the position of the peak, as higher opacity would result in a falsely low efficiency at certain wavelengths. Normalising the transparency across the spectrum and assuming *all* light travels through a dense mesh of silver nanowires, Figure 6.7, top left shows the normalised absorption from 500 to 290 nm, top right shows how the normalised output corresponds to photons reaching the semiconductor. Bottom left shows the efficiency accounting for this loss and bottom right shows a Tauc plot of the raw efficiency, with an intercept of 343 nm and also normalised to silver nanowire absorption, showing an intercept at 353, demonstrating the small shift. This shows that accounting for the silver nanowire absorption does not account for the dramatic difference in expected absorption onset and that observed.

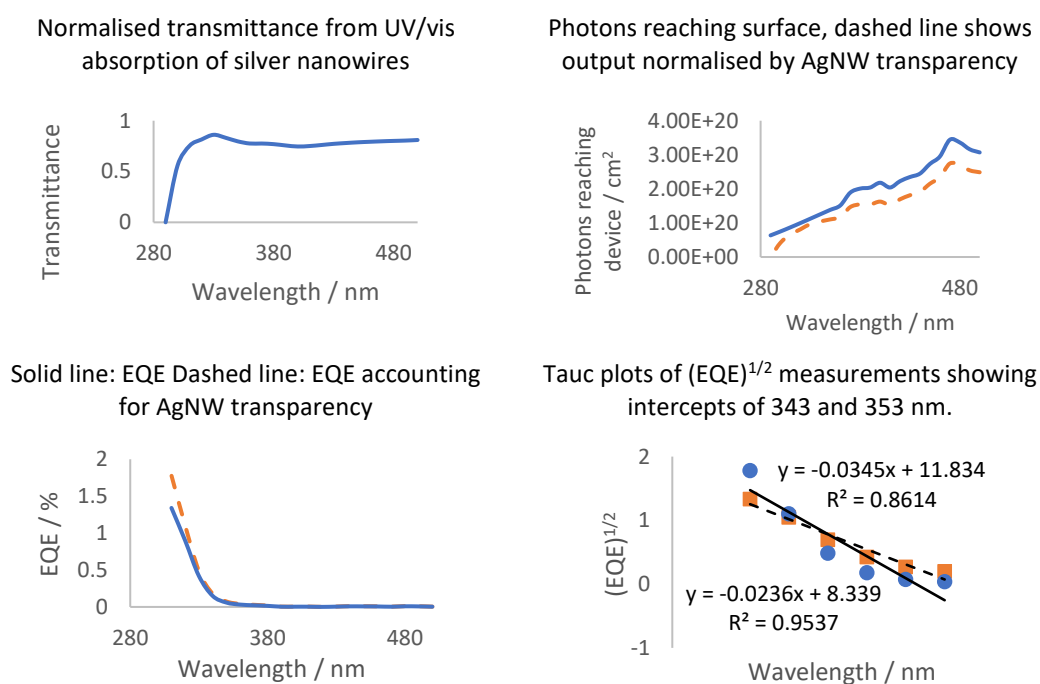


Figure 6.7: Normalised transmittance of silver nanowires in isopropanol (top left), the output from the lamp accounting for transmittance of the nanowires (top right), the impact of this on calculated efficiencies (bottom left) and Tauc plots (bottom right). Silver nanowires are transparent in the visible region and less transparent in the UV region due to the absorption of plasmonic absorption in these regions.

Setting a convention

There are two current directions possible in a diode, forward and reverse. Given the implications of “positive” and “negative” with electrochemical devices, these terms cannot be used unambiguously here. The “reverse” photocurrent is what is expected of a photoexcitation across a semiconductor at a Schottky barrier interface and results from the drift of electrons into the semiconductor (in an n-type device) and holes into the contacting metal. This is the same current direction that would be observed if the device was under reverse bias.

However, an opposing photocurrent was also often observed. This was where the electrons were travelling into the contacting metal. This is despite the evidence that there is indeed a Schottky barrier formed at the interface, as observed by current-voltage characteristics. This will be referred to as the “forward” photocurrent and is the current of electron flow if the diode is forward biased. The results in this chapter explain the impact of both current directions in the UV region. The following chapter details the impact of the results in the visible region.

### 6.3.3. The simplest case: P25 on an early device

A very early device, fabricated from P25 sol on 316 stainless steel, showed two opposing peaks in the photocurrent, Figure 6.8.

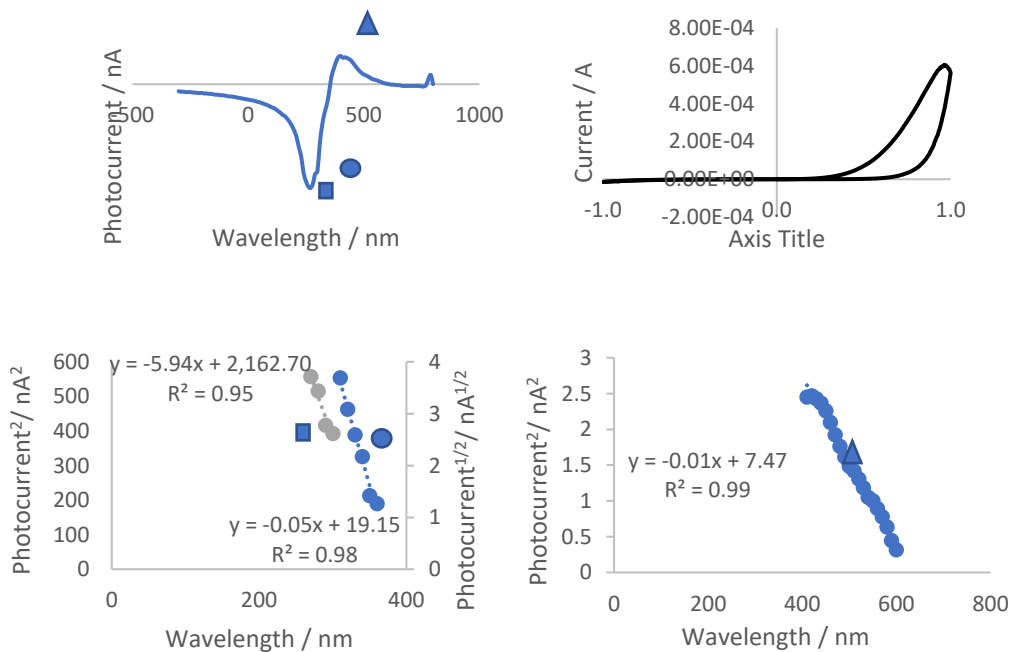


Figure 6.8: Photocurrent from a P25 based device (top left) showing opposing peaks. IV curve of this device (top right) showing rectifying behaviour of the junction. Photocurrent<sup>2</sup> (grey points) and photocurrent<sup>1/2</sup> (blue points) and best fits from absorption for the "negative" peaks (bottom left). Photocurrent<sup>2</sup> fits from absorption spectrum (bottom right).

From the structure of a Schottky barrier device, which the IV suggests is present (Figure 6.8 – top right), the generation of current would be expected to be through direct excitation of the semiconductor.

Indeed, the absorption of the peaks at ~270 and ~ 290 nm are better described by Abs<sup>2</sup> and Abs<sup>1/2</sup> respectively and give intercepts of 3.4 eV and 3.24 eV respectively. Anatase has an indirect band gap of 3.2 eV.<sup>201</sup> However, the other, lower energy peak shows a better linear fit to the Abs<sup>1/2</sup> vs wavelength plot. The intercept of this plot is 633 nm, or 1.96 eV. This is well below the band gap of the semiconductor.

#### 6.3.4. Chromia layers

One possible mechanism is that the back contact is steel. For later devices, a diffusion barrier was intentionally grown on steel prior to the TiO<sub>2</sub> deposition. However, Cr<sub>2</sub>O<sub>3</sub> is a p-type semiconductor with a large band gap, ~3.5 eV, larger than the band gap of TiO<sub>2</sub>, Figure 6.9. Given the unexpected nature of so many positive responses, and the bulk of them occurring on samples fabricated on 316 grade stainless steel, known to form better chromium rich diffusion blocking layers, than 304 stainless steel (Chapter 3), the influence of a potential p-type material on the photocurrent must be considered as the origin of one of these peaks.

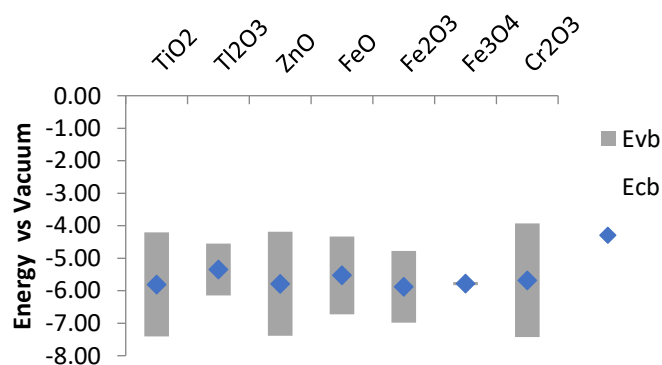


Figure 6.9: Selected band gaps of semiconductors.<sup>2</sup>

Firstly then, the higher energy peak could be due to excitation across the  $\text{Cr}_2\text{O}_3$  but this would not be in keeping with the direction measured as the electrons generated would need to traverse the Schottky barrier region into the  $\text{TiO}_2$  film.

The low energy peak could be due to excitation across the  $\text{Cr}_2\text{O}_3$  band gap, but the intercept from the above section and other studies show intercepts near 2 eV. A p-n junction could be formed with a lower band gap could be formed.

A strong argument against this, however, has been discussed in different guise in Chapter 3. A saturated NaCl IPA solution was used to treat the steel prior to annealing the sol this indeed resulted in a smaller measured series resistance, indicating that diffusion barriers formed on steel may indeed contribute to resistance by formation of less conductive oxides. Na and K salts are known to disrupt protective chromia layers, forming chromium rich islands that offer little protection of the steel.

The photocurrents of those same devices show the “positive” and “negative” peaks seen in previous devices, Figure 6.10, despite the disrupted  $\text{Cr}_2\text{O}_3$  layers.

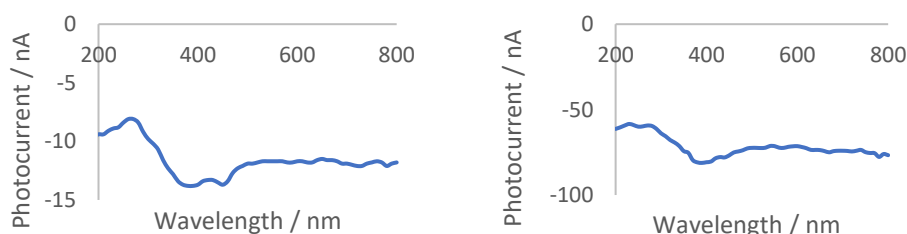


Figure 6.10: Photocurrents for two amorphous devices passivated with tartaric acid passivation showing two opposing current directions.

Similarly, strong acid and base have been used to disrupt the chromia layer and also show both photocurrent directions. Further, when a sol was annealed on a steel substrate for an extended period of time, from 90 to 240 minutes, there was no “opposing” current seen, though there would be an expected to be thicker chromia layers.

Also, there are a range of conditions under which the opposing current can be enhanced on a device such as by use of organics and silver nitrate.

Further, the "positive" response is also seen for dye functionalised devices, so chromia would have to be binding  $\text{Ru}(\text{dcbpy})_2(\text{NCS})_2$  dye. This impact of change at the surface is suggestive that this is a surface effect and is not a result of the protective layer on the substrate. Section 6.3.6 details experiments for short annealing times where there were large changes in magnitude and directions of the photocurrent peaks. Finally, the  $\text{TiO}_2$  layer is sintered above the  $\text{Cr}_2\text{O}_3$  film.  $\text{TiO}_2$  effectively absorbs UV light, so UV penetration to the substrate would be expected to be low.

### 6.3.5. Current direction

From the results, it became imperative to measure the absolute direction of current in the device. To measure the current direction without ambiguity through the amplifier, an arbitrary convention was chosen for the terminal such that the current flowing from the (positive) terminal of the battery (or electrons from the negative terminal) gives a negative response on the ammeter.

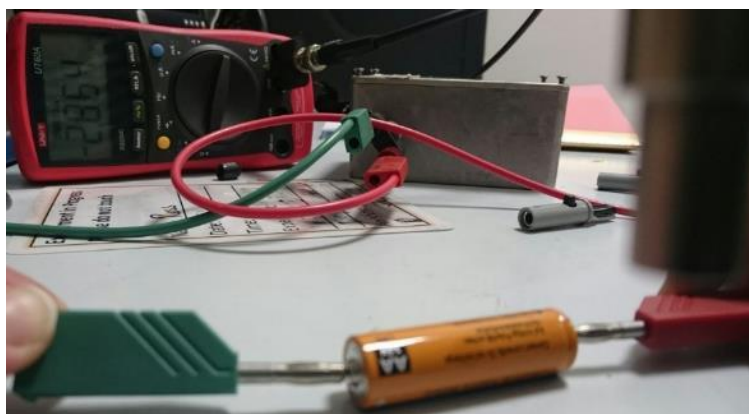


Figure 6.11: Picture of battery control, showing a battery as analogous to the cell. By keeping the configuration the same, the electrons travel through the negative contact (red) through the red contact to the amplifier, whereby they show a negative response, as is seen by the reading of -2.864 on the ammeter.

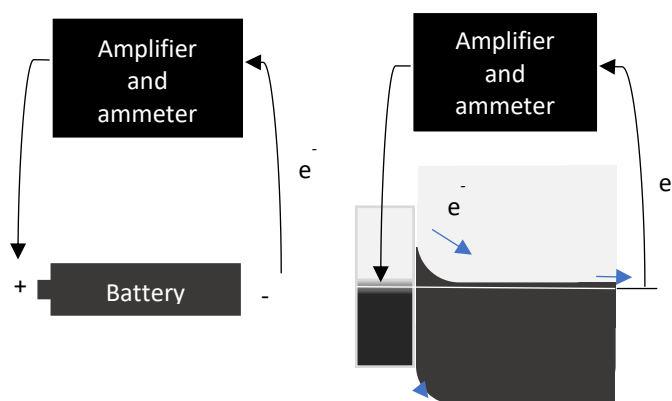


Figure 6.12: Diagram to show battery as analogous to the Schottky barrier device under light.

Figure 6.11 and 6.12 illustrate how a battery can be used to compare to the currents from a Schottky barrier device. Assuming the current is generated in the depletion region or even plasmonically in the silver nanowires and that electrons travel into the TiO<sub>2</sub>, they will eventually be collected in steel, making this the negative terminal.

It would be expected that, with this configuration, with the black terminal connected to the positive terminal (silver nanowire top contact or (+) battery terminal) that the response of the ammeter would be negative, as it is for a battery (Figure 6.11 and Figure 6.12). The electrons will then flow through the external circuit and return to the silver nanowires. Therefore, for the “negative” response to be measured by ammeter, the electrons must be travelling into the TiO<sub>2</sub> when connected in this configuration. This is the “reverse” current and that expected for a Schottky barrier device.

A device previously reported in the group synthesised on polished titanium followed by oxidation at high temperature shows this predictable negative response, above the band gap of rutile TiO<sub>2</sub> 3.0 eV or 413 nm, Figure 6.13.<sup>133,150</sup>

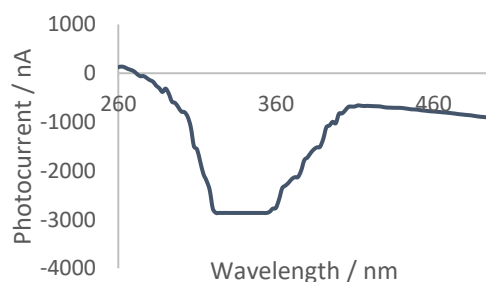


Figure 6.13: Polished titanium device fabricated by D. Jacques, showing a photocurrent in the "reverse" direction, consistent with band gap excitation.

To illustrate the importance of this method, some of the most dramatic results are shown for partly crystalline devices. Where the photocurrent is seen in the opposite direction, with a Tauc plot giving a best fit to  $(\alpha h\nu)^2$  with an intercept of 3.6 eV. This suggests an indirect mechanism for excitation.

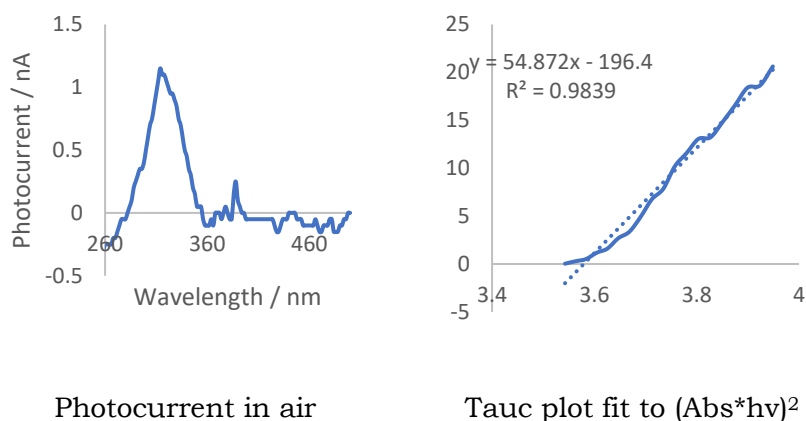
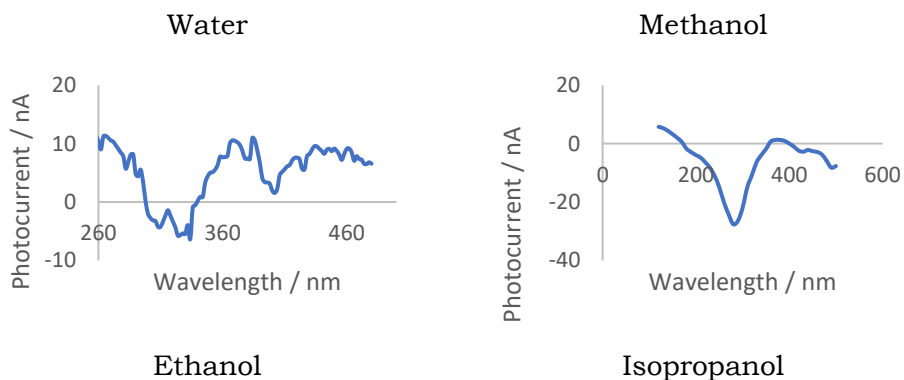


Figure 6.14: Photocurrent (left) and Tauc plot demonstrating a current in the opposite direction to that expected for a "reverse" current (right).

However, when water or alcohol was added to the devices, the direction of the photocurrent changes. For a device in air (Figure 6.14) is compared to the same devices deposited with water and alcohol (Figure 6.15). For some scans, the due to the flash of the arc lamp on adjusting to the starting wavelength, peaks around 500 nm had to be removed. The Tauc plot for the water photocurrent showed a better fit to the  $(\alpha h\nu)^{1/2}$  plot ( $R^2 = 0.91$  for  $(\alpha h\nu)^2$  and  $R^2 = 0.97$  for  $(\alpha h\nu)^{1/2}$ ) with an intercept of 3.24 eV.



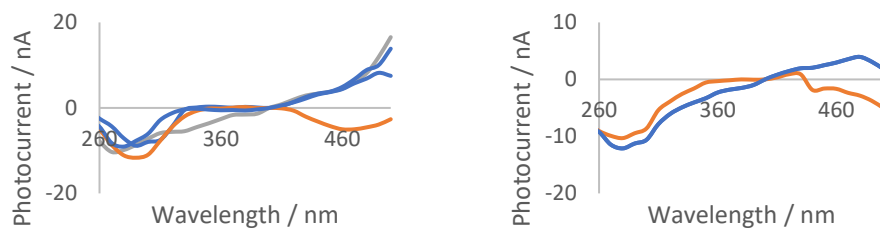


Figure 6.15: Deposition of water and alcohols on the device shown in Figure 6.14 showing a reversal of the current direction.

This does not mean the forward photocurrent is not present, it may simply be that it is dwarfed by the reverse photocurrent. With water and solvents, these peaks are above the band gap of the semiconductor. This is the same for the negative peak as seen earlier for the P25 device, which also shows a direct fit, with a band gap of 3.24 eV. Whilst the energy range is expected for a direct transition within the semiconductor, followed by the separation of charge in the space charge region, however, the direct nature of the transition is unexpected as the lowest energy band gap transition in anatase  $\text{TiO}_2$  is indirect.

There seem few mechanisms that explain this current that don't require the transport of holes through the semiconductor itself. Holes that could be injected from high energy hole states in the valence band would likely undergo recombination from defect or n-doping states.

However, if reactions such as organics or adsorbed water on the surface result in oxidation on silver and reduction on  $\text{TiO}_2$ , a photoelectrochemical cell is effectively set up with a silver anode and  $\text{TiO}_2$  cathode. Plasmonic driven redox reactions are discussed in the introduction and oxidations on  $\text{TiO}_2$  are also well documented. Further, the accumulation of holes at the Schottky barrier and the surface would be favourable in the depletion region around the silver nanowires.

For this reason, a plasmon enhanced photocatalysis seems likely from the limited evidence. When an equilibration with the surface states is reached, the elimination of holes or reduction by electrons from the Fermi level would complete this cycle. This would result in a current effectively travelling from the substrate to the silver nanowires, not requiring transport of holes through the n-type film.

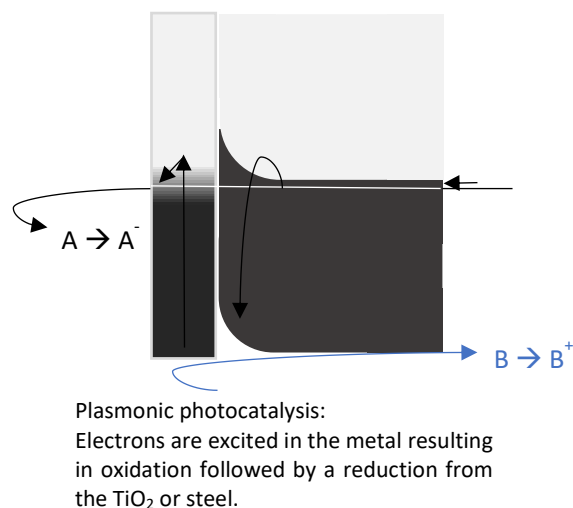


Figure 6.16: Potential mechanism for a plasmonic redox reaction that leads to current observed in the opposite direction to that of direct excitation across the band gap.

The criticism of this reaction is the reliance on holes in TiO<sub>2</sub> existing long enough to react, however, one of the most widely studied processes on TiO<sub>2</sub> is the catalytic production of water. In studies on TiO<sub>2</sub>, electrons and holes are generated within 200 fs and the hole reacts 2 to 3 orders of magnitude faster than the electron (10 – 100 μs) at 0.3, 1 and 3 ns for methanol, ethanol and 2-propanol respectively.<sup>202</sup>

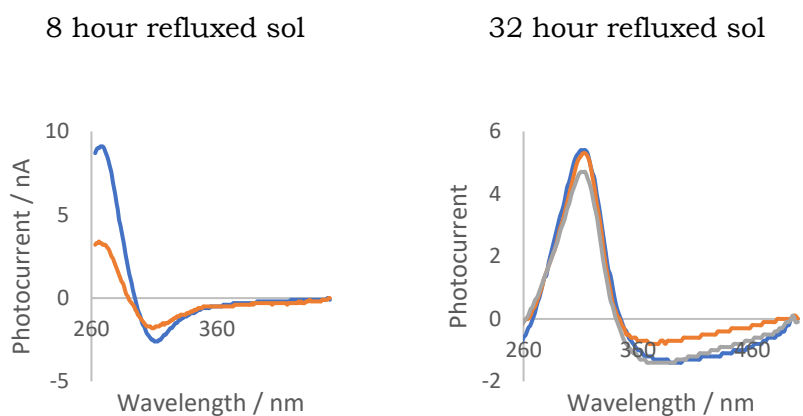
Holes may react extremely quickly. Surface redox reactions take longer, as seen for the electron. These surface reactions of H<sub>3</sub>O<sup>+</sup> with an electron on the surface leads to adsorbed hydrogen, the adsorbed hydrogen can react with another H<sub>3</sub>O<sup>+</sup> and electron to produce hydrogen and the desorption of hydrogen. The hydrogen evolution rate depends on the electrode.

As for the oxidation, DFT suggests the overpotential needed to oxidise water is related to the binding of the oxygen radical. The oxygen evolution activity depends on the occupancy of the 3d electrons with an e<sub>g</sub> orbital of surface transition metal cations in an oxide. (188)

The defect states could provide this of 3d density in the form of defect states. Using photoelectrochemical splitting, the main overall determinant of water splitting rate was activity of the hydrogen evolution catalyst.<sup>202</sup> Again, consistent with this mechanism, as the plasmonically driven reduction must be faster or the electrons would be accelerated into the semiconductor.

6.3.6. Directionality and energy of peaks in increasing crystallinity of sols  
 Directionality was found to change with the crystallinity of the sol used to create the devices. As discussed in Chapter 3, the crystallite size increased exponentially under extended solvothermal conditions. This resulted in a final crystallite size of > 31 nm from the Scherrer Equation.

Appendix 2 shows the plots and Tauc fits for the absorptions in the UV for these samples. Figure 6.17 shows the results for the devices produced from the 8 and 32 hour refluxed sol. These samples were produced on pre-annealed steel and annealed for 1 minute, as described in the next section to prevent metal diffusion.



High energy peak intercepts to  $(Abs \cdot hv)^2$ : 296 and 293 nm

High energy peak intercepts to  $(Abs \cdot hv)^2$ : 353, 334 and 348 nm

Low energy peak intercepts to  $(Abs \cdot hv)^{1/2}$ : 375 and 389 nm

Low energy peak intercepts to  $(Abs \cdot hv)^2$ : 496, 455 and 474 nm

Figure 6.17: Comparing the UV response of devices fabricated from sols having undergone 8 hour (left) and 32 hour (right) reflux times.

The high energy peak decreases in energy initially but is near constant for the samples from 28 hours, showing an onset of 3.7 eV and an indirect transition. For the low energy, mainly negative peak, the indirect transition occurring from the 20-hour sol onwards shows intercepts from 2.5 to 2.9 eV, Table 6.1. The onset of excitation being slightly below the band gap probably results from excitation from defect states.

Following deposition of water, the devices show predominantly negative peaks, with indirect absorptions, showing band gaps between 2.8 and 3.6 eV, Table 6.2. This is in the direction of excitation across the band gap. This variation might be due to confinement effects leading to a slightly higher peak position and lower energies from surface states.

Time of reflux	Low energy				High energy			
	Best fit	Intercept / nm		Direction	Best fit	Intercept		Direction
		nm	eV			nm	eV	
8	½	375	3.3	<b>Negative</b>	2	296	4.2	Positive
	½	389	3.2	<b>Negative</b>	2	293	4.2	Positive
12	½	340	3.6	Positive				
	½	373	3.3	Positive				
16	½	422	2.9	Positive				
	½	406	3.1	Positive				
	½	438	2.8	Positive				
20	2 or ½	355 or 457	3.5 or 2.7	<b>Negative</b>				
24	2	434	2.9	<b>Negative</b>	½	353	2.9	Positive
28	2	450	2.8	<b>Negative</b>	2	335	3.7	Positive
	2	488	2.5	<b>Negative</b>	2	334	3.7	Positive
	2	492	2.5	<b>Negative</b>	2	338	3.7	Positive
32	2	496	2.5	<b>Negative</b>	2	336	3.7	Positive
	2	455	2.7	<b>Negative</b>	2	334	3.7	Positive
	2	474	2.6	<b>Negative</b>	½ or 2	348 or 334	3.6 or 3.7	Positive

Table 6.1: Tauc plot intercepts for low and high energy peaks with their direction, in air.

Time of reflux	Peak				Time of reflux	Peak			
	Best fit	Intercept /		Direction		Best fit	Intercept /		Direction
		nm	eV				nm	eV	
8	½	413	<b>3.0</b>	<b>Negative</b>	24	½	797	1.6	<b>Negative</b>
	½	718	1.7	Negative		2	421	<b>2.9</b>	<b>Negative</b>
12	2	297	4.2	Positive		½	519	2.4	<b>Negative</b>
	2	344	3.6	Positive		2	376	<b>3.3</b>	<b>Negative</b>
16	2	330	3.8	Positive		½	669	1.9	<b>Negative</b>
	2	343	3.6	Positive		2	439	<b>2.8</b>	<b>Negative</b>
	2	341	3.6	Positive		½	588	2.1	<b>Negative</b>
20	2	360	<b>3.4</b>	<b>Negative</b>		2	444	<b>2.8</b>	<b>Negative</b>
	2	346	<b>3.6</b>	<b>Negative</b>		½	503	2.5	<b>Negative</b>
	½	358	<b>3.5</b>	<b>Negative</b>		2	395	<b>3.1</b>	<b>Negative</b>
	2	545	2.3	<b>Negative</b>		½	523	2.4	<b>Negative</b>
	2	355	<b>3.5</b>	<b>Negative</b>		2	395	<b>3.1</b>	<b>Negative</b>
24	2	360	<b>3.4</b>	<b>Negative</b>	28	½	399	<b>3.1</b>	<b>Negative</b>
	2	346	<b>3.6</b>	<b>Negative</b>	2	347	<b>3.6</b>	<b>Negative</b>	
	½	358	<b>3.5</b>	<b>Negative</b>	½	654	1.9	<b>Negative</b>	
	2	545	2.3	<b>Negative</b>	2	417	<b>3.0</b>	<b>Negative</b>	
	2	355	<b>3.5</b>	<b>Negative</b>	½	730	1.7	<b>Negative</b>	
	2	355	<b>3.5</b>	<b>Negative</b>	2	493	2.5	<b>Negative</b>	
28	2	360	<b>3.4</b>	<b>Negative</b>	32	½	662	1.9	<b>Negative</b>
	2	346	<b>3.6</b>	<b>Negative</b>	2	430	<b>2.9</b>	<b>Negative</b>	
	½	358	<b>3.5</b>	<b>Negative</b>	½	397	<b>3.1</b>	<b>Negative</b>	
	2	545	2.3	<b>Negative</b>	2	360	<b>3.4</b>	<b>Negative</b>	
	2	355	<b>3.5</b>	<b>Negative</b>	½	414	<b>3.0</b>	<b>Negative</b>	
	2	355	<b>3.5</b>	<b>Negative</b>	2	368	<b>3.4</b>	<b>Negative</b>	

Table 6.2: Tauc plot intercepts for low and high energy peaks with their direction, in water. Negative here refers to “reverse” photocurrents, positive to “forward” photocurrents.

Further, the positive response showed little dependency on the time of annealing. This suggests that charge separation in the semiconductor or the efficient transport across the film are not limiting factors in the forward photocurrent.

Although there is variation in the responses, the average reverse response increases with hours of reflux, which relies on band gap excitation. This is as expected as the crystallinity of the sol would be expected to help with the reduction of series resistance and lower recombination through the device. When water is deposited on the surface the reverse response is weakly related to the time of reflux, Figure 6.18.

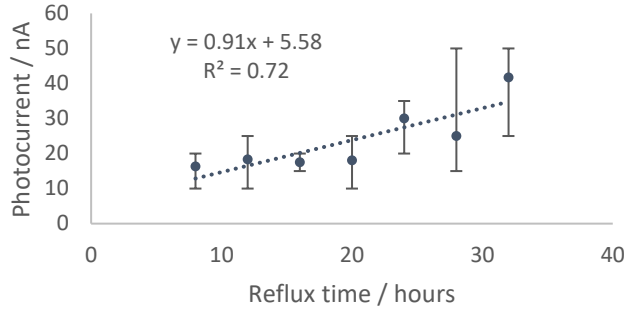
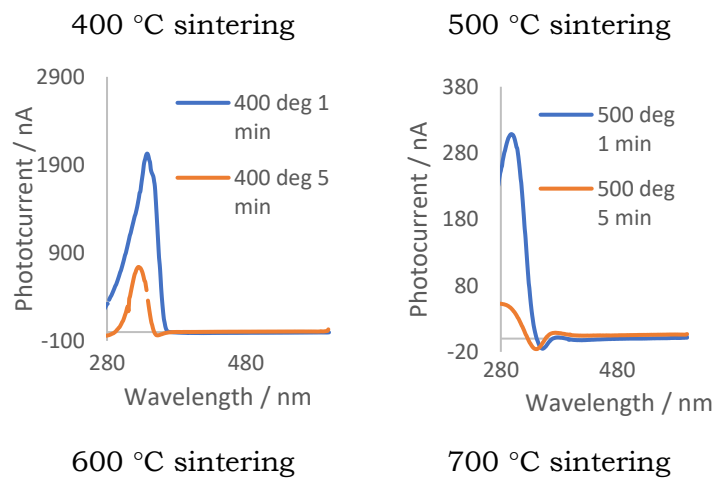


Figure 6.18: Average reverse photocurrent, error bars calculated from the range of devices at these reflux times.

### 6.3.7. Temperature and time of annealing

Comparing to the above forward and reverse responses for the above devices, the high energy peak is likely to be in the forward direction. The lower energy peak is likely to be due to excitation across the band gap and thus in the reverse directions.

A further experiment on pre-annealed 316 stainless steel with a highly crystalline sol showed that the magnitude of the peaks was very sensitive to the time and temperature of annealing. The decrease in the high energy peak is exponential and is not expected to be related to metal diffusion in this case, as the steel was pre-annealed to form a diffusion layer, especially 1 to 5 minutes at 400 °C, would hardly be expected to make such a marked difference, Figure 5.19.



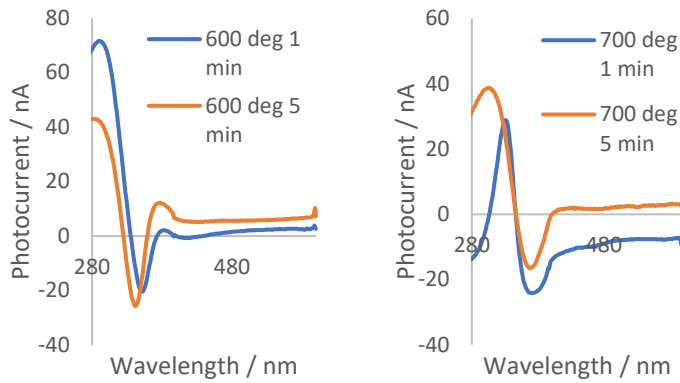


Figure 6.19: Impact of sintering temperature and times on photocurrents.

The highest energy peak decreases exponentially in magnitude for both 1 ( $R^2 = 0.94$ ) and 5 minute ( $R^2 = 0.79$ ) annealing, whilst the lower energy peak photocurrent increases linearly, Figure 6.20.

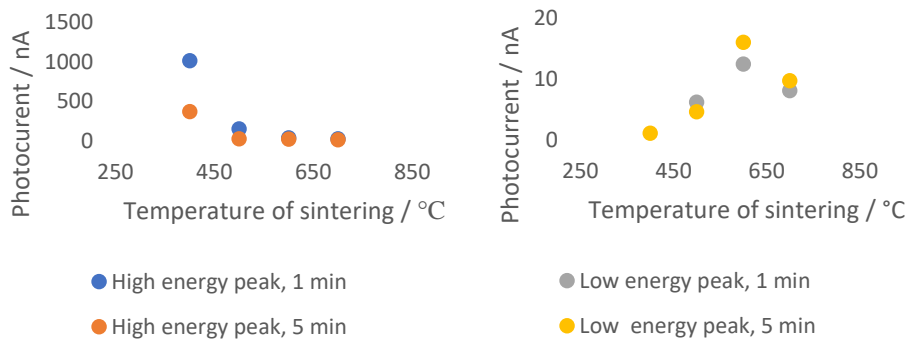


Figure 6.20: effect of temperature and time of sintering for the high energy and low energy peaks.

The size of the “positive” response is high, relative to the highest photocurrent response is for a TiN device. This suggests the origin of this peak can be at least as efficient as the separation of charge in the space charge region.

The prolonged cooling of the higher temperature devices and even the 5-minute device may be enough to eliminate some of these defects at the surface. Strain may also relax in crystals at these high temperatures. The higher temperature devices would therefore have fewer surface defects up to a certain point. Given the photocurrents start to fall at 700 °C, whereby diffusion or rutile crystallisation may begin, it would appear this is a good hypothesis for the reverse current and as expected for band gap excitation.

Similarly, the forward current could increase due to increases in the depletion regions as there are fewer defects.

### 6.3.8. UV-vis studies

There is a remarkable agreement between the positive response position for photocurrent of devices refluxed for over 20 hours and UV-vis spectroscopy results showing an estimated effective band gap of 3.7 eV and the peak in the absorption spectra seen for the silver nanowire mesh. For this reason, whatever the mechanism of the current in the “positive” direction, it is likely that it begins with plasmonic absorption or amplification.

#### UV/vis absorption studies

To study the absorption of the system without the complicating factors of the device, including but not limited to the impact of metal diffusion from the substrate and possible loss of photocurrent through series resistances, a UV-vis study was done of dilute sols with silver nanowire suspensions. There are peaks attributed to plasmonics at 400 nm and 350 nm and a decrease at 320 nm, Figure 6.21, from the silver nanowire suspension.

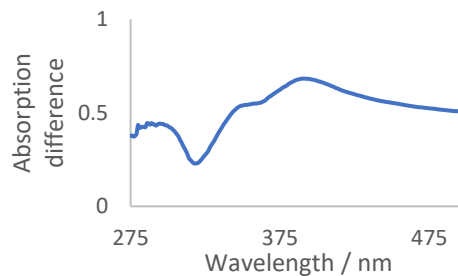


Figure 6.21: Absorption of silver nanowires subtracting solvent background.

A plasmonic peak is observed when the dielectric constant is at a minimum as discussed in the introduction to this chapter. The silver nanowire concentration influenced the absorption non-linearly. Between 2 and 48  $\mu\text{L}$  of 0.25 v/v % of AgNW on an area of 0.32  $\text{cm}^2$ , the lowest absorption per density of nanowire mesh was  $\sim 30 \mu\text{L}$ .

#### Concentration studies

Silver nanowires and  $\text{TiO}_2$  sol were mixed and studied with UV-vis spectroscopy. To deduce how the mixture behaved differently from expected, estimates of the degree of absorption were made from the lowest

concentration of silver nanowires and an in intermediate volume of TiO<sub>2</sub> sol. The observed spectra minus the values for TiO<sub>2</sub> absorption and the expected silver nanowire absorption for its concentration gave the difference spectra, Figure 6.22.

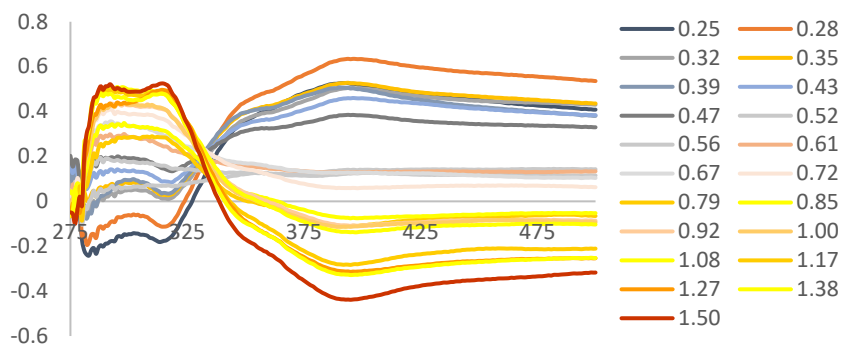


Figure 6.22: UV-vis difference spectra of TiO<sub>2</sub>/AgNW mixtures showing non-linearity in absorption. The legend values refers to the ratio of TiO<sub>2</sub> to AgNW (e.g. 10 uL of TiO<sub>2</sub> to 40 uL of AgNW = 0.25)

For a higher proportion of TiO<sub>2</sub>, the absorption is less than expected across wavelengths above 330 nm whilst it is higher below 330 nm. This may be important for the lack of response in the devices between 330 nm.

From these studies, it would appear the higher the proportion of TiO<sub>2</sub> the lower the absorption of the composite relative to the expected absorption from the sum of the absorption of the parts. It would appear however, that above ~330 nm, this is no longer the case and the absorption of both parts is more than the sum of the components.

However, silver absorption is non-linear with respect to concentration, to separate these effects, increasing concentration plots of the absorption of AgNW and TiO<sub>2</sub> are shown in Figure 6.23, left and right respectively.

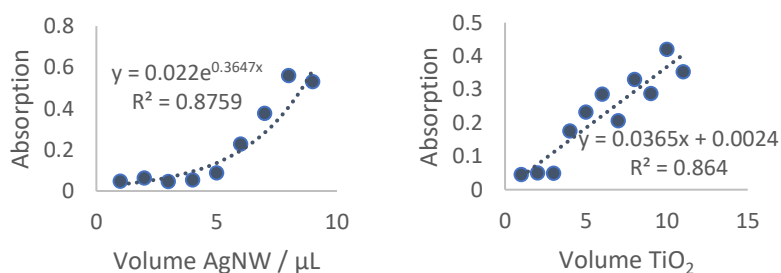


Figure 6.23: Absorption of increasing volumes of AgNW (left) and TiO<sub>2</sub> (right) showing an exponential fit to the former and linearity of the latter at 400 nm.

The mixture of the two materials shows a stronger absorption than the individual components with the difference being a considerable part of the absorption total.

The highest absorptions and differences occur for the highest concentrations of silver nanowires. Amongst the highest concentration of TiO<sub>2</sub>, the absorption in the visible region can be lower than expected, Figure 6.24 (right) showing a negative difference for the highest TiO<sub>2</sub> concentration. This suggests that the TiO<sub>2</sub> sol is interacting with the plasmonic absorption and suggests that denser and therefore higher conductivity silver nanowire meshes could be made more transparent as a less dense one by use of a sol.

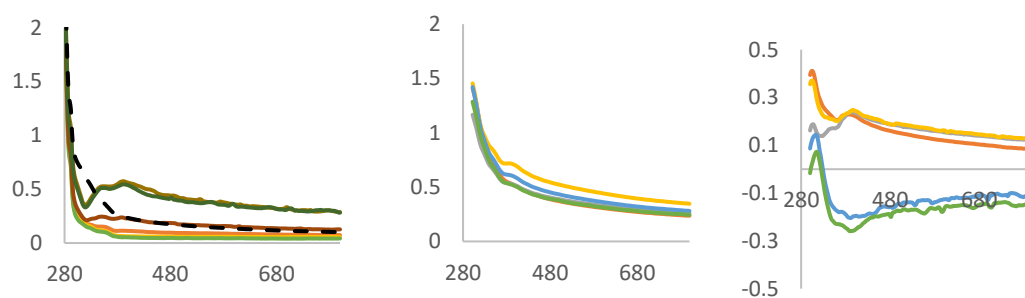


Figure 6.24: 26 to 48 uL of silver nanowires and a 10 uL TiO<sub>2</sub> sol (1/10<sup>th</sup> conc.) control (dashed line) (left) the same volumes of AgNW with 10 uL TiO<sub>2</sub> sol (1/10<sup>th</sup> conc.) (centre) and difference between the observed and estimated absorptions (right).

Previous work in the group found that high density meshes of AgNW showed lower reflectivity at visible wavelengths on Si than the control glass substrate. This was attributed to increased forward scattering of the silver nanowires at wavelengths near the LSPR for the nanomesh. This effect was also observed for AgNW meshes on Si, but the opposite trend was seen on glass and was attributed to the increase in scattering depends on the local density of optical states.<sup>49</sup> TiO<sub>2</sub> would absorb strongly in the UV region so could provide a good surface for scattering plasmons.

### Impact of solvent

A range of solvents were used to investigate the effect of dielectric constant on the absorption. No shift of the peak positions was seen, nor was the peak intensity related to the dielectric constant of the solvent, however it is related to the pKa of the solvents, Appendix 3.

The more acidic the solvent, the smaller the absorption of the silver nanowires and the dye, Figure 6.25. Thus, an acidic solvent reduces absorption of silver nanowires at 550 and 400 nm. For non-protic solvents, the absorption of the dye and solvents is more than the sum of both.

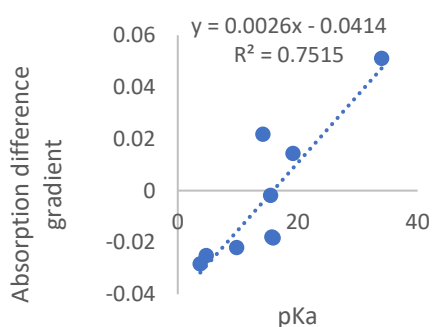


Figure 6.25: Gradient in absorption difference at 400 nm vs pKa of the solvent.

This is an unexpected result as the relative dielectric constant of the medium, here altered from ~6 to 79 showed no impact on the position or intensity of the peaks. The lack of impact could be due to remaining pluronic polymer present from synthesis or the presence of a thin layer of Ag<sub>2</sub>O. Ag<sub>2</sub>O interlayers have been reported in synthetic work on Ag/TiO<sub>2</sub> composites, for instance, as discussed in Chapter 3. The impact of acid could be due to its effect on the silver surface, perhaps providing surface states to effectively scatter LSPR resonances.

### 6.3.9. Temperature studies

As discussed by Linic et al., the temperature dependency of plasmonic reactions is different to photocatalytic semiconductor reactions.<sup>186</sup> In semiconductor photovoltaic systems, there is usually a negative temperature dependence as increasing temperature increases the rate of recombination. Often this is a trade-off, with maximum short circuit currents increase

slightly as the band gap is slightly narrower at higher temperature, increasing the amount of the light that can overcome the band gap.

Plasmonic photocatalysis would be expected to increase in rate with temperature as the distribution of electrons will be on average at higher energies. For a sol based device, Figure 6.26 shows photocurrents across a range of temperatures.

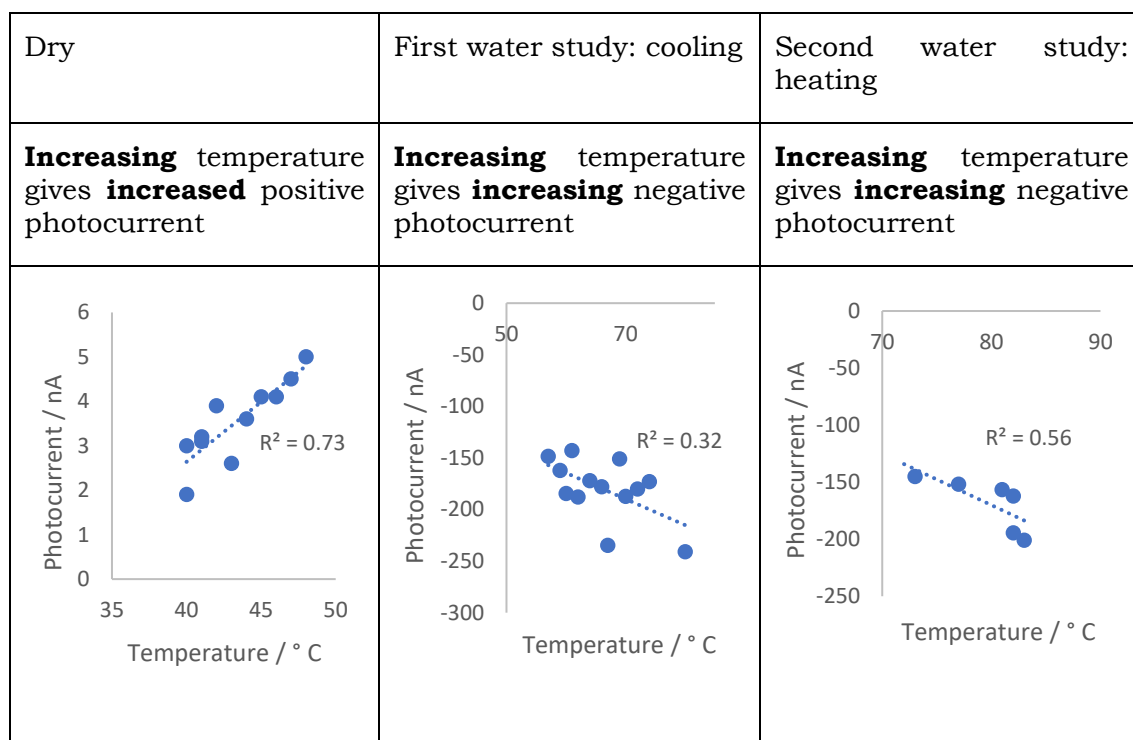


Figure 6.26: Photocurrents measured for a device at a range of temperatures for a device. Left shows photocurrents that increase in magnitude at higher temperatures for a device in air. Centre and right also show an increase in magnitude of the photocurrent with increasing temperature.

The cooling of the device in water (Figure 6.26, centre) will also correlate with the amount of time under the UV light. This could increase the amount of photocurrent through “light soaking” effects, the eventual passivation of surface states through illumination. For this reason, the same device was heated, whilst still illuminated and showed the same photocurrent dependence, with an increase in magnitude with temperature.

Given this experiment was performed with an LED with all approximately equal in energy photons (+/- 5 nm wavelength peak width), a reduced band

gap due to the higher temperatures makes a poor explanation for a doubling in photocurrent in a 20 ° C temperature differential.

A more accurate cooling experiment for another sol derived device, Figure 6.27, shows the temperature dependency following equilibration. These results can be fitted to the Arrhenius equation, where photocurrent generation is assumed to be the rate determining step. The activation energy calculated, at 15.38 kJ mol<sup>-1</sup>, or 0.67 eV, is similar to the values estimated for the height of the Schottky barrier (Chapter 4), Figure 6.27.

Thus, the mechanism suggested by the temperature study is one in which there is a positive temperature coefficient for the device, whereby its efficiency improves at higher temperature, in contrast with semiconductor devices. Further, the activation energy is in the region of the barrier height. This may suggest a plasmonic mechanism or suggest that the rate determining step is one in which a charge carrier must overcome the Schottky barrier.

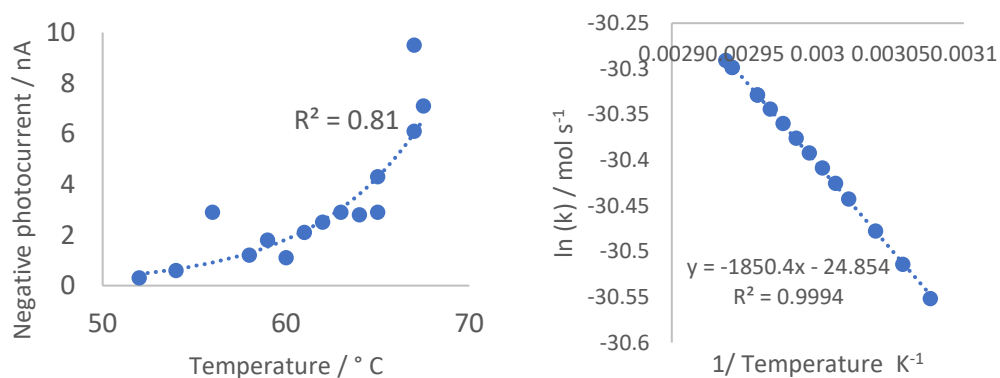


Figure 6.27: Photocurrent measurements for a range of temperatures for a device (right) and an Arrhenius plot of the results (right).

## 6.4. Conclusions

From the study of directionality, for most devices in air, the direction of excitation is in opposition to band gap excitation and at an energy higher than the band gap.

It seems highly likely that, given most of the peaks seen previously for devices such as these are in the same region, that this competing mechanism has dominated the photocurrent results until more highly crystalline devices, devices produced from TiN and passivation by water or organic acids have been fabricated.

Devices formed at extremely low annealing times demonstrate the impact of time and temperature on the magnitudes of these photocurrents. For the high energy photocurrent response, the magnitude decreases exponentially for increased annealing times and for increased temperatures of annealing.

As the solvothermal process produces highly crystalline sols but with a large amount of strain as discussed in Chapter 2, increases in crystallinity in the low temperature range are unlikely and yet large differences are measured in these photocurrents for devices annealed at 400 and 500 degrees for 1 and 5 minutes. Therefore, it seems likely that a surface reorganisation is occurring at these high temperatures and the slow cooling may reduce the amount of defects or vacancies in the film. The high photocurrent in the “forward” direction might depend on the presence of such vacancies, explaining its absence in the presence of passivating agents such as water or tartaric acid and in TiN derived devices.

The lower energy peak, concurrent with the onset of TiO<sub>2</sub> absorption increases linearly with temperature and time between 1 and 5 minutes and this may be due to improved sintering of the particles and reduced defects. A highly crystalline film would be expected to be an advantage in a Schottky barrier device.

Similarly, for sol derived devices of increasing crystallinity, the “forward” direction showed activation energies between 2.8 and 3.6 eV and showed little dependence on the extent of crystallinity. For the “reverse” direction peaks, the Tauc plots suggest band gaps of 2.5 – 3.5 eV for dry devices, usually slightly lower than the band gap energy for TiO<sub>2</sub>, likely due to a small amount of excitation from an oxygen vacancy, consistent with reported values for an anatase TiO<sub>2</sub> device.<sup>152</sup>

The TiN derived devices following passivation with water show peaks mainly in the direction of direct excitation and usually around 3.6eV with an indirect mechanism. The differences may be a difference in crystallinity between the

sol derived devices. The TiN devices are more ideal, with higher barriers and likely larger depletion region. The sol derived devices are likely to have more defect and surface states.

The temperature dependence studies suggest a process for the “reverse” direction that increases in efficiency with temperature under an LED. This was observed both heating and cooling the device to control for the impact of “light soaking”. This is counter to what would be expected from a purely photocatalytic reaction driven by the excitation of electrons in the semiconductor. The Arrhenius fit suggests an activation energy of nearly 0.7 eV, approximately the Schottky barrier height. This suggests the activation energy of the rate determining step depends on overcoming the barrier.

The “forward” positive photocurrent can be as large in magnitude as the best band gap excitation currents. As discussed in the following chapter, it has also been observed for dye sensitized devices.

A similar set of results are reported for FTO/TiO<sub>2</sub>/Au and FTO/Au/TiO<sub>2</sub> contacts, due to the existence of an energy well formed between the two contacts. From capacitance measurements, the carrier density of the FTO/Au/TiO<sub>2</sub> contacts was much higher, suppressing the width of the space charge layer and promoting the cathodic mechanism.<sup>203</sup>

# 7. Competing photocurrent processes in the visible region

## 7.1. Overview

In Chapter 5 the improvements in the photocurrents for these Schottky barrier devices are reported, including the more efficient devices seen when forming low defect films of  $\text{TiO}_2$  on TiN films. In Chapter 6, the observation of two opposing peaks was discussed and a plasmonic photocatalytic mechanism proposed involving the silver nanowires absorbing light and driving an oxidation reaction.

However, following functionalisation of these devices with organic dyes, the same dichotomy in photocurrent directions can be seen. The significance of this is that many composite systems are used to study dyes, to better understand the activity of photocatalysts that may be able to degrade organic pollutants. The comparison of this device with literature on plasmonic

photocatalysis may give some insights into mechanisms of these devices and vice versa.

For that reason, this Chapter will begin with the advantages of a dye-sensitized Schottky barrier device and an overview of literature on metal nanoparticle/semiconductor photocatalysis in the visible region. Results showing that some dyes can sensitise the photocatalytic mechanism responsible for the “forward” current shown in Chapter 5. If this is the case and the reaction is the oxidation of water, this could lead to better photoelectrocatalytic device and a greater understanding of the impact of plasmonically driven reactions on dyes.

## 7.2. Introduction

### 7.2.1. Dye functionalisation of Schottky barriers

The visible light sensitization of Schottky barriers with quantum dots have been shown previously, but dyes offer several important advantages, including;

- the areas available to functionalise are very small, and even quantum dots are much larger than the cross section of an adsorbed dye
- many dyes have already been optimised for use in similar devices
- there is no post-deposition treatment required
- dyes may optimise the performance of Schottky barrier devices
- the study of dyes on Schottky barriers may provide insights into dye functionalisation, such as which transitions result in photocurrent, degradation and impact of plasmonic nanostructures.

$\text{Ru}(\text{dcbpy})_2(\text{NCS})_2$  and similar dyes have been studied extensively. If there is good overlap between the LUMO and the conduction band of the semiconductor, the electron transfer could be activationless and given the speed of injection, this might occur from non-thermalised vibrationally excited states, complete in 100 fs, and with nearly unity quantum efficiency.<sup>204,205</sup> The LUMO of  $\text{Ru}(\text{dcbpy})_2(\text{NCS})_2$  is reported to be 0.3 V above the conduction band.<sup>204,205</sup>

### 7.2.2. Dye degradation

Over  $1 \times 10^5$  tons of dye makes its way into streams and water bodies annually from textile and paper waste effluents, causing large amounts of environmental damage.<sup>206</sup> Photocatalysts could offer a potential environmental remediation strategy and experiments on organic dyes might provide insight into how other environmental pollutants can be oxidised.

Composites often show more photocatalytic activity than the individual components. The visible response of dye and metal semiconductor systems results in a range of possible mechanisms including:

- Plasmonic particles result in higher absorption of light
- Amplification of dye absorption by plasmonic excitation
- Dye excitation and injection of electrons into the conduction band, followed by dye cation breakdown
- Direct excitation over the band gap of the material, resulting in reactive electrons and holes which can destroy the dye
- Metal nanoparticles acting as electron sinks, prolonging the charge-separated state
- and as sites for the reduction of oxygen, providing a catalytic site.

Other potential mechanisms include the destruction of the dye through superheating around the plasmonic structure causing thermal breakdown and an increase in scattering, causing better light harvesting.

The mechanisms possible apart from breakdown of the dye photocatalytically are shown in Figure 7.1.

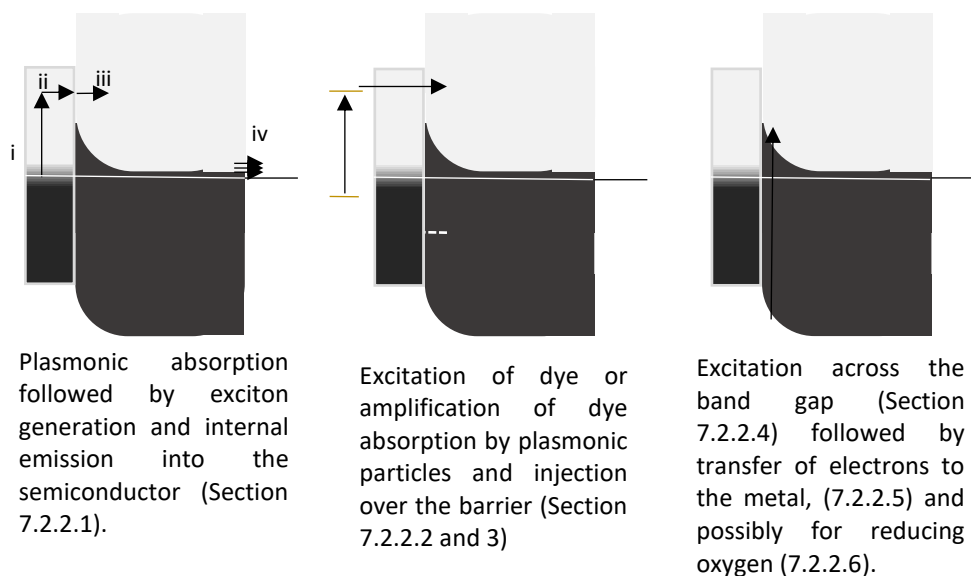


Figure 7.1: Diagrams showing possible mechanisms to produce reactive species through excitation of plasmonic modes, dyes and across semiconductor band gaps.

Due to the possibility of many mechanisms being possible for a system under UV light, reports on visible region active photocatalysts have attracted criticism due to the difficulty in identifying good controls and identifying the light absorbing species.<sup>207</sup>

### 7.2.3. Material considerations in dye degradation

Generally in dye photodegradation experiments, the catalyst is suspended in the dye solution and irradiated. To study decoloration, samples are taken and centrifuged. For this reason, many dye degradation experiments are not comparable as the volume of the catalyst, dye, pH, degree of agglomeration, surface area, particle morphology, irradiation and agitation may be different. Too much catalyst or dye could block light to active parts of the catalyst.<sup>206</sup>

To achieve visible light photocatalysis,  $\text{TiO}_2$  is often doped with metals, such as Ni, which allows the formation of inter-band states and therefore allows absorption in the visible region. These defects have also been hypothesised to help with the formation of surface oxygen vacancies.<sup>208</sup> The dopants may increase the rate of recombination but this may be an acceptable trade off as the absorption can be shifted into the visible region.

In contrast, doping has also been used to prevent recombination. The doping of  $\text{TiO}_2$  with Bi shows an enhanced visible region absorption. The

photoluminescence indicates lower intensity for Bi doped catalysts, therefore the presence of Bi is hindering the electron-hole recombination.<sup>209</sup>

There is frequently an optimum doping rate reported, with more metal nanoparticles yielding a poorer response past a certain concentration, attributed to shadowing and providing a site for recombination, reducing the space charge region, inducing surface states, shunting the interface or reducing contact with an electrolyte.<sup>210 211 212</sup> In the degradation of methylene blue on silver nanoparticle functionalised TiO<sub>2</sub>, there is an optimum Ag nanoparticle concentration of 2% between 0 and 10%.<sup>210</sup> Similarly, for AgNPs on P25, for the degradation of methyl orange under UV light, follows the doping concentrations of 0.5 % > 1.5% > 3 % > 0 % > P25 whereby the silver is proposed to increase mid-gap band gap states, resulting in poor efficiencies at high concentrations.<sup>211</sup>

#### 7.2.4. Mechanisms for dye photocatalysis

Each of the mechanisms from Figure 7.1 will be briefly introduced.

##### Increased light harvesting

Christopher et al showed methylene blue degraded under 3.4 eV radiation on Ag nanoparticle functionalised TiO<sub>2</sub> compared to unfunctionalized controls. The LSPR of the nanoparticles was at 2.2 eV. There was no difference in the activity with Au nanoparticles, though the Schottky barrier would be expected to change, suggesting electron transfer to the metal nanoparticle at the Schottky barrier is not having an impact on the catalysis.

<sup>213</sup>

Indeed, electron transfer to and from the particles appears unlikely due to an insulating layer of polymer, PVP. There is no shift in absorption due to the removal of electrons from the metal nanoparticle, nor is there an absorption in TiO<sub>2</sub> due to electrons in the conduction band.<sup>213</sup>

Given a lack of sensible mechanisms, the authors attribute the higher activity of Ag nanoparticle functionalised TiO<sub>2</sub> to radiative transfer from the metal nanoparticle. Further, the metal nanoparticles appear to fill traps on the surface, as evidenced by improved photoluminescence. Nano-cubes showed better absorption properties than spheres for the same mass, with improvement in rate correlating with integrated areas for the particles for the

UV-vis spectrum, suggesting improved absorption results in higher photocatalytic efficiency.<sup>213</sup>

#### Amplification of absorption by dyes

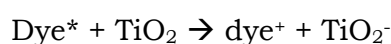
The increased absorption of the dye/plasmon systems have been reported widely. As well as the intense absorption of the nanoparticle itself, with the absorption cross section is much larger than the particle itself. The field around nanoparticles can also increase the absorption of dyes.

A study of Ag nanoparticles deposited on TiO<sub>2</sub> nanotubes functionalised with N719 dye shows more absorption than the sum of its components. The photocurrent improvements of such devices were thought to be due to the fields around plasmonic particles being helpful in dye excitation. The increased fill factor in these devices was attributed to the binding of silver nanoparticles to high energy defect sites.<sup>214</sup>

A DFT model of the amplification of Ru(dcbpy)<sub>2</sub>(NCS)<sub>2</sub> modes by enhancement by plasmonic silver interactions predicts a rapid drop in enhancement with distance. It also shows that the absorption peaks of Ru(dcbpy)<sub>2</sub>(NCS)<sub>2</sub> are not equally enhanced, with the peak at 407 nm showing a large enhancement and the peak at 311 nm showing very little. This is ascribed to the direction of the transition dipole within the molecule and the directions of enhancement of the nanoparticle field.<sup>176</sup>

#### Sensitization mechanism

Under visible light, dye photocatalysis could occur by the electron injection into the semiconductor, followed by breakdown of the dye cation.



Early studies on aerated P25 suspension degradation of alizarin red suggests a self-sensitisation mechanism under white light (<420 nm). The photo-efficiency of decolouration of dye solution was 5 times greater under visible light than UV radiation with zeroth order kinetics. No organo-peroxides were formed, whilst the OH radical was closely related to the degradation of dye, as measured by ESR. Once discoloured however, chemical oxygen demand does not change, suggesting the sensitization mechanism must be necessary for degradation.

A similar result is found in the breakdown of sulfurodamine-B (SRB) dye, under a UV filtered lamp with first order kinetics on a Pt functionalised TiO<sub>2</sub> catalyst, which was 3 times faster than the control. The increase in activity is proposed to be due to the nanoparticle acting as an electron sink and reducing O<sub>2</sub> to the superoxide radical, following excitation by the dye. In this study, ESR was used to show the O<sub>2</sub> superoxide formed when the catalyst was irradiated. Cu<sup>II</sup> and Fe<sup>III</sup> ions suppressed the catalysis, due to the interference with the reduction of oxygen. To act as a control for the visible light absorbing dye, 2,4-DCP was used as a control as it does not absorb visible light and showed no photocatalysis.<sup>215</sup>

De Souza et al. report on a bifunctional linked AgNP-TiO<sub>2</sub> (P25) nanoparticle system used for the degradation of alizarin dye, which was more effective than the controls under UV. This is hypothesised to be due to the electron scavenging by the metal due to the Schottky barrier at the interface. However, under UV filtered light, the silver nanoparticles hindered the catalysis, attributed to competition with the dye.<sup>216</sup>

Under UV/vis light, excitation across the semiconductor is considered the mechanism of oxidation, with the Schottky barrier potentially working as an electron trap to mediate the transfer of electrons to O<sub>2</sub> or other species. Under just visible light the mechanisms of sensitization of TiO<sub>2</sub> and plasmonic absorption are used to explain the photocatalysis.<sup>210,216</sup>

#### Interaction of the LUMO and the conduction band

Similarly to Ru(dcbpy)<sub>2</sub>(NCS)<sub>2</sub> which shows hybridised LUMO-conduction band orbitals, facilitating the direct transfer of charge into TiO<sub>2</sub>, alizarin red has also been modelled by DFT to contain hybridised LUMO-conduction band orbitals.

There is a stabilising effect of the LUMO on the TiO<sub>2</sub> cluster. As the size of the nanocluster grows, the dye LUMO moves into the TiO<sub>2</sub> cluster, being favourable for a "type-II", one step electron injection mechanism, which can occur adiabatically in 6 femtoseconds. In unbound alizarin, the LUMO is modelled to be distributed over the whole molecule, whilst after binding the Ti, there is a noticeable contribution from the Ti, particularly in LUMO + 1 and +2 states. Some authors suggest the shift in the energy levels are

stabilised by the field of the semiconductor, this DFT study suggests this is not the case.<sup>217</sup>

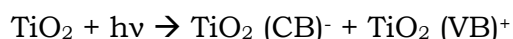
The uniqueness of the alizarin complexes, is as reported by Iorio et al. is the presence of redox-active groups, namely the 9,10-dioxo and 1,2-catechol groups, which could both excite electrons into the TiO<sub>2</sub> conduction band or receive electrons from TiO<sub>2</sub>. For this reason, the authors report the reduction of alizarin molecules on TiO<sub>2</sub>. The DFT model assumed binding to a solvated Ti atom, justified by the LUMO being mainly localised on the dye.<sup>218</sup>

There would appear to be a small driving force for the reduction of alizarin molecules on TiO<sub>2</sub>, though most of the carriers recombine. The presence of IPA as a radical scavenger inhibited the degradation of alizarin molecules, suggesting dye degradation may result from hydroxyl radicals.<sup>218</sup> The reduction of alizarin on TiO<sub>2</sub> occurs with or without reducible alcohol and the same kind of spectral changes are also accomplished by the addition of alizarin to a pre-irradiated solution and the original alizarin molecule is recovered by introduction of oxygen.<sup>218</sup> Therefore the authors conclude that the efficient reduction of alizarin red requires a hole scavenger in order to allow the accumulation of reducing equivalents to break down alizarin red.<sup>218</sup>

Similarly, in a study of alizarin red on Bi doped TiO<sub>2</sub>, a self-sensitization mechanism with the concurrent production of hydroxyl radicals at the Bi 6s states is used to describe dye degradation and explain the sensitivity of the reaction to hydroxyl radical scavengers but lack of sensitivity to electron or oxygen radical scavengers.<sup>209</sup>

Direct excitation over the band gap of a material

Band gap excitation can involve photoexcitation across the semiconductor photocatalyst;



The holes can oxidise water, to produce an adsorbed OH radicals and H<sup>+</sup>. The conduction band electron can reduce adsorbed oxygen, which can undergo further reactions with water to form hydroxyl radicals.<sup>206</sup>

Au nanoparticles double the water splitting activity of TiO<sub>2</sub> under AM 1.5 illumination. As filtering the UV light resulted in the loss of over 99% of the

activity, the advantage of metal nanoparticles is likely the passivation of trap states, evidenced by shorter half-lives for photovoltage decay. There is limited activity in the visible region, but electric field amplification and hot electron generation are the likely mechanisms for photocatalysis.<sup>212</sup>

An advantage of ferroelectric materials is the ability to separate charge carriers due to the internal fields in the asymmetric crystal, and as such, they may yield useful information about dye degradation. In a study of a ferroelectric material, BaTiO<sub>3</sub> with Ag nanoparticles, the organic dye Rhodamine B was degraded. It was found that with simulated solar light that the UV component was vital and no detectable degradation was occurring below the band gap of the material.<sup>219</sup>

The LUMO for the Rhodamine B dye is reported as 1.1 eV and HOMO of -1 eV vs NHE, placing the LUMO above the CB edge for the material at -0.94 eV. Upward bending of the semiconductor of the ferroelectric makes electron transfer to the semiconductor unlikely, consistent with a lack of activity in the visible wavelengths.<sup>219</sup>

#### 7.2.5. Impact of surface states on dye degradation

The transparent TiO<sub>2</sub> system on a conductive substrate provides the opportunity to study the formation of anions controllably at the surface of TiO<sub>2</sub>. A potential was applied to form O<sub>2</sub><sup>-</sup> radicals using a 3-electrode setup. Under -0.5 V potential under visible light (>420 nm), there is a 2.4 fold rate increase compared to the dark. There is a synergistic effect between the potential and the radiation for Rhodamine B dye mineralisation. This reaction also depended on the presence of oxygen. Under +0.5 V potential, mineralisation was inefficient and de-alkylation was seen instead. No reactive oxygen species were observed by ESR.<sup>220</sup>

Cationic dyes (rhodamine B and malachite green) could be mineralised whilst the anionic dyes could not under positive or negative potentials, though all could be degraded on TiO<sub>2</sub> under illumination. By outcompeting a cationic dye with a cationic competitor at the surface, the degradation could be inhibited, demonstrating the impact of attraction to the TiO<sub>2</sub> surface. The authors suggest the possibility that the relative charges of the conduction band allows both a superoxide radical can form alongside the cationic dye.<sup>220</sup>

Similarly, in a study of the breakdown of methylene blue on AgNPs on TiO<sub>2</sub> (rutile), there was a pH dependence that favoured higher pH and was inhibited by Ni(II) ions. Both effects were explained by the interaction by the dye (cationic) with the (negative) surface of the TiO<sub>2</sub> and competition for catalytic sites.<sup>221</sup>

#### 7.2.6. Metal nanoparticles as electron sinks

In many instances, the increased photocatalysis seen in these systems is explained with the Ag nanoparticles providing an electron sink when the electron-hole pair is generated. The transfer of electrons from the semiconductor has been measured by a lower photoconductance in the semiconductor in some cases.<sup>29</sup> In this explanation, the electrons on the silver nanoparticles can then react with other species such as oxygen or water to produce the active superoxide or radical hydroxide species.<sup>221,222</sup> One of the reasons for the transfer to the metal in this case is the relative energies of the conduction band and the Fermi level of the TiO<sub>2</sub> and Ag, though this neglects the formation of the Schottky barrier. This mechanism is used to explain the photocatalysis of methylene blue on “bamboo” type TiO<sub>2</sub> rods.<sup>223</sup>

For instance, a study of Pd/TiO<sub>2</sub> (20 nm size) was used to catalyse the breakdown of Rhodamine B. The plasmonic absorption of the Pd on the TiO<sub>2</sub> resulted in an estimated of 8% of available solar wavelengths, due to its very small size and the permittivity of the environment.<sup>224</sup> There are two proposed mechanisms; that the LSPR plasmonic excites electrons over the Schottky barrier (reported as 1.1 eV) into the TiO<sub>2</sub>, therefore the holes in the metal provide the catalytic site. The other mechanism is excitation over the bandgap, whereby the catalytic species will clearly be holes in semiconductor, or accumulated holes in the Pd following migration to the metal, and thus increased carrier lifetime. It is proposed that activity is due to a combination of these effects, strengthened by the extended contacts between the Pd and the semiconductor due to the growth method.<sup>224</sup>

#### 7.2.7. Reduction of oxygen

In many studies, the reduction of oxygen is assumed to take place following the transfer of electrons from the metal nanoparticles. However, some assume electrons are scavenged from the conduction band of TiO<sub>2</sub>, as is

hypothesised in the degradation of methylene blue on a Ag nanoparticle functionalised anatase surface.

The degradation of methylene blue using silver nanoparticles on anatase  $\text{TiO}_2$  showed a dependency on the present of oxygen. However, it was also found that pore size had a larger impact on degradation than doping, suggesting a sensitization mechanism.<sup>225</sup>

15 nm Au nanoparticles were deposited uniformly onto  $\text{TiO}_2$  photonic crystals made by using spherically porous photonic crystal of  $\text{TiO}_2$ , resulting in enhanced light absorbing by the LSPR and the photonic crystal and increasing the electron-hole lifetime, resulting in the breakdown of 2,4-dichlorophenol by 2.3-fold compared to simply Au nanoparticles on nanoparticulate  $\text{TiO}_2$ .<sup>226</sup>

To investigate the mechanism of breakdown of 2,4-dichlorophenol, a hole scavenger did not hinder the catalysis, though a radical scavenger did. The presence of  $\text{O}_2$  enhanced the photocatalysis and this suggests oxygen and OH radicals are an important reactant in this system and ESR confirmed both species, formed from the transfer of electrons from the conduction band of  $\text{TiO}_2$ .<sup>226</sup>

The presence of chemisorbed oxygen species is also used to explain an extremely rapid degradation of a range of dyes with  $\text{NaBH}_4$  on Ce- $\text{TiO}_2$ , particularly in the presence of Au nanoparticles which extends the absorption into the visible region and provides a catalytic site for the reduction of  $\text{NaBH}_4$  to reduce methylene blue, methyl orange, congo red, rhodamine B and malachite green.<sup>227</sup>

#### 7.2.8. Prevention of electron transfer

A thin layer of  $\text{Al}_2\text{O}_3$  was grown as a shell on  $\text{TiO}_2$ , preventing electron transfer and improving dye binding. This composite was found to have a higher activity for the degradation of dyes, including alizarin red. The increase in activity is attributed to the inhibition of electron transfer.<sup>228</sup>

A similar method was used by Bandara and Pradeep to alter the flat band potential of  $\text{SiO}_2$  and  $\text{TiO}_2$  by growing a layer of MgO. For the largest amounts of MgO (10% wt/wt) resulted in a shift of -0.85 for  $\text{TiO}_2$  resulting in a more efficient DSSCs, as the open circuit potential between the quasi-Fermi level

in the film and the energy of the redox couple is larger. The effect of the MgO layer is proposed to be effective by blocking back-electron transfer.<sup>229</sup>

### 7.2.9. Summary of literature results

Many of the above experimental details and some others outlined in literature are detailed in the Table 7.1 for easier comparison. Photocatalysts and dyes have been studied under a range of conditions, and authors report many mechanisms. Many authors discuss the possibilities of two mechanisms, one for the UV region, usually an amplification of fields, or radiative transfer.

In the visible region, there are fewer options such as self-sensitization mechanisms and plasmon absorption leading to high fields in the proximity of metal nanoparticles on semiconductors. In some cases, where a lack of activity below the active material band gap, or through introduction of an electron transfer blocking layer, self-sensitization is no longer a plausible mechanism.

The inhibition of catalysis by Ni(II) ions was thought to be due to competition with dyes for cationic sites on TiO<sub>2</sub>, suggesting electrons are transferred away from the site with the dye.<sup>221</sup> Many studies suggest the degradation of dyes may be due to the transfer of electrons to metal nanoparticles but a study of Ag on a photonic crystal used to break down 2,4 dichlorophenol showed no hindrance by the presence of a hole scavenger and an enhancement when an electron scavenger (O<sub>2</sub>) was present, suggesting the excited electron reduction of the acceptor species may be more important.<sup>220,226</sup>

Experiment	Conclusions	Ref.
<b>Degradation of methylene blue</b> by oxidative process with O <sub>2</sub> as electron scavenger. First order in MB at 365 nm (15mW/cm <sup>2</sup> ). Gold controls were made and showed little difference in activity.	The authors hypothesise no electron transfer to or from TiO <sub>2</sub> as there are no absorption observed for electrons in TiO <sub>2</sub> or electrons from TiO <sub>2</sub> to metal and as the nature of the metal makes little difference.  The authors conclude a radiative transfer mechanism, assisted by scattering.	213
<b>Enhancement of DSSC currents using N719 dye</b> through use of Ag nanoparticles on TiO <sub>2</sub> nanotubes.	Exciton generation by enhanced light harvesting through the enhanced field helping with the excitation of the dye. Increased fill factor was thought to be due to preferential Ag deposition at traps.	214

<p><b>Ferroelectric material with silver nanoparticles for degradation of Rhodamine B</b> was tested for effectiveness. Only the UV component of the light was active.</p>	<p>The position of the flat band was calculated from electron affinity, work function and band gap and determined to hinder electron injection.</p> <p>Given only the UV component is active, which is over the band gap of the material is 3.1 eV.</p>	219
<p>Pt on TiO<sub>2</sub> was synthesised. 0.2% was optimum. <b>Sulfurodamine-B was degraded in the visible region using a 500 W lamp</b> with a 420 nm filter.</p>	<p>A UV absorbing organic was used as a control which showed no degradation. The authors hypothesise a H<sub>2</sub>O<sub>2</sub> mediated reaction, with O<sub>2</sub> reduction followed by reaction with protons. To back this up, Cu<sup>II</sup> and Fe<sup>III</sup> controls were used to compete with reduction of oxygen, which can be observed by ESR.</p>	215
<p><b>Degradation of alizarin red on unfunctionalised and silver nanoparticle functionalised P25.</b> The composite outperformed the P25. With UV filtered light, the catalysis is hindered on the composite. Rates of degradation were reported as 5.09 x 10<sup>-2</sup> min<sup>-1</sup> for the composite under all light and 1 x 10<sup>-2</sup> min<sup>-1</sup> for UV-filtered light for the 260 chromophoric peak from the dye.</p>	<p>The composite outperforming the P25 was attributed to electron scavenging by the silver nanoparticles due to the Schottky barrier. Under just visible light, the composite was outperformed by P25. The sensitization is followed by the electron in the conduction band reducing oxygen to form O<sub>2</sub> and hydroxyl radicals which, with the dye cation, react with species in the bulk media.</p>	216
<p>Silver nanoparticles (laser induced reduction of AgNO<sub>3</sub> in IPA, 3-6 nm particles produced, visible absorption max of approx. 470 nm) were deposited on TiO<sub>2</sub> (P25). <b>Degradation of methylene blue</b> was achieved to 82.3 % in 2 hrs following illumination with a 150 W halogen lamp. Adsorption takes approximately 20 mins to equilibrate. Optimum pH of 6.9. Rate did not correlate with silver concentration.</p>	<p>The UV-vis absorption does not correlate with the amount of silver in the catalyst. More silver must be inhibiting a higher rate. The increase in silver is hypothesised to be due to competitive binding with dye or O<sub>2</sub>, shadowing or by facilitating recombination of electrons and holes at the surface.</p>	210
<p><b>Water oxidation was attempted on gold functionalised rutile TiO<sub>2</sub> films.</b> 8 nm particles were attached to TiO<sub>2</sub> nanorods using MPA. 3-electrode setup with Pt counter electrode was used to measure water oxidation. Currents under light of 1.49 mA/cm<sup>2</sup> at 0V, twice the TiO<sub>2</sub> control. Cutting off wavelengths less than 430 nm, the current is 0.011 mA/cm<sup>2</sup>, suggesting a small impact of SPR. Only nanoparticles improved response under white light, nanorods did not.</p> <p>The enhancement of activity in the visible region was incompatible with electric field magnification and scattering as the light is below the band gap of the semiconductor. The half-life of the photovoltage was lower for nanoparticles compared to the rods and controls, suggesting the particles have an impact on trap states.</p>	<p>The absorption for the LSPR corresponds to the IPCE.</p> <p>The authors conclude the enhancement in the UV regions are due to surface passivation and electric field amplification. In the visible region, field amplification and hot electron generation is the likely mechanism.</p>	212
<p>Sol TiO<sub>2</sub> was electrodeposited on an ITO surface followed by sintering. UV-vis shows a small band gap of 1.8 eV, attributed to mid band gap defect states as well as the expected band gap.</p>	<p>The lowest band gap sample was sintered for 2 hours at 400 °C, which may be due to diffusion.</p>	127

<p>Pseudo first order kinetics were observed for <b>Reactive Red 2 and Disperse Yellow 231 degradation</b>. Rate twice as high for RR2 and 50% higher for DY231.</p>	<p>The rates are compared to the unsintered, low temperature film. The rate is not considerably higher considering the expected large increase in crystallinity that would be expected.</p>	
<p><b>Al<sub>2</sub>O<sub>3</sub> thin interlayer grown on the outside of TiO<sub>2</sub> particles.</b> This is accomplished by forming an Al and Ti hydroxide from precursors, the Al is eliminated from the centre by sintering. <b>The dyes studied; Rhodamine B, Rhodamine 6G, Rhodamine 101, Malachite green and Alizarin Red</b> was found to bind Al<sub>2</sub>O<sub>3</sub> preferentially to TiO<sub>2</sub>. The enhanced photocatalysis was proposed to be due to the inhibition of electron injection. The rates of degradation were nearly 5 fold the pure TiO<sub>2</sub> catalyst.</p>	<p>Al<sub>2</sub>O<sub>3</sub> could prevent electron transfer by the higher CB position. This suggests electron transfer to TiO<sub>2</sub> is a hindrance to the degradation of dyes.</p>	228
<p>In a breakdown <b>of methylene blue on Ag nanoparticle functionalised TiO<sub>2</sub></b>, showing a pH dependence that favoured high pH and was inhibited by Ni(II) ions.</p>	<p>Suggest there is a competition for negative sites on TiO<sub>2</sub>. However, the metals are proposed to provide an electron sink when the electron-pair is generated. Electrons on the silver react with oxygen or water to produce the active oxidising species.</p>	221
<p><b>15 nm Ag particles on a TiO<sub>2</sub> photonic crystal show enhanced breakdown of 2,4-dichlorophenol</b> by 2.3 times compared to nanoparticles on a nanoparticle film. <b>Formic acid as a hole scavenger does not hinder photocatalysis.</b> The presence of O<sub>2</sub> enhances it and radical scavenger reduces it.</p>	<p>As well as the extended light absorption due to the plasmonic particles amplified by the photonic crystal. The enhanced photocatalysis is proposed to be due to the increases in electron-hole lifetime.</p> <p>The reduction in activity with radical scavengers but enhancement in the presence of oxygen suggests the OH radicals, as does the ESR studies.</p> <p><b>The proposed mechanism is the transfer of electrons from the metal to the conduction band of TiO<sub>2</sub>.</b></p>	226
<p>TiO<sub>2</sub> silver composite (P25) was used to show degrade acetone.</p>	<p>The silver is hypothesised to be acting as an electron capturer.</p>	156
<p>Dyes are stable under visible light, but degrade in the presence of TiO<sub>2</sub>. <b>Applied potential results in cationic dyes on negatively charged TiO<sub>2</sub> with visible light.</b> Anionic dyes could not be mineralised with either potential. Cationic competitors inhibit degradation, whilst anions do not.</p>	<p>Oxygen has been hypothesised to suppress recombination or direct participation. Due to the potential of an electron in a conduction band of TiO<sub>2</sub> and the formation of oxygen radical, <b>the dye cation and the oxide radical can coexist.</b></p>	220
<p>Alizarin red degradation at 365 nm was performed on Ni doped TiO<sub>2</sub>, 1.5% was optimum, ~3.5 times faster than the P25. The undoped anatase phase also showed better catalysis than P25.</p>	<p>Anatase phase by this synthetic method is more effective than the anatase/rutile mix of P25, even though charge separation occurs at the interfaces between anatase and rutile.</p> <p>Ni could help in the visible absorption of the photocatalyst, but here, absorption is occurring above the band gap of the semiconductor. However, the presence of Ni<sup>2+</sup> ions is not hindering the dye degradation. The reactions occurring could be faster than thermalisation with defect states.</p>	208

	A cationic dye state is unlikely to be part of this degradation.	
Silver and gold nanoparticles offer the advantage of enhanced absorption of dyes, though strongly oxidising redox shuttles may degrade the particles. The use of a wetting layer can reduce the amount of TiO <sub>2</sub> that needs to be grown to protect the particles. The red shifting of the absorption of the particles is linear with the thickness of the particles. It then plateaus.	The 10 nm thickness of TiO <sub>2</sub> on metal nanoparticles is reported to be the sensing distance, which is relatively small, on account of the high refractive index of TiO <sub>2</sub> .	230
Sol gel Bi doped TiO <sub>2</sub> catalysts were crystalline with high surface area. They have Bi doping into a TiO <sub>2</sub> lattice. The inhibition of electron-hole recombination resulted in lower photoluminescence. Due to sensitization mechanism, dye is degraded on TiO <sub>2</sub> to some extent. Activities increase up to 1%.	IPA and KI was used as ·OH or hole scavengers and slowed degradation. Formic acid as an electron scavenger had little effect. Sodium azide was similarly ineffectual at slowing rate, suggesting the importance of hydroxyl radicals to dye degradation.	209

Table 7.1: Selected papers on dye degradation detailing the study and the conclusion the authors draw from their results.

### 7.3. Results

The size of the currents measured for the UV response has always been low due to the low active areas of the device. The active areas measured by thermionic emission model are very low. Light above the band gap of the semiconductor excites the TiO<sub>2</sub> within the depletion region. However, in the sensitized device, there is another factor, the absorption of light by the dye and the injection of electrons into the semiconductor followed by the reduction of the dye by the silver nanoparticle. For the ruthenium dyes commonly used to produce DSSCs, the quantum efficiency for absorption and injection of charge is usually extremely high. However, in this system, there is likely to be much more band bending than would be seen in a DSSC, resulting in a lower efficiency of electron injection into the semiconductor.

As before, the extremely limited areas of these devices would be expected to compound these problems. For this reason, few early devices showed a visible photocurrent that was large enough to measure. Also, several dyes show photocurrents in both directions. This suggests that some dyes may be capable of participating in plasmonic photocatalytic reactions discussed in Chapter 6. There is also a large amount of literature on dye photocatalysis and some results would appear to be contradictory. The transfer of electrons to metal nanoparticles does not seem likely in the presence of a Schottky

barrier accelerating electrons into the semiconductor, however it is observed for several dyes on devices in this work.

### 7.3.1. Optimisation

Early results in the UV regions suggest that improvements in processing to increase crystallinity or reduce diffusion from substrates and altering the surface properties through passivation contribute to higher visible light efficiencies. This tends to be repeated in these results for the visible response. To repeat earlier results on TiO<sub>2</sub> films grown on polished titanium, early results were functionalised with quantum dots.

#### Amorphous devices and quantum dots

This is different to the spun coat devices that form the semiconductor layer as discussed in Chapter 4. In this case, the quantum dots are used as sensitizer on a barrier formed on TiO<sub>2</sub>. As would be expected, there were some very small responses in the visible region. This response is very small, which is unsurprising given the low efficiency of the UV region. (Figure 7.2)

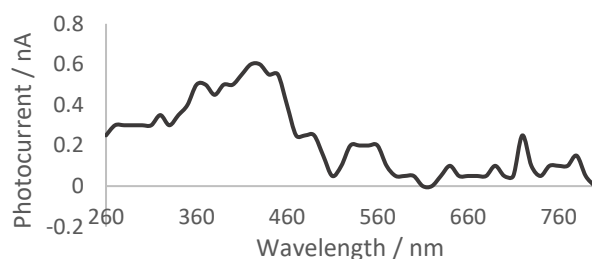


Figure 7.2: CdS drop cast on amorphous devices showing a small visible light photocurrent response.

What is noteworthy for these systems is the same need to remove the insulating ligands from these devices and the need to use solvents friendly to the silver nanowires. As may be expected, solvents such as chloroform and toluene appeared to be incompatible with the maintenance of the conductivity of the mesh of the silver nanowires. The heating of the device may also help with the removal of the ligands.

#### Partially crystalline devices

Using an 8-hour refluxed sol, the photocurrent responses were improved drastically. A series of devices were made and those with a measurable UV

response were functionalised with quantum dots in order to separate the effects of the UV response.

These devices were functionalised in separate ways to investigate optimum quantum dot quantities and deposition techniques. A typical set of results are shown below showing a visible photocurrent, Figure 7.3.

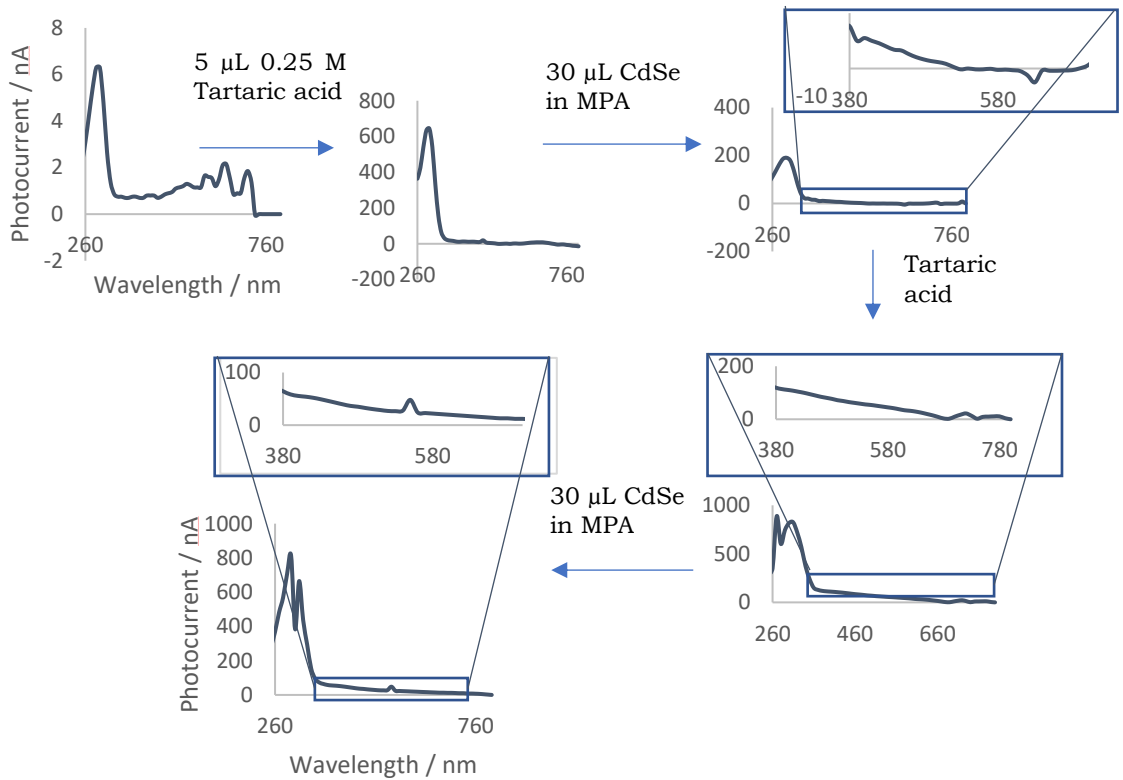


Figure 7.3: The visible photocurrent response for a device functionalised with CdTe quantum dots.

The EQE's after this functionalisation is shown in Figure 7.4.

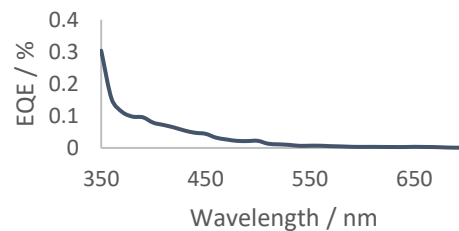


Figure 7.4: The visible photocurrent response for a device functionalised with CdS quantum dots.

To compare different quantum dots efficiencies are reported as their wavelength of maximum absorption differs for different quantum dots. It seems that the CdTe dots appear to give a better visible efficiency than the CdS. This may be due to the higher relative conduction band of the CdTe band compared to the CdS band, resulting in a higher driving force for injection over the barrier, Table 7.2 and Table 7.3.

<b>Maximum EQE 700-350 nm</b>	<b>Tartaric acid / %</b>	<b>+ Cd QDs / %</b>	<b>+ tartaric acid / %</b>
30 $\mu$ L 0.5 mg / ml CdTe in MPA	0.010	<b>0.022</b>	0.01
	-	0.007	<b>0.01</b>
	-	0.0074	<b>0.03</b>
	0.036	0.0067	<b>0.04</b>
60 $\mu$ L 0.5 mg / ml CdTe in MPA followed by 5 $\mu$ L tartaric acid (0.25 M)	N/A	<b>0.01</b>	0.0064
		0.01	<b>0.066</b>
		0.03	<b>0.11</b>
		<b>0.04</b>	0.013
30 $\mu$ L 0.25 mg / ml CdS in MPA	0.0068	0.00061	<b>0.002</b>
	0.0034	0.0016	<b>0.005</b>
	0.056	0.022	<b>0.04</b>
	0.015	<b>0.040</b>	0.032

Table 7.2.: Quantum efficiencies of visible response for quantum dot functionalised devices for up to

Deposition agents can also impact the dispersal of the quantum dots and the silver nanowires.

<b>EQE 700- 350 nm</b>	<b>Water / %</b>	<b>+ Tartaric acid / %</b>	<b>Pyridine / %</b>	<b>+ Tartaric acid / %</b>	<b>MPA / %</b>	<b>+ Tartaric acid / %</b>
1	0.016	0.046	0.0073	0.22	0.0013	-
2	0.034	0.00045	0.068	0.11	0.0049	0.13
3	0.025	-				
4	0.0029	0.34				

Table 7.3: Quantum efficiencies of visible response for quantum dot functionalised devices treated with organic additives.

Early devices synthesised using CdS in toluene and MPA show opposing currents as observed for some dyes in latter sections, Figure 7.5.

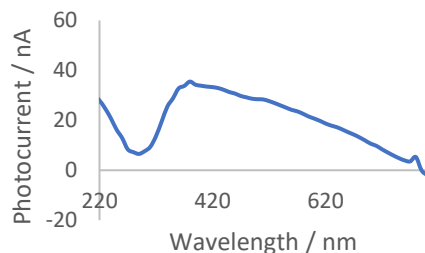


Figure 7.5: Photocurrent of a CdS functionalised device deposited with MPA in EtOH deposited device.

When treated with tartaric acid, the visible photocurrent is in the same direction as the UV response. These experiments were inconclusive due to the low numbers of reliable devices produced. However, a visible response is seen due to sensitization of the semiconductor.

### 7.3.2. The use of dyes

Given the low surface areas of the devices, the maximisation of light harvesting in the space available requires the smallest possible visible light absorption. Although quantum dots are typically only a few nanometres in diameter, this is still many times the volume of a dye molecule. Also, dyes have been developed that show extremely high yields for the absorption of light and the injection of electrons into  $\text{TiO}_2$  films. For these reasons, as well as others such as the availability of a large variation in characteristics and the concern of the presence of dyes in the wider environment, dyes are used throughout the rest of the research.

Further, many methods involving the use of quantum dots involve a heating stage to remove organic ligands. The advantage of organic dye methods is all heating stages can occur before their application with solvent and simply dried. Post-processing quantum dots in the form of heating may be incompatible with the silver nanowire mesh.

Also, the abundance and safety of the materials used in these devices are one of their strengths, but the use of cadmium in many quantum dots makes them a poor choice environmentally. Whilst other materials are being investigated for their potential use in quantum dots, organic dyes are already produced in bulk from organic materials.

### 7.3.3. Ru(dcbpy)<sub>2</sub>(NCS)<sub>2</sub> dye on amorphous devices

As with the quantum dot and UV response, the amorphous devices tend to be low efficiency. For some of the best devices in these cases, the photocurrents and photovoltages were low, though somewhat clearer than the responses seen for the quantum dots.

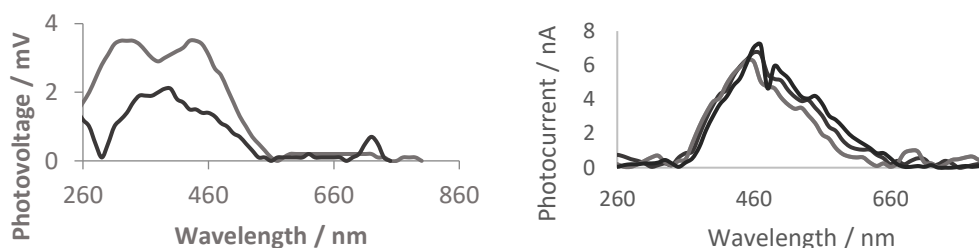


Figure 7.6: Ru(dcbpy)<sub>2</sub>(NCS)<sub>2</sub> functionalised amorphous devices photovoltages (left) and photocurrent (right).

Currents are similarly small but unambiguously in the same direction in the UV and the visible region, Figure 7.7. There is also little detail in these photocurrents.

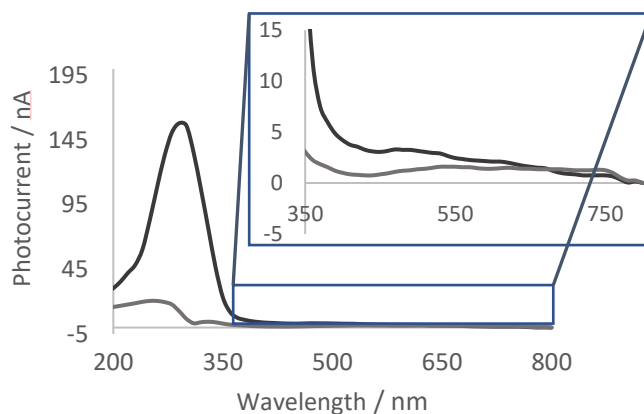


Figure 7.7: Visible dye, Ru(dcbpy)<sub>2</sub>Cl<sub>2</sub>, treated with tartaric acid, showing a very small response in the visible region.

### 7.3.4. TiN devices

The UV region response was much higher for the TiN derived devices. This was attributed to the lower defects in these films, resulting in lower levels of recombination. Unsurprisingly then, the visible responses with dyes are larger and more consistent, Figure 7.8.

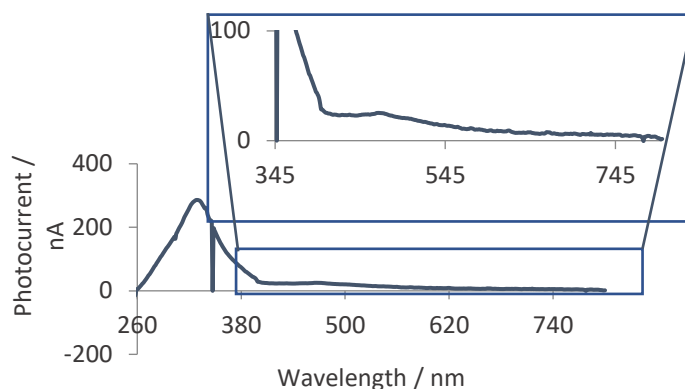


Figure 7.8: Ru(dcbpy)(NCS)<sub>2</sub> functionalised TiN derived device.

To investigate the stability of this photocurrent to show it is not through excitation of finite surface states, a measurement was recorded at every nanometre wavelength for 10 seconds, over the range between 345 to 400 nm. There is little correlation between time and photocurrent though there is a small amount of photocurrent loss under wavelengths of 365 nm, Figure 7.9.

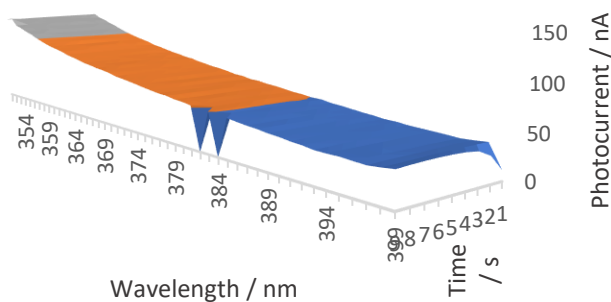


Figure 7.9: The photocurrent measurements for a Ru(dcbpy)<sub>2</sub>(NCS)<sub>2</sub> over 345 nm to 400 nm for 10 seconds at each wavelength, showing a mainly constant photocurrent for most wavelengths.

Some devices show a more distinctive separate peak for ruthenium dyes on TiN devices, such as shown in Figure 7.10. This could be due to lower lifetimes due to lower numbers of defects. However, the efficiency is lower in the visible region, Figure 7.10.

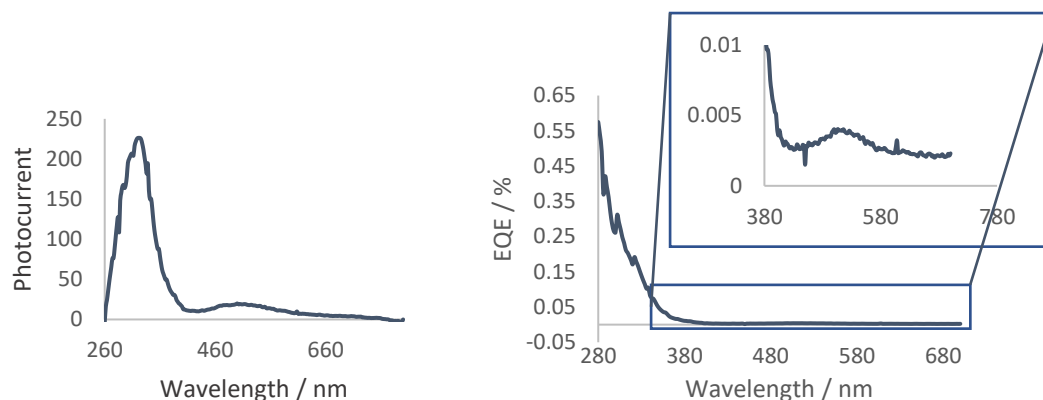


Figure 7.10: Photocurrent showing the measured UV and visible response in photocurrent (left) and the external quantum efficiency (right).

### 7.3.5. Area estimates

Taking a more typical  $1.5 \times 10^{-3} \%$  peak efficiency in the visible region, this corresponds to  $4.24 \times 10^{10}$  electrons per second, of a  $5 \mu\text{L}$  of  $2 \times 10^{-3} \text{ M}$  solution of  $\text{Ru}(\text{dcbpy})_2(\text{NCS})_2$  results in deposition of  $6.02 \times 10^{15}$  molecules per  $\text{cm}^2$ . Using the argument of an area of  $0.00000265 \%$  of the device as presented in Chapter 4, this results in dyes in an active area, the area of the depletion region of the device from thermionic emission theory is estimated as  $265 \mu\text{m}^2$ , resulting in  $1.6 \times 10^{10}$  molecules in the depletion region, from the concentrations of deposited dye, which is of the same magnitude as the number of charge carriers generated per second. It may result from each dye undergoing several turnovers per second. Using better measurements of area may result in the possibility of measuring the efficiency of the dye ground state regeneration.

The efficiency of excitation of injection of electrons into  $\text{TiO}_2$  is reported to be near unity. The dyes may preferentially bind at depletion regions, as they are in close proximity to both  $\text{TiO}_2$  and silver surfaces and therefore might allow for binding both  $-\text{CO}_2\text{H}$  and  $-\text{NCS}$  simultaneously. This again suggests that the area estimates are reasonable given the relative orders of magnitudes of the electrons and photons on adsorbed molecules. It also underlines the problem of area, as the process of adsorption and charge separation at these interfaces would appear to be efficient.

### 7.3.6. Organic dyes

Similar results are found for a range of other dyes, shown in Figure 7.11, were used to functionalise TiN devices.

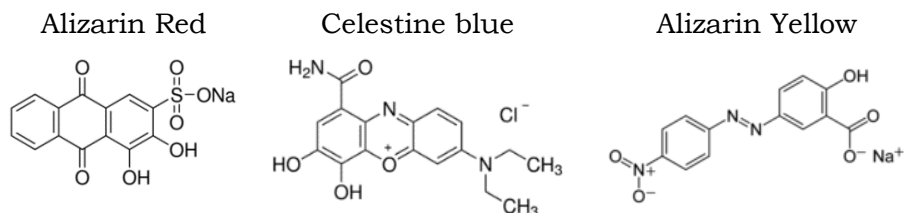


Figure 7.11: The dyes used to investigate the sensitisation of the device.

Similar responses are seen as the ruthenium dyes, with the visible absorption profile changing, Figure 7.12 and Figure 7.13.

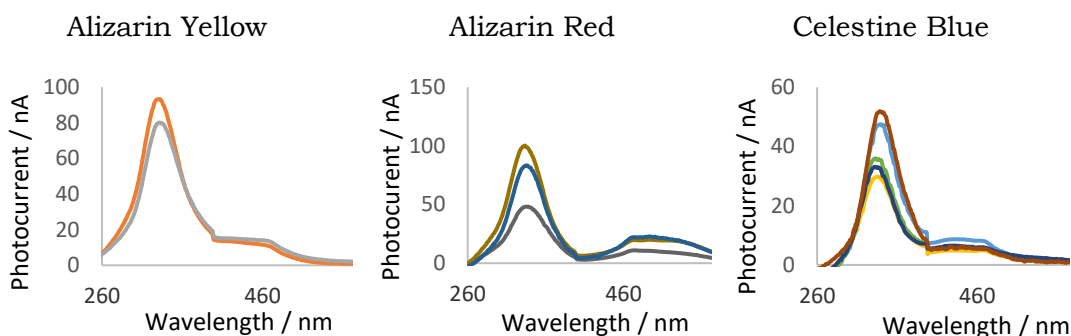


Figure 7.12: Photocurrents for a range of organic dye functionalised devices demonstrating different absorption profiles in the visible region.

The EQE plots demonstrate further the variation in the visible absorption with different dyes.

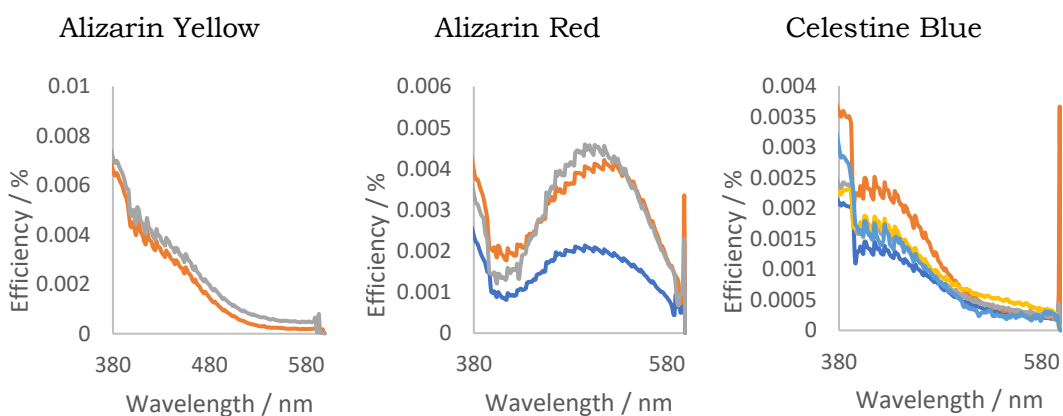


Figure 7.13: EQEs for a range of organic dye functionalised devices a peak in efficiency in different visible region.

The visible responses for these devices are reasonably reliable, as seen by the photocurrents measured for many devices are similar. Variation is likely to be due to changes in the active area. The photocurrents are similar in magnitude to that of the ruthenium dye devices. From the EQE plots, the maximum efficiency of a range of devices, is in the order alizarin yellow > alizarin red > celestine blue.

As with many electrochemical studies, there is little comparable data across studies as they are performed under a range of conditions. Alizarin red oxidation in 0.1 M KCl at 5 mV s<sup>-1</sup> on Pt was reported ~+0.7 V against Ag/AgCl.<sup>231</sup> Similarly, Alizarin red oxidation is +0.8 V in 0.1 M HClO<sub>4</sub> against Ag/AgCl at 200 mV s<sup>-1</sup>,<sup>232</sup> and +0.739 V on a carbon electrode with 0.2 M acetate buffer (pH 3.5) at a scan rate of 50 mV/S.<sup>233</sup> Alizarin Yellow has shown two peaks for oxidation, with the lowest energy peak at +0.243 V in 0.1 M phosphate buffered saline (pH 7.0) at 100 mV s<sup>-1</sup> vs SCE.<sup>234</sup> A celestine blue oxidation on a NiO<sub>x</sub> modified glassy carbon electrode in 0.1 M phosphate buffer (pH 2) at 10 mV s<sup>-1</sup> was ~+0.05 V vs Ag/AgCl.<sup>235</sup>

This corresponds to an oxidation potential of +0.9 V for alizarin red and +0.48 V for alizarin yellow, +0.25 V for celestine blue vs NHE, assuming the conditions are comparable. From Koopmans' Theorem, there is a relationship between the HOMO and the redox potential. As is commonly encountered in electrochemical experiments compared to DFT studies of electrode potentials, Koopmans' theory often breaks down in practice.

Taking the lowest energy peak of absorption as the HOMO-LUMO distance from peak absorption, this gives an estimates potential of -1.7, -2.1 and -2.0 V vs NHE for Celestine blue, alizarin yellow and alizarin red respectively, using the peaks in visible absorption to measure HOMO-LUMO gap.

However, this high oxidation potential of the LUMO may explain the higher currents as there is more energy to overcome the barrier. From this, the difference between the LUMO and the flat band potential of the conduction band would be expected to be alizarin yellow >= alizarin red > celestine blue. This is the order of the maximum efficiency in the visible region for each dye; 0.0051 % > alizarin red 0.0046 % > 0.0025 %. This could suggest a sensitization mechanism and suggest a mechanism for the improvement of such devices by using dyes with a high energy LUMO.

Though only 3 results, this would suggest that the potential of the LUMO does relate to the photocurrent. Further, the ease of oxidation of the dyes is celestine blue>alizarin yellow>alizarin red. Not only does the maximum efficiency not follow this order, it runs counter to this, suggesting that oxidation in the visible wavelengths is not occurring.

### 7.3.7. Dyes on sol substrates

The devices formed on TiN, where TiN is oxidised to  $\text{TiO}_2$  and is similar to those made from titania sols. The IV characteristics are similar, with diodes formed on both. The forward current is in the same direction. The visible response for the dyes on sol devices however, can be in the opposite direction to that observed on TiN. The mechanisms are discussed in Section 7.4.

#### Partially crystalline sol

A mainly amorphous sol showed a number of photocurrents in the same direction as the UV response. As described in Chapter 6, the UV responses were not as they seemed, with many UV responses showing currents in the opposite direction.

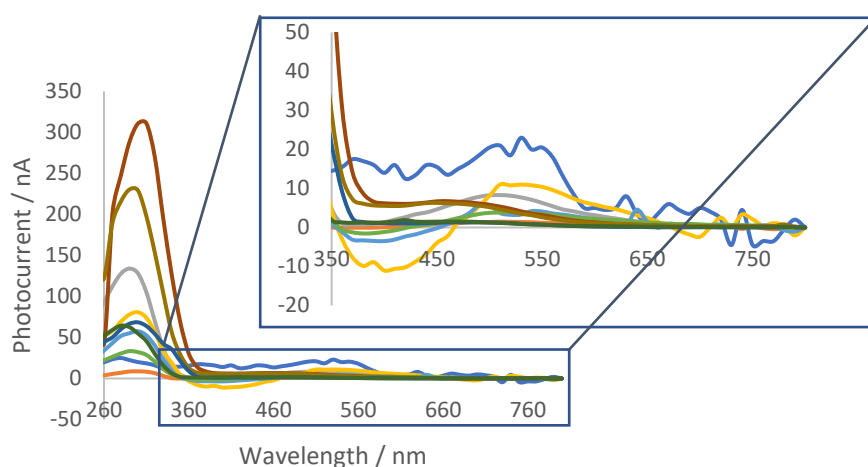


Figure 7.14: 8-hour IPA refluxed sol, partially crystalline soaked in  $\text{Ru}(\text{dcbpy})_2(\text{NCS})_2$ , showing a UV/visible response, which varies in direction with wavelength.

However, the same device in a water refluxed sol showed that the response in the visible region was in a different direction to the UV response. This suggests there is more than one mechanism of action. As argued in Chapter 6, the higher energy peak tends to show an unexpected forward photocurrent response, indicating a direction of current the same as the diode in forward

bias, i.e. electrons travel to the silver nanowires from the semiconductor. This is counter to the hypothesis of a sensitized barrier. The hypothesis from Chapter 6 was a plasmonic driven reduction at silver, as reported in literature, but these results suggest dyes are able to participate in this forward mechanism in the visible region, Figure 7.15.

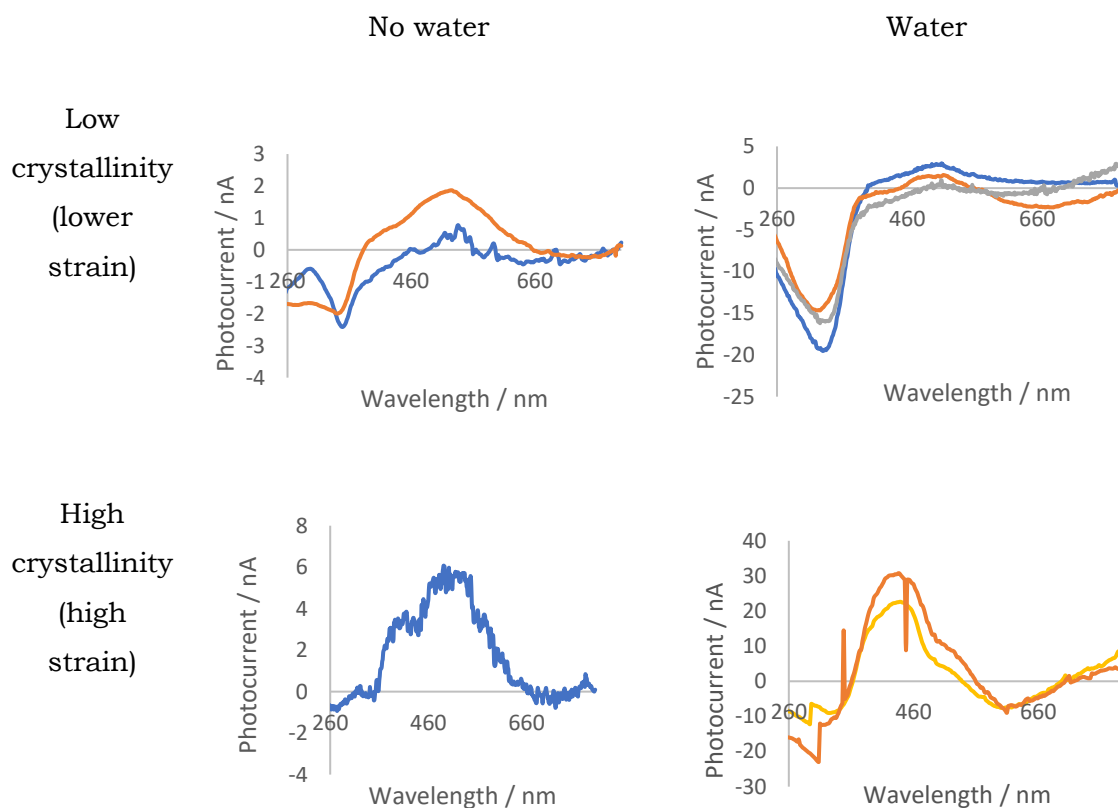


Figure 7.15: Ru(dcbpy)<sub>2</sub>(NCS)<sub>2</sub> dye on range of devices fabricated from sols, demonstrating directions that oppose the UV response for water passivated devices.

This shows the Ru(dcbpy)<sub>2</sub>(NCS)<sub>2</sub> dye shows a photocurrent in the opposite direction to the UV response, measuring counter to the expected direction, as discussed in Chapter 6.

Aurintricarboxylic acid, Figure 7.16, was also used on these devices, to gain more data. With another organic dye to compare, the direction observed in the visible region differs depending on the dye chosen, with some showing a photocurrent in the same direction in the UV region whilst some show the opposite, Figure 7.17.

### Aurintricarboxylic acid

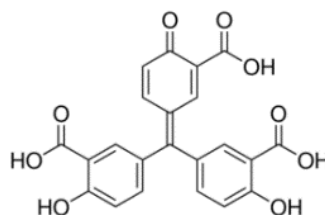


Figure 7.16: Structure of aurintricarboxylic acid.

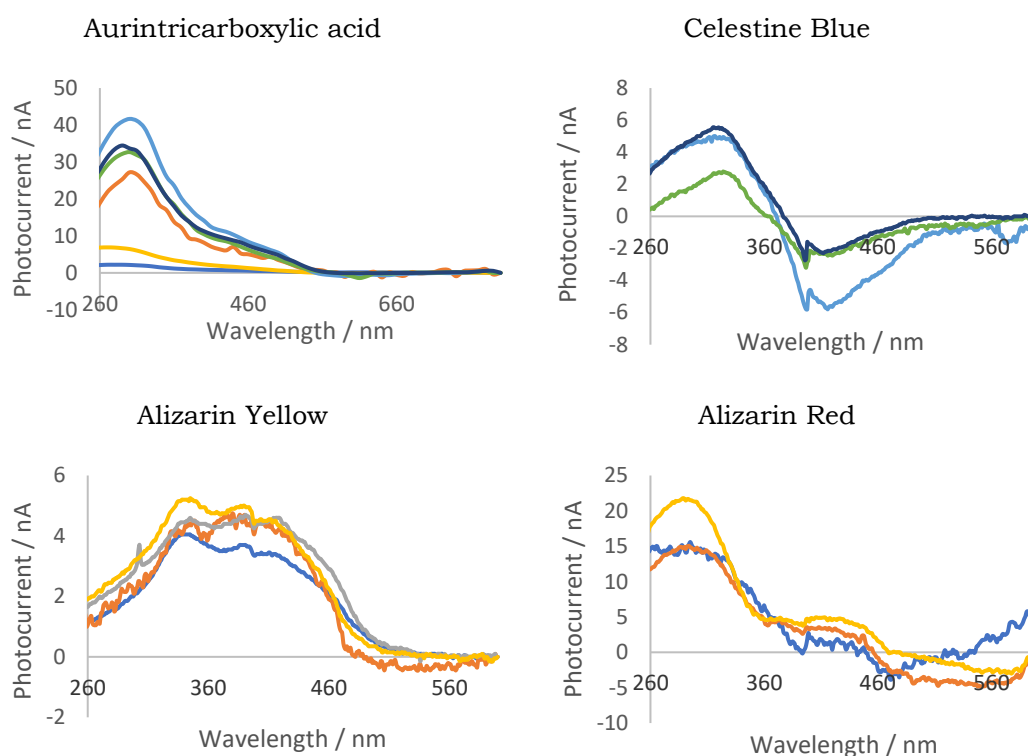


Figure 7.17: A range of dyes on highly crystalline sols, showing that the visible region response is opposing the UV region response for celestine blue but agrees in the cases of the other dyes for these devices.

Aurintricarboxylic acid was only sparingly soluble in water. An attempt was made at dissolution in an EtOH/water 1:1 v/v solvent but resulted in an exothermic reaction. There was no similar reaction in water. There are three acid groups that may be able to esterify, though there is the lack of reports on this in the literature. The dye also undergoes polymerisation. Though no obvious polymerisation was observed in the form of precipitates. Michael additions to enolates are reported extensively, which could explain this result. A Michael addition is an addition of a nucleophile to an unsaturated

compound. In alizarin yellow, there is an unsaturated double bond which can react with an alcohol or other nucleophile.

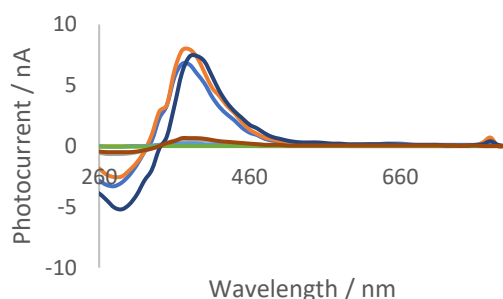


Figure 7.18: Aurintricarboxylic acid functionalised partially crystalline devices following using aurintricarboxylic acid in water/EtOH solution.

This change in the dye molecule direction is reversed again following the deposition of tartaric acid, Figure 7.18. This suggests that the change in aurintricarboxylic acid made by dissolution in ethanol is recovered by the deposition of tartaric acid.

The role of the tartaric acid was originally as a passivation agent. Whilst it may also be present as a substrate for oxidation, it would suggest that in the case of aurintricarboxylic acid, the reaction that occurs with ethanol may prevent it passivating the surface, suggesting the presence of surface states may attenuate the mechanism of forward current, as would be expected from its absence on TiN devices.

#### Single wavelength radiation

Though the spectra was useful to demonstrate the response of a device to the incident light, single wavelengths were chosen to ensure the wavelengths supplied are just above or below the band gap of the semiconductor, for instance, the blue LED was driven with a 2.9 V forward voltage, so even neglecting internal resistances, the maximum wavelength produced was 425nm, and has constant response that can be measured over hours at high irradiation, allowing measurements of kinetics.

For a substrate with a highly crystalline sol could be irradiated with the UV LED with a peak at 400 nm shows a predictable response, here showing a reverse current, indicating electrons travelling into the substrate following illumination at the band gap as expected, Figure 7.19.

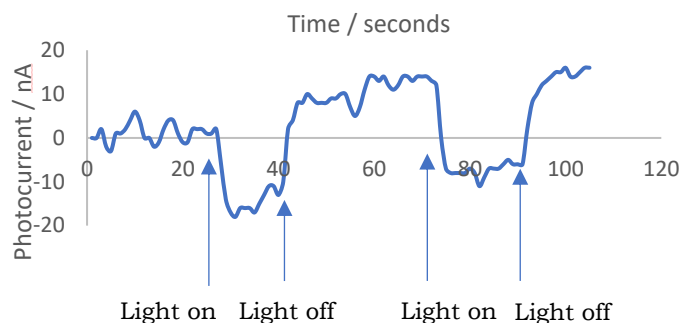


Figure 7.19: Photocurrent under 400 nm LED demonstrating the reverse direction under illumination.

Under water, the currents are boosted, as before, by more than an order of magnitude. This again suggests there is a mechanism by which water increases the efficiency of devices. As water is known to be able to passivate the oxygen vacancies on the surface of the  $\text{TiO}_2$  as discussed in Chapter 4 and 5, this may be the mechanism by which the efficiencies are improved, both by reducing the number of recombination sites but also possibly unpinning the Schottky barrier, as under UV illumination under water, it appears to increase in height (Figure 4.17). This could result in higher fields at the interface.

However, on turning the light off in this case, there is a sharp spike in the opposite direction, which decays over a similar time scale to its excitation, Figure 7.20. This suggests that the build-up of something reactive that is produced under UV light. The production of hydrogen and oxygen on  $\text{TiO}_2$  catalysts such as that observed by Honda and Fujishima has been reported, though on particulate catalysts, the small amounts of dissolved oxygen and hydrogen in small amounts can react spontaneously to produce the current when the light is off. <sup>198</sup>

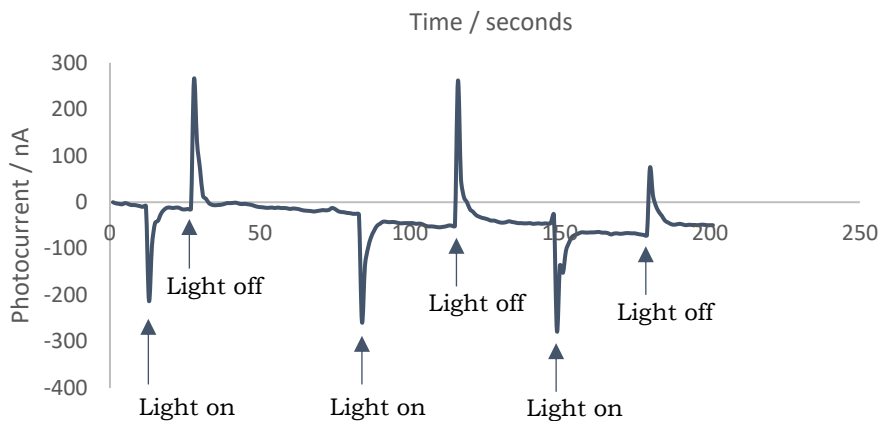


Figure 7.20: Photocurrents for a device in water demonstrating a large reverse response but a compensation for this when the light it turned off.

When a solution of alizarin red replaced some of the water, the current upon excitation with the LED was in the positive (“forward”) direction. This indicates that even in under the presence of above band gap radiation, the electrons travel into the silver nanowires. The positive (“forward”) responses are higher than that seen for the “reverse” direction current seen above for the devices under water. Further, there is no obvious peak in the opposite direction as there was in water, suggesting this is not a build-up of reactive species, Figure 7.21. There is a small decrease in the photocurrents measured over time.

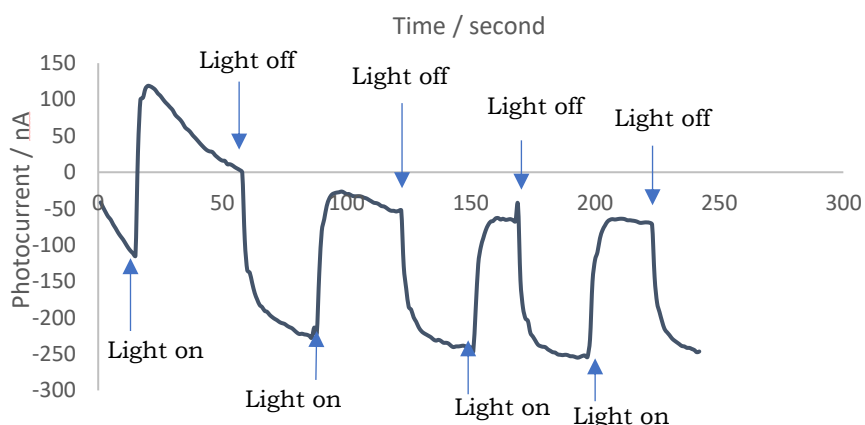


Figure 7.21: Photocurrents for a device in the presence of alizarin red showing a large forward response, in the opposite direction to that observed in the presence of water.

However, this positive response, indicating electrons travelling out of the TiO<sub>2</sub> film and into the silver nanowires is not observed for all dyes, with

methylene blue showing the opposite, and expected, negative response, Figure 7.22.

Alizarin red is shown to be a reporter molecule for plasmonic particles for SERS applications.<sup>236</sup> Its reactions may not be representative, this is itself informative as it has been used for photocatalytic degradation studies, though it may not be a representative organic dye or pollutant.

The negative response shown here for a methylene blue sensitized device is consistent with sensitization mechanisms, increasing the quantity of electrons travelling into the semiconductor.

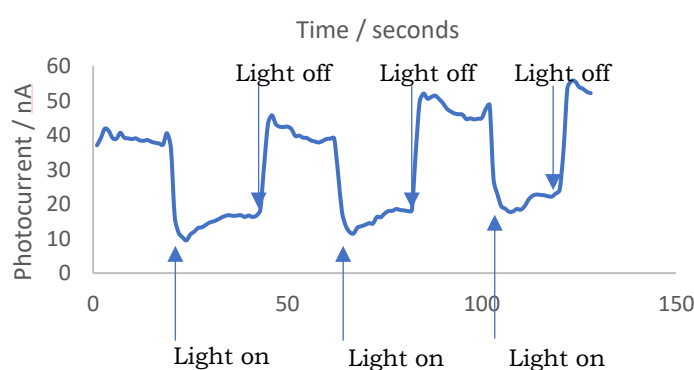


Figure 7.22: Methylene blue photoresponse under UV light.

Many of the mechanisms discussed in the introduction discuss photocatalytic mechanisms that depend on the excitation of electrons above the conduction band and then into metal nanoparticles, where they reduce  $O_2$  or water to radicals, whilst dyes are oxidised by holes on the surface.

This would appear to not be the case for these devices, as electrons can be measured travelling into the semiconductor. This is smaller than the water oxidation currents measured, so may represent the sum of the currents, whereby the negative response of -200 nA is tempered by the positive response of +170nA, resulting in the small negative response. If under UV light, oxygen radicals are produced which react with dye, this may result in a lower negative response.

To test this, a visible wavelength LED was used, with a maximum output of 425 nm, below the band gap of  $TiO_2$ . The response was also negative at -28.1 nA. -27.6 nA and -31.0 nA for three consecutive measurements at a lower intensity. This would suggest the negative response is not the negative

response of the device tempered by the presence of dye, but a negative response induced by the dye itself. This suggests the transport of electrons into the TiO<sub>2</sub> film under visible light excitation.

The decreases in photocurrent over time for each peak decreases with first order kinetics over time. This may be the establishment of an equilibration, as seen in some of the literature. There is no clear pattern in the rate constant in the fits of the 19 degradations studied. The maximum photocurrent appears to converge over the 19 studies, Figure 7.23. A fit of these points gives a poor correlation and an intercept of -40.7.

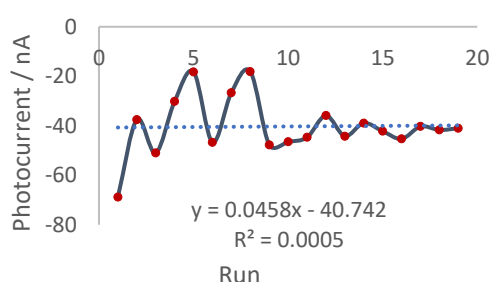


Figure 7.23: Plot of maximum photocurrents of 19 consecutive illuminations of a methylene blue functionalised device shows convergence around approximately 41 nA.

Though sampling was performed to try to relate any change in photocurrent to a change in the UV-vis spectra, no change in absorption in the visible region was observable, but the samples were very small and any change may not be detectable. It does not appear that there is dye degradation and there is no relation with the maximum photocurrent observed for this device.

There is, however, a small decrease in photocurrent over time for this device, following a period of equilibration. This decrease in photocurrent appears to be a logarithmic decrease, though it does not fit first order or second order kinetics. These photocurrents were measured after equilibration with dye and following previous photocurrent experiments. This study was performed over 20 minutes, Figure 7.24. This suggests the mechanism for initial loss of photocurrent shows complicated kinetics.

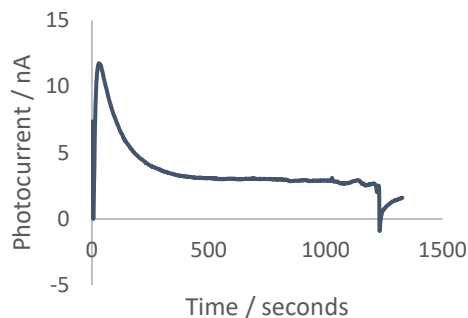


Figure 7.24: Decrease in photocurrent over 20 minutes for a methylene blue functionalised device under UV light showing a “positive” forward current that decreases over time.

From the lack of a fit to first or second order kinetics or to a log-log plot in time, suggesting photocurrent or its change in time does not correlate with degradation. If desorption or migration to a reactive site pre-empts degradation, with two kinetics constants and concentration dependencies.

#### 7.3.8. UV-vis studies silver nanowires

The use of silver in DSSCs has been used to amplify the absorption by the molecule. Assuming this excitation is simply an amplification, the modes of excitation would be the same. Dyes containing donor and acceptor groups result in a spatially separated HOMO and LUMO with the LUMO centred on the acid group. On titania, the hybridised orbitals with titania can result in a direct transfer.

However, the dilute dye without background in IPA absorption is shown in Figure 7.25, left, but with increasing amount of silver nanowires is shown on the right.

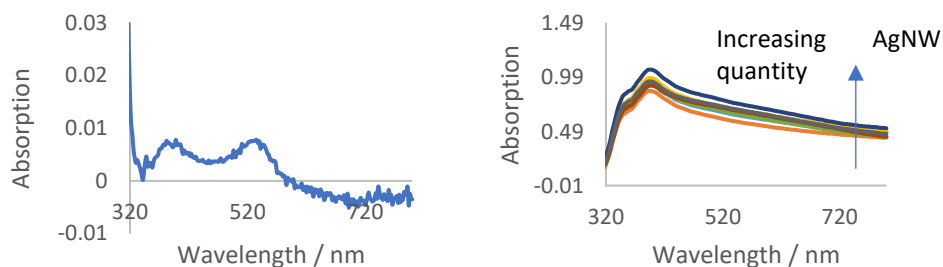


Figure 7.25: Ru(dcbpy)<sub>2</sub>(NCS)<sub>2</sub> dye (left) and Ru(dcbpy)<sub>2</sub>(NCS)<sub>2</sub> dye amplified by silver nanowires of increasing concentration in IPA.

Comparing photocurrents and Ru(dcbpy)<sub>2</sub>(NCS)<sub>2</sub>

To study the interactions between the three components in this system, UV-vis studies were performed. These often give dramatic and non-linear results. For instance, Ru(dcbpy)<sub>2</sub>(NCS)<sub>2</sub> dye absorption is enhanced by contact with silver nanoparticles, hence their use for increased light harvesting in DSSCs. This is generally attributed to the enhancement of absorption due to the field surrounding plasmonic fields. Figure 7.26 shows an increasing concentration of silver nanowires, left, the raw absorption of the silver nanowires with 50 nM Ru(dcbpy)<sub>2</sub>(NCS)<sub>2</sub>, centre, the difference between the two is shown on the right. A similar result is seen for the TiO<sub>2</sub> sol, though with a smaller enhancement for the lower energy peak.

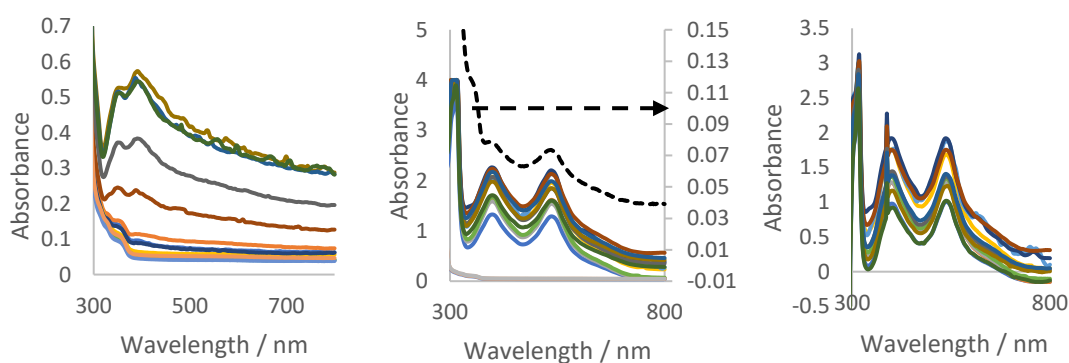


Figure 7.26: Left increasing concentration in silver nanowires, Centre shows the raw absorption of dye and silver nanowires. The dashed line is against the secondary axis, showing the much weaker absorption of dye. Right shows the difference between the two spectra showing the difference in caused by nanowires.

The difference at 400 and 540 nm is parabolic in silver nanowire concentration, with an optimum for both wavelengths, with a peak difference in the middle of these ranges.

The UV-vis spectra of the  $\text{TiO}_2/\text{AgNW}/\text{Ru}(\text{dcbpy})_2(\text{NCS})_2$  show the absorption of the three-component system needs more consistent controls due to all components having an impact on the absorption. By comparing to the devices photocurrents to the sum of  $\text{TiO}_2$  and silver and to the sum of silver with  $\text{Ru}(\text{dcbpy})_2(\text{NCS})_2$ , there is an observable photocurrent of devices.

The sum of the three components, minus the sum of the  $\text{AgNW}/\text{TiO}_2$  composite with the impact of dye removed as a constant, Figure 7.27, left, therefore shows a different result to the spectra when the  $\text{AgNW}/\text{Ru}(\text{dcbpy})_2(\text{NCS})_2$  is used as the control and  $\text{TiO}_2$  sol is subtracted as a constant, right. Both are shown in comparison to two device responses, one on a sol, which shows both current directions, the other is a TiN device which shows only one current direction, functionalised with the same dye.

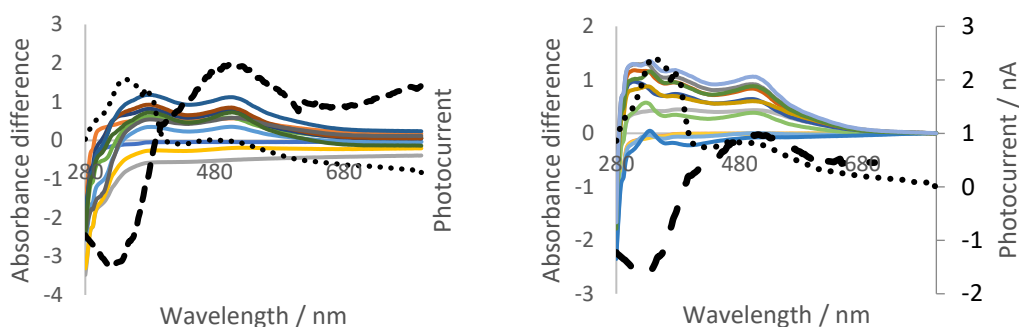


Figure 7.27: Photocurrents (black lines) for TiN derived devices (dotted) and  $\text{TiO}_2$  sol derived devices (dashed) and absorbance difference (solid lines) for a range of concentrations of silver nanowires and  $\text{TiO}_2$ .

For Figure 7.27, left, the absorption at higher ( $> \sim 380$  nm) energy is less than predicted, suggests accounting for the silver nanowire/ $\text{TiO}_2$  impact suggests a high absorption at high energy with dye is considerably lower than expected. The absorption peak is logarithmic in silver nanowire concentration in the presence of sol, but is hindered by the presence of dye. This could be competitive as the dye absorbs strongly in the UV and could prevent excitation of the plasmonic modes, which may have otherwise reinforced excitation in other silver nanowires or  $\text{TiO}_2$ .

Figure 7.28 demonstrates the absorption difference for a range of concentrations of silver nanowires and  $\text{TiO}_2$ . The dye is hindering the mechanism by which  $\text{TiO}_2$  and AgNW have an impact on their overall absorption, Figure 7.28, below. Similarly to the impact of the some sols, this may suggest the inclusion of a dye may already result in a more transparent AgNW film.

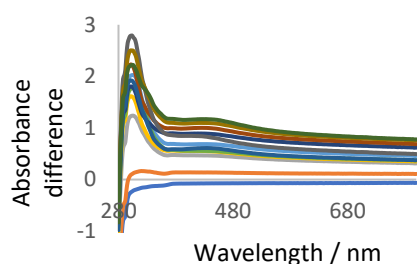


Figure 7.28: Absorption difference for a range of silver nanowires and  $\text{TiO}_2$  sol demonstrating a strong absorption at  $\sim 300$  nm above the sum of both components at this wavelength.

There is good agreement between the photocurrents of the devices and the position of the peaks from spectroscopy. The reinforcement of the visible and UV peaks accounting for the impact of the dye/AgNW system shows a similar absorption to that of the photocurrent for the single direction device.

#### Impact of dye choice

The visible photocurrent direction depended on the dye used with  $\text{Ru}(\text{dcbpy})_2(\text{NCS})_2$  showing celestine blue dye showed some forward responses whilst alizarin red and aurintricarboxylic acid did not. UV-vis studies showed that absorption decreased in the presence of dye for high volumes of nanowires for the dyes which showed the “forward” current but not the other dyes which have no impact on the absorption of silver nanowires.

#### Impact of solvent

A range of solvents were used to investigate the effect of dielectric constant on the absorption of  $\text{Ru}(\text{dcbpy})_2(\text{NCS})_2$  dye. For a particular solvent, the absorption of the silver/dye system either increases or decreases with volume of silver nanowires. This gradient is reported in Appendix 3.

There was no shift in the peak positions, nor was the peak intensity related to the dielectric constant of the solvent, however it was related to the pKa of the solvents, Figure 7.29.

The more acidic the solvent, and the more silver nanowires, the smaller absorption of the silver nanowires and the dye. Thus, an acidic solvent helps to increase transparency of silver nanowires at 550 and 400 nm. A more basic solvent appears to decrease this transparency.

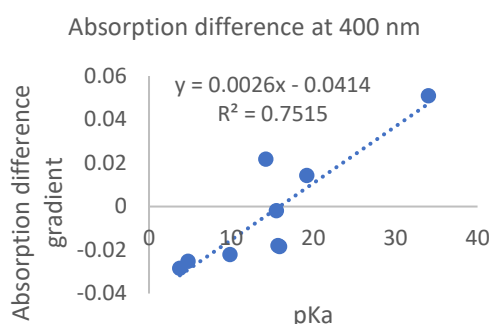


Figure 7.29: The impact of pKa of the solvent used on the change in absorption of increasing concentrations of silver nanowires and sols.

## 7.4. Discussion of mechanism

Though the mechanism where “negative” or reverse currents are observed are clear and are, due to the evidence thought to be due to band gap excitation of the semiconductor in the space charge region or the sensitization of that region by dye.

The dye can inject electrons into the  $\text{TiO}_2$ . Holes may undergo reaction or transport into the metal nanowires. Though this may be expected to be slow, spatially, the electrons will be accelerated towards them due to the Schottky barrier formed between the valence band and the metal. The depletion regions where the electrons and holes could be separated is, by definition, proximate to the nanowires. On TiN, all the dyes studied here show the possibility of sensitization mechanism is possible and photocurrent may correspond to the level of the LUMO relative to the height of the Schottky barrier.

However, the opposite mechanism is less clear. The positive response for photocurrent for these devices under UV light for some dyes such as

methylene blue and celestine blue (as well as  $\text{Ru}(\text{dcbpy})_2(\text{NCS})_2$ ) runs counter to this direction however. Though sensitization clearly can occur, as it can be seen on the TiN devices, the mechanism involves transfer of electrons from the dye into the silver, followed by repopulation of the dye HOMO from the  $\text{TiO}_2$ . Plasmonic photocatalytic reductions have been reported in the literature as discussed in the Introductions to this Chapter and Chapter 6.

The mechanisms for excitation into the silver nanowires leaves few options because the Schottky barrier should accelerate electrons away from the interface into the semiconductor. Plasmon enhanced absorption by the dye or semiconductor simply amplifies the mechanism. In the case of the dye sensitized mechanism, this is occurring in the visible region, which is not near the LSPR of the silver nanoparticles. However, from UV-vis studies of the silver nanowires with dyes, the absorption across the UV-vis region is amplified by the silver nanowires.

From the UV-vis results, the negative absorption, where absorption of the 3-component system is less than the sum of its parts is where it is compared to the AgNW/ $\text{TiO}_2$  system, suggesting the dye disrupts the absorption by the silver nanowires or their reinforcing effect on  $\text{TiO}_2$  or silver nanowires, which is exponential for a AgNW/ $\text{TiO}_2$  system. This may be due to scattering of the plasmons by defects. For the peak at lower energy, however, the absorption of all three components is higher than the sum of the AgNW and the dye system with  $\text{TiO}_2$  sol. This suggests the dye is reinforcing the absorption by each component.

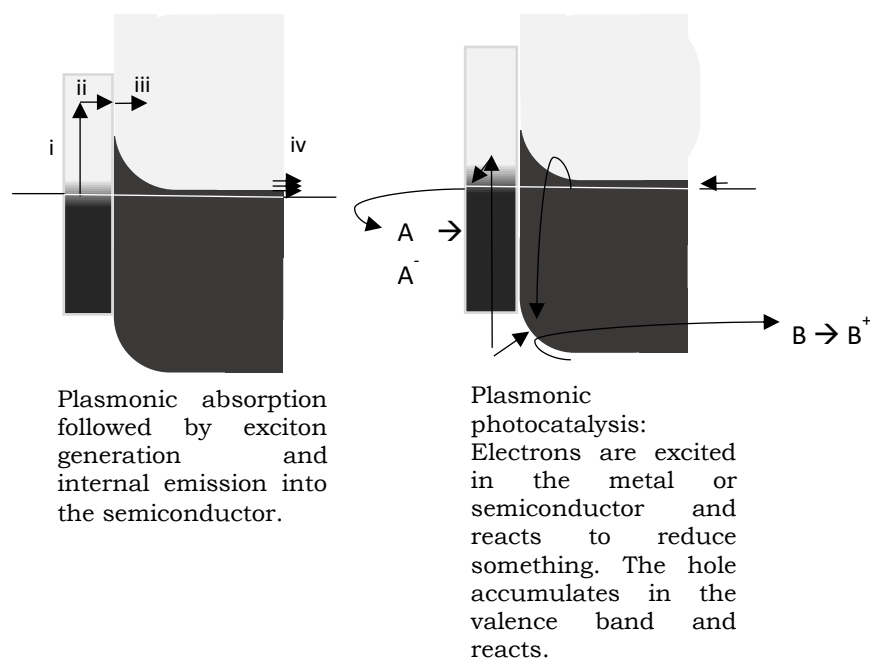


Figure 7.30: Mechanisms of plasmonic mechanisms on metal/semiconductor systems.

The photocurrents in the “forward” direction and the UV-vis results suggest the photocurrent is due to a plasmonic interaction which is increased by the presence of dye.

#### 7.4.2. Impact of pseudo-Fermi level and redox behaviour of dyes

As described in Section 1.3.7, the diffusion lengths are described by the Einstein-Smoluckwoski equations, Equation 1.3 and 1.4, which relates the diffusion length is proportional to the square root of its lifetime. Similarly, this relation is used in the modelling of Schottky barrier films, such as discussed in Section 2.3.3. The movement of the Fermi level due to the occupation of surface states in contact with the FTO results in a decrease in the potential drop at the interface and an increase in efficiency.<sup>237</sup>

However, defining diffusion lengths in TiO<sub>2</sub> films can be a challenge. The diffusion lengths measured by front and rear illumination of TiO<sub>2</sub> films are often different and further, rates of recombination (and therefore diffusion lengths) are sometimes not linearly related to electron concentration. Therefore, the ratio of diffusion length from front and back electrodes and the efficiency is dependent on illumination intensity. The ratios approach 1 when there is a high intensity, as does the diffusion lengths.<sup>237</sup>

The recombination events from TiO<sub>2</sub> films depend on the effective Fermi level of electrons in the TiO<sub>2</sub> film and electron transfer process may be due to surface states and transfer coefficients.<sup>237</sup>

Under illumination, the quasi-Fermi level increases with distance from the substrate, whilst the electron density at the TiO<sub>2</sub>/electrolyte interface will depend on the photovoltage in the DSSC. The decay of photovoltage for a DSSC with and without blocking layers differs; although a fast component is independent of blocking layer, a slow component is dependent on the concentration of electrons in the TiO<sub>2</sub> film. At low photovoltages, the TiO<sub>2</sub> layers can block electron transfer to I<sub>3</sub><sup>-</sup>. Under illumination, the quasi-Fermi level rises along with the driving force to electron transfer to I<sub>3</sub><sup>-</sup>.<sup>238</sup>

The phenomena of the direction of excitation changing for alizarin sensitized films has been directly addressed by Di Iorio. The cathodic photocurrents are attributed to electron transfer from the conduction band of the semiconductor to an acceptor in solution. Alizarin, described as electrochemically amphoteric, containing two redox active groups, one capable of electron donation and one of electron acceptance. Using reported oxidation values for redox of alizarin, the values of excited alizarin are estimated. This demonstrates a shift to more negative potentials for both the HOMO and the LUMO orbitals and a shift of the LUMO below the level of the conduction band (a flat band is assumed) TiO<sub>2</sub>.<sup>239</sup>

The applied negative potential required to facilitate electron transfer “to” alizarin, or cathodic photocurrent, is found to depend on dye loading, atmosphere (air versus N<sub>2</sub>), the electrolyte and the pH. The mechanism for the cathodic current is discussed, the authors speculate that a surface state carrier transport through the otherwise insulating TiO<sub>2</sub> interface, resulting in a reduced alizarin molecule, mediating in the reduction of oxygen. The importance of surface states is demonstrated through the peak in dye concentration dependence of photocurrents, with too much passivation by the dye proposed to hinder current. Chemisorbed oxygen is likely to be retained on purging, explaining the lower but present cathodic photocurrent in purged devices.<sup>239</sup>

In a study of alizarin breakdown, it was observed that alizarin red was stable in an irradiated solution of TiO<sub>2</sub> nanoparticles, though not larger particles.

The low efficiency for alizarin red was related to the low efficiency of oxygen reduction. This may be due to the equilibration of conduction band electrons with surface states in nano-, but less so in micro-, sized  $\text{TiO}_2$ , resulting in less oxygen reduction. To test this, a Cr(VI) compound reducible by the surface states was indeed reduced in light comparably in both air and nitrogen. From evidence from UV-vis spectroscopy, the mechanism appears to be an electron transfer from alizarin red to  $\text{TiO}_2$  then to the Cr(VI) complex.<sup>240</sup>

With redox active sites in alizarin red, particularly the reducible quinone group, and the above arguments, a possible mechanism for the “reverse” current for the Schottky barrier is the reduction of available dye reduction states. The shifted level of the LUMO of the excited dye below the conduction band may facilitate this. The mechanism for hole transport through n-type  $\text{TiO}_2$  could be due to surface states, providing a somewhat conductive path to the substrate, explaining the lack of this mechanism seen in the lower defect  $\text{TiO}_2$  films derived from TiN.

For the analogous process for the UV response, this only occurs under high energy illumination and may be due to the direct reduction of oxygen by energetic conduction band electrons.

The slow decrease in current (on the order of seconds) can be seen in the dark could be due to a slow equilibration. The kinetics were not described by first or second order kinetics and may allow for a study of transport through films via surface states. This system also allows for the study of electron recombination without the presence of a competing electrolyte system.

This could allow the study of electron recombination rates from surface states in films as well as the diffusion of these states through a  $\text{TiO}_2$  film. Models of transport through a  $\text{TiO}_2$  film have shown the importance the quasi-Fermi level in the  $\text{TiO}_2$  surface has on the occupation of surface states, which differs under illumination from the thermal steady state.<sup>241</sup> Applying a potential to the Schottky barrier may result in the ability to study this relationship.

## 7.5. Conclusion

The direct excitation across the band gap and the sensitized reactions both show high efficiency relative to the likely areas under consideration as discussed in Chapter 6. This could also result in a high efficiency sensitized device through a different geometry. The LUMO level may correlate with highest average photocurrents.

However, in the presence of water, as discussed in Chapter 6, the efficiencies for high purity devices are much higher than the efficiency expected from the areas, but are likely higher than can be accounted for by the depletion region. This suggests that a plasmonic mechanism is important. Given the strong binding between dyes such as alizarin red and  $\text{Ru}(\text{dcbpy})_2(\text{NCS})_2$  with titania, even reporting hybridised LUMO- $\text{TiO}_2$  conduction band orbitals, this is an unusual result which suggests there is a powerful reductive mechanism that can dominate the reaction.

Further, this is only possible on surfaces with high defect densities. This suggests the dyes can sensitize a reduction on the silver nanowires, followed by oxidation on  $\text{TiO}_2$  at these reactive surface states. A study of alizarin red under these conditions did not show any degradation when following this mechanism under visible light, suggesting this could provide a mechanism for the visible light reduction and oxidation of water. Early studies might also show  $\text{Ru}(\text{dcbpy})_2(\text{NCS})_2$  might show a small amount of degradation, which is an extremely stable dye and this might provide some insights into the degradation of otherwise stable ruthenium dyes.

# 8. Chapter Eight: Conclusions and Future Work

The aims of the work from Chapter 1 were:

“develop potential architectures and methods to produce a third-generation photovoltaic cell based on a Schottky barrier formed with silver nanowires. The novelty of this device will be its production compatible with lower cost, abundant sheet materials, such as stainless steel.

The aims will be achieved through:

- Fabrication of a rectifying device on stainless steel and its electrical characterisation
- Optimisation of the device to produce a UV response
- Activating the visible region through the use of dyes
- Analysis to understand how these devices can be further improved.”

These aims have been met, the Schottky barrier could be formed and a limited UV photocurrent was measured. Thermionic emission studies suggest the active areas of the devices are small but the devices are efficient in these areas. It is also possible to see a visible photocurrent response on functionalising the devices with dyes. Both the UV and visible responses can show a bidirectionality, possibly due to a photocatalytic mechanism. This may result in a device where it is possible to study plasmonic photocatalysis, particularly for dye breakdown mechanistic studies.

## 8.1. Conclusion

In conclusion, a range of methods were used to fabricate Schottky barrier devices on stainless steel. Two types of steel were used. 304 and 316

stainless steel form p-type protective oxides which protect the steel from oxidation by forming a diffusion barrier. With increased temperature and time, ohmic rather than Schottky contacts form, attributed to the shorting of the barrier. This is attributed to diffusion of metal ions. The protective scales that form on each grade result in a different temperature and time dependence for different grades of steel.

As the times and temperatures used in usual sintering of TiO<sub>2</sub> nanoparticle films could not be used, the films were found to be mostly amorphous. However, literature reports octahedral geometries and anatase crystallites forming at much lower temperatures and sol formation typically involves a reflux step in literature. As nucleation is typically much slower than growth, the presence of seed crystallites from the solvothermal step may result in a much more crystalline film than without them. Hydrothermal methods are also widely reported.

The extent of crystallisation of films is rarely reported, though formation of anatase phase is. There are few reports of the result of solvothermal methods on the extent of crystallinity of the sol, but here, a method of extended solvothermal synthesis resulted in a highly crystalline sol, as evidenced by the lack of confinement as observed by UV-vis spectroscopy and narrow XRD peaks, suggestive of large crystallites.

The improvements in method allowed production of devices that showed predictable diodic electrical characteristics. The closeness of the fits to exponential equations allowed the fitting of device characteristics to the diode equation using built-in fitting functions. This eliminated the error prone iterative code, though an iterative step was used to vary the pre-exponential factor to account for the larger variability in TiN devices and avoid error.

However, despite the quality of fits to the ideal diode equation, the fits of the ideal diode equation to thermionic emission theory was challenging. This revealed a complexity to the transport mechanisms as speed studies revealed the importance of diffusion to the measured electrical characteristics. The drift of oxygen vacancies is widely reported in literature on TiO<sub>2</sub> and will have an impact on the dominant transport mechanism. Further, the influence of water on the TiO<sub>2</sub> surface results in a change in electrical characteristics at

temperatures relevant to its desorption. To avoid these problems, devices were studied at faster rates and under water, but good fits to thermionic emission theory were still elusive. Fits to other voltage dependencies were no more successful. The defect assisted tunnelling and thermionic emission theory fits together may describe the electrical characteristics more fully. Under a nitrogen atmosphere, the defect dependent mechanism may be eliminated, allowing for better thermionic emission studies under nitrogens.

Capacitance studies showed non-linear doping profiles. Without accurate areas for many of the devices, dopant concentrations could not be calculated for many devices. Where it was, however, the depletion regions are like those reported in literature for nanoparticulate films. This allows an estimation of areas for the entire depletion region, assuming the metal contacts are represented by a cross-section of silver nanowires.

These devices show a photocurrent that can be improved by reducing the annealing times on increasing the crystallinity of the sol used in fabrication as well as the methods. Illuminating the devices with UV light can generate a current. Comparing the light to the area suggests a good efficiency for the separation of charge carriers over the band gap of the semiconductor. This efficiency is high in TiN devices, which may be due to a larger depletion region and a lack of recombination through defects.

The functionalisation of such devices with dye suggests similar efficiencies. The number of electrons generated is similar to the number of dye molecules expected to be in the depletion region of the Schottky barrier.

However, the photocurrent response is complicated and it not simply due to direct excitation across the band gap or excitation from defect states. Both visible and UV photocurrents can show two opposing directions in current. One of the most telling results is that by measuring the direction compared to a battery, some UV results are in the opposite direction to that expected from an excited diode. This is referred to as “forward” photocurrent, analogous to the direction when a Schottky diode is forward biased.

This suggests two competing mechanisms for this device. Given the wide reports of plasmon driven reductions in literature and the transfer of electrons to oxygen invoked in TiO<sub>2</sub> photocatalysis, this would appear to be a likely mechanism. In support of this; the photocurrent in the “forward”

direction shows no dependence on the extent of crystallinity of the sol, but a large sensitivity to the sintering times and temperatures used for the sol, decreasing exponentially with time and temperature for the “forward” current. The “negative” response does correlate linearly with sintering temperature, as expected.

The photocurrent dependence on temperature also agreed with a plasmonic photocatalytic mechanism or plasmonic sensitisation, rather than a Schottky barrier photovoltaic mechanism. Fitting to the Arrhenius equation, the activation energy is on the order of the barrier height. The UV response under water is much higher than can be accounted for by sensitization of the depletion region in some cases.

However, in contrast with an expected plasmonic absorption, the whilst the absorption of a TiO<sub>2</sub> sol with silver nanowires is non-linear, the position of the peaks do not correlate with the dielectric constant. This could be due to the insulation of the silver nanowires from this environment by remaining organics or oxide surfaces or TiO<sub>2</sub>.

By measuring at band gap energies with a narrow wavelength LED, there is a direction dependence of the photocurrent with choice of dye. This is important, as the literature on dye degradation by plasmonic/photocatalytic systems discussed in literature speculates widely on direction. Further, it demonstrates the dye has an impact on the “forward” current.

The UV-vis studies of the dye with composite systems show that 2 dyes which show the unusual “forward” currents also show a sensitivity to the volume of silver nanowires. In contrast, 2 dyes which show the expected “reverse” photocurrents show no sensitivity to the concentrations of silver nanowires. This suggests that the visible dye absorption has an impact on the mechanism accounting for the “forward” current and that the process can be sensitized to the visible region.

For devices grown on TiN coated steel, resulting in low defect films, sensitized with dye, all show a predictable response with all dyes in the “reverse” direction. Further, the efficiencies are high considering the areas. This suggests that improvements in the architecture of the device could result in large improvements in quantum efficiencies. Further, these devices could provide a method for studying the photodegradation of dyes, whilst allowing

the study of direction of electron transfer, which could in turn provide useful insights into how efficiency can be improved. Also, these studies suggest that dyes that can interact with the plasmons may be a poor choice for photocatalytic studies.

## 8.2. Future Work

From the previous 5 chapters, this work is highly divergent and many future directions could be chosen depending on the aim of the final device. For this reason, the future work will follow from each of the Chapters 2 to 6, detailing the possible future directions.

### 8.2.1. Chapter 3

This work focussed on the need to form these devices at low temperature due to the short-circuiting effect of metal diffusion from substrates. This could be visually observed, with titania sols grown on a range of metals and showing dramatic colour changes. The heat treatment of steel was found to be useful in preventing this effect. However, the absolute quantities and profiles of the metals was not studied. This could provide more information for providing better films for use in DSSCs. By using sputtering or IR heating may result in better films and the possibility of forming these devices on ITO. The advantage of semi-transparent devices is discussed in Chapter 2.

There is also a lack of literature on the solvothermal synthesis of  $\text{TiO}_2$  in water and in many studies, the degree of crystallinity is lacking. XRD suggests a build-up of strain in the crystals, however, this could be further studied in order to build up kinetic models of the growth of  $\text{TiO}_2$  crystals at such low temperatures. Rietveld analysis would offer an insight into the strain. Temperature studies could also be performed to find the optimum conditions for the reduction of this strain. This method may also provide highly reactive  $\text{TiO}_2$  surfaces due to the qualities of defects.

### 8.2.2. Chapter 4

Chapter 3 demonstrates the simplicity in the modelling of the basic device as a diode using the ideal diode equation. Though better fits are doubtless possible, the high  $R^2$  values derived for most fits and the irrelevance of the "n" term. Whilst in ideal diode equations, this value gives an indication of the degree of recombination in the depletion region, it is less useful in these

devices, where it would be expected to be very high. Thermionic emission studies resulted in only a small quantity of useable data. The devices change dramatically due to the presence of water and the speed of the scans used, which suggests the mechanism may be dependent on the presence of vacancies at the interface. The drift of vacancies also results in hysteresis in the current-voltage curves. Though attempts were made at control of these factors in order to better fit thermionic emission curves, generally submerging the device in water resulted in high conductivity resulting in an inability to fit the device to the diode equation. Fast scans were also performed in an attempt to eliminate the impact of vacancy diffusion, but there was not enough data to result in reliable fits.

One of the possible uses of Schottky barriers is as sensors. These devices are sensitive to temperature and the presence of water and light. Whilst a complete change in architecture would be necessary for the production of high quality sensors, large scale sensors might be possible. The sensitivity to temperatures at 20-100 °C and the presence of water could result in a use in building control. As memristors are considered an alternative to active memory components and this device demonstrates a sensitivity to applied potential, it could offer the possibility of integration with building components to result in a "logical" material building control system rather than a "smart" one, whereby the outputs of photovoltaics, temperature and humidity could be harnessed to control internal environments of buildings.

### 8.2.3. Chapter 5

Photocurrent experiments demonstrated the predictable dependency of crystallinity and temperature. Passivating surfaces also results in higher photocurrents. It was also possible to show relatively high photocurrent on TiN devices. From IV and capacitance studies, TiN derived devices show relatively low numbers of defects, which may result in high photocurrent.

It was also possible to improve the photocurrent response by improvement to the active area of the device by deposition of sol onto a working device. This expands the area around the nanowires that can be functionalised. This can be done by depositing sol onto nanowires. It has also been achieved by the repeated deposition of silver nanowires onto TiO<sub>2</sub> and sol resulting in a sandwich structure.

#### 8.2.4. Chapter 6

By studying the direction of the charge transfer by comparison to a battery, the high energy peak tends to be in the opposite direction to the expected direction from the excitation across a depletion region in a semiconductor. The direction of charge transfer suggests electrons travel into the silver nanowires, not the TiO<sub>2</sub> film. From studies of crystallinity and passivation, the presence of defects may help drive plasmonic reductions. Studying these through their intentional doping or measurement through the conductivity of the film may result in new insights into the reactivity of TiO<sub>2</sub> and this might explain some of the variation in literature results. Raman microscopy may be of use.

The dendritic growth of silver electrodes is well documented. Dendritic growth from silver nanowires may provide a vast surface area. Dendritic nanostructures have shown promise as SERS materials and may help with the reaction at the silver nanowires. Also, providing substrates for the plasmonic driven reaction.

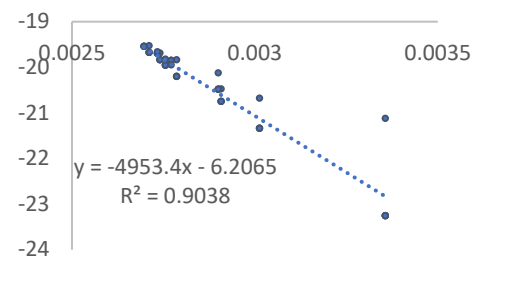
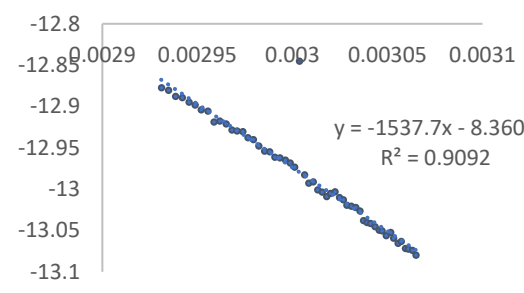
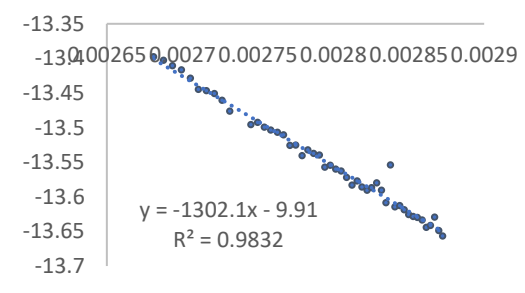
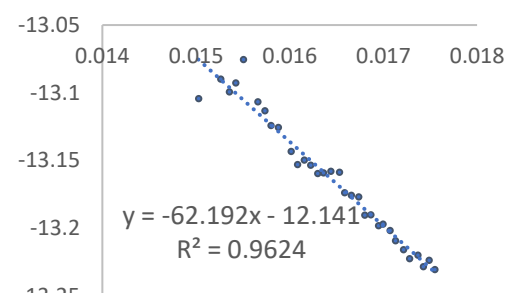
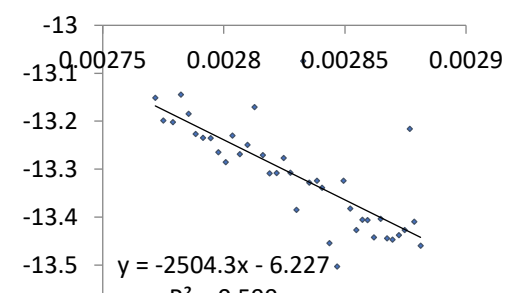
#### 8.2.5. Chapter 7

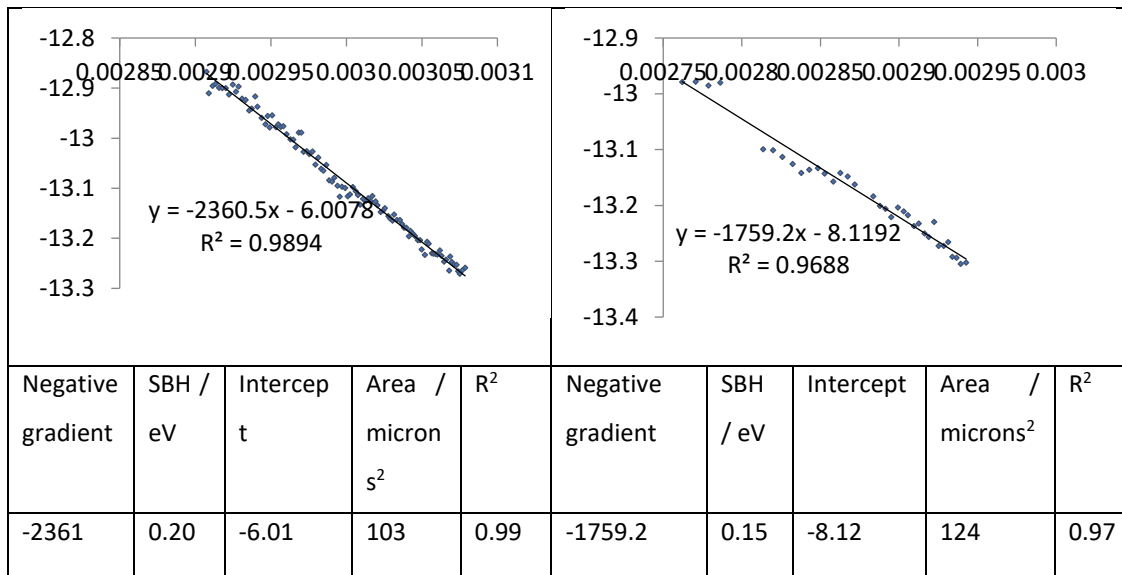
Some literature has used different protective layers, for instance, Al<sub>2</sub>O<sub>3</sub> to prevent charge transfer. This may be helpful in further unravelling the possible reactions of dyes at TiO<sub>2</sub>/metal surfaces.

Further improvements in fabrication, including control over the defect density of the TiO<sub>2</sub>, could further this understanding. An increase in area of the devices would allow for more detailed study of the excitation of the dyes. This could be illuminating as the literature on plasmonic internal photoemission suggests electrons travel into the semiconductor. For Schottky barriers, light is excited across the semiconductor band gap. However, the mechanism of metal enhancement of photocatalysis is the transfer of electrons into metal nanoparticles. This work suggests this may depend on the wavelength of light used and the choice of dye. Degradation can be shown for some dyes but not others and understanding the sensitization mechanism or the plasmonic mechanism may result in much more efficient photocatalysts for environmental remediation.

# Appendix 1: Thermionic emission fits for sol devices

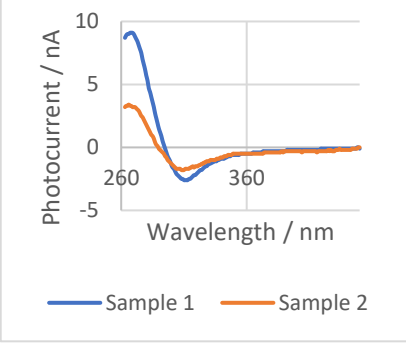
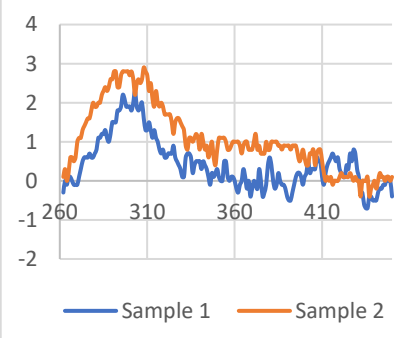
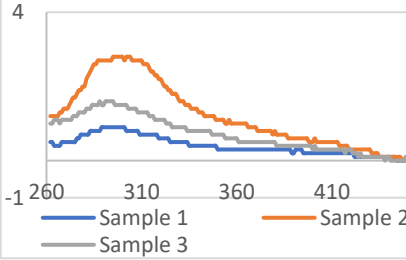
Batch					1				
Negative gradient	SBH / eV	Intercep t	Area / $\mu\text{m}^2$	$R^2$	Negative gradient	SBH / eV	Intercept	Area / $\mu\text{m}^2$	$R^2$
-6151.4	0.53	-4.08	$7.1 \times 10^2$	0.88	-10543	0.91	8.09	$1.4 \times 10^8$	0.98
Batch					2				
Negative gradient	SBH / eV	Intercep t	Area / $\mu\text{m}^2$	$R^2$	Negative gradient	SBH / eV	Intercept	Area / $\mu\text{m}^2$	$R^2$
-4365.1	0.38	-10.85	$8.05 \times 10^{-1}$	0.86	-11433	0.99	13.853	$4.34 \times 10^{10}$	0.9
Negative gradient	SBH / eV	Intercep t	Area / $\mu\text{m}^2$	$R^2$	Negative gradient	SBH / eV	Intercept	Area / $\mu\text{m}^2$	$R^2$

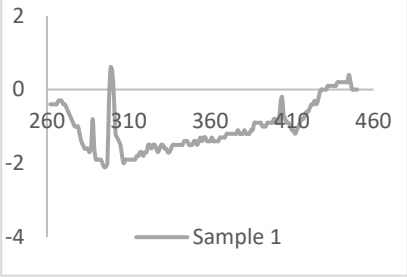
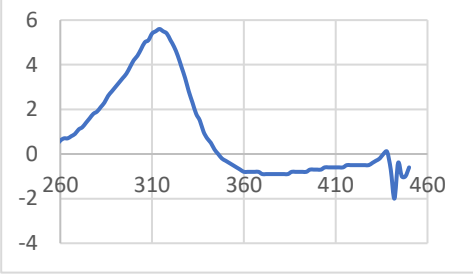
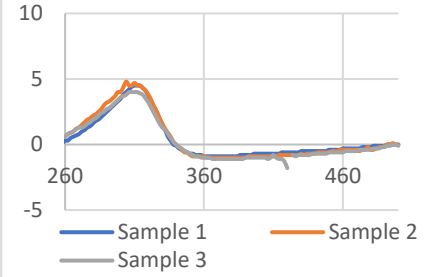
-4559.7	0.39	-10.707	93.3	0.83	-2246	0.19	-18.387	4.31 x 10 <sup>4</sup>	0.88
Batch					3				
									
-4953.4	0.43	-6.21	8.4 x 10 <sup>1</sup>	0.90					
Batch					4				
									
Negative gradient	SBH / eV	Intercep t	Area / micron s <sup>2</sup>	R <sup>2</sup>	Negative gradient	SBH / eV	Intercept	Area / microns <sup>2</sup>	R <sup>2</sup>
-1537	0.13	-8.36	9.744	0.91	-1302	0.11	-9.91	2.07	0.98
									
Negative gradient	SBH / eV	Intercep t	Area / micron s <sup>2</sup>	R <sup>2</sup>	Negative gradient	SBH / eV	Intercept	Area / microns <sup>2</sup>	R <sup>2</sup>
-2361	0.20	-6.01	103	0.99	-1759.2	0.15	-8.12	124	0.97



9 of 11 values are within a sensible set of values, with a maximum value of  $1 \times 10^4 \mu\text{m}^2$  to give a maximum possible area approximately  $1 \times 10^8 \mu\text{m}^2$ . The average value is  $124 \mu\text{m}^2$ .

## Appendix 2: UV-vis photocurrent and Tauc fits for increasing solvothermal reflux times

8 hour refluxed sol	Best fit low energy peak	Best fit high energy peak
	<p>17: (Sample 1)  <math>(Abs*hv)^{1/2}</math> (<math>R^2 = 0.989</math>)  <b>Intercept: 375 nm</b></p> <p>19: (Sample 2)  <math>(Abs*hv)^{1/2}</math> (<math>R^2 = 0.9702</math>)                      Intercept: 389 nm</p>	<p>17: (Sample 1)  <math>(Abs*hv)^2</math> (<math>R^2 = 0.987</math>)  <b>Intercept: 296 nm</b></p> <p>19: (Sample 2)  <math>(Abs*hv)^2</math> (<math>R^2 = 0.994</math>)  <b>Intercept: 293 nm</b></p>
<p>12 hour refluxed sol</p> 	<p>26: (Sample 1)  <math>(Abs*hv)^{1/2}</math> (<math>R^2 = 0.943</math>)                      Intercept: 340 nm</p> <p>27: (Sample 2)  <math>(Abs*hv)^{1/2}</math> (<math>R^2 = 0.792</math>)                      Intercept: 373 nm</p>	<p>N/A</p>
<p>16 hour refluxed sol</p> 	<p>30: (Sample 1)  <math>(Abs*hv)^{1/2}</math> (<math>R^2 = 0.934</math>)                      Intercept: 422 nm</p> <p>31: (Sample 2)  <math>(Abs*hv)^{1/2}</math> (<math>R^2 = 0.982</math>)                      Intercept: 406 nm</p> <p>33: (Sample 3)  <math>(Abs*hv)^{1/2}</math> (<math>R^2 = 0.945</math>)                      Intercept: 438 nm</p>	<p>N/A</p>
<p>20 hour refluxed sol</p>		

	<p>36: (Sample 1)  <math>(Abs*hv)^2</math> (<math>R^2 = 0.685</math>)  Intercept: 355 nm  OR  36: (Sample 1)  <math>(Abs*hv)^{1/2}</math> (<math>R^2 = 0.675</math>)  Intercept: 457 nm</p>	<p>N/A</p>
24 hour refluxed sol		
	<p>45: (Sample 1)  <math>(Abs*hv)^{1/2}</math> (<math>R^2 = 0.966</math>)  Intercept: 353 nm</p>	<p>45: (Sample 1)  <b><math>(Abs*hv)^2</math> (<math>R^2 = 0.956</math>)</b>  <b>Intercept: 434 nm</b>  OR  <math>(Abs*hv)^{1/2}</math> (<math>R^2 = 0.930</math>)  Intercept: 538 nm</p>
28 hour refluxed sol		
	<p>47: (Sample 1)  <b><math>(Abs*hv)^2</math> (<math>R^2 = 0.926</math>)</b>  <b>Intercept: 450 nm</b>  OR  <math>(Abs*hv)^{1/2}</math> (<math>R^2 = 0.926</math>)  Intercept: 621 nm</p> <p>48: (Sample 2)  <b><math>(Abs*hv)^2</math> (<math>R^2 = 0.897</math>)</b>  <b>Intercept: 488 nm</b>  OR  <math>(Abs*hv)^{1/2}</math> (<math>R^2 = 0.882</math>)  Intercept: 764 nm</p> <p>51: (Sample 3)  <b><math>(Abs*hv)^2</math> (<math>R^2 = 0.837</math>)</b>  <b>Intercept: 492 nm</b></p>	<p>47: (Sample 1)  <b><math>(Abs*hv)^2</math> (<math>R^2 = 0.982</math>)</b>  <b>Intercept: 335 nm</b>  OR  <math>(Abs*hv)^{1/2}</math> (<math>R^2 = 0.968</math>)  Intercept: 349 nm</p> <p>48: (Sample 2)  <b><math>(Abs*hv)^2</math> (<math>R^2 = 0.955</math>)</b>  <b>Intercept: 334 nm</b>  OR  <math>(Abs*hv)^{1/2}</math> (<math>R^2 = 0.933</math>)  Intercept: 357 nm</p> <p>51: (Sample 3)  <b><math>(Abs*hv)^2</math> (<math>R^2 = 0.993</math>)</b>  <b>Intercept: 338 nm</b>  OR  <math>(Abs*hv)^{1/2}</math> (<math>R^2 = 0.975</math>)  Intercept: 350 nm</p>
32 hour refluxed sol		

	<p>55: (Sample 1)  <b><math>(Abs*hv)^2</math> (<math>R^2 = 0.964</math>)</b>  <b>Intercept: 496 nm</b>  OR  <math>(Abs*hv)^{1/2}</math> (<math>R^2 = 0.954</math>)  Intercept: 719 nm</p>	<p>55: (Sample 1)  <b><math>(Abs*hv)^2</math> (<math>R^2 = 0.975</math>)</b>  <b>Intercept: 336 nm</b>  OR  <math>(Abs*hv)^{1/2}</math> (<math>R^2 = 0.983</math>)  Intercept: 353 nm</p>
	<p>57: (Sample 2)  <b><math>(Abs*hv)^2</math> (<math>R^2 = 0.954</math>)</b>  <b>Intercept: 455 nm</b>  OR  <math>(Abs*hv)^{1/2}</math> (<math>R^2 = 0.951</math>)  Intercept: 538 nm</p>	<p>57: (Sample 2)  <b><math>(Abs*hv)^2</math> (<math>R^2 = 0.988</math>)</b>  <b>Intercept: 334 nm</b>  OR  <math>(Abs*hv)^{1/2}</math> (<math>R^2 = 0.974</math>)  Intercept: 354 nm</p>
	<p>58: (Sample 3)  <math>(Abs*hv)^2</math> (<math>R^2 = 0.970</math>)  Intercept: 474 nm  OR  <math>(Abs*hv)^{1/2}</math> (<math>R^2 = 0.984</math>)  Intercept: 603 nm</p>	<p>58: (Sample 3)  <b><math>(Abs*hv)^2</math> (<math>R^2 = 0.980</math>)</b>  <b>Intercept: 334 nm</b>  OR  <math>(Abs*hv)^{1/2}</math> (<math>R^2 = 0.980</math>)  Intercept: 348 nm</p>

## Appendix 3: Dielectric constants, pKa and the impact of solvent on the difference gradient for increasing silver nanowire concentration

Gradients of absorption at 400 nm or 500 nm for increasing silver nanowire concentrations with a range of solvents. At both wavelengths, the change in absorption is influenced by the pKa of the solvent system but not its dielectric constant.

Solvent	pKa	$\epsilon$	Abs. 400 nm		Abs 550 nm	
			gradient	R2	gradient	R2
IPA	16.5		0.0028	0.08	0.0039	0.22
Ethyl acetate	25	6	-0.0281	0.78	-0.0159	0.56
water	15.7	79	-0.0179	0.84	-0.0088	0.88
ethanol	15.9	24	-0.0183	0.61	-0.0076	0.9
methanol	15.5	32.6	-0.0019	0.02	0.0038	0.14
acetone	19.2	20.7	0.0143	0.45	0.0126	0.55
hexane	34	2	0.051	0.67	0.0345	0.41
acetic acid	4.76	6.5	-0.0251	0.72	-0.0168	0.75
oleic acid	9.85	2.5	-0.022	0.23	-0.0231	0.43
formic acid	3.75	57.9	-0.0283	0.9	-0.017	0.91
ethylene glycol	14.22	37	0.0218	0.8	-0.0138	0.59

# References

1. ASTM. ASTM G173-03 Reference Solar Spectral Irradiance: Air Mass 1.5.
2. Kasap, S. & Capper, P. *Springer Handbook of Electronic and Photonic Materials*. (Springer, 2007).
3. Luther, J. M. *et al.* Schottky Solar Cells Based on Colloidal Nanocrystal Films. *Nano Lett.* **8**, 3488–3492 (2008).
4. Zhang, H. & Banfield, J. F. Kinetics of Crystallization and Crystal Growth of Nanocrystalline Anatase in Nanometer-Sized Amorphous Titania. *Chem. Mater.* **14**, 4145–4154 (2002).
5. Randall, D. A. *et al.* Climate models and their evaluation. in *Climate change 2007: The physical science basis. Contribution of Working Group I to the Fourth Assessment Report of the IPCC (FAR)* 589–662 (Cambridge University Press, 2007).
6. UNFCCC. Nationally Determined Contributions. Available at: <https://unfccc.int/process-and-meetings/the-paris-agreement/nationally-determined-contributions-ndcs>. (Accessed: 5th March 2018)

7. *Government Climate Change Act 2008 – Carbon target and budgeting – The target for 2050.* (2008).
8. *Stern Review: The Economics of Climate Change, Summary of Conclusions.* (2006).
9. Intergovernmental Panel on Climate Change & Working Group III. *Emissions scenarios. a special report of IPCC Working Group III.* (Intergovernmental Panel on Climate Change, 2000).
10. Change, I. P. O. C. *Climate change 2007: The physical science basis. Agenda* **6**, 333 (2007).
11. McKulka, T. *Women, Gender Equality and Climate Change.*
12. Jones, R. *Energy Poverty: How to Make Modern Energy Access Universal?* (2010).
13. Grätzel, M. *Photoelectrochemical cells. Nature* **414**, 338 (2001).
14. Fu, R., Feldman, D. J., Margolis, R. M., Woodhouse, M. A. & Ardani, K. B. *US solar photovoltaic system cost benchmark: Q1 2017.* (National Renewable Energy Laboratory (NREL), Golden, CO (United States), 2017).
15. Department for Business, Energy and Industrial Strategy. *Solar Photovoltaics Deployment in the UK.* (2017).
16. KPMG. *UK solar beyond subsidy: the transition.* (2015).
17. Briscoe, J., Shoaee, S., Durrant, J. R. & Dunn, S. *Piezoelectric Enhancement of Hybrid Organic/Inorganic Photovoltaic Device. J. Phys. Conf. Ser.* **476**, 012009 (2013).
18. El Chaar, L., lamont, L. A. & El Zein, N. *Review of photovoltaic technologies. Renew. Sustain. Energy Rev.* **15**, 2165–2175 (2011).

19. Schockley, W. & Queisser, H. J. Detailed balance limit of efficiency of p-n junction solar cells. *J. Appl. Phys.* **32**, 263–268 (2014).
20. Rosenberg, H. M. *The Solid State*. (Oxford University Press, 1988).
21. Tauc, J. Optical properties and electronic structure of amorphous Ge and Si. *Mater. Res. Bull.* **3**, 37–46 (1968).
22. Viezbicke, B. D., Patel, S., Davis, B. E. & Birnie, D. P. Evaluation of the Tauc method for optical absorption edge determination: ZnO thin films as a model system: Tauc method for optical absorption edge determination. *Phys. Status Solidi B* **252**, 1700–1710 (2015).
23. Diebold, U. The surface science of titanium dioxide. *Surf. Sci. Rep.* **48**, 53–229 (2003).
24. Landmann, M., Rauls, E. & Schmidt, W. G. The electronic structure and optical response of rutile, anatase and brookite TiO<sub>2</sub>. *J. Phys. Condens. Matter* **24**, 195503 (2012).
25. Zhang, J., Zhou, P., Liu, J. & Yu, J. New understanding of the difference of photocatalytic activity among anatase, rutile and brookite TiO<sub>2</sub>. *Phys. Chem. Chem. Phys.* **16**, 20382–20386 (2014).
26. Asahi, R., Morikawa, T., Ohwaki, T., Aoki, K. & Taga, Y. Visible-Light Photocatalysis in Nitrogen-Doped Titanium Oxides. *Science* **293**, 269–271 (2001).
27. Zaleska, A. Doped-TiO<sub>2</sub>: A Review. *Recent Pat. Eng.* **2**, 157–164 (2008).
28. Schaub, R. *et al.* Oxygen Vacancies as Active Sites for Water Dissociation on Rutile TiO<sub>2</sub> (110). *Phys. Rev. Lett.* **87**, (2001).

29. Linsebigler, A. L., Lu, G. & Yates, J. T. Photocatalysis on TiO<sub>2</sub> Surfaces: Principles, Mechanisms, and Selected Results. *Chem. Rev.* **95**, 735–758 (1995).
30. Xiong, Z., Wu, H., Zhang, L., Gu, Y. & Zhao, X. S. Synthesis of TiO<sub>2</sub> with controllable ratio of anatase to rutile. *J. Mater. Chem. A* **2**, 9291–9297 (2014).
31. Hodes, G. & Kamat, P. V. Understanding the Implication of Carrier Diffusion Length in Photovoltaic Cells. *J. Phys. Chem. Lett.* **6**, 4090–4092 (2015).
32. van de Lagemaat, J., Park, N.-G. & Frank, A. J. Influence of Electrical Potential Distribution, Charge Transport, and Recombination on the Photopotential and Photocurrent Conversion Efficiency of Dye-Sensitized Nanocrystalline TiO<sub>2</sub> Solar Cells: A Study by Electrical Impedance and Optical Modulation Techniques. *J. Phys. Chem. B* **104**, 2044–2052 (2000).
33. Snaith, H. J. & Grätzel, M. The Role of a “Schottky Barrier” at an Electron-Collection Electrode in Solid-State Dye-Sensitized Solar Cells. *Adv. Mater.* **18**, 1910–1914 (2006).
34. Wochnik, A. S., Handloser, M., Durach, D., Hartschuh, A. & Scheu, C. Increasing Crystallinity for Improved Electrical Conductivity of TiO<sub>2</sub> Blocking Layers. *ACS Appl. Mater. Interfaces* **5**, 5696–5699 (2013).
35. Hendry, E., Koeberg, M., O’Regan, B. & Bonn, M. Local Field Effects on Electron Transport in Nanostructured TiO<sub>2</sub> Revealed by Terahertz Spectroscopy. *Nano Lett.* **6**, 755–759 (2006).
36. Hansen, M. *et al.* A double barrier memristive device. *Sci. Rep.* **5**, 13753 (2015).

37. Yang, J. J. *et al.* Memristive switching mechanism for metal/oxide/metal nanodevices. *Nat. Nanotechnol.* **3**, 429–433 (2008).
38. Jameson, J. R. *et al.* Field-programmable rectification in rutile TiO<sub>2</sub> crystals. *Appl. Phys. Lett.* **91**, 112101 (2007).
39. Gupta, S. M. & Tripathi, M. A review of TiO<sub>2</sub> nanoparticles. *Chin. Sci. Bull.* **56**, 1639–1657 (2011).
40. Fisher, A. C. *Electrode Dynamics*. (1996).
41. Rajeshwar, K. 1 Fundamentals of Semiconductor Electrochemistry and Photoelectrochemistry. in *Encyclopedia of Electrochemistry, Semiconductor Electrodes and Photochemistry* **6**, 52 (Wiley, 2002).
42. Gutknecht, P. & Strutt, M. J. O. Schottky barrier height dependence on Si crystal orientation. *Appl. Phys. Lett.* **21**, 405–407 (1972).
43. Sharma, B. L. *Metal-Semiconductor Schottky Barrier Junctions and Their Applications*. (1984).
44. McCaldin, J. O., McGill, T. C. & Mead, C. A. Schottky barriers on compound semiconductors: The role of the anion. *J. Vac. Sci. Technol.* **13**, 802–806 (1976).
45. Cowley, A. M. & Sze, S. M. Surface States and Barrier Height of Metal-Semiconductor Systems. *J. Appl. Phys.* **36**, 3212–3220 (1965).
46. Cowley, A. M. & Sze, S. M. Surface States and Barrier Height of Metal-Semiconductor Systems. *J. Appl. Phys.* **36**, 3212–3220 (1965).
47. Tung, R. T. (董梓則). The physics and chemistry of the Schottky barrier height. *Appl. Phys. Rev.* **1**, 011304 (2014).

48. Carroll, D. L., Wagner, M., Rühle, M. & Bonnell, D. A. Schottky-barrier formation at nanoscale metal-oxide interfaces. *Phys. Rev. B* **55**, 9792 (1997).
49. Jarrett, R. Characterisation of silver nanowires as transparent conductive electrodes designed for photovoltaic solar cell. (University of Leeds, 2015).
50. Xie, S., Ouyang, Z., Jia, B. & Gu, M. Large-size, high-uniformity, random silver nanowire networks as transparent electrodes for crystalline silicon wafer solar cells. *Opt. Express* **21**, A355–A362 (2013).
51. Li, Y. *et al.* High-efficiency robust perovskite solar cells on ultrathin flexible substrates. *Nat. Commun.* **7**, 10214 (2016).
52. Oh, M. *et al.* Silver Nanowire Transparent Conductive Electrodes for High-Efficiency III-Nitride Light-Emitting Diodes. *Sci. Rep.* **5**, 13483 (2015).
53. Sargent, E. H. Infrared photovoltaics made by solution processing. *Nat. Photonics* **3**, 325–331 (2009).
54. Koleilat, G. I. *et al.* Efficient, Stable Infrared Photovoltaics Based on Solution-Cast Colloidal Quantum Dots. *ACS Nano* **2**, 833–840 (2008).
55. Piliago, C., Protesescu, L., Bisri, S. Z., Kovalenko, M. V. & Loi, M. A. 5.2% efficient PbS nanocrystal Schottky solar cells. *Energy Environ. Sci.* **6**, 3054 (2013).
56. Takahashi, K. *et al.* Sensitization Effect of Porphyrin Dye on the Photocurrent of Al/Polythiophene Schottky-Barrier Cells. *J. Phys. Chem. B* **107**, 1646–1652 (2003).

57. Chen, Q. *et al.* Schottky barrier detectors on GaN for visible-blind ultraviolet detection. *Appl. Phys. Lett.* **70**, 2277–2279 (1997).
58. Han, N. *et al.* GaAs nanowire Schottky barrier photovoltaics utilizing Au–Ga alloy catalytic tips. *Appl. Phys. Lett.* **101**, 013105 (2012).
59. Ma, Z. H., Sou, I. K., Wong, K. S., Yang, Z. & Wong, G. K. L. ZnSTe-based Schottky barrier ultraviolet detectors with nanosecond response time. *Appl. Phys. Lett.* **73**, 2251–2253 (1998).
60. Liao, M., Koide, Y. & Alvarez, J. Photovoltaic Schottky ultraviolet detectors fabricated on boron-doped homoepitaxial diamond layer. *Appl. Phys. Lett.* **88**, 033504 (2006).
61. Binet, F. *et al.* Properties of a photovoltaic detector based on an n-type GaN Schottky barrier. *J. Appl. Phys.* **81**, 6449–6454 (1997).
62. Johnston, K. W. *et al.* Efficient Schottky-quantum-dot photovoltaics: The roles of depletion, drift, and diffusion. *Appl. Phys. Lett.* **92**, 122111 (2008).
63. Asif Khan, M., Kuznia, J. N., Olson, D. T., Blasingame, M. & Bhattarai, A. R. Schottky barrier photodetector based on Mg-doped *p*-type GaN films. *Appl. Phys. Lett.* **63**, 2455–2456 (1993).
64. Soyulu, M. & Yakuphanoglu, F. Photovoltaic and interface state density properties of the Au/n-GaAs Schottky barrier solar cell. *Thin Solid Films* **519**, 1950–1954 (2011).
65. Anderson, W. A., Delahoy, A. E. & Milano, R. A. An 8% efficient layered Schottky-barrier solar cell. *J. Appl. Phys.* **45**, 3913–3915 (1974).
66. McFarland, E. & Tang, J. A photovoltaic device structure based on internal electron emission. *Nature* **421**, 616–618 (2003).

67. Tang, J., White, M., Stucky, G. D. & McFarland, E. W. Electrochemical fabrication of large-area Au/TiO<sub>2</sub> junctions. *Electrochem. Commun.* **5**, 497–501 (2003).
68. Su, Y. H., Lai, W. H., Teoh, L. G., Hon, M. H. & Huang, J. L. Layer-by-layer Au nanoparticles as a Schottky barrier in a water-based dye-sensitized solar cell. *Appl. Phys. A* **88**, 173–178 (2007).
69. Dittrich, T., Zabel, P., Lenzmann, F., Morales, G. & Otero, L. The TiO<sub>2</sub>/Ru(dcbpyH<sub>2</sub>)<sub>2</sub>(NCS)<sub>2</sub>/Au Schottky junction. *Thin Solid Films* **516**, 7234–7236 (2008).
70. Kılıçoğlu, T. Effect of an organic compound (Methyl Red) interfacial layer on the calculation of characteristic parameters of an Al/Methyl Red/p-Si sandwich Schottky barrier diode. *Thin Solid Films* **516**, 967–970 (2008).
71. Koole, R., Liljeroth, P., Oosterhout, S. & Vanmaekelbergh, D. Chemisorption Determines the Photovoltage of a Ti/TiO<sub>2</sub>/Au/Dye Internal Electron Emission Photovoltaic Cell. *J. Phys. Chem. B* **109**, 9205–9208 (2005).
72. Ji, X., Zupperro, A., Gidwani, J. M. & Somorjai, G. A. The Catalytic Nanodiode: Gas Phase Catalytic Reaction Generated Electron Flow Using Nanoscale Platinum Titanium Oxide Schottky Diodes. *Nano Lett.* **5**, 753–756 (2005).
73. Park, J. Y., Lee, H., Renzas, J. R., Zhang, Y. & Somorjai, G. A. Probing Hot Electron Flow Generated on Pt Nanoparticles with Au/TiO<sub>2</sub> Schottky Diodes during Catalytic CO Oxidation. *Nano Lett.* **8**, 2388–2392 (2008).

74. McEvoy, A. J. & Gissler, W. A ruthenium dioxide-semiconductor Schottky barrier photovoltaic device. *J. Appl. Phys.* **53**, 1251–1252 (1982).
75. Shafiei, M. *et al.* Reversed bias Pt/nanostructured ZnO Schottky diode with enhanced electric field for hydrogen sensing☆. *Sens. Actuators B Chem.* **146**, 507–512 (2010).
76. Thankappan, A. *et al.* Highly efficient betanin dye based ZnO and ZnO/Au Schottky barrier solar cell. *Thin Solid Films* **583**, 102–107 (2015).
77. Chen, T.-Y., Fan, C.-M., Wu, J.-Y. & Lin, T.-L. Hybrid Silver Nanowire/Titanium Oxides Nanocomposites as Anode for Dye-Sensitized Solar Cell Application. *J. Chin. Chem. Soc.* **56**, 1244–1249 (2009).
78. Tsang, M.-Y. *et al.* Enhanced Photocatalytic Hydrogen Generation Using Polymorphic Macroporous TaON. *Adv. Mater.* **24**, 3406–3409 (2012).
79. Carnie, M. J. *et al.* A one-step low temperature processing route for organolead halide perovskite solar cells. *Chem. Commun.* **49**, 7893–7895 (2013).
80. HU, H. *et al.* Preparations of TiO<sub>2</sub> film coated on foam nickel substrate by sol-gel processes and its photocatalytic activity for degradation of acetaldehyde. *J. Environ. Sci.* **19**, 80–85 (2007).
81. World Steel Association. WORLD STEEL IN FIGURES 2016. (2016).
82. Guillamet, R., Lopitiaux, J., Hannyoy, B. & Lenglet, M. Oxidation of stainless steels (AISI 304 and 316) at high temperature. Influence on the metallic substratum. *J. Phys. IV* **3**, C9–349 (1993).

83. Visnapuu, A., Volosin, J. S. & Schluter, R. B. *Annealing study of stainless steel to conserve critical metals. Report of investigations/1994.* (1994).
84. Hansson, A. N., Hattel, J. H., Dahl, K. V. & Somers, M. A. J. Modelling Cr depletion under a growing Cr<sub>2</sub>O<sub>3</sub> layer on austenitic stainless steel: the influence of grain boundary diffusion. *Model. Simul. Mater. Sci. Eng.* **17**, 035009 (2009).
85. Habib, K. A., Damra, M. S., Saura, J. J., Cervera, I. & Bellés, J. Breakdown and Evolution of the Protective Oxide Scales of AISI 304 and AISI 316 Stainless Steels under High-Temperature Oxidation. *Int. J. Corros.* **2011**, 1–10 (2011).
86. Kim, J. J. & Young, Y. M. Study on the passive film of type 316 stainless steel. *Int J Electrochem Sci* **8**, 11847–11859 (2013).
87. Ahamad Mohiddon, M. *et al.* Chromium oxide as a metal diffusion barrier layer: An x-ray absorption fine structure spectroscopy study. *J. Appl. Phys.* **115**, 044315 (2014).
88. Nomura, K. & Ujihira, Y. Analysis of oxide layers on stainless steel (304, and 316) by conversion electron Mössbauer spectrometry. *J. Mater. Sci.* **25**, 1745–1750 (1990).
89. Pettersson, J., Asteman, H., Svensson, J.-E. & Johansson, L.-G. KCl Induced Corrosion of a 304-type Austenitic Stainless Steel at 600°C; The Role of Potassium. *Oxid. Met.* **64**, 23–41 (2005).
90. Pettersson, J., Asteman, H., Svensson, J.-E. & Johansson, L.-G. KCl Induced Corrosion of a 304-type Austenitic Stainless Steel at 600°C; The Role of Potassium. *Oxid. Met.* **64**, 23–41 (2005).

91. Karlsson, S., Pettersson, J., Johansson, L.-G. & Svensson, J.-E. Alkali Induced High Temperature Corrosion of Stainless Steel: The Influence of NaCl, KCl and CaCl<sub>2</sub>. *Oxid. Met.* **78**, 83–102 (2012).
92. Duan, Y. *et al.* Sn-Doped TiO<sub>2</sub> Photoanode for Dye-Sensitized Solar Cells. *J. Phys. Chem. C* **116**, 8888–8893 (2012).
93. Kabre, J. & LeSuer, R. J. Modeling Diffusion of Tin into the Mesoporous Titanium Dioxide Layer of a Dye-Sensitized Solar Cell Photoanode. *J. Phys. Chem. C* **116**, 18327–18333 (2012).
94. Andrei, C. & Zerulla, D. Optimisation of Ruthenium Dye Sensitised Solar Cells Efficiency via Sn Diffusion into the TiO<sub>2</sub> Mesoporous Layer. *PLoS ONE* **8**, e63923 (2013).
95. Zhao, D. *et al.* Enhanced photocatalytic degradation of dye pollutants under visible irradiation on Al(III)-modified TiO<sub>2</sub>: structure, interaction, and interfacial electron transfer. *Environ. Sci. Technol.* **42**, 308–314
96. Zhu, Y., Zhang, L., Wang, L., Fu, Y. & Cao, L. The preparation and chemical structure of TiO<sub>2</sub> film photocatalysts supported on stainless steel substrates via the sol–gel method. *J. Mater. Chem.* **11**, 1864–1868 (2001).
97. Tobaldi, D. M., Pullar, R. C., Seabra, M. P. & Labrincha, J. A. Fully quantitative X-ray characterisation of Evonik Aeroxide TiO<sub>2</sub> P25®. *Mater. Lett.* **122**, 345–347 (2014).
98. Pham, H. H. & Wang, L.-W. Oxygen vacancy and hole conduction in amorphous TiO<sub>2</sub>. *Phys Chem Chem Phys* **17**, 541–550 (2015).
99. Ohtani, B., Ogawa, Y. & Nishimoto, S. Photocatalytic Activity of Amorphous–Anatase Mixture of Titanium(IV) Oxide Particles

- Suspended in Aqueous Solutions. *J. Phys. Chem. B* **101**, 3746–3752 (1997).
100. Kumar, S. G. & Rao, K. S. R. K. Polymorphic phase transition among the titania crystal structures using a solution-based approach: from precursor chemistry to nucleation process. *Nanoscale* **6**, 11574–11632 (2014).
101. Mehranpour, H., Askari, M. & Ghamsari, M. S. Nucleation and growth of tio2 nanoparticles. in *Nanomaterials* (InTech, 2011).
102. Charbonneau, C., Gauvin, R. & Demopoulos, G. P. Nucleation and growth of self-assembled nanofibre-structured rutile (TiO<sub>2</sub>) particles via controlled forced hydrolysis of titanium tetrachloride solution. *J. Cryst. Growth* **312**, 86–94 (2009).
103. Yanagisawa, K., Yamamoto, Y., Feng, Q. & Yamasaki, N. Formation mechanism of fine anatase crystals from amorphous titania under hydrothermal conditions. *J. Mater. Res.* **13**, 825–829 (1998).
104. Khatim, O. *et al.* Amorphous–anatase phase transition in single immobilized TiO<sub>2</sub> nanoparticles. *Chem. Phys. Lett.* **558**, 53–56 (2013).
105. Mahshid, S., Askari, M. & Ghamsari, M. S. Synthesis of TiO<sub>2</sub> nanoparticles by hydrolysis and peptization of titanium isopropoxide solution. *J. Mater. Process. Technol.* **189**, 296–300 (2007).
106. Yin, S., Uchida, S., Fujishiro, Y., Aki, M. & Sato, T. Phase transformation of protonic layered tetratitanate under solvothermal conditions. *J. Mater. Chem.* **9**, 1191–1195 (1999).
107. Sugimoto, T. & Zhou, X. Synthesis of Uniform Anatase TiO<sub>2</sub> Nanoparticles by the Gel–Sol Method. *J. Colloid Interface Sci.* **252**, 347–353 (2002).

108. Shin, H., Jung, H. S., Hong, K. S. & Lee, J.-K. Crystallization Process of TiO<sub>2</sub> Nanoparticles in an Acidic Solution. *Chem. Lett.* **33**, 1382–1383 (2004).
109. Zhang, G., Roy, B. K., Allard, L. F. & Cho, J. Titanium Oxide Nanoparticles Precipitated from Low-Temperature Aqueous Solutions: I. Nucleation, Growth, and Aggregation. *J. Am. Ceram. Soc.* **91**, 3875–3882 (2008).
110. Seo, D.-S., Lee, J.-K., Lee, E.-G. & Kim, H. Effect of aging agents on the formation of TiO<sub>2</sub> nanocrystalline powder. *Mater. Lett.* **51**, 115–119 (2001).
111. Seo, D.-S., Lee, J.-K. & Kim, H. Synthesis of TiO<sub>2</sub> nanocrystalline powder by aging at low temperature. *J. Cryst. Growth* **233**, 298–302 (2001).
112. Hsiang, H.-I. & Lin, S.-C. Effects of aging on the phase transformation and sintering properties of TiO<sub>2</sub> gels. *Mater. Sci. Eng. A* **380**, 67–72 (2004).
113. Agarwala, S. *et al.* Mesophase Ordering of TiO<sub>2</sub> Film with High Surface Area and Strong Light Harvesting for Dye-Sensitized Solar Cell. *ACS Appl. Mater. Interfaces* **2**, 1844–1850 (2010).
114. Xie, H., Xi, T., Zhang, Q. & Wu, Q. *Study on the phase transformation behavior of nanosized amorphous TiO<sub>2</sub>.* **19**, (2003).
115. Matthews, A. The crystallization of anatase and rutile from amorphous titanium dioxide under hydrothermal conditions. *Am. Mineral.* **61**, 419–424 (1976).

116. Akrapopulu, K. C., Kordulis, C. & Lycourghiotis, A. Effect of temperature on the point of zero charge and surface charge of TiO<sub>2</sub>. *J. Chem. Soc. Faraday Trans.* **86**, 3437–3440 (1990).
117. Gao, M., Rui, Y., Wang, H., Li, Y. & Zhang, Q. Submicrometer@nano Bimodal TiO<sub>2</sub> Particles as Easily Sintered, Crack-Free, and Current-Contributed Scattering Layers for Dye-Sensitized Solar Cells. *J. Phys. Chem. C* **118**, 16951–16958 (2014).
118. Miyasaka, T., Ikegami, M. & Kijitori, Y. Photovoltaic Performance of Plastic Dye-Sensitized Electrodes Prepared by Low-Temperature Binder-Free Coating of Mesoscopic Titania. *J. Electrochem. Soc.* **154**, A455–A461 (2007).
119. Yun, Y. J., Chung, J. S., Kim, S., Hahn, S. H. & Kim, E. J. Low-temperature coating of sol–gel anatase thin films. *Mater. Lett.* **58**, 3703–3706 (2004).
120. Sugimoto, T., Zhou, X. & Muramatsu, A. Synthesis of uniform anatase TiO<sub>2</sub> nanoparticles by gel–sol method. *J. Colloid Interface Sci.* **259**, 43–52 (2003).
121. Yune, J., Karatchevtseva, I., Triania, G., Wagner, K. & Officer, D. A study of TiO<sub>2</sub> binder-free paste prepared for low temperature dye-sensitized solar cells. **28**, (2013).
122. Kim, H.-J., Park, S. Y. & Kwak, S.-Y. Photovoltaic Performance of a Novel TiO<sub>2</sub> Electrode consisting of a Mesoporous TiO<sub>2</sub> layer and a compact TiO<sub>2</sub> Blocking layer for Dye-sensitized solar cells. in *2010 International Conference on Biology, Environment and Chemistry IPCBEE vol. 1 (2011)* IACSIT Press, Singapore (2011).

123. Hočevar, M. *et al.* Sol-gel based TiO<sub>2</sub> paste applied in screen-printed dye-sensitized solar cells and modules. *J. Ind. Eng. Chem.* **19**, 1464–1469 (2013).
124. Mori, R. *et al.* Organic solvent based TiO<sub>2</sub> dispersion paste for dye-sensitized solar cells prepared by industrial production level procedure. *J. Mater. Sci.* **46**, 1341–1350 (2011).
125. Choi, W., Termin, A. & Hoffmann, M. R. The Role of Metal Ion Dopants in Quantum-Sized TiO<sub>2</sub>: Correlation between Photoreactivity and Charge Carrier Recombination Dynamics. *J. Phys. Chem.* **98**, 13669–13679 (1994).
126. Barbé, C. J. *et al.* Nanocrystalline Titanium Oxide Electrodes for Photovoltaic Applications. *J. Am. Ceram. Soc.* **80**, 3157–3171 (2005).
127. Clara Anthoniamma, S. & Gurumallesh Prabu, H. Photocatalytic activity of TiO<sub>2</sub> films prepared by sol-gel and electrodeposition on the decolourization of monoazo dyes. *J. Sol-Gel Sci. Technol.* **73**, 118–126 (2015).
128. Galhenage, R. P. *et al.* Understanding the Nucleation and Growth of Metals on TiO<sub>2</sub>: Co Compared to Au, Ni, and Pt. *J. Phys. Chem. C* **117**, 7191–7201 (2013).
129. Yuan, J. & Tsujikawa, S. Characterization of Sol-Gel-Derived TiO<sub>2</sub> Coatings and Their Photoeffects on Copper Substrates. *J. Electrochem. Soc.* **142**, 3444–3450 (1995).
130. Karuppuchamy, S., Andou, Y. & Endo, T. Preparation of nanostructured TiO<sub>2</sub> photoelectrode for flexible dye-sensitized solar cell applications. *Appl. Nanosci.* **3**, 291–293 (2013).

131. Lee, C.-H., Chiu, W.-H., Lee, K.-M., Hsieh, W.-F. & Wu, J.-M. Improved performance of flexible dye-sensitized solar cells by introducing an interfacial layer on Ti substrates. *J. Mater. Chem.* **21**, 5114 (2011).
132. Tsai, T.-Y., Chen, C.-M., Cherng, S.-J. & Suen, S.-Y. An efficient titanium-based photoanode for dye-sensitized solar cell under back-side illumination. *Prog. Photovolt. Res. Appl.* **21**, 226–231 (2013).
133. Jacques, D. A. Demonstration and Evaluation of a Nanocrystal-Nanowire Solar Cell (Unpublished doctoral thesis). (2015).
134. Kehres, J. *et al.* Combined in situ small and wide angle X-ray scattering studies of TiO<sub>2</sub> nano-particle annealing to 1023 K. *J. Appl. Crystallogr.* **43**, 1400–1408 (2010).
135. Lin, H. *et al.* Size dependency of nanocrystalline TiO<sub>2</sub> on its optical property and photocatalytic reactivity exemplified by 2-chlorophenol. *Appl. Catal. B Environ.* **68**, 1–11 (2006).
136. Li, C.-T. *et al.* Efficient titanium nitride/titanium oxide composite photoanodes for dye-sensitized solar cells and water splitting. *J Mater Chem A* **3**, 4695–4705 (2015).
137. Bisquert, J. *Nanostructured energy devices: equilibrium concepts and kinetics.* (Crc Press, 2014).
138. Adachi, M., Sakamoto, M., Jiu, J., Ogata, Y. & Isoda, S. Determination of Parameters of Electron Transport in Dye-Sensitized Solar Cells Using Electrochemical Impedance Spectroscopy. *J. Phys. Chem. B* **110**, 13872–13880 (2006).
139. Tyagi, M. S. *Introduction to semiconductor materials and devices.* (Wiley).
140. Fromille, S. & Phillips, J. Super Dielectric Materials. *Materials* **7**, (2014).

141. Reynolds, N. D., Panda, C. D. & Essick, J. M. Capacitance-voltage profiling: Research-grade approach versus low-cost alternatives. *Am. J. Phys.* **82**, 196–205 (2014).
142. Gelderman, K., Lee, L. & Donne, S. W. Flat-Band Potential of a Semiconductor: Using the Mott–Schottky Equation. *J. Chem. Educ.* **84**, 685 (2007).
143. O'Malley, J. *Schaum's outline of theory and problems of basic circuit analysis*. (McGraw-Hill, 1992).
144. Chiu, F.-C. A Review on Conduction Mechanisms in Dielectric Films. *Adv. Mater. Sci. Eng.* **2014**, 1–18 (2014).
145. Lu, M.-Y., Lu, M.-P., You, S.-J., Chen, C.-W. & Wang, Y.-J. Quantifying the barrier lowering of ZnO Schottky nanodevices under UV light. *Sci. Rep.* **5**, (2015).
146. Dökme, İ. The analysis of I–V characteristics of Schottky diodes by thermionic emission with a Gaussian distribution of barrier height. *Microelectron. Reliab.* **51**, 360–364 (2011).
147. Sze, S. . & Hg, K. . *Physics of Semiconductor Devices*. (Wiley, 2006).
148. Könenkamp, R. & Rieck, I. Electrical properties of Schottky diodes on nano-porous TiO<sub>2</sub> films. *Mater. Sci. Eng. B* **69–70**, 519–521 (2000).
149. Hagfeldt, A., Björkstén, U. & Grätzel, M. Photocapacitance of Nanocrystalline Oxide Semiconductor Films: Band-Edge Movement in Mesoporous TiO<sub>2</sub> Electrodes during UV Illumination. *J. Phys. Chem.* **100**, 8045–8048 (1996).
150. Hardy, P. K. Fabrication and characterisation of a nanocrystal activated Schottky barrier solar cell. (University of Leeds, 2014).

151. Blagojevic, V., Chen, Y.-R., Steigerwald, M., Brus, L. & Friesner, R. A. Quantum Chemical Investigation of Cluster Models for TiO<sub>2</sub> Nanoparticles with Water-Derived Ligand Passivation: Studies of Excess Electron States and Implications for Charge Transport in the Gratzel Cell. *J. Phys. Chem. C* **113**, 19806–19811 (2009).
152. Chinnamuthu, P., Dhar, J. C., Mondal, A., Bhattacharyya, A. & Singh, N. K. Ultraviolet detection using TiO<sub>2</sub> nanowire array with Ag Schottky contact. *J. Phys. Appl. Phys.* **45**, 135102 (2012).
153. Song, T.-B. *et al.* Nanoscale Joule Heating and Electromigration Enhanced Ripening of Silver Nanowire Contacts. *ACS Nano* **8**, 2804–2811 (2014).
154. Zhu, S.-Q. *et al.* Gold nanoparticle thin films fabricated by electrophoretic deposition method for highly sensitive SERS application. *Nanoscale Res. Lett.* **7**, 613 (2012).
155. Filippo, E., Serra, A., Buccolieri, A. & Manno, D. Green synthesis of silver nanoparticles with sucrose and maltose: Morphological and structural characterization. *J. Non-Cryst. Solids* **356**, 344–350 (2010).
156. Lin, Y.-C. Applying Surface Charge Attraction to Synthesizing TiO<sub>2</sub>/Ag Composition for VOCs Photodegradation. *Aerosol Air Qual. Res.* (2013). doi:10.4209/aaqr.2012.09.0247
157. Luan, C. *et al.* A Strategy for Improving the Interfacial Crystallinity and Carrier Mobility of SnO<sub>2</sub> Porous Nanosolids. *ArXiv Prepr. ArXiv150806822* (2015).
158. Ha, H., Yoshimoto, M., Koinuma, H., Moon, B. & Ishiwara, H. Open air plasma chemical vapor deposition of highly dielectric amorphous TiO<sub>2</sub> films. *Appl. Phys. Lett.* **68**, 2965–2967 (1996).

159. Busani, T. & Devine, R. A. B. Dielectric and infrared properties of TiO<sub>2</sub> films containing anatase and rutile. *Semicond. Sci. Technol.* **20**, 870–875 (2005).
160. Alam, M. J. & Cameron, D. C. Preparation and Characterization of TiO<sub>2</sub> Thin Films by Sol-Gel Method. *J. Sol-Gel Sci. Technol.* **25**, 137–145 (2002).
161. Clifford, J. P., Johnston, K. W., Levina, L. & Sargent, E. H. Schottky barriers to colloidal quantum dot films. *Appl. Phys. Lett.* **91**, 253117 (2007).
162. Gao, P. *et al.* The critical role of point defects in improving the specific capacitance of  $\delta$ -MnO<sub>2</sub> nanosheets. *Nat. Commun.* **8**, 14559 (2017).
163. Kılıçoğlu, T. Effect of an organic compound (Methyl Red) interfacial layer on the calculation of characteristic parameters of an Al/Methyl Red/p-Si sandwich Schottky barrier diode. *Thin Solid Films* **516**, 967–970 (2008).
164. Olsen, L. C., Bohara, R. C. & Urie, M. W. Explanation for low-efficiency Cu<sub>2</sub>O Schottky-barrier solar cells. *Appl. Phys. Lett.* **34**, 47–49 (1979).
165. Tvrdy, K., Frantsuzov, P. A. & Kamat, P. V. Photoinduced electron transfer from semiconductor quantum dots to metal oxide nanoparticles. *Proc. Natl. Acad. Sci.* **108**, 29–34 (2011).
166. Hines, D. A. & Kamat, P. V. Quantum Dot Surface Chemistry: Ligand Effects and Electron Transfer Reactions. *J. Phys. Chem. C* **117**, 14418–14426 (2013).
167. Chakrapani, V., Baker, D. & Kamat, P. V. Understanding the Role of the Sulfide Redox Couple (S<sup>2-</sup>/Sn<sup>2-</sup>) in Quantum Dot-Sensitized Solar Cells. *J. Am. Chem. Soc.* **133**, 9607–9615 (2011).

168. Lee, Y.-L. & Chang, C.-H. Efficient polysulfide electrolyte for CdS quantum dot-sensitized solar cells. *J. Power Sources* **185**, 584–588 (2008).
169. Xie, H., Xi, T., Zhang, Q. & Wu, Q. Study on the Phase Transformation Behavior of Nanosized Amorphous TiO<sub>2</sub>. *J. Mater. Sci. Technol.* **19**, 463–466
170. Jakubowicz, J., Koper, J. K., Adamek, G., Polomska, M. & Wolak, J. Silver nano-trees deposited in the pores of anodically oxidized titanium and Ti scaffold. *Int J Electrochem Sci* **10**, 4165–4172 (2015).
171. Xie, S. *et al.* Fast Growth Synthesis of Silver Dendrite Crystals Assisted by Sulfate Ion and Its Application for Surface-Enhanced Raman Scattering. *J. Phys. Chem. C* **115**, 9943–9951 (2011).
172. Yi-Ming Chang and Wen-Yung Yeh and Pin-Chu Chen. Highly foldable transparent conductive films composed of silver nanowire junctions prepared by chemical metal reduction. *Nanotechnology* **25**, 285601 (2014).
173. Alam, M. J. & Cameron, D. C. Preparation and Characterization of TiO<sub>2</sub> Thin Films by Sol-Gel Method. *J. Sol-Gel Sci. Technol.* **25**, 137–145 (2002).
174. Papageorgiou, A. C. *et al.* Electron traps and their effect on the surface chemistry of TiO<sub>2</sub>(110). *Proc. Natl. Acad. Sci.* **107**, 2391–2396 (2010).
175. Hou, W. & Cronin, S. B. A Review of Surface Plasmon Resonance-Enhanced Photocatalysis. *Adv. Funct. Mater.* **23**, 1612–1619 (2013).
176. Chen, H., Schatz, G. C. & Ratner, M. A. CHAPTER 4 Plasmon-enhanced Solar Chemistry: Electrodynamics and Quantum Mechanics. in *Solar Energy Conversion: Dynamics of Interfacial Electron and Excitation*

- Transfer* 111–134 (The Royal Society of Chemistry, 2013).  
doi:10.1039/9781849735445-00111
177. Durrant, A. *Quantum Physics of Matter*. (Open University Worldwide, 2008).
178. Barnes, W. L., Dereux, A. & Ebbesen, T. W. Surface plasmon subwavelength optics. *Nature* **424**, 824 (2003).
179. Qi, J., Dang, X., Hammond, P. T. & Belcher, A. M. Highly Efficient Plasmon-Enhanced Dye-Sensitized Solar Cells through Metal@Oxide Core–Shell Nanostructure. *ACS Nano* **5**, 7108–7116 (2011).
180. Ma, X.-C., Dai, Y., Yu, L. & Huang, B.-B. Energy transfer in plasmonic photocatalytic composites. *Light Sci. Appl.* **5**, e16017 (2016).
181. Manjavacas, A., Liu, J. G., Kulkarni, V. & Nordlander, P. Plasmon-Induced Hot Carriers in Metallic Nanoparticles. *ACS Nano* **8**, 7630–7638 (2014).
182. Li, Q. & Zhang, Z. Bonding and Anti-bonding Modes of Plasmon Coupling Effects in TiO<sub>2</sub>-Ag Core-shell Dimers. *Sci. Rep.* **6**, 19433 (2016).
183. Clavero, C. Plasmon-induced hot-electron generation at nanoparticle/metal-oxide interfaces for photovoltaic and photocatalytic devices. *Nat. Photonics* **8**, 95–103 (2014).
184. Zhang, X., Chen, Y. L., Liu, R.-S. & Tsai, D. P. Plasmonic photocatalysis. *Rep. Prog. Phys.* **76**, 046401 (2013).
185. Wei, H., Pan, D. & Xu, H. Routing of surface plasmons in silver nanowire networks controlled by polarization and coating. *Nanoscale* **7**, 19053–19059 (2015).

186. Linic, S., Christopher, P. & Ingram, D. B. Plasmonic-metal nanostructures for efficient conversion of solar to chemical energy. *Nat. Mater.* **10**, 911–921 (2011).
187. Xin, B., Jing, L., Ren, Z., Wang, B. & Fu, H. Effects of Simultaneously Doped and Deposited Ag on the Photocatalytic Activity and Surface States of TiO<sub>2</sub>. *J. Phys. Chem. B* **109**, 2805–2809 (2005).
188. Tian, Y. & Tatsuma, T. Mechanisms and Applications of Plasmon-Induced Charge Separation at TiO<sub>2</sub> Films Loaded with Gold Nanoparticles. *J. Am. Chem. Soc.* **127**, 7632–7637 (2005).
189. Christopher, P., Xin, H. & Linic, S. Visible-light-enhanced catalytic oxidation reactions on plasmonic silver nanostructures. *Nat. Chem.* **3**, 467 (2011).
190. Linic, S., Christopher, P. & Ingram, D. B. Plasmonic-metal nanostructures for efficient conversion of solar to chemical energy. *Nat. Mater.* **10**, 911–921 (2011).
191. Zheng, B. Y. *et al.* Distinguishing between plasmon-induced and photoexcited carriers in a device geometry. *Nat. Commun.* **6**, 7797 (2015).
192. White, T. P. & Catchpole, K. R. Plasmon-enhanced internal photoemission for photovoltaics: Theoretical efficiency limits. *Appl. Phys. Lett.* **101**, 073905 (2012).
193. Liu, Z., Hou, W., Pavaskar, P., Aykol, M. & Cronin, S. B. Plasmon Resonant Enhancement of Photocatalytic Water Splitting Under Visible Illumination. *Nano Lett.* **11**, 1111–1116 (2011).

194. Cui, L., Wang, P., Fang, Y., Li, Y. & Sun, M. A plasmon-driven selective surface catalytic reaction revealed by surface-enhanced Raman scattering in an electrochemical environment. *Sci. Rep.* **5**, (2015).
195. Xiong, L.-B., Li, J.-L., Yang, B. & Yu, Y. Ti<sup>3+</sup> in the Surface of Titanium Dioxide: Generation, Properties and Photocatalytic Application. *J. Nanomater.* **2012**, 1–13 (2012).
196. Stevens, N., Priest, C. I., Sedev, R. & Ralston, J. Wettability of Photoresponsive Titanium Dioxide Surfaces. *Langmuir* **19**, 3272–3275 (2003).
197. Kazuhito Hashimoto and Hiroshi Irie and Akira Fujishima. TiO<sub>2</sub> Photocatalysis: A Historical Overview and Future Prospects. *Jpn. J. Appl. Phys.* **44**, 8269 (2005).
198. Fujishima, A. & Honda, K. Electrochemical Photolysis of water at a Semiconductor Electrode. *Nature* **238**, 238 (1972).
199. Hisatomi, T., Takanabe, K. & Domen, K. Photocatalytic Water-Splitting Reaction from Catalytic and Kinetic Perspectives. *Catal. Lett.* **145**, 95–108 (2015).
200. David M King and Xiaohua Du and Andrew S Cavanagh and Alan W Weimer. Quantum confinement in amorphous TiO<sub>2</sub> films studied via atomic layer deposition. *Nanotechnology* **19**, 445401 (2008).
201. Li, C., Zhao, Y. F., Gong, Y. Y., Wang, T. & Sun, C. Q. Band gap engineering of early transition-metal-doped anatase TiO<sub>2</sub>: first principles calculations. *Phys Chem Chem Phys* **16**, 21446–21451 (2014).

202. Hisatomi, T., Kubota, J. & Domen, K. Recent advances in semiconductors for photocatalytic and photoelectrochemical water splitting. *Chem Soc Rev* **43**, 7520–7535 (2014).
203. Chen, H., Liu, G. & Wang, L. Switched photocurrent direction in Au/TiO<sub>2</sub> bilayer thin films. *Sci. Rep.* **5**, (2015).
204. Kallioinen, J., Benkő, G., Sundström, V., Korppi-Tommola, J. E. I. & Yartsev, A. P. Electron Transfer from the Singlet and Triplet Excited States of Ru(dcbpy)<sub>2</sub>(NCS)<sub>2</sub> into Nanocrystalline TiO<sub>2</sub> Thin Films. *J. Phys. Chem. B* **106**, 4396–4404 (2002).
205. Tachibana, Y., Moser, J. E., Grätzel, M., Klug, D. R. & Durrant, J. R. Subpicosecond Interfacial Charge Separation in Dye-Sensitized Nanocrystalline Titanium Dioxide Films. *J. Phys. Chem.* **100**, 20056–20062 (1996).
206. Ajmal, A., Majeed, I., Malik, R. N., Idriss, H. & Nadeem, M. A. Principles and mechanisms of photocatalytic dye degradation on TiO<sub>2</sub> based photocatalysts: a comparative overview. *RSC Adv* **4**, 37003–37026 (2014).
207. Rochkind, M., Pasternak, S. & Paz, Y. Using Dyes for Evaluating Photocatalytic Properties: A Critical Review. *Molecules* **20**, 88–110 (2014).
208. Rodríguez-González, V., Ruiz-Gómez, M. A., Torres-Martínez, L. M. & Gómez, R. Photocatalytic Decomposition of Synthetic Alizarin Red S by Nickel Doped TiO<sub>2</sub>. *Top. Catal.* **54**, 490–495 (2011).
209. Sood, S., Mehta, S. K., Umar, A. & Kansal, S. K. The visible light-driven photocatalytic degradation of Alizarin red S using Bi-doped TiO<sub>2</sub> nanoparticles. *New J Chem* **38**, 3127–3136 (2014).

210. Whang, T.-J., Huang, H.-Y., Hsieh, M.-T. & Chen, J.-J. Laser-Induced Silver Nanoparticles on Titanium Oxide for Photocatalytic Degradation of Methylene Blue. *Int. J. Mol. Sci.* **10**, 4707–4718 (2009).
211. Chaker, H., Chérif-Aouali, L., Khaoulani, S., Bengueddach, A. & Fourmentin, S. Photocatalytic degradation of methyl orange and real wastewater by silver doped mesoporous TiO<sub>2</sub> catalysts. *J. Photochem. Photobiol. Chem.* **318**, 142–149 (2016).
212. Pu, Y.-C. *et al.* Au Nanostructure-Decorated TiO<sub>2</sub> Nanowires Exhibiting Photoactivity Across Entire UV-visible Region for Photoelectrochemical Water Splitting. *Nano Lett.* **13**, 3817–3823 (2013).
213. Christopher, P., Ingram, D. B. & Linic, S. Enhancing Photochemical Activity of Semiconductor Nanoparticles with Optically Active Ag Nanostructures: Photochemistry Mediated by Ag Surface Plasmons. *J. Phys. Chem. C* **114**, 9173–9177 (2010).
214. Kawamura, G. *et al.* Ag nanoparticle-deposited TiO<sub>2</sub> nanotube arrays for electrodes of Dye-sensitized solar cells. *Nanoscale Res. Lett.* **10**, (2015).
215. Zhao, W. *et al.* Photodegradation of Sulforhodamine-B Dye in Platinized Titania Dispersions under Visible Light Irradiation: Influence of Platinum as a Functional Co-catalyst. *J. Phys. Chem. B* **106**, 5022–5028 (2002).
216. de Souza, M. L. & Corio, P. Effect of silver nanoparticles on TiO<sub>2</sub>-mediated photodegradation of Alizarin Red S. *Appl. Catal. B Environ.* **136–137**, 325–333 (2013).
217. Sánchez-de-Armas, R. *et al.* Real-Time TD-DFT Simulations in Dye Sensitized Solar Cells: The Electronic Absorption Spectrum of Alizarin

- Supported on TiO<sub>2</sub> Nanoclusters. *J. Chem. Theory Comput.* **6**, 2856–2865 (2010).
218. Di Iorio, Y., Brusa, M. A., Feldhoff, A. & Grela, M. A. Electron Transfer from Photoexcited TiO<sub>2</sub> to Chelating Alizarin Molecules: Reversible Photochromic Effect in Alizarin@TiO<sub>2</sub> under UV Irradiation. *ChemPhysChem* **10**, 1077–1083 (2009).
219. Cui, Y., Goldup, S. M. & Dunn, S. Photodegradation of Rhodamine B over Ag modified ferroelectric BaTiO<sub>3</sub> under simulated solar light: pathways and mechanism. *RSC Adv.* **5**, 30372–30379 (2015).
220. Yang, J., Chen, C., Ji, H., Ma, W. & Zhao, J. Mechanism of TiO<sub>2</sub>-Assisted Photocatalytic Degradation of Dyes under Visible Irradiation: Photoelectrocatalytic Study by TiO<sub>2</sub>-Film Electrodes. *J. Phys. Chem. B* **109**, 21900–21907 (2005).
221. Kumar, R., Rashid, J. & Barakat, M. A. Zero valent Ag deposited TiO<sub>2</sub> for the efficient photocatalysis of methylene blue under UV-C light irradiation. *Colloids Interface Sci. Commun.* **5**, 1–4 (2015).
222. Reza, K., Asw, K. & Gulshan, F. *Parameters affecting the photocatalytic degradation of dyes using TiO<sub>2</sub>: a review.* (2015). doi:10.1007/s13201-015-0367-y
223. Luan, X. & Wang, Y. Preparation and photocatalytic activity of Ag/bamboo-type TiO<sub>2</sub> nanotube composite electrodes for methylene blue degradation. *Mater. Sci. Semicond. Process.* **25**, 43–51 (2014).
224. Lacerda, A. M., Larrosa, I. & Dunn, S. Plasmon enhanced visible light photocatalysis for TiO<sub>2</sub> supported Pd nanoparticles. *Nanoscale* **7**, 12331–12335 (2015).

225. Chowdhury, I. H., Ghosh, S. & Naskar, M. K. Aqueous-based synthesis of mesoporous TiO<sub>2</sub> and Ag-TiO<sub>2</sub> nanopowders for efficient photodegradation of methylene blue. *Ceram. Int.* **42**, 2488–2496 (2016).
226. Lu, Y., Yu, H., Chen, S., Quan, X. & Zhao, H. Integrating Plasmonic Nanoparticles with TiO<sub>2</sub> Photonic Crystal for Enhancement of Visible-Light-Driven Photocatalysis. *Environ. Sci. Technol.* **46**, 1724–1730 (2012).
227. Saikia, P., Miah, A. T. & Das, P. P. Highly efficient catalytic reductive degradation of various organic dyes by Au/CeO<sub>2</sub>-TiO<sub>2</sub> nano-hybrid. *J. Chem. Sci.* **129**, 81–93 (2017).
228. Zhao, D. *et al.* Enhanced Photocatalytic Degradation of Dye Pollutants under Visible Irradiation on Al(III)-Modified TiO<sub>2</sub>: Structure, Interaction, and Interfacial Electron Transfer. *Environ. Sci. Technol.* **42**, 308–314 (2008).
229. Bandara, J. & Pradeep, U. W. Tuning of the flat-band potentials of nanocrystalline TiO<sub>2</sub> and SnO<sub>2</sub> particles with an outer-shell MgO layer. *Thin Solid Films* **517**, 952–956 (2008).
230. Standridge, S. D., Schatz, G. C. & Hupp, J. T. Distance Dependence of Plasmon-Enhanced Photocurrent in Dye-Sensitized Solar Cells. *J. Am. Chem. Soc.* **131**, 8407–8409 (2009).
231. Tanjila, N., Rayhan, A., Alam, M. S., Siddiquey, I. A. & Hasnat, M. A. Electrochemical and spectroscopic insights of interactions between alizarin red S and arsenite ions. *RSC Adv* **6**, 93162–93168 (2016).
232. Carretero-González, J., Castillo-Martínez, E. & Armand, M. Highly water-soluble three-redox state organic dyes as bifunctional analytes. *Energy Env. Sci* **9**, 3521–3530 (2016).

233. Mahanthesha, K. R. *et al.* Cyclic voltammetric investigations of alizarin at carbon paste electrode using surfactants. *Int J Electrochem Sci* **4**, 1237–1247 (2009).
234. Zhang, K. *et al.* Amperometric sensing of hydrogen peroxide using a glassy carbon electrode modified with silver nanoparticles on poly(alizarin yellow R). *Microchim. Acta* **173**, 135–141 (2011).
235. Noorbakhsh, A. & Salimi, A. Amperometric detection of hydrogen peroxide at nano-nickel oxide/thionine and celestine blue nanocomposite-modified glassy carbon electrodes. *Electrochimica Acta* **54**, 6312–6321 (2009).
236. de Souza, M. & Corio, P. Surface-enhanced Raman scattering study of alizarin red S. *Vib. Spectrosc.* **54**, 137–141 (2010).
237. Villanueva-Cab, J., Wang, H., Oskam, G. & Peter, L. M. Electron Diffusion and Back Reaction in Dye-Sensitized Solar Cells: The Effect of Nonlinear Recombination Kinetics. *J. Phys. Chem. Lett.* **1**, 748–751 (2010).
238. Cameron, P. J. & Peter, L. M. Characterization of Titanium Dioxide Blocking Layers in Dye-Sensitized Nanocrystalline Solar Cells. *J. Phys. Chem. B* **107**, 14394–14400 (2003).
239. Di Iorio, Y., Rodríguez, H. B., San Román, E. & Grela, M. A. Photoelectrochemical Behavior of Alizarin Modified TiO<sub>2</sub> Films. *J. Phys. Chem. C* **114**, 11515–11521 (2010).
240. Iorio, Y. D., Román, E. S., Litter, M. I. & Grela, M. A. Photoinduced Reactivity of Strongly Coupled TiO<sub>2</sub> Ligands under Visible Irradiation: An Examination of an Alizarin Red@TiO<sub>2</sub> Nanoparticulate System. *J. Phys. Chem. C* **112**, 16532–16538 (2008).

241. Bisquert, J., Zaban, A. & Salvador, P. Analysis of the Mechanisms of Electron Recombination in Nanoporous TiO<sub>2</sub> Dye-Sensitized Solar Cells. Nonequilibrium Steady-State Statistics and Interfacial Electron Transfer via Surface States. *J. Phys. Chem. B* **106**, 8774–8782 (2002).